AGGREGATION AND DEPOSITION OF ESTUARIAL FINE SEDIMENT

By

WILLIAM H. MCANALLY

A DISSERTATION PRESENTED TO THE GRADUATE SCHOOL
OF THE UNIVERSITY OF FLORIDA IN PARTIAL FULFILLMENT
OF THE REQUIREMENTS FOR THE DEGREE OF
DOCTOR OF PHILOSOPHY

UNIVERSITY OF FLORIDA

1999

ACKNOWLEDGMENTS

TABLE OF CONTENTS

NOTATION

A = Hamaker constant, a proportionality factor in the London-van der Waals force

A_k and A_l = coefficients characteristic of sediment and size classes k and j, respectively

a_W = radius of the velocity meter cup wheel to center of cups

B_ρ = function relating aggregate density to concentration, salinity, temperature, and collisions

B_τ = function relating aggregate strength to concentration, salinity, temperature, and collisions

B_1, B_2, ... B_{14} and B_A, B_B, ... B_W = empirical coefficients

$\dot{c}_d$ = mass deposition rate

$\dot{c}_{d,i}$ = mass deposition rate for size class i

$\dot{c}_e$ = erosion rate in mass per time per unit area

$\dot{c}_{e,m}$ = empirical erosion constant

$\dot{c}_{e,NO}$ = reference value of the ratio $\dot{c}_{e,m}/\tau_s$

C = total sediment mass concentration

$\overline{C}$ = depth-averaged total sediment mass concentration

C_i = sediment mass concentration of size class i

$\overline{C_i}$ = depth-averaged concentration of size class i

$C_i(0+)$ = concentration of the i class just above the bed

$\dot{C_j}$ = mass change rate in class j sediment

$\dot{C_i} (agg)$ = rate of class i mass change by aggregation

$\dot{C_i} (flux)$ = rate of class i mass inflow from advection-diffusion and bed erosion/deposition

$\dot{C_i} (shear)$ = rate of class i mass change by flow-induced disaggregation

$\dot{C_i} (sum)$ = sum of rate of class i mass changes by all processes

C_0 = reference sediment concentration

C_1 , C_3 = zone concentration limits for mean settling velocity equations

C_2 = total concentration at the onset of hindered settling

C_D = drag coefficient

C_{DL} = drag coefficient for the rounded side of the left velocity meter cup

C_{DR} = drag coefficient for the open side of the right velocity meter cup

CEC = sediment cation exchange capacity

CEC_0 = reference cation exchange capacity

C_r = dimensionless sediment concentration = C/C_0

C_{ul} = upper concentration limit for enhanced settling

C_v = volume concentration

C_{z0} = sediment concentration just above the interface

D_1 = reference particle size

$D_{99.9}$ = near-equilibrium aggregate diameter, when rate of diameter growth is less than 0.1 percent in 1 min

D_a = aggregate diameter

$D_{a,lim}$ = limiting aggregate size

$D_{a,max}$ = maximum aggregate size

$D_{a,median}$ = median of aggregate diameter distribution

$D_{a,mode}$ = mode of aggregate diameter distribution

$D_{c,im}$ = diameter of collision sphere for an i class particle encountering an m class particle

D_e = aggregate equilibrium diameter

D_g = primary grain diameter

$D_{g,mode}$ = mode of grain diameter distribution

D_i = diameter of particle from size class i (also classes j, k, m, and l)

E_g = Brownian diffusion coefficient of the primary grain

E_{im} = relative diffusion coefficient for two particles

E_r = dimensionless collision intensity function

$EV(iK)$ = event in which any i particle collides with a particular k particle, referred to as K

$EV(Km)$ = event in which the K particle collides with any m particle

E_z = vertical diffusion coefficient

E_{zn} = diffusion coefficient for non-stratified flows

$f(K)$, $f(I)$, $f(M)$, $f(Ch)$ = weight fractions of the sample composed of kaolinite, illite, montmorillonite, and chlorite, respectively

f_c = adjustment to collision diameter function, F_c, to account for changing particle-size distribution

f_g = decimal fraction of material in the suspension that is strongly cohesive

f_τ and f_ρ = shear strength and density functions, respectively

f_p = factor in particle strength equation equal to $B_\tau / B_\rho^{2/(n_f-3)}$

F_c = collision diameter function

F_{ik} = force exerted on colliding i and k class particles

$F_p = F_p{}' \cos\theta$

$F_p{}'$ = coefficient representing the relative depth of interparticle penetration

F_y = yield strength of aggregates

g = acceleration of gravity

g_m = body acceleration force

g_{m0} = reference body acceleration force

G_L = measure of flow shear

G_{egr} = nondimensional measure of collision-inducing flow forces

G_0 = reference shearing rate

G_r = nondimensional shearing rate = G/G_0

h = water depth

H = hindered settling factor

$i, j, k, l, m, i1, i2,$ and l' = size class indices

$J\{i + k\}$ = class of a new particle formed by aggregation of an i class particle with a k class particle

k_e = turbulent kinetic energy

k_s = roughness size

$m_1, m_2 ... m_9, m_D, m_h,$ and m_t = empirical exponent coefficients

M_i = mass of i class sediment particle (also $k, j,$ and m)

M_{ik} = mass of a combined particle after collision of particles with mass M_i and M_k

$M_j(lower)$ = lower limit on particle mass in class j

$M_j(upper)$ = class upper limit on particle mass in class j

n = Manning roughness coefficient

n_f = fractal dimension of aggregates

n_i = number of particles per unit volume in size class i (also classes j, k, m, and l)

N_{ik} = number of two-particle (i and k) collisions per unit volume per unit time

N_{ikm} = number of three-body (i, k, and m) collisions per unit volume per unit time

N_{iklm} = number of four-body (i, k, l, and m) collisions per unit volume per unit time

N_R = random number, 0 to 1

$\mathbb{N}_k$ = total number of two-body and three-body collisions experienced by a k class particle per unit time per unit volume

$p(l=i1:i2)$ = the probability mass function for the likelihood that a particle disaggregation fragment will fall into a given size class

P_{aim} = probability of cohesion of colliding particles of size classes i and m

P_{dim} = probability of disaggregation of size class i into size class m

$\Pr[EV(iK)]$ = probability of event $EV(iK)$

Q, m_f, K_f, r, and q = empirical coefficients

R^2 = correlation coefficient

R_h = hydraulic radius

$\mathbb{R}_{ep}$ = particle Reynolds Number

$\mathbb{R}_g$ = gradient Richardson Number

$\mathbb{R}_{gc}$ = critical value of gradient Richardson number

$\mathbb{R}_{go}$ = global Richardson number

s = number of sediment size (mass) classes

S = fluid salinity

S_0 = reference salinity

S_r = dimensionless salinity = S/S_0

t = time

t_{ik} = duration of collision between an i class particle and a k class particle

t_{ikm} = total duration of a three-body collision between i, k, and m class particles

t_{median} = time for aggregate to grow to 90 percent of its steady-state size

T = temperature in deg Kelvin

T_c = temperature in deg Celsius

T_0 = reference temperature, deg Celsius

$T_{99.9}$ = time to reach $D_{99.9}$ from dispersed particle distribution

T' = normalized temperature = T_c/T_0

u_* = shear velocity

u_b = flow velocity just outside the bottom boundary layer

u_i = velocity of the i particle relative to another particle (also k and m)

u_{ik} = translational velocity of an aggregate formed by collision of an i particle and a k particle

u' = turbulent velocity fluctuation

U = resultant horizontal flow velocity magnitude

U_0 = free stream flow speed

U_L = mean flow velocity acting on the velocity meter left cup

U_R = mean flow velocity acting on the velocity meter right cup

$w = log_{10} \mathbb{R}_{ep}$

W_s = settling velocity

$W_{s,50}(C,T_c)$ = concentration and temperature-dependent median settling velocity

W_{sf} = free settling independent of concentration

$W_{s,i}$ = settling velocity of class i particle

W_{so} = reference settling velocity

$\overline{W_s}$ = mean settling velocity

x = length dimension or coordinate

x_i, x_m = displacement of particles i and m, respectively, in time t

x_W = distance from the wall

Y_e = standard error of estimate from regression equation

z = vertical length coordinate

α_a = aggregation efficiency factor

α_c = collision efficiency

α_d = collision disaggregation efficiency

α_{ikm} = three-body collision efficiency

α' = apparent collision efficiency

α'_a = Winterwerp's aggregation efficiency parameter

α'_d = Winterwerp's disaggregation efficiency parameter

α'_e = Winterwerp's diffusion efficiency parameter

β = particle collision frequency function

β_{im} = collision frequency functions between two particles of size classes i and m

$\beta_{B,im}$ = collision frequency function for Brownian motion

$\beta_{D,im}$ = collision frequency function for differential settling

$\beta_{s,im}$ = collision frequency function for shear

γ_{lk} = probability that a particle of size class k will form after disaggregation of a particle of size l

δ = thickness of the boundary layer

$\Delta\rho_a$ = aggregate density difference, $\rho_a - \rho$

$\Delta\rho_i$ = density difference of the i class particle, $\rho_i - \rho$

ΔM_k = mass of a fragment which breaks from a k particle

ΔR = interpenetration distance for two colliding aggregates

Δt = time interval

Δu_0 = velocity difference across the mud-water interface

Δy_l = thickness of the eroded layer

ϵ = rate of energy dissipation of flow

ϵ_0 = reference rate of energy dissipation of flow

ζ = exponent in size distribution equation

θ = angle between direction of u_i and the line connecting colliding i and k particle centers

Θ = angle between x axis and a location on the sphere's surface

κ = Boltzman constant

κ_v = von Karman coefficient

λ_o = Kolmogorov turbulence microscale length

λ_T = Taylor microscale length

μ = dynamic viscosity of the fluid

ν = kinematic viscosity of the fluid

Π = a function of nondimensional terms

Π_a = nondimensional function for combined effects of collision, aggregation, and disaggregation efficiency

Π_A = nondimensional function for aggregation efficiency

Π_c = nondimensional function for collision efficiency

Π_d = nondimensional function for disaggregation efficiency

ρ = fluid density

ρ_a = aggregate density

ρ_i = density of particles of size class i (also k, j, and m)

ρ_{el} = bulk density of the eroded layer

ρ_{fm} = density of the fluid mud

τ_a = aggregate shear strength

τ_b = boundary shear stress

$\tau_{cd,i}$ = critical shear stress for deposition of the i class (also k, j, and m)

τ_{ce} = critical shear stress for erosion

$\tau_{ik,k}$ = shear stress imposed on a k class particle by an i-k collision

$\tau_{ikm,k}$ = shear stress imposed on a k class particle by an i-k-m collision

τ_i = shear strength of the i class particle (also k, j, and m)

$\tau_{ik,k}^*$ = two-body (i-k) collision shear stress on k particle modified to account for randomness

$\tau_{ikm,k}^*$ = three-body (i-k-m) collision shear stress on k particle modified to account for randomness

τ_s = critical shear stress for mass erosion

τ_u = shear stress imposed on a particle by a velocity gradient across the particle

γ = ratio of number of three-body collisions to number of two-body collisions

ϕ = solids weight fraction

ϕ_l = minimum value of ϕ, below which $\tau_s = 0$

ω = angular speed of the velocity meter cup assembly.

AGGREGATION AND DEPOSITION OF ESTUARIAL FINE SEDIMENT

By

WILLIAM H. MCANALLY

May 1999

Chairperson: Ashish J. Mehta
Major Department: Coastal and Oceanographic Engineering

Estuarial fine sediments make both positive and negative contributions to the coastal environment and present significant challenges to the conservation and management of water resources; yet, tools to predict their transport are seriously deficient.

Aggregation processes dominate fine sediment transport. This work's objective was to develop an improved fine sediment aggregation processes description based on governing sediment and flow characteristics. A combined statistical and deterministic representation of aggregation processes was combined with the one-dimensional convection-diffusion equation for multiple size classes. The number of two-body and three-body particle collisions was expressed by simple statistical relationships, using a new collision-efficiency parameter. Possible collision outcomes were used with collision theory to calculate the rate of sediment mass change for each size class.

Kaolinite and Atchafalaya Bay mud deposition experiments were conducted in a 100-m long flume. Significant variability in measured suspended sediment concentrations can be explained as intermittent perturbation and upward mixing of a high concentration stirred layer flowing close to the bed, below the lowest sampling point.

The calculation method was applied to aggregation chamber and flume experiments. The aggregation processes calculation method was found suitable for use as a primary component of sediment transport numerical modeling, but it is computationally intensive.

Experiments showed that the number of three-body collisions in the estuarial environment is small with respect to two-body collisions, but they can contribute significantly to aggregation processes in sediment suspensions. Equilibrium median aggregate size is generally proportional to sediment concentration and inversely proportional to flow shearing rate. Aggregation speed may be either directly or inversely proportional to those two parameters, depending on fluid, flow, and suspension characteristics.

Production-level application of the aggregation calculations will require that they be incorporated in a three-dimensional, coupled, hydrodynamic and multi-grain-size sediment transport model. The method will provide a significant improvement to the tools available to those charged with conserving and managing water resources where fine sediments constitute a significant challenge.

CHAPTER 1
INTRODUCTION

1.1 Need for Research

Waterborne estuarial sediments are a valuable resource in many coastal areas, where they are needed to offset land and marsh losses (e.g., Boesch et al., 1994). Yet elsewhere excess fine sediments clog navigation facilities and smother valuable benthic habitat. In some locations, these sediments bind with contaminants such as PCBs that make them extremely hazardous. In each of these circumstances estuarial sediments challenge water resources agencies to provide active and informed management.

As an illustration of these challenges, consider one aspect of navigable waterway dredging. The United States spends more than $500,000,000[*] annually to dredge the nation's 40,000 km of waterways and to dispose of the dredged material. Ensuring that those dredging activities are accomplished at minimum public expense and with beneficial, or at least no adverse, impacts on fisheries habitat or water quality is the responsibility of water resources managers in multiple state and federal agencies. For example, open-water placement of dredged sediments must be accomplished in a way that (a) minimizes their return to the channels from which they were dredged, (b) prevents their accumulation in

---

[*] Personal communication, V. R. Pankow, U.S. Army Corps of Engineers Dredging Information Center, Alexandria, VA.

1

sensitive aquatic habitats, and/or (c) ensures that they will be transported to areas where they are needed to nourish shores or wetlands. The tools and techniques available to resource managers at present cannot reliably provide the quantitative information needed to evaluate dredging and disposal plans against these criteria. The absence of this capability exacts large economic costs, erodes public confidence, and may contribute to unacceptable environmental impacts.

Traditional estuarial physical model sedimentation investigations have all but disappeared from the engineer's tool chest because they are costly and fail to represent some important physical processes such as aggregation of fine-grained sediment particles (Letter and McAnally, 1981). Physical models have been replaced in part by concentration-based numerical models that also fall short in some important respects. The present generation of fine-grained sediment transport numerical models mainly use one of two approaches for geophysical scale computations—highly parameterized Eulerian methods that produce estimates of sediment concentration fields and macro-scale deposition/erosion rates (e.g., Thomas and McAnally, 1985) or Lagrangian calculations of inert (non-aggregating) particles' trajectories (e.g., Hess, 1988). None provide the true tracking of continuously aggregating sediment particles that is needed to best manage estuarial water resource projects. Better methods are needed.

Given these limitations and needs, the objective of this work and associated principal tasks are given below.

1.2 Objective and Tasks

The objective of this work is to develop an improved, physics-based representation of fine sediment aggregation based on sediment and flow characteristics in estuarial waters.

The principle tasks undertaken to achieve this objective were:

1.   to develop a conceptual approach for suspended fine sediment transport,

2.   to develop an analytic representation of fine sediment aggregation,

3.   to devise a method for calculating deposition of fine sediment with ongoing aggregation,

4.   to assess the method's domain of applicability by testing against experimental results, and

5.   to assess future research needs in these areas.

1.3 Approach

1.3.1 Overall Approach

To achieve the above objective, an engineering method has been developed that integrates continuing fine sediment aggregation process calculations with a multiple size class deposition algorithm. The method was tested against simple mixing-chamber data to ensure rigor, then against laboratory-flume data to ensure successful reproduction of the physical processes. Finally, it was used to explore some basic aggregation processes.

Conclusions were drawn as to the future research needed to improve knowledge of estuarial sediment aggregation and to provide better calculation methods.

1.3.2 Sediment Aggregation and Deposition

The sediment aggregation and deposition calculation method consists of three parts:

1. a multiple sediment class scheme that accurately characterizes size, density settling velocity, and strength;

2. calculation of changes in the sediment particles characteristics (additional mass, size, shape, and settling velocity) as they are altered by particle and/or flow-induced aggregation/disaggregation processes; and

3. computation of sediment deposition rate under the influences of settling, mean flow, and turbulence.

Figure 1-1 illustrates the concept of a fine sediment particle undergoing aggregation processes, possible settling to the bed, and pickup from the bed. A particle, either an individual grain or an aggregate of many grains, may originate in the water column or in the bed. Once in suspension, it is subject to forces due to gravity, inertia, mean flow, turbulent fluctuations, and collisions with other particles in suspension. It may undergo aggregation processes in the water column, bonding with other particles and breaking apart from them. If the aggregate grows large enough, it settles toward the bed and enters a stirred layer of high sediment concentration and high shear. There it may deposit to the soft mud layer and eventually become part of the bed, or it may be broken into smaller particles and be picked up by the flow and begin the process anew.

1.3.2.2 Sediment Aggregation Processes

As particles move through the water, they undergo aggregation and disaggregation according to a rate model developed in Chapter 3. The method calculates particle aggregation and disaggregation as a function of concentration, temperature, flow shearing,
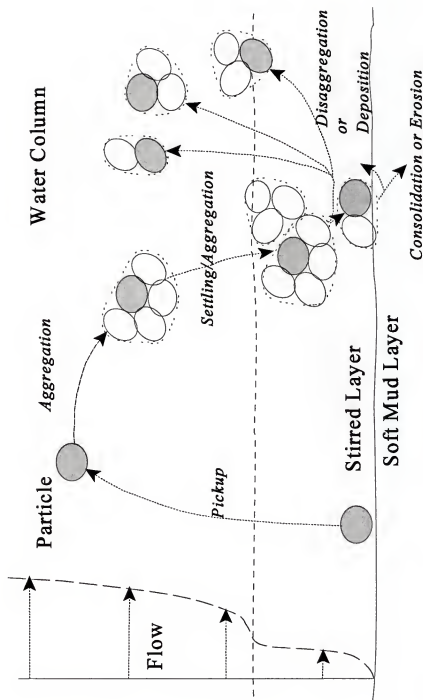
Figure 1.1. Path of an idealized sediment particle undergoing aggregation processes and transport.

and differential settling for a spectrum of particle sizes. As described below, particle characteristics and numbers are also changed by interaction with the bed. The method calculates the sediment mass in each designated class as aggregation moves mass to larger sizes and disaggregation moves mass to smaller classes.

1.3.2.4 Settling and Deposition

Particles in transport settle toward the bed and are mixed by turbulence as modified by water-column stratification. When sediment particles approach the bed through settling, they enter a stirred layer of very high concentrations and imposed stresses. Particles with strength sufficient to resist breakup may be deposited onto the soft mud layer below the stirred layer, while weaker particles are broken and picked up by the flow, returning to suspension. A simple algorithm for calculating multiple size class transport and deposition with ongoing aggregation is described in Chapter 4.

1.3.3 Assessment of Applicability

The method was tested for:

1. proof of concept—the aggregation algorithm was tested to ensure that it conserves sediment mass and reproduces observed general trends in aggregating fine sediment size spectra.

2. reproduction of physical processes—the aggregation algorithm was tested against laboratory mixing chamber aggregation experiments using Detroit River, Amazon Delta, and kaolinite sediments; and

3. realism—the combined aggregation and deposition calculation method was tested against flume experiments using fine-grained sediments of kaolinite, Atchafalaya Bay, and San Francisco Bay sediments.

1.4 Scope

The work described here is concerned with the aggregation, disaggregation, and deposition of fine-grained, estuarial sediments—processes shown in the central portion of Figure 1-1. The sediment grains considered typically have diameters less than 63 µm and form aggregates consisting of mineral grains and organic materials. As they undergo aggregation and settle they often form soft, low-density layers (called fluff or fluid mud) on the bed. In this work, formation of a fluff layer is addressed, but its possible flow or entrainment is neglected. The role of organic materials and biological processes in fine sediment aggregation is acknowledged, but is not explicitly included in the analysis.

Estuaries are semi-enclosed bodies of water having a free connection to the open sea and within which seawater is measurably diluted with freshwater derived from land drainage (Pritchard, 1952). The hydraulic regime considered is that typical of United States estuaries—flows under the combined effects of tides, river discharge, winds, and density gradients. Although short-period (wind) waves are important to sediment transport in many estuaries, they are neglected here in favor of testing the basic formulation of the problem.

1.5 Presentation Outline

This dissertation consists of seven chapters:

1. Introduction

2. Fine sediment transport - characterizes fine waterborne sediments and their behavior.

3. Aggregation processes - proposes an aggregation model for use in sediment transport calculations.

4. Multi-class deposition with aggregation - presents an algorithm for settling and deposition of multiple size classes with ongoing aggregation.

5. Sediment transport and deposition experiments - describes experiments used to test the method's accuracy and reliability.

6. Method application - compares results from the aggregation model and the aggregation and deposition calculation method with experiments.

7. Conclusions - summarizes the method and tests, gives conclusions on the method's applicability and aggregation processes, and recommends future work.

CHAPTER 2
FINE SEDIMENT TRANSPORT

2.1 Estuarial Sediments

Sediments carried by estuarial waters typically encompass a range of sizes from less than 2 µm to more than 4 mm, but the finer sizes dominate most estuaries. In a few, such as the Columbia River Estuary in the United States and the Changjiang River Estuary in China, the beds are composed primarily of sand sizes greater than 62 µm, at least in the main body of the estuary. The bed and banks of most estuaries, however, tend to be dominated by clays and silts, with sand and larger sizes depositing either at the head of the estuary (upstream sources) or at the ocean entrance (downstream sources). Notable U.S. examples of fine sediment dominance include San Francisco Bay, Galveston Bay, Charleston Harbor, and the Hudson River Estuary/New York Harbor (CTH, 1971).

The primary focus here is on fine-grained sediments—clay sizes and some silts. These sediments include both inorganic and organic materials and are almost universally called muds, the primary exception being the U.S. scientific community, which seems to find the word "mud" unattractive. Further, while this chapter deals with the spectrum of fine sediment processes, the emphasis is on aggregation of fine particles which occurs in the estuary and how that aggregation influences other sedimentary processes.

2.2 Fine Sediments Classification

For transport purposes fine sediments are characterized by their size, by constituent composition, and by cohesion. The following describes those distinctions and introduces the terminology used to describe fine sediments and fine sediment processes.

2.2.1 Size

Sediments in waterborne transport are usually classified as fine if the grain size is less than 63 µm (0.063 mm), the Wentworth Scale division between sands and silts.

The Wentworth size scale divides fines into silts (size > 4 µm) and clays (size < 4 µm) and then further divides each category into coarse, medium, fine, and very fine. However, within the general class of fine sediments, those size distinctions are less important to transport processes than sediment cohesion, although size and cohesion are related as shown in Table 2-1.

Table 2-1. Size and Cohesion in Fine Sediments.

Size µm	Wentworth Scale Classification	Cohesion
40 - 62	Medium silt to coarse silt	Practically cohesionless
20 - 40	Fine silt to medium silt	Cohesion increasingly important with decreasing size
2 - 20	Coarse clay to very fine silt	Cohesion important
< 2	Very fine clay to medium clay	Cohesion very important

Source: Mehta and Li, 1997.

2.2.2 Constituents

Fine sediments in estuaries are mixtures of inorganic minerals, organic materials, and biochemicals (Mehta, 1991). Mineral grains consist of clays (e.g., montmorillonite, illite, and kaolinite) and non-clay minerals (e.g., quartz and carbonate). Use of the word "clay" to distinguish both a size class and mineral composition causes some confusion, and here the word "clay" will be used to describe the mineral composition only, except when referring to Wentworth Scale size classifications. Organic materials include plant and animal detritus and bacteria. The relative organic/non-organic composition of estuarial sediments varies over wide ranges between estuaries and within the same estuary spatially and seasonally (Kranck, 1980c). Luettich et al. (1993) reported organic fractions in suspended sediment ranging from 18 percent to 85 percent in Cape Lookout Bight, NC, with higher organic concentrations in February than November.

2.2.3 Cohesion

Cohesion describes the tendency of fine sediment grains to bind together (aggregate) under some circumstances, which significantly affects sediment behavior, as described below. In general, smaller grains are more cohesive, with diameters greater than 40 μm essentially cohesionless, and cohesion becoming progressively more important as grain size decreases, as shown in Table 2-1 (Mehta and Li, 1997).

Clay minerals consist of silicates of aluminum and/or iron plus magnesium and water and typically contain sorbed anions (e.g., NO_3^-) and cations (e.g., Na^+) which can be

exchanged with ions in the surrounding fluid (Grim, 1968; Partheniades, 1971; Mehta and Li, 1997). Clay crystals occur in platelike and rod shapes, usually with the long faces exhibiting a negative electrical charge and the edges exhibiting a positive charge due to the exposed lattice edges and sorbed ions. The surface charges are measured in terms of the ease with which cations held within the lattice can be exchanged for more active cations in the surrounding fluid—the cation exchange capacity (CEC) being expressed in milliequivalents per 100 gm of clay. Table 2-2 lists the four most common clay minerals, their characteristic size, their CEC, and the salinity critical to aggregation (also called flocculation or coagulation), which is discussed below.

The cohesion of estuarial fine sediments may be changed from that of their constituent clay minerals by metallic or organic coatings on the particles (Gibbs, 1977; Kranck, 1980b).

Table 2-2. Common Clay Minerals and Their Typical Characteristics.

Clay Mineral	Grain Size μm	Equivalent Circle Diameter μm	Cation Exchange Capacity meq/100g	Critical Salinity for Aggregation ppt
Kaolinite	1 by 0.1	0.36	3 - 15	0.6
Illite	0.01 by 0.3	0.062	10 - 40	1.1
Smectite (Montmorillonite)	0.001 by 0.1	0.011	80 - 150	2.4
Chlorite	0.01 by 0.3	0.062	24 - 45	--

Sources: Mehta and Li (1997); CTH (1960); Grim (1968); Ariathurai et al. (1977).

Immersed grains of micron-sized clay minerals cannot settle in a quiescent fluid, since Brownian motion is sufficient to overcome their small submerged weight. Only when

many individual grains are bound together by intergrain forces into an aggregate do they gain

sufficient weight to settle, and therefore the aggregation process is critically important to fine

sediment transport.

2.2.4 Terminology

From the sometimes slippery terminology regarding fine sediments, the following

definitions have been adopted for use here:

aggregate: a number of grains bound together by interparticle forces, or a cluster of several smaller aggregates, often called a floc

aggregation: the process by which colliding particles bind together into aggregates, often called flocculation

aggregation process: mechanisms by which the flow environment and interparticle collisions cause particles to form aggregates, aggregates to grow larger, or aggregates to break into smaller particles (disaggregation)

bed: that portion of the sediment profile where particle-to-particle contact provides a continuous structure and no horizontal movement occurs

concentration: mass of sediment per unit volume of sediment-water mixture

consolidation: change in volume of the sediment bed to an applied loading which squeezes water out of the pore spaces, i.e., process by which the bed density increases

deposition: the process by which a particle comes in contact with the bed and binds with it

disaggregation: the process by which an aggregate's bonds are severed and two or more smaller particles result

entrainment: upward movement through a lutocline of a particle that has previously settled through the lutocline into a high-concentration (stirred) layer near the bed

erosion: stripping of particles from the bed or an aggregate by flow-induced stresses

grain: an individual, solid piece of sediment composed of a single mineral or material

lutocline: a pycnocline caused by suspended sediment concentration stratification

number concentration: number of particles per unit volume of sediment-water mixture

particle: a sediment grain or aggregate

pickup: movement of a sediment particle into the flow after erosion or entrainment

pycnocline: a density interface or sharp density gradient in the water column

settling: gravity-induced net downward movement of a particle

volume concentration: volume of sediment per unit volume of sediment-water mixture

These definitions lead to the following notation used in subsequent equations: subscript "g" indicates a grain property and subscript "a" indicates an aggregate property.

2.3 Aggregation Processes

Aggregation of fine sediment grains into larger, multiple-grain particles occurs when a collision brings two particles close enough together for mutually attractive forces to overcome repulsive forces, and the two particles bond as a result of those attractive forces. Similarly, fluid forces and collisions exceeding aggregate strength will break aggregates apart. The following sections discuss aggregation processes as they affect the size, shape, density, and strength of the aggregates, and thus their settling velocity and ability to deposit and remain on the bed.

2.3.1 Interparticle Forces

The forces acting on waterborne sediment particles (grains and aggregates) include:

1.   Fluid forces

   a.   Brownian motion impacts. Thermal motion of the fluid molecules causes impacts between the molecules and individual sediment grains, imparting "kicks" that move the grains in random directions.

   b.   Turbulent normal stresses. Very small-scale turbulent fluid eddies apply pressure forces that, like Brownian motion, impart random motion to particles of size similar to the eddies.

   c.   Shear stresses. Both laminar and turbulent shear flows impose shearing stresses on particles that are of the same size order as the distance over which the velocity changes significantly.

   d.   Mean flow drag. Any difference between the mean flow velocity and the particle mean velocity will result in a drag force due to pressure and frictional forces.

2.   Particle forces

   a.   Van der Waals attraction. Generated by mutual influence of electron motion within the sediment grains, van der Waals forces act between all matter and are extremely strong, but decay very rapidly (to the 3rd to 7th power) with distance, so sediment grains must be very close together before the forces exert a significant influence (Partheniades, 1971).

   b.   Electric surface attractions and repulsions. The surface electrical charges of fine sediment grains induce both attractive and repulsive forces between two similar grains.

   c.   Collisions. Colliding sediment particles impart forces and torques on one another.

3.   Other forces. Once two or more fine sediment particles bond together, additional forces may act on them, including chemical cementation, organic cementation, and the forces due to pore fluid motion at extremely small scales (Partheniades, 1971).

The electrical forces of item 2b above include predominantly negative surface charges of most fine sediment grains (exceptions are some metal hydroxides that have positive face charges and negative edge charges) that give most fine sediment grains a net negative charge which induces a repulsive force between two similar grains. If the overall repulsive force is reduced and the positive edge of one grain approaches the negative face of another, the two grains may bond in a T formation. The overall charge of a grain attracts a cloud of opposite-charge ions if they are available in the surrounding fluid. The cloud of ions, called the double layer, balances the grain's net charge and represents an equilibrium in the ion field between the electrical attraction toward the grain and diffusion away from it. The double layer exerts a repulsive force on other like-charged sediment grains and their double layer, just as the net charge does, and also extends outward some distance to keep grains farther apart. These electrical forces are weaker than the van der Waals force, but they decay more slowly with distance, so they dominate the net force between grains unless other processes come into play as discussed below. In a fluid with abundant free ions the double-layer thickness is suppressed, reducing the distance over which the repulsive forces act and permitting grains to approach more closely (Partheniades, 1971). The electrically neutral unit consisting of a mineral grain and its double layer is called a clay micelle.

2.3.2 Environmental Effects

2.3.2.1 Salinity

In nearly ion-free water the net grain charge keeps cohesive grains apart, and only those collisions bringing an edge (typically positive) directly to an oppositely charged face

can bring the two close enough together to allow the van der Waals forces to bind them in a T-shaped configuration. Adding only a few free ions (for example, by dissolving salt in the fluid) creates large ionic double layers and retards aggregation by repulsing grains at larger spacings, but at some higher ionic concentration the double layer's diffusion is suppressed and it shrinks, permitting closer approach between grains and collisions that overcome the faces' electrical repulsion so that the short-range van der Waals forces can bind them face to face. The critical ion concentration at which aggregation begins to increase varies with the clay minerals present, as shown in Table 2-2. Aggregate size, strength, and settling velocity are functions of salinity up to about 10-12 parts per thousand (ppt), after which they are commonly believed to no longer vary with ion concentration (Krone, 1986). In laboratory experiments Burban et al. (1989) found that the mean aggregate size of Lake Erie sediments was larger in fresh water than in sea water, and at intermediate salinities the mean size seemed to be a salinity-weighted average of freshwater and saltwater sizes.

Under low ionic concentrations aggregate structures are likened to a house of playing cards, with large pore spaces, low density, and low strength, since the edge-to-face connection puts only a few molecules within the range of the attractive forces. Such aggregates commonly occur in freshwater lakes. At the higher dissolved ion concentrations of upper estuaries and some rivers, the orientation of aggregated grains tends toward face-to-face contacts and most often resembles a deck of cards that has been messily stacked. With larger contact areas and shorter moment arms, such structures are significantly stronger than edge-to-face orientation.

2.3.2.2 Concentration

Collisions between particles, and thus aggregation rate, rises with increasing concentration of sediment. As discussed in subsequent sections, a distinct correlation between settling velocity and concentration is observed.

2.3.2.3 Organics

Organic materials may make up a large fraction of suspended sediments, and they can alter the behavior of nonorganic sediment components. Organic materials in sediments include plant and animal parts, animal waste products, and living bacteria. Mucous filaments formed by bacteria are observed coating some aggregates and appear to reinforce the physico-chemical bonds holding them together (Kranck, 1986; Luettich et al., 1993). McCave (1984) showed that active contributions to oceanic aggregation by zooplankton filtering can be significant compared to inorganic processes alone, and Kranck and Milligan (1992) reported that a mixture of 50 percent organic and 50 percent nonorganic sediments settles an order of magnitude faster than an equivalent concentration of 100 percent mineral grains. The effect has not been well quantified and thus is generally included implicitly with collision mechanisms (described below) when considering aggregation of fine sediments that are composed primarily of mineral grains.

2.3.2.4 Others

Temperature affects aggregation; however, over a normal range of temperatures in temperate estuarial waters the effect is usually considered to be small (Partheniades, 1971) and may be dominated by biogenic effects. Slightly acid waters likewise appear to increase

aggregation (Tsai and Hu, 1997), but pH is not highly variable in estuarial waters and thus is usually ignored (CTH, 1960; Partheniades, 1971).

2.3.3 Collisions Among Particles

Given a suspension of cohesive grains with sufficient dissolved salts and enough grains to permit aggregation, five mechanisms are responsible for collisions that can lead to aggregation.

1.   Brownian motion affects grains and small aggregates of only a few grains and is thus most important in the early stages of aggregation and in very quiet waters. Hunt (1982) found that Brownian motion was the most common collision mechanism when particle volumes were less than 0.1 cu μm, which corresponds to a cube size less than 0.5 μm on a side, or the same order as the grain sizes in Table 2-2. Brownian motion is considered to be a negligible factor in estuarial waters aggregation (Partheniades, 1993; van Leussen, 1994).

2.   The local velocity gradient in laminar or turbulent fluid shearing allows one particle to overtake and capture another. Since the particles must be large enough to experience an effective velocity gradient across one average diameter, shear accounts for the aggregation of two particles already containing a number of individual grains. Hunt (1982) concluded that shear was the most common aggregation mechanism for particles of volume 10 to 1000 cu μm, or 2 to 10 μm-size cubes.

3.   Differential settling results in collisions as faster-settling particles overtake slower-settling ones and capture them. The fluid around a solid sphere overtaking another solid sphere tends to push the slower sphere out of the way before contact occurs; however, the open structure of aggregates permits a greater incidence of collisions than would occur for solid particles. Hunt (1982) found that differential settling became the most common collision mechanism at particle volumes greater than 10^5 cu μm, which corresponds to cubes larger than about 50 μm on a side or spheres of about 60 μm diameter.

4.   Inertial response to local fluid acceleration by particles of different mass produces different particle velocities and thus collisions. McCave (1984) found inertial response to be significant for particle size differences of about 1000 μm.

5. Biogenic aggregation occurs when zooplankton sweep or filter water, inducing collisions among the trapped sediment particles (McCave, 1984).

The relative importance of these mechanisms varies with particle size and flow conditions, and assertions that one or another is negligible are abundant in the literature, depending on the authors' processes of interest and range of experimental conditions. For example, Stolzenbach and Elimelich (1994) concluded from settling-column experiments that differential settling is much smaller than traditionally assumed and is even absent in some environments, whereas Hawley (1982) found differential settling to be the governing non-biological process in lakes and the ocean. Creation of very large aggregates such as seen in the deep ocean or other very quiet waters are usually attributed to aggregation by differential settling (Kranck, 1980a; Lick et al., 1993).

These mechanisms can produce characteristic aggregates. Brownian motion and differential settling tend to produce lower density and weaker aggregates than those formed by shear (Krone, 1978), and differential settling produces significantly nonspherical shapes, as discussed in a subsequent section.

2.3.4 Aggregation

Krone (1963) observed that given the known interparticle forces, every individual grain or low-order aggregate collision results in aggregation for salinities greater than about 1 ppt, and that collision frequency was a function of temperature, concentration, the cube of the sum of particle radii, differential settling velocity, and shear rate. He noted that larger, more fragile colliding aggregates may break, so not all such collisions will produce a lasting

bond. Collision probabilities can be computed for each of the mechanisms listed in the preceding section (Smoluchowski, 1917; Overbeek, 1952; McCave, 1984), and together with the concept of collision efficiency (in which it is assumed that only some collisions result in aggregation) are used in aggregation models (e.g., van Leussen, 1997) in the form:

$$N_{ik} = \alpha' \beta \, n_i \, n_k \tag{2-1}$$

where

N_{ik} = frequency of two-particle (i and k) collisions,

α' = apparent collision efficiency factor,

β = collision function that is dependent on mechanism, environment, and particles, and

n_i, n_k = number concentration of i and k class particles.

The apparent collision efficiency factor is a function of free ions, particle surface charge, temperature, and geometry of the particles (Teeter, 1999a). O'Melia (1985) estimated that the value of the collision efficiency is on the order of 0.001 to 0.1. Edzwald and O'Melia (1975) found in laboratory experiments that the efficiency increased with salinity up to about 18 ppt and ranged from about 0.02 to 0.15 for pure mineral clays. Ten Brinke (1997) calculated α' values ranging from 0.02 to 0.23 by fitting a representative grain size model to data from the Oosterschelde. Han (1989) developed an aggregation-only numerical model and found it required efficiency values ranging from 1×10^{-5} to 1×10^{-1} for fluid shear collisions and from 1×10^{-4} to 1×10^{-1} for differential settling collisions. The range in orders of magnitude in experimentally derived efficiencies suggests that too many

disparate effects have been lumped into that single parameter, transforming the efficiency into a very large tuning knob.

As noted, Equation 2-1 applies to two-particle collisions. Assertions in the general literature as to the importance of three-particle collisions rival the variety of those concerning the four different collision mechanisms, ranging from statements that three-body collisions ". . . almost never occur . . ." in organic chemistry reactions (Fort, 1997) to those saying they dominate, as in plasma flows (MacFarlane, 1997). In sediment studies Lick and co-workers (e.g., Lick et al., 1992) concluded that three-body collisions contribute significantly to disaggregation processes. Three-body collisions are treated further in Section 3.3.2.

2.3.5 Disaggregation

Once formed, aggregates may disaggregate, that is, break under flow shearing or collision with other aggregates. Disaggregation by flow shear alone far from a boundary may be small, since free aggregates can rotate with a shear stress imbalance and thus reduce shear across the particle (Lick and Lick, 1988), but may become a dominant mechanism in the near-bed zone where the sharpest velocity gradients and bursting phenomena occur and where even a brief contact with the bed can halt rotation and greatly increase stresses in the aggregate (Mehta and Partheniades, 1975). Argaman and Kaufman (1970) asserted that stripping of individual grains from aggregates was an important disaggregation mechanism.

Burban et al. (1989) found that a model of aggregate growth and breakage, including Brownian motion, fluid shear, and two-body particle collisions, could not reproduce observed data unless three-body collisions were at least indirectly considered. As would be

expected, the three-body collision effect increased with increasing concentration. Indirectly including three-body collisions in a later version of the same model, Lick et al. (1992) showed that the terms representing disaggregation by fluid shear alone (without collisions) had a negligible effect on disaggregation except perhaps at very low shears and very low concentrations.

Disaggregation occurs primarily as the tearing of aggregates, rather than their shattering into many pieces (Hogg et al., 1985), and according to Krone's order of aggregation model (see following section), should occur by stripping off the largest aggregate with the correspondingly weakest bond. Tsai and Hwang (1995) found that aggregates tended to break into two roughly equal-sized pieces when disaggregating.

2.3.6 Aggregate Formation Descriptors

2.3.6.1 Order of aggregation

Krone (1963) inferred a conceptual model of aggregation from rheological tests of fine sediment suspensions. In his model, initial aggregation creates small, compact aggregates of primary grains with strong bonds. He referred to these initial aggregates as particle aggregates or "zero order aggregates" (p0a). Subsequent collisions between particle aggregates create slightly weaker bonds between two or more particle aggregates, leading to an assemblage of p0a's, a particle aggregate aggregate, or first order aggregate (p1a). Successive levels (orders) of aggregation lead to particle aggregate aggregate aggregates (p2a) and so on. Figure 2-1 illustrates the concept.
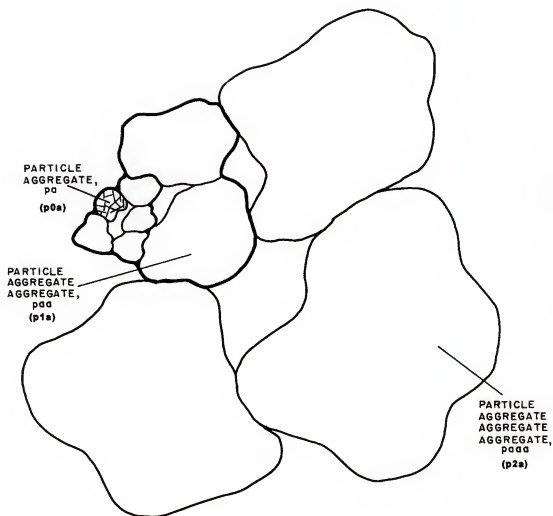
Figure 2-1 A third order (paaaa or p3a) aggregate is formed by the aggregation of second order aggregates (p2a), which consist of first order aggregates (p1a), which consist of zero order aggregates (p0a) made up of sediment grains. Source: Krone (1963). Reprinted with permission.

From experiments with sediments from five locations covering the U.S. Atlantic, Gulf of Mexico, and Pacific coasts, plus one inland river, Krone (1963) calculated up to 6 orders of aggregation with corresponding densities and strengths for each. His results for San Francisco Bay sediment are shown in Table 2-3.

Table 2-3. Characteristics of Orders of Aggregation in San Francisco Bay Sediment.

Order of Aggregation	Aggregate Density[a] kg/m^3	Aggregate Strength Pa
0	1,269	2.2
1	1,179	0.39
2	1,137	0.14
3	1,113	0.14
4	1,098	0.082
5	1,087	0.036
6	1,079	0.020

Source: Krone (1963).
[a] Aggregates in sea water of density 1,025 kg/m^3.

Krone (1963, 1986) defined the following relationships between orders of aggregation:

1. An aggregate exists in one of several orders determined by growth history or shear disaggregation, whichever is limiting.

2. Aggregate size is independent of order, except that for a given aggregate an increase in order means an increase in size and vice versa.

3. An increase in aggregate order results in an increase in settling velocity and vice versa.[*]

_____

[*] This relationship may not be universal; it is examined further in Section 2.4.3.

4.   Shearing rates in normal flows far from boundaries such as the bed are low with respect to those needed to break aggregates of high order.

5.   Normal flow shearing rates at the bed are of the same general magnitude as those needed to break high-order aggregates, and so limit the order of aggregation (See Mehta et al., 1983).

6.   At low bed shears, higher-order aggregates can deposit on the bed.

2.3.6.2 Fractals

A model of aggregate structure based on the fractal principle of self-similar geometry has been used to examine aggregate properties (e.g., Meakin, 1988; Kranenburg, 1994; and Winterwerp, 1998, 1999). The basic model, which has long been used in wastewater treatment research, assumes that aggregate structure conforms (at least approximately) to the fractal property of self-similarity at all scales. Self-similar structure will lead to a power-law relationship between aggregate size and properties such as density and surface area. For example, the relationship between density and diameter for a three-dimensional aggregate can be expressed as:

$$\rho_a \propto D_a^{n_f - 3} \tag{2-2}$$

where

ρ_a = aggregate density,

D_a = aggregate diameter, and

n_f = fractal dimension.

For bodies in three-dimensional Cartesian space, $1 \le n_f \le 3$. For a non-fractal solid sphere, n_f would have a value of 3. Wiesner (1992) showed that for Brownian motion aggregation, an irreversible process, n_f should have a value of about 1.78. For reaction-limited, reversible processes such as shear-induced collisions, it should be about 1.9 to 2.1. He noted, however, that for distinct scales of structure (such as Krone's order-of-aggregation model) each scale may be characterized by a different fractal dimension and the overall apparent dimension will be larger, perhaps 2.1 to 2.6 for a two-level (p1a) structure.

Kranenburg (1994) noted that it would be naive to assume that the complex, multi-component structure of real muds possesses completely self-similar geometry. He concluded that muds were probably only approximately self-similar, but that the concept seemed useful in interpreting experimental results. The following section includes some of those interpretations as well as those of Krone's model.

2.4 Characterizing Aggregates

From the transport perspective, the most important aggregate characteristics are settling velocity and strength, for the first determines (along with the flow) the relative sediment concentration vertical profile and how rapidly settling particles approach the bed, and the second dictates whether or not an aggregate survives disaggregating forces to deposit and whether or not a deposited aggregate is resuspended. Other aggregate properties, such as shape, size, and density, affect settling velocity and strength, so they are examined first.

2.4.1 Shape

Krone (1986) noted that the aggregates in his experiments were nearly spherical, and many microphotographs of estuarial aggregates (e.g., Kranck et al., 1993; Lick and Huang, 1993; Wells and Goldberg, 1993) support that observation. However, the shape appears to be related to the forming mechanisms, and in low shear conditions (not typical of estuarial flows) nonspherical shapes are produced. Aggregates formed by differential settling in the laboratory appear crescent-shaped in two-dimensional photos (e.g., Lick and Huang, 1993) and in the deep ocean are long and chain-like (e.g., Wells and Goldberg, 1993; Heffler et al., 1991).

Gibbs (1985) reported that about 80 percent of measured aggregates from upper Chesapeake Bay (2 ppt salinity) displayed cylindrical shapes, with the long axis (on average 1.6 times as long as the narrow axis) parallel to the direction of settling. He further found that the drag coefficient for cylinders best fit the observed settling velocities. Luettich et al. (1993) analyzed suspended sediment from near Cape Lookout, NC, and reported that particles larger than 100 μm had sphericities (ratio of surface area of a sphere to surface area of particle if both have the same volume) of 0.6 to 0.7.

2.4.2 Size

The aggregate sizes reported below are expressed in terms of the diameter of the circle/sphere with area/volume equal to that measured, an estimate which assumes a spherical shape.

2.4.2.1 Size spectra

Like individual sediment grains, fine sediment aggregates occur in a range of sizes. Figure 2-2 shows a typical size distribution[*] for a sediment suspension before and during aggregation and when aggregation is complete at a given turbulence level (Kranck, 1973; Kranck et al., 1993). The initial distribution of grain sizes is wide and flat (a low kurtosis in statistical terms, "poorly sorted" in oceanographic terms, and "well graded" in soil mechanics terms). Aggregation drives the distribution to an order-of-magnitude larger sizes and a narrower peak.

The picture of size distribution evolution given in Figure 2-2 must be understood in terms of the sedimentary environment; that is, the figure represents an environment in which neither deposition nor erosion is occurring, so particles can pump upward in size limited only by the maximum size permitted by the stress and concentration levels. In a depositional environment the largest sizes settle out of suspension as they form, and so the distribution curve falls off more rapidly at larger aggregate sizes, skewing the distribution toward smaller sizes and possibly decreasing the modal value (Kranck, 1973; Kranck et al., 1993). In erosional environments the injection of particles eroded from the bed can increase the mean diameter (Teeter et al., 1997).

Figure 2-3 shows aggregate size distributions in San Francisco Bay measured by microphotography and the size distributions of disaggregated sediment grains from water

---

[*] The ordinate of the distribution in Figures 2-2 to 2-4 is the volumetric concentration density, or volume of sediment relative to the sample volume per unit of the log size class of the abscissa. The abscissa is the diameter of a circle with the same projected area as the irregularly shaped aggregates measured in photographs.
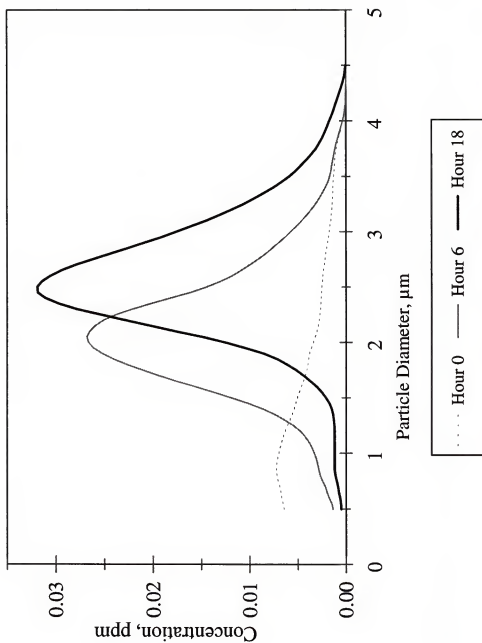
Figure 2-2. Sediment particle size distribution at 0, 6, and 18 hours for a progressively aggregating cohesive sediment suspension. Adapted from Kranck (1973). Used with permission from *Nature*, copyright (1973) Macmillan Magazines, Ltd.
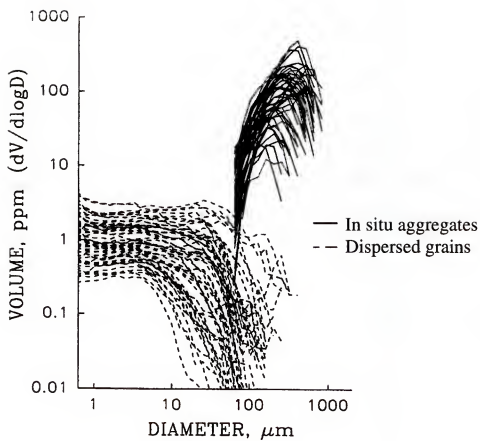
Figure 2-3. Size spectra of San Francisco Bay suspended sediment over a tidal cycle. Source: Kranck et al. (1993). Reprinted with permission.

samples taken at the same time (Kranck et al., 1993). Aggregates of 100 to 500 µm were formed of grains mainly less than 100 µm in size. The aggregate distribution was unimodal with high kurtosis and somewhat skewed to finer sizes, while the grains' distribution was like that of Figure 2-2—low kurtosis and heavily skewed to finer grains. The data represent hourly sampling for 11 hours (capturing both ebb and flood flows in the bay's mixed tide regime) at 5 depths and include total suspended sediment concentrations of 0.015 to 0.118 kg/m³. Kranck et al. (1993) noted that essentially all the fine sediments in their San Francisco Bay samples were aggregated and thus concluded that aggregation in that environment was nearly instantaneous.

Kranck et al. (1993) also collected size data from Skagitt Bay in the U.S., the Nith River (freshwater) in Canada, and on the Amazon Delta, Brazil. Figure 2-4 shows examples of aggregate size distributions from each, along with a distribution for the Scheldt estuary in The Netherlands. The similarity of all the curves is striking, as is the quantitative agreement of the San Francisco, Nith, Amazon, and Dutch distributions. Kranck et al. (1993) interpreted these results to suggest a common controlling mechanism in high-concentration environments that favors the size distribution shown in Figure 2-4.

Kranck and Milligan (1992) found that the distributions of both dispersed mineral grains and the aggregates they formed could be fit to the following equation with suitable adjustment of the coefficients:

$$C_v = Q D_a^{m_f} e^{-K_f \zeta D_a^2} \tag{2-3}$$

where
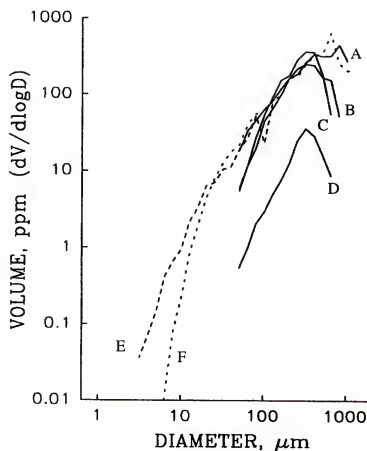
Figure 2-4. Typical in situ sediment aggregate size spectra from five locations: A-Amazon Delta; B-Nith River; C-San Francisco Bay; D-Skagitt Bay; E-Nith River by settling tests; and F-Scheldt estuary. All measurements except the Nith River data were obtained photographically. Source: Kranck et al. (1993). Reprinted with permission.

C_v = volume concentration,

Q, m_f, K_f = empirical coefficients,

g = acceleration of gravity,

v = kinematic viscosity of fluid,

ρ = density of fluid, and

$\zeta = \dfrac{g}{18\,v}\left(\dfrac{\rho_a - \rho}{\rho}\right)$.

2.4.2.2 Growth rates

In a series of papers Lick and co-workers (Tsai et al., 1987; Lick and Lick, 1988; Burban et al., 1989; Lick et al., 1992) expressed the rate of aggregate formation in the kth size class as a sum of aggregation and disaggregation terms in Equation 2-4, where the terms on the right side represent the rates at which k^{th} size class particles are, respectively:

1. gained by aggregating collisions between i and j class particles, $j < k$

2. lost by aggregating collisions between k class and all other particles

3. lost to smaller sizes by shear-induced disaggregation of k class aggregates

4. gained by shear-induced disaggregation of aggregates larger than k

5. lost by disaggregating collisions between k class and all other particles

6. gained by disaggregating collisions between i and l class particles, $l > k$.

$$\frac{dn_k}{dt} = \begin{cases} + \dfrac{1}{2} \displaystyle\sum_{i+j=k} P_{aij}\beta_{ij}n_i n_j \\[2mm] - n_k \displaystyle\sum_{i=1}^{\infty} P_{aik}\beta_{ik}n_i \\[2mm] - A_k n_k \\[2mm] + \displaystyle\sum_{l=k+1}^{\infty} \gamma_{lk} A_l n_l \\[2mm] - n_k \displaystyle\sum_{i=1}^{\infty} P_{dik}\beta_{ik}n_i \\[2mm] + \displaystyle\sum_{l=k+1}^{\infty} \gamma_{lk} n_l \displaystyle\sum_{i=1}^{\infty} P_{dil}\beta_{il}n_i \end{cases} \qquad (2\text{-}4)$$

where

n_k, n_i, n_j, n_l = number of particles per unit volume in size classes k, i, j, and l, respectively,

i, j, l = general size class index, sizes smaller than class k, and sizes larger than k, respectively,

P_{aim} = probability of cohesion of colliding particles of size classes i and m, where $m = j$ and k, respectively (determined empirically to be fit by the expression $P_{aim} = P_a[D_g/(D_i + D_m)]^{0.5}$ and where P_a = 0.15 for fresh water and 0.30 for salt water),

D_g = grain diameter,

A_k, A_l = coefficients characteristic of sediment and size classes k and j, respectively, determined empirically,

γ_{lk} = probability that a particle of size class k will form after disaggregation of a particle of size l, given by $2/(l-1)$,

P_{dim} = probability of disaggregation of size class i into size class m, where $m = j$ and l, respectively (determined empirically to be fit by the expression $P_{dim} = P_d(D_i + D_m)/D_g$, where P_d is a function of both shear and concentration and ranges from 0.0006 to 0.030),

β_{im} = collision frequency functions between two particles of size classes i and m, where $m = j, k,$ or $l,$ and given by:

$$\beta_{im} = \begin{cases} \dfrac{2}{3} \dfrac{\kappa T}{\mu} \dfrac{(D_i + D_m)^2}{D_i D_m} & \textit{Brownian Motion} \\[2ex] \dfrac{G_L}{6} (D_i + D_m)^3 & \textit{Fluid Shear} \\[2ex] \dfrac{\pi g}{72\mu} (D_i + D_m)^2 \, |\Delta\rho_i D_i^2 - \Delta\rho_m D_m^2| & \textit{Differential Settling} \end{cases}$$ (2-5)

where

κ = Boltzman constant,

T = absolute temperature,

μ = dynamic viscosity of fluid,

D_i, D_m = size of colliding particles from i and m size classes, respectively,

$\Delta\rho_i, \Delta\rho_m = \rho_i - \rho$ and $\rho_m - \rho$, respectively,

ρ_i, ρ_m = density of particles of i and m size classes, respectively, and

G_L = measure of flow shear, given by:

$$G_L = \sqrt{\dfrac{\epsilon}{\nu}} = \dfrac{\nu}{\lambda_o^2}$$ (2-6)

where

ϵ = flow energy dissipation per unit mass of fluid per unit time,

ν = kinematic viscosity of fluid,

λ_o = Kolmogorov turbulence micro-scale, and

x = length dimension.

The term P_d is considered to represent three-body collisions implicitly through its dependence on concentration (Lick et al., 1992).

Lick et al. (1992) solved a mass form of Equation 2-4 for thousands of size classes and for reduced sets of ten, five, and three size classes. They found that ten classes gave results as accurate (compared to experiments) as thousands did, but five and three classes represented tradeoffs between speed and accuracy. They note, however, that the fewer size classes might be adequate if they were chosen to represent a specific known spectrum.

Application of Equation 2-4 to a laboratory experiment using 0.1 kg/m³ concentration mineral grains with median grain size of 4 µm in a uniform shear of 100 1/sec showed that it led to an equilibrium particle size on the order of 100 µm in about 1 hour.

Winterwerp (1998) constructed a model for aggregate growth rate by linear addition of terms for aggregate-forming collisions (first term) and disaggregation by shear only (second term) as given by:

$$\frac{dD_a}{dt} = B_A C G_L D_a^{(4-n_f)} - \frac{B_D \alpha'_d}{nf} D_a G_L \left(\frac{D_a}{D_g}\right)^r \left(\frac{\mu D_a^2 G_L}{F_y}\right)^q \qquad (2\text{-}7)$$

where

D_a = aggregate diameter,

D_g = primary grain diameter,

C = mass concentration,

n_f = fractal dimension (value of 1.4 for very fragile aggregates, 2.2 for strong estuarial aggregates, average value about 2),

B_D = empirical coefficient for disaggregation rate,

α'_d = disaggregation efficiency parameter,

F_y = yield strength of aggregates,

r and q = empirical coefficients, and

B_A = aggregate growth coefficient given by:

$$B_A = \frac{3\alpha'_a \alpha'_e \pi}{2 n_f} \frac{1}{\rho_g D_g} \tag{2-8}$$

and

α'_a = aggregation efficiency parameter,

α'_e = diffusion efficiency parameter, and

ρ_g = sediment grain density.

2.4.2.3 Representative sizes

Several size definitions characterize the spectrum of particle sizes. Mean, median, and modal sizes are defined in the tradition of standard statistics. A maximum aggregate size is sometimes used to indicate the upper limit of the size spectrum, and is usually defined as the maximum size permitted by fluid shear or kept in suspension by fluid forces. Winterwerp (1998) also employs the concept of an equilibrium size, which is the maximum size attained in a steady state condition and represents a balance between aggregation and disaggregation.

Modal Size. Kranck (1973) and Kranck et al. (1993) found a relationship (with a correlation coefficient = 0.941) between modal aggregate size and modal grain size within

the aggregates to be:

$$D_{a,mode} = 2.80 \, D_{g,mode}^{0.772} \qquad \textbf{(2-9)}$$

where both diameters are expressed in µm.

Dyer (1989) presented a schematic description of the dependence of aggregate modal diameter upon both turbulence and sediment concentration as shown in Figure 2-5. At very low concentrations and shear stresses, collisions are rare and aggregates remain small. Up to a point, increasing fluid shear increases aggregate size by increasing the number of collisions, but after that point increasing turbulence slowly decreases aggregate size because of disaggregation. Increasing sediment concentration increases the number of collisions, so modal size increases. Above a limiting lower concentration the rate of size increase is rather steep until an upper limit is reached in which collisions induce more disaggregation than growth, so sizes begin to decrease.

Median Size. Lick et al. (1993) tested Detroit River sediment and related median aggregate size to sediment concentration and turbulence by the power function:

$$D_{a,median} = B_D \, (C \, G)^{m_D} \qquad \textbf{(2-10)}$$

where

C is in g/cm^3,

B_D = 9 for fresh water and 10.5 for sea water, and

m_D = -0.56 for fresh water and -0.40 for sea water.
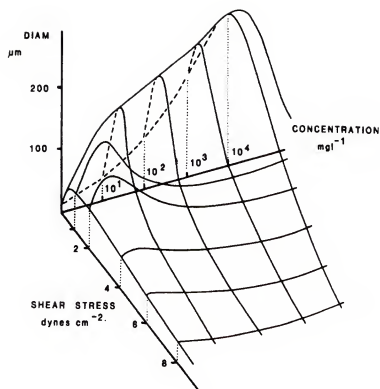
Figure 2-5. Schematic of effect of shear stress and sediment concentration on aggregate size.
Source: Dyer (1989). Reprinted with permission.

Equation 2-10 differs from Figure 2-5 and some other research results (e.g., van Leussen, 1994; Tsai and Hwang, 1995) in that aggregate size is an inverse function of shear instead of a direct function. Such a difference may be the result of experimental conditions falling within different segments of the surface in Figure 2-5 or it may reflect differences in cohesion among sediment from different locations.

Lick et al. (1993) found that the time required for the median aggregate size to reach 90 percent of its steady-state size was:

$$t_{median} = B_t (CG)^{m_t} \tag{2-11}$$

where

C is in g/cm^3,

$B_t = 12.2$ for fresh water and 4.95 for sea water, and

$m_t = -0.36$ for fresh water and -0.44 for sea water.

Equilibrium Size. Winterwerp (1998) used Equation 2-7 to derive an equilibrium aggregate size (growth balanced by disaggregation) of:

$$D_e = \frac{B_A C}{B_B \sqrt{G}} \tag{2-12}$$

where

$$B_B = \frac{B_D \alpha'_d \sqrt{\mu/F_y}}{nf} \frac{}{D_g} \tag{2-13}$$

with the terms defined in Equation 2-11.

Winterwerp calibrated Equation 2-7 to equilibrium aggregate sizes in settling column experiments with Ems Estuary muds at a concentration of about 1 kg/m³, and the equation gave times to reach equilibrium size of about 3 min to 60 min for shear rates ranging from 81 to 7 1/sec, respectively.

Maximum Size. Winterwerp (1998) added a limit to the maximum aggregate size, $D_{a,\lim}$, by noting that the volumetric concentration cannot exceed unity, so:

$$D_{a,\lim} \leq -\frac{\rho_g}{C} D_g \qquad (2\text{-}14)$$

Krone (1963) derived a limiting aggregate size for shearing-induced aggregation by assuming that aggregates in shear flow rotate under the applied torque of the velocity gradient, and thus are not broken by the torque; however, when particles collide and cohere, rotation is halted momentarily and the combined particle experiences the full torque. If the internal strength of the particles is smaller than the applied stress, the combined particles break. Using Stokes drag to calculate the fluid drag on an infinitesimal strip of a spherical particle, he calculated the limiting particle diameter to be:

$$D_{a,\lim} = \frac{2\,\tau_a\,\Delta R}{\mu\,\dfrac{\partial u}{\partial z}} \qquad (2\text{-}15)$$

where

τ_a = aggregate strength, shown in Table 2-1 for San Francisco Bay sediment,

ΔR = interpenetration distance for two colliding aggregates, and

$\partial u/\partial z$ = velocity gradient.

Krone (1963) concluded that aggregates larger than $D_{a,lim}$ could no longer grow by attaching to aggregates of their own size and larger, but could continue to sweep up much smaller particles that did not significantly affect their rotation. He hypothesized that as more and more aggregates reached this limiting size, fewer collisions would result in bonds and a comparatively uniform size distribution (narrow spectrum) would result. The observations of Kranck et al. (1993) support that hypothesis.

A number of investigators have related the maximum aggregate size to either the Kolmogorov scale, λ_o, or the fluid energy dissipation rate, ϵ, both of which can be expressed as:

$$D_{a,\max} \propto \epsilon^{-m_1} \tag{2-16}$$

where values for m_1 from selected literature are given in Table 2-4. All the investigations listed indicate that maximum aggregate size decreases as turbulence increases, indicating that the range of tested stresses and concentrations is high enough to be past the initial maxima in Figure 2-5. Kranck et al. (1993) showed field aggregate size spectra (for concentrations over 0.05 kg/m^3) converging to a common shape with nearly common modal values and nearly common maximum sizes over a range of flow conditions, as shown in Figure 2-4. That suggests that natural waterway stresses and concentrations tend to fall on the broad, flat portion of Figure 2-5, where aggregate size is relatively constant over orders-of-magnitude change in concentration and doubling of shear stresses.

Table 2-4. Values for Maximum Aggregate Size Coefficient in Equation 2-16.

Reference	Data Sources	m_l	Constraints
Parker et al., 1972	Sewage sludge experiments	0.17 to 0.35	--
Parker et al., 1972	Theory	0.5 to 2.0	--
Hunter and Liss, 1982	Latex grains in mixing chamber	0.21	Laminar shear
Dyer, 1989	Survey of literature	0.29 to 1.0	
Partheniades, 1993	Theory and experiment	0.40 to 0.50 0.37 to 0.33	$D_{max} \gg \lambda_o$ $\lambda_o \gg D_{max}$

A Need for Caution. The relationships reported above for aggregate size reveal a startling variety. Not only does the exponent magnitude in Equation 2-16 vary, but its sign varies in some experiments (see Equation 2-10). This variability may result from differences in the measured parameters (modal versus mean versus maximum diameters) or differences in measurement technique but, as noted above, is most likely caused by differences in experimental conditions (type of sediment, concentration range, shear range) that place the experimental results in different locations on the surface displayed in Figure 2-5.

Measurement of aggregate size is difficult, since sampling tends to disrupt the aggregates, altering the size distribution. Dyer et al. (1996) reported that the standard Owen Tube (similar to the Niskin bottle), which samples a column of water in the field and then becomes an on-deck settling column, gives aggregate sizes an order of magnitude smaller than direct photographic methods. Still photography, video photography, and laser methods are less likely to break aggregates, but can still yield misleading results (van Leussen, 1994; Fennessy et al., 1997). Gibbs et al. (1989) used three-dimensional holographic photos to

demonstrate that two-dimensional photos can exaggerate aggregate size by mistaking for a single aggregate an image of multiple aggregates overlapping within the depth of view.

Despite these difficulties, size remains a basic measurement of aggregates simply because it can be measured, albeit imperfectly. However, the literature demonstrates that extreme caution must be employed in selecting any aggregate size data or empirical expression for use.

2.4.3 Density

Estuarial mineral grains have densities of about 2,650 kg/m^3; however, the porous structure of aggregates exhibits typical densities of 1,060 to 1,300 kg/m^3, very close to that of the water (1,000 to 1,025 kg/m^3) in which they are formed and which is captured within the aggregate structure. Krone (1963) concluded that an increase in aggregation order led always to a decrease in aggregate density as shown for San Francisco Bay sediment in Table 2-3. Fennessy and Dyer (1996) found that in the Elbe River small aggregates showed a wide range of densities, but all large aggregates exhibited low density.

Logically, aggregate density should be a function of the shearing intensity, sediment concentration, and salinity. In practice it is usually inferred from measured aggregate size and settling velocity, assuming Stokes drag. Aggregate density is often expressed by the

power law relationship:

$$\Delta\rho_a = \rho_a - \rho = B_2 D_a^{-m_2} \tag{2-17}$$

where

ρ_a = aggregate density,

ρ = fluid density, and

B_2, m_2 = coefficients incorporating concentration, shearing rate, and salinity effects.

Table 2-5 lists some experimental values of B_2 and m_2. The range of m_2 is large, and the scatter in the data used to find the values is also large, suggesting that significant variables may have been lumped into the coefficients of Equation 2-17. However, a sizeable body of evidence (Kranenburg, 1994; Johnson, et al., 1996; Winterwerp, 1999) indicates that Equation 2-17 follows fractal relationships with the exponent $m_2 = 3 - n_f$, where n_f is the fractal dimension, usually about 2 for suspended aggregates. Figure 2-6 shows some examples of power-law curves fit to estuarial sediment data. McCave (1984) followed Tambo and Watanabe (1979) in using a piecewise fit to the density-versus-size curve, also shown in Figure 2-6.

2.4.4 Settling Velocity

Aggregate terminal settling velocity is a function of its size, shape, weight, and surface roughness, along with fluid properties. Terminal settling velocity for a single particle

Table 2-5. Values for Aggregate Density Coefficients in Equation 2-17.

Reference	Data Sources	B_2 $\mu m^{m_2} kg/m^3$	m_2
Gibbs, 1985	Chesapeake Bay	--	0.97
Burban et al., 1989	Lab experiments	$1650(4)^{m_2}$	$(1-C)(1-0.001G_L)$
Dyer, 1989	Literature Survey	--	0.25 to 2
Kranck et al., 1993	San Francisco Bay	35,000	1.09
Kranck et al., 1993	Nith River	43,000	1.18
Lick and Huang, 1993	Theory	--	-0.1 to 2.0
Kranenburg, 1994	Fractal theory	$f(\rho_g - \rho, D_g^{-m_2})$	$3 - n_f$

can be expressed as:

$$W_s = \sqrt{\frac{4gD_a}{3C_d}\left(\frac{\Delta\rho_a}{\rho}\right)} \qquad (2\text{-}18)$$

where

C_D = drag coefficient, which equals $24/\mathbb{R}_{ep}$ for $\mathbb{R}_{ep} < 0.1$ and is a variable function of $\mathbb{R}_{ep}$ (see Section 4.2) at $\mathbb{R}_{ep} > 0.1$, and

$\mathbb{R}_{ep}$ = particle Reynolds Number, given by:

$$\mathbb{R}_{ep} = \frac{W_s D_a}{\nu} \qquad (2\text{-}19)$$
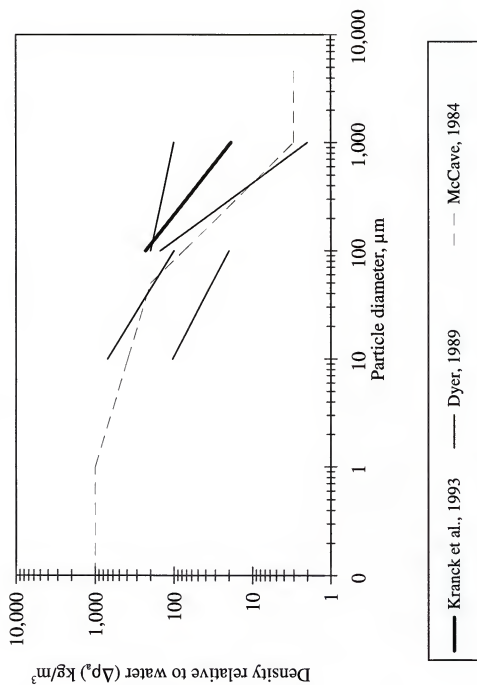
Figure 2-6. Aggregate density as a function of size for several estuaries. Kranck et al. (1993) data are from San Francisco Bay. Dyer (1989) data are summarized from several estuaries. McCave (1984) is a hypothesized curve for ocean aggregates.

Aggregate settling velocities typically range from 1×10^{-5} to 1×10^{-1} m/sec (e.g., Dyer, 1989), translating to a Reynolds Number range of 1×10^{-4} to 100 for particles of size 10 to 1000 µm.

Substituting for $\mathbb{R}_{ep}$ and $\Delta\rho_a$ in Equation 2-18 yields:

$$W_s \propto D_a^{2-m_2} \qquad (2\text{-}20)$$

Thus, for simplified conditions and the density parameters of Table 2-5, W_s is proportional to particle diameter to a power between about zero and 2.1, yielding the implausible conclusion that settling velocity can range from being completely independent of aggregate size to being proportional to the square of the diameter. Attempts to empirically fit Equation 2-20 to data have been unsatisfactory in that the relationship proves not to be unique from one site to another, or at the same site from one season to another (Burban et al., 1989; Heffler et al., 1991; Lick et al., 1993). The problem stems in part from the way measurements are taken (settling velocity measured in situ, by Niskin bottles, or by settling columns) and in part from varying shapes, but primarily from density of the aggregates varying over a very wide range.

The difficulties noted in Equation 2-20 also bear on Krone's (1963) observation number 3 relating to orders of aggregation (Section 2.3.5.1). For San Francisco Bay sediment, the density parameters in Table 2-5 yield a settling velocity proportional to $D_a^{0.91}$, confirming Krone's statement that an increase in aggregation, and thus size, increases settling velocity in San Francisco Bay sediment up to the maximum size of less than 1000 µm (Kranck et al., 1993). Yet data from other waters do not necessarily support that observation.

For example, Heffler et al. (1991) found that among aggregates from the Gulf of St. Lawrence the largest particles (maximum size 1240 µm) sometimes settled more slowly than smaller particles. The difference may lie in the densities and sizes created by the energy levels of the system. If the density-size relationship exponent in Equation 2-20 is 2.0 or larger (a steeply descending curve in Figure 2-6), the settling velocity will not increase with increasing size.

2.4.4.1 Effect of concentration

The simplest models assume a power law relationship between mean settling velocity and sediment concentration for suspensions of less than about 2 kg/m³, as in:

$$\overline{W_s} = B_3 \, C^{\,m_3} \qquad \qquad \textbf{(2-21)}$$

where B_3 and m_3 are empirically determined coefficients. Table 2-6 lists a few examples from the literature. In laboratory experiments m_3 is usually found to be very near to 1.33, but in field experiments the values cover a substantial range, as shown. The fit is seldom satisfactory, since data scatter is large and the coefficients tend not to be transferable (Burt, 1986). Van Leussen and Cornellisse (1993) found it fit observations locally, but the same coefficients could not be used for an entire estuary.

A more general expression for settling velocity given by Mehta and Li (1997) was based in part on work by Hwang (1989) and divided the settling range into four zones—Free

Settling, Flocculation (aggregation) Settling, Hindered Settling, and Negligible Settling, which are depicted in Figure 2-7 (and echoed in Figure 2-5). Sediment suspensions in the Hindered Settling zone form fluff or fluid mud layers as discussed in a later section.

Table 2-6. Values for Settling Velocity Coefficients in Equation 2-21.

Reference	Data Source	B_3^*	m_3
Burt, 1986	Owen Tube	--	1.37
Dyer, 1989	Literature survey	--	0.61 to 2.6
Kranck et al., 1993	Video	0.08 to 0.11	0.78 to 0.90
Kranck and Milligan, 1992	Video	--	0.92
Ross, 1988	Settling column	0.11	1.6
Teeter, 1993	Niskin Bottle	1.13	1.33

Note: * C expressed in kg/m³, W_s in cm/sec.

Mehta and Li (1997) expressed the settling velocity variation across these three zones by:

$$\overline{W_s} = \begin{cases} W_{sf} & C < C_1 \\ B_4 \dfrac{C^{m_4}}{\left(C^2 + B_5^2\right)^{m_5}} & C_1 < C < C_3 \\ \sim Negligible & C_3 < C \end{cases} \tag{2-22}$$

where

$\overline{W_s}$ = mean settling velocity in m/s,

W_{sf} = free settling independent of concentration,

B_4 = empirical coefficient, typically about 3,

B_5 = empirical coefficient, typically 1 to 10,

52
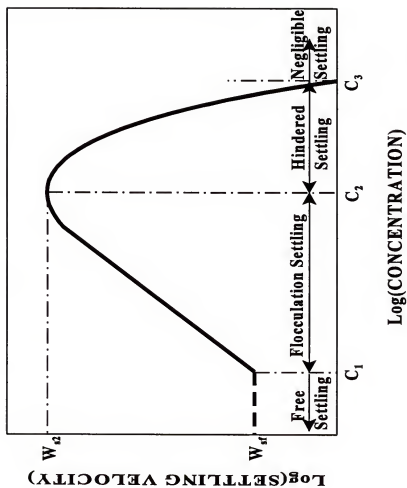
Figure 2-7. A qualitative description of settling velocity variation with suspension concentration. Source: Mehta and Li (1997). Reprinted with permission.

m_4 = empirical coefficient, typically 0.8 to 2,

m_5 = empirical coefficients, typically 1.0 to 3.0,

C_1 , C_3 = zone concentration limits as shown in Figure 2-7, and

C = concentration in kg/m³.

2.4.4.2 Effect of turbulence

Van Leussen (1994) proposed the expression:

$$\overline{W_s} = W_{so} \frac{1 + B_6 G}{1 + B_7 G^2}$$ (2-23)

where

W_{so} = reference settling velocity and

B_6 , B_7 = empirical constants.

Malcherek and Zielke (1995) used a form of Equation 2-23 (with W_{so} = 3.5C) in a 3-dimensional numerical model of the Weser Estuary and reported it worked well for large aggregates (D_a greater than 500 µm). Teeter (1999a) found that Equation 2-23 worked only for concentrations less than 0.05 kg/m³, or in the Flocculation Settling zone of Equation 2-26.

2.4.4.3 Other effects

Density and viscosity of the fluid through which the particle settles affect the settling velocity by altering fluid drag (Whitehouse et al., 1960). Density of the water entrained within the aggregate also affects settling velocity. Sakamoto (1972) observed that aggregates forming in salinity-stratified flow settled to the fresh/salt interface and remained there for

some time before salt water diffused into the aggregates and they continued settling through the saline layer.

Jiang (1999) found that kaolinite depositional data from flume experiments of Lau (1994) showed a well-defined temperature dependence of the form:

$$W_{s,50}(C,T_c) = \Phi W_{s,50}(C,15) \tag{2-24}$$

where $W_{s,50}(C,15)$ = concentration-dependent median settling velocity as defined by Equation 2-22 at 15 deg C, and

$$\Phi = 1.776(1 - 0.875 T') \tag{2-25}$$

where T' = normalized temperature, $T_c/15$, with T_c in deg C. This finding suggests that the mean aggregate size declines with increasing temperature, a reasonable conclusion since thermal activity of the clay micelle ions will tend to increase the repulsive effect between grains, reducing the number of collisions available to pump sediment mass up the size distribution in an aggregational environment.

<u>2.4.4.4 Comprehensive equations</u>

Teeter (1999a) proposed a settling velocity expression that reflects the contribution of both sediment concentration and turbulence and is separable by aggregate size class, given by:

$$W_{s,k} = W_{s,50} \left(\frac{C}{C_2} \right)^{m_{6,k}} \left| \frac{1 + B_6 G}{1 + B_7 G^2} \right| e^{\left(1 - B_8 \frac{C}{C_2} \right)} \tag{2-26}$$

where

k = particle size class index,

C = concentration of all size classes,

C_2 = upper concentration limit for enhanced settling (see Figure 2-7), typically 1-50 kg/m³,

$m_{6,k}$ = empirical coefficient for particle size class k,

B_6, B_7, B_8 = empirical coefficients, and

G = flow shearing rate.

Unlike many of the equations given here, Equation 2-26 offers a dimensionally correct form.

Winterwerp (1998) used Kranenburg's (1994) fractal model as a framework to formulate settling velocity relationships based directly on grain and aggregate size, producing the equation:

$$W_s = \begin{cases} B_9 \dfrac{\Delta \rho_a g}{\mu} D_g^{3-n_f} D_a^{n_f-1} & \mathbb{R}_{ep} < 100 \\[4mm] B_{10} \sqrt{\dfrac{1}{C_D} \dfrac{\Delta \rho_a g}{\rho} D_g^{3-n_f} D_a^{n_f-1}} & \mathbb{R}_{ep} \geq 100 \end{cases} \qquad (2\text{-}27)$$

where B_9 and B_{10} = empirical coefficients.

2.4.5 Strength

Aggregate strength (resistance to disaggregation) is a function of grain-to-grain cohesion, size and orientation of particles within the aggregate, and organic content (Partheniades, 1971; Wolanski and Gibbs, 1995; Mehta and Parchure, 1999) and to a lesser

extent on salinity and pH (Raveendran and Amirtharajah, 1995). Experimental results (e.g., Krone, 1963; Hunt, 1986; Mehta and Parchure, 1999) have shown that as aggregate size and organic content increase, both aggregate density and strength decrease. Partheniades (1993) reported that Krone's (1963) data for critical aggregate yield stress fit the expression:

$$\tau_a = B_{11} \Delta \rho_a^{m_7} \qquad (2\text{-}28)$$

where

τ_a = aggregate strength in Pa, and

B_{11}, m_7 = empirical coefficients (1.524×10^{-7} and 3, respectively, for San Francisco Bay sediment).

The fractal model of Kranenburg (1994) results in a aggregate strength that follows Equation 2-28, except that the exponent $m_7 = 2/(3-n_f)$. Kranenburg reported that his expression brackets Krone's (1963) data for $n_f = 2.1$ and 2.3.

2.5 Bed Exchange Processes

The various processes by which fine sediment particles move between the water column and the bed—erosion and entrainment, deposition and bed formation—are interdependent and cyclical. Despite their interdependence, each of these is usually expressed mathematically as a distinct process.

2.5.1 Suspension and Bed Profiles

The fluid column transition from water with some suspended sediment to muddy water to watery mud is gradual in estuaries laden with fine sediment, and distinguishing those transitions can be challenging (Parker and Kirby, 1982). Vertical fine sediment concentration profiles result from the relative magnitude of submerged weight pushing the particles toward the bed versus lift and drag imposed by the flow. A suspension of constant size individual grains or aggregates with settling velocity too small to settle through the flow will maintain a nearly uniform concentration over the water column. With continuing aggregation the aggregates' settling velocity increases and the concentration profile may shift to one like the schematic shown in Figure 2-8. In the upper portion of the water column the concentrations are low enough that free settling (Figure 2-7) occurs and the concentration gradient is small. Lower in the column the concentration increases, and increased settling and non-isotropic diffusion lead to formation of lutoclines (sediment-induced pycnoclines) (Parker et al., 1980; Mehta and Li, 1997; and others). Multiple lutoclines may form a characteristic stepped structure like that of Figure 2-8. Near the bottom of the profile the primary lutocline marks a zone where settling is hindered by the inability of entrained water to rapidly escape the mixture and fluid mud forms. The fluid mud may have a upper, mobile, layer in which horizontal flow occurs, and a lower, stationary, layer that does not flow horizontally. At some concentration in the fluid mud layer particle to particle structure develops and a low density sediment bed forms, but concentration and density continue to increase with depth. The structure shown in Figure 2-8 varies with flow intensity, sediment
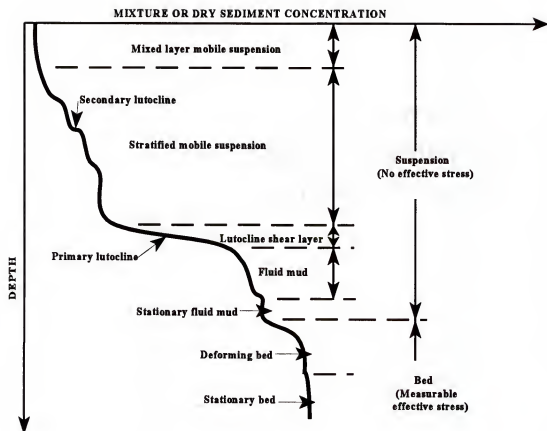
Figure 2-8. Vertical mixture density (or dry sediment concentration) profile classification for fine sediment suspension. Source: Mehta and Li (1997). Reprinted with permission.

concentration, and sediment character (Mehta and Li, 1997). For example, the lutocline and fluid mud layer may be absent or minimal in low concentration, low deposition rate environments.

In the U.S., significant fluid mud layers occur in a number of estuaries, most notably in the Savannah River estuary and the Sabine-Calcasieu area. In Mobile Bay and the James River meter-thick layers of fluid mud form where dredged material is disposed in open water and flows slowly (less than 0.2 m/sec) away from the point of discharge at slopes of about 1 vertical to 2000 horizontal (Nichols and Thompson, 1978). It is generally believed to flow only on such relatively steep slopes since evidence suggests that it will be entrained before it flows under the drag exerted by flow above the lutocline (e.g., Einstein and Krone, 1962; Mehta and Srinivas, 1993).

As depicted in Figure 2-8, concentration/density and erosion resistance increase (generally) gradually with depth through somewhat mobile fluid mud, to stationary soft sediment layers with significant structure but little resistance to erosion, to poorly consolidated bed, until fully consolidated bed occurs at some depth (Parchure, 1984). Krone (1986) characterized the bed structure as a series of layers, each no more than a few centimeters thick and each thinner than the layer above, with particle to particle contact of decreasing orders of aggregation as the bed consolidates. Further, the bed surface in a depositional environment is one order of aggregation higher than the aggregates settling to it (Krone, 1986 and 1993). Thus, if fourth order sediment aggregates are depositing, the top layer of the bed will have fifth order aggregation with a strength lower than that of the depositing aggregates. The second layer down in the bed will have fourth order bonds, the

third layer will have third order bonds, and so on until a well consolidated bed (possibly consisting of zero order aggregates) occurs.

2.5.2 Bed Exchanges

Figure 2-9 shows a simplified sediment concentration profile and the processes by which particles move between the water column and bed in the presence of fluid mud. Particles move from the flow-supported sediment suspension to the fluid mud layer by settling and may remain there or be entrained into the flow. Particles in the fluid mud layer(s) may deposit onto the low density bed and may remain there or be eroded from the bed. Within the bed self-weight consolidation expels water and increases bed density with depth (Parchure, 1984).

Two principal conceptual models are used to describe the exchange of particles between the bed and the flow. The first (e.g., Partheniades, 1977; Parchure, 1984; Teeter et al., 1997) assumes that erosion and deposition are mutually exclusive and the second (e.g., Krone, 1962; Lick et al., 1995) assumes simultaneous erosion and deposition similar to the live bed concept of cohesionless sediment transport. Both types of models can reasonably reproduce experimental data, but Teeter (1999b) concluded that the latter model's success in describing experimental results was an artifact of the simplifying assumption of a single grain size and settling velocity, and that if a more realistic multiple grain size calculation is made, the exclusive model more accurately predicts experimental results. Partheniades (1977) showed that a single mathematical model could describe both, but the erosion-resisting force for cohesive sediments must include not only weight and interparticle friction
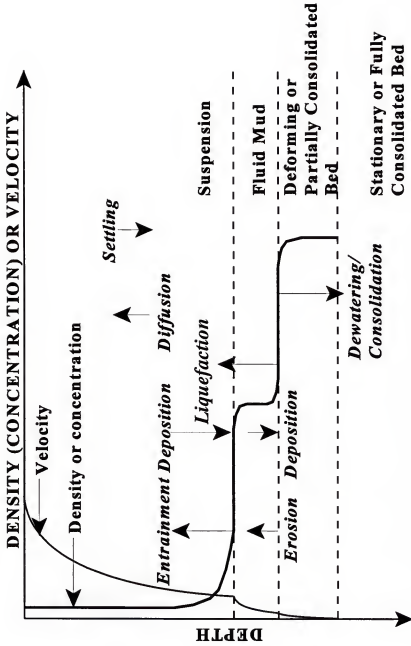
Figure 2-9. Sediment transport fluxes determining sediment density or concentration profile dynamics.
Source: Adapted from Mehta and Li (1997). Reprinted with permission.

but also interparticle cohesion. Under that unified model, it is easy to conceive of a fine sediment bed in which bed shear stress fluctuations exceed bed erosion resistance so rarely that erosion is insignificant when deposition is occurring.

Mehta (1991) used the concept of a stirred layer near the suspension-bed interface to describe sediment exchanges. In that model high concentration convective cells form in a comparatively thin layer just above the bed where sediment diffuses upward and settles downward. Since at the top of this layer sediment can be simultaneously moving upward and downward while either erosion or deposition is occurring at the bottom of the stirred layer, the concept can be used to bridge the gap between the simultaneous and exclusive models. A high concentration stirred layer will serve as a sediment reservoir during either erosion or deposition, and if flow suddenly stops, it will quickly form a particle-supported matrix that can become part of the stationary bed through dewatering and gelling (Mehta, 1991). Cervantes et al. (1995) used the stirred layer model to help explain bursts of suspended sediment concentration observed in the water column during flow transients.

2.5.2.1 Erosion and resuspension

Erosion, i.e., removal of sediment from the bed by the flow, occurs through three related mechanisms—surface erosion of aggregates, mass erosion of bed layers, and entrainment of fluff or fluid mud. Surface erosion, the slowest of the three, is most often characterized as proportional to the excess bed shear stress, the amount by which the applied stress exceeds a critical value (Mehta and Parchure, 1999).

$$\dot{c}_e = \dot{c}_{e,m} \left(\frac{\tau_b - \tau_{ce}}{\tau_{ce}} \right)^{m_s} \qquad \tau_b > \tau_{ce} \qquad (2\text{-}29)$$

where

$\dot{c}_e$ = erosion rate in mass per time per unit area,

$\dot{c}_{e,m}$ = empirical erosion constant,

τ_b = shear stress exerted by the flow on the bed,

τ_{ce} = critical shear stress for erosion, and

m_8 = empirical coefficient, usually assumed to be 1.

This widely employed equation is applicable to both current and wave-generated bed shear stresses (Mehta, 1996). The coefficient $\dot{c}_{e,m}$ and the critical shear stress τ_{ce} are functions of sediment character, eroding fluid chemistry, and temperature, and must be determined by experiment for each site. Published values of $\dot{c}_{e,m}$ range from about 10^{-1} to 10^{-3} kg/(m^2-min) and τ_{ce} ranges from nearly zero for highly organic sediments to 10 Pa for hard packed clays (Mehta, 1991). The form of Equation 2-29 is consistent with the concept of mutually exclusive deposition and erosion, since the net erosion rate is not a function of sediment concentration in the flow.

Critical shear stresses for freshly deposited, low density beds are typically equal to the values of shear strength given in Table 2-3 for higher order aggregates (Mehta, 1991), indicating that the bonds between aggregates in an unconsolidated bed are similar to those within high order aggregates. That observation supports the conclusion of Krone (1986, 1993) that the order of aggregation of a freshly-deposited bed surface will be one order of aggregation higher than that of the depositing aggregates. Given that model, continuing erosion will uncover progressively higher order bonds that resulted from self-weight

consolidation of the bed, so the shear strength of the bed (and thus τ_{ce}) will increase with depth (Lee and Mehta, 1994).

Despite widespread practical success of Equation 2-29, the range of variation in its empirical coefficients indicates that significant improvement can be achieved by incorporating more physics. A more rigorous form (below) has been proposed by Mehta and Parchure (1999), but they point out that the expression should be used with great caution, since it was developed using data from a number of independent experiments that differed in methods and materials.

$$\dot{\varepsilon}_e = \dot{\varepsilon}_{e,NO} e^{-B_{12}\left[B_{13} - B_{14}(\phi - \phi_l)^{m_9}\right]^{m_9}} \left[\tau_b - B_{14}(\phi - \phi_l)^{m_9}\right] \left(T e^{\left[m_{10} - \frac{m_{11}}{T}\right]}\right) \qquad (2\text{-}30)$$

where

$\dot{\varepsilon}_{e,NO}$ = reference value of the ratio $\dot{\varepsilon}_{e,m}/\tau_s$,

ϕ = solids weight fraction,

ϕ_l = minimum value of ϕ, below which $\tau_{ce} = 0.$, and

B_{12}, B_{13}, B_{14}, and m_9 = empirical coefficients.

Mass erosion pulls patches out of the bed suddenly as a plane of failure occurs within the sediment bed. It can be characterized either by a form of Equation 2-29 with a critical shear stress greater than that for surface erosion (Mehta, 1991) or by the simple expression given below (Ariathurai et al., 1977).

$$\dot{\varepsilon}_e = \frac{\rho_l \Delta y_l}{\Delta t} \qquad\qquad \tau_b > \tau_s(l) \qquad (2\text{-}31)$$

where

ρ_l = bulk density of the eroded layer,

Δy_i = thickness of the eroded layer,

Δt = characteristic time, and

$\tau_s(l)$ = critical shear stress for mass erosion of the layer.

Entrainment of fluid mud can be described by an expression paralleling that used to quantify fluid entrainment from a stratified flow interface. Li (1996) (see also Li and Parchure, 1998) developed a net flux equation for entrainment by waves or waves plus a weak current over fluid mud, in which the first term below represents entrainment upward and the second term below represents sediment settling into the fluid mud.

$$\dot{c}_e = \begin{cases} \rho_m u_b B_{14} \left(\dfrac{\mathbb{R}_{gc}^2}{\mathbb{R}_{go}} - \mathbb{R}_{go} \right) - W_s C_{z0} & \mathbb{R}_{go} < \mathbb{R}_{gc} \\ 0 & \mathbb{R}_{go} \geq \mathbb{R}_{gc} \end{cases} \qquad \textbf{(2-32)}$$

where

ρ_{fm} = density of the fluid mud,

u_b = flow velocity just outside the bottom boundary layer,

B_{14} = empirical coefficient,

$\mathbb{R}_{gc}$ = critical value of gradient Richardson number, about 0.043,

C_{z0} = sediment concentration just above the interface, and

$\mathbb{R}_{go}$ = global Richardson number given by:

$$\mathbb{R}_{go} = \frac{(\rho_m - \rho)g\delta^2}{\rho\,\Delta u_0^2} \tag{2-33}$$

with

δ = thickness of the boundary layer, and

Δu_0 = velocity difference across the interface, which in the case of wave action must be obtained from a wave-mud interaction model (Mehta and Li, 1997).

2.5.2.2 Deposition

If a settling sediment aggregate approaches the bed, where concentrations, collision frequency, and shearing rates are high, it will either break apart and be entrained in the flow or bond with particles in the bed and deposit as shown in Figure 1-1. Thus the deposition rate will be a function of aggregate settling velocity, concentration, and near-bed shearing rates. Mehta (1973) characterized deposition as the outcome of interaction between two stochastic processes occurring just above the bed—interfloc collisions causing both aggregate breakage and growth that creates a distribution of aggregate sizes and strengths, and the probability that an aggregate of a given strength and size will deposit.

Mehta and Li (1997) defined three depositional modes based on the relationship between bed shear stress, τ_b, and certain critical stresses for deposition, τ_{cd}:

1. No deposition: $\tau_{cd,max} < \tau_b$

2. Deposition of a fixed fraction of sediment: $\tau_{cd,min} < \tau_b < \tau_{cd,max}$

3. Deposition of all suspended sediment: $\tau_b < \tau_{cd,min}$.

Mode 1 occurs with uniform size sediment mixtures or very high shearing rates, mode 2 is typical of sediment size mixtures and the moderate shearing rates common to estuaries, and mode 3 occurs with more uniform sediment sizes and very low shearing rates which may occur at slack water or in closed end basins. For an ideal sediment with uniform grain size, $\tau_{cd,min} = \tau_{cd,max} = \tau_{cd}$.

A widely used expression for sediment deposition rate when only one size class is considered is (Krone, 1962, 1993):

$$\dot{c}_d = \frac{W_s \overline{C}}{h} \left(1 - \frac{\tau_b}{\tau_{cd}} \right) \tag{2-34}$$

where

$\overline{C}$ = depth averaged total sediment concentration, and

h = water depth.

Mehta and Li (1997), following Mehta and Lott (1987), extended Equation 2-34 to multiple grain sizes with:

$$\dot{c}_{d,i} = \frac{W_{s,i} \overline{C}_i}{h} \left(1 - \frac{\tau_b}{\tau_{cd,i}} \right) \tag{2-35}$$

where

$\dot{c}_{d,i}$ = mass deposition rate for size class i,

$\overline{C}_i$ = depth-mean concentration of size class i, and

$\tau_{cd,i}$ = critical shear stress for deposition of size class i.

2.6 Concluding Observation

The fine sediment processes material reviewed here could be seen as supporting the sometimes heard assertion that very little is really known about those processes. Widely varying, sometimes even contradictory, results have been obtained by researchers in the field. As noted in section 2.4.2, these variations may be the result of differences in experimental conditions and measurement methods, but is almost certainly also the result of the significant processes' complexity. Lee and Mehta (1996) found over 100 parameters of potential importance to erosion examined in the literature. This state of uncertainty may gladden the hearts of us who want lots of interesting research topics, but it dismays those who rely upon research to provide useful engineering tools. However, as demonstrated by Mehta and Li (1997), McAnally (1989) and others, the existing state of knowledge can be profitably used for engineering solutions if it is employed with attention to its limitations.

CHAPTER 3
AGGREGATION PROCESSES

This chapter develops a physics-based representation for fine sediment aggregation processes. It presents first a conceptual framework for aggregation processes, then expresses those concepts in mathematical terms as subcomponents for particle description, collisions, and aggregation/disaggregation. The goal of the chapter is to provide a procedure for calculating the size distribution changes caused by aggregation and disaggregation of sediment particles in a fine sediment suspension under estuarial flow conditions.

3.1 Conceptual Framework

The aggregation processes model is based on the following assumptions about conditions and processes:

1.   An aqueous sediment suspension exhibiting interparticle cohesion and consisting of fine sediment mineral grains with some organic materials is transported by estuarial flows.

2.   The flow environment is typical of many micro tidal to meso tidal estuaries, with tide ranges of 0.25 to 4 m, flow speeds from slack to about 3 m/sec and salinities ranging from 1 to 35 ppt with occasional hypersaline conditions of up to 60 ppt.

3.   The suspension has experienced aggregation and includes a spectrum of particle sizes ranging from micron-size individual mineral grains to aggregates containing perhaps millions of grains. Most of the sediment mass occurs in approximately spherical aggregates of order 10 to 1000 μm diameter. The continuous spectrum of sizes can be represented by a finite number of discrete classes.

4. Particle size, density, and strength are related by empirical power law expressions and settling velocity can be expressed by Stokes Law.

5. Sediment aggregation and disaggregation are an ongoing process as a result of particle collisions and fluid forces.

6. A particle may encounter another particle, i.e., pass at close range, without colliding since viscous incompressible behavior of the fluid between approaching particles exerts pressure on both particles and resists collision. Two kinds of close encounter occur—an encounter of the first kind in which fluid cushioning prevents a collision, and an encounter of the second kind in which a collision occurs. Every encounter of the second kind results in a collision and a bond at the points of contact.

7. Particle encounters are caused by Brownian motion, fluid flow shear, and differential settling, which are assumed to be linearly additive. Other encounter mechanisms have a small effect compared to these three.

8. Two- and three-body collisions account for all particle collisions and their frequency can be described by standard stochastic methods. Particle aggregation or both aggregation and disaggregation may occur in a collision, depending upon the cohesion-induced strength of the colliding particles compared with shearing forces exerted on them by the collision.

9. Fluid flow forces will cause disaggregation of a particle if the imposed shear stress exceeds the particle's strength.

10. Particle mass is conserved during collisions. The mass of a disaggregated particle fragment in a single disaggregating collision is a random variable, and over many collisions exhibits a Gaussian distribution over the discrete size spectrum; however, the mass of aggregating particles is determined uniquely by conservation of the colliding particles' masses.

11. A near-bed stirred layer with high sediment concentration and high shear rates exchanges particles with the bed and with the water column. The intense shear and multiple two- and three-body collisions occurring within the stirred layer rapidly aggregate smaller, strong particles and break larger, weaker particles, exerting a control on the aggregate size available for resuspension or deposition over the bed.

12. Particles deposit on the bed or in a layer of fluid mud, forming high order bonds with the particles on the surface. Individual grains and aggregates enter the flow from the bed/fluid mud when the flow-imposed shear stress exceeds the particle to bed bond strength. For the aggregation model, the sediment bed and fluid mud layer act as a

sink and source for grains and aggregates, with nonsimultaneous bed erosion/ entrainment or deposition.

13.   Vertical advection/diffusion and deposition of sediment by size class can be described by the one-dimensional algorithm described in Chapter 4.

3.2 Particle Definitions

3.2.1 Size Distribution

The fundamental descriptor of a sediment particle is its mass, and other parameters (e.g. its dimensions, settling velocity, strength and density) are determined from that characteristic. The continuous spectrum of particle sizes, from single grains to aggregates containing perhaps millions of grains, is characterized by a finite set of discrete, mass class intervals defined as:

Class Index:	$j = 1$ to s	
Class Lower Limit on Particle Mass:	$M_j(lower)$	(kg)
Class Upper Limit on Particle Mass:	$M_j(upper)$	(kg)
Mass Concentration of Particles in Class:	C_j	(kg/m^3)

The mass intervals need not be uniform, but the range from $M_1(lower)$ to $M_s(upper)$ must include both the smallest and largest mass particles to be modeled. Krone's (1963) order of aggregation model implies that particle sizes change in discrete steps as they aggregate and disaggregate, and simple geometric considerations indicate that the diameters approximately double with each aggregation, so a size distribution that doubles diameter or mass with each increasing class interval is a reasonable physical model.

Total sediment mass within each class at a given location can change with time by the following processes, which are depicted graphically in Figure 3-1:

1.   Increase or decrease from flux by:

    a.   advection and diffusion

    b.   erosion or deposition to the bed.

2.   Increase by aggregation of particles from smaller classes.

3.   Increase by disaggregation of particles from larger classes.

4.   Decrease by aggregation or disaggregation of particles within the class.

Item 1 is computed by the algorithm described in Chapter 4. Items 2 to 4 are caused by particle collisions and flow shear, which are considered in the following sections.

Each class, containing particles each with a mass between $M_j(lower)$ and $M_j(upper)$, is represented by a particle of mass M_j. While a particular mass distribution will dictate the optimum form of the relationship between the representative mass and the upper and lower class limits, the mass distribution itself changes with time under ongoing aggregation processes. This model employs the simplest, most general form—a linear mean of $M_j = \dfrac{M_j(lower) + M_j(upper)}{2}$.

The initial number concentration of particles in each class is calculated from the known mass concentrations via the equation:

$$n_j = \frac{C_j}{M_j} \tag{3-1}$$
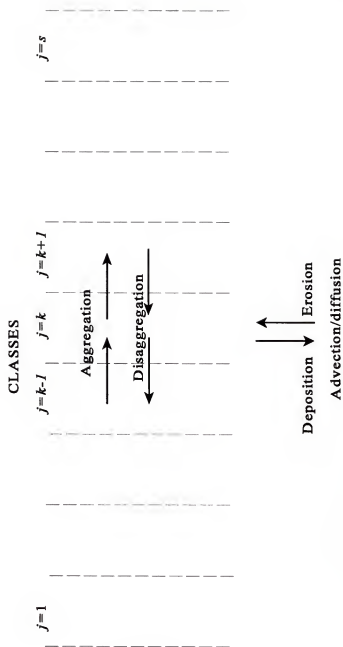
Figure 3-1. Sediment mass within a class may increase by aggregation of smaller particles or disaggregation of particles within the class, decrease by aggregation of larger particles or disaggregation of particles within the class, and either increase or decrease by deposition, erosion, and advection-diffusion.

The particles are assumed to be approximately spherical, so that the representative particle diameter can be calculated from the mass by:

$$D_j = \left(\frac{6 M_j}{\pi \rho_j} \right)^{\frac{1}{3}} \tag{3-2}$$

where ρ_j = density of representative particle, given by an adaptation of Equation 2-17:

$$\rho_j = smaller\ of \begin{cases} \rho_g \\ \rho + B_\rho(C, G_c, S, T) \left(\dfrac{D_g}{D_j} \right)^{3 - n_f} \end{cases} \tag{3-3}$$

where

ρ = fluid density,

ρ_g = sediment grain density,

$B_\rho(C, G_c, S, T)$ = sediment-dependent function,

C = sediment concentration,

G_c = measure of collision-inducing flow forces,

S = salinity,

T = temperature, and

n_f = fractal dimension, usually about 2.

An empirical fit of Equation 3-3 to San Francisco Bay sediment data is shown in Figure 3-2.
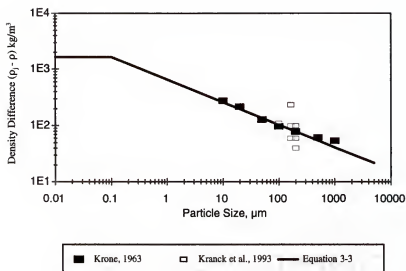
Figure 3-2. Density as a function of particle size by Equation 3-3 ($B_\rho = 1650$; $nf = 2.6$) and measured San Francisco Bay sediment. Diameters for Krone's (1963) results are estimated. Maximum, median, and minimum density (45 measurements) shown for Kranck et al. (1993).
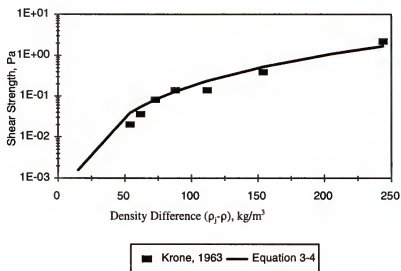
Figure 3-3. Particle strength as a function of density by Equation 3-4 ($B_\tau = 200$, $nf = 2.2$) and as measured for San Francisco Bay sediment.

3.2.2 Settling Velocity

Settling velocity for each class, $W_{s,j}$, is given by Equation 2-18 up to the point of hindered settling, with the drag coefficient selected for the appropriate particle shape (Graf, 1984) and particle diameter and density given by Equations 3-2 and 3-3, respectively. This straightforward equation, which is independent of sediment concentration and flow turbulence, is made possible by the aggregation model's consideration of those effects on a class-by-class basis, with aggregation processes accounting for concentration changes among classes and thus the suspension median settling velocity.

3.2.3 Shear Strength

Particle strength is given by an adaptation of Equation 2-28:

$$\tau_j = B_\tau(C, G_c, S, T) \left(\frac{\Delta \rho_j}{\rho} \right)^{\frac{2}{3-n_f}} \tag{3-4}$$

where B_τ = empirical sediment-dependent function.

This general form of equation, used by Partheniades (1993), Kranenburg (1994), Winterwerp (1999) and others, requires fitting to empirical data, as has been done and plotted in Figure 3-3 for San Francisco Bay sediment.

3.3 Particle Collisions

One suspended particle encounters another particle when fluid, flow, and particle effects bring them close together. However, before they can make physical contact, fluid must flow out of the narrowing gap between the particles. The pressure increase required to force the fluid out exerts repelling forces on the particles and may or may not prevent a collision, depending on fluid viscosity and the particles' positions, porosities, masses, and relative velocity. This section deals with the number of collisions that can be expected to occur in sediment suspensions under these circumstances. As stated in the conceptual framework above and discussed in Section 3.5, this model assumes that estuarial fine-grained sediment always exhibits cohesion; thus, while the following collision treatment explicitly cites cohesion only in Section 3.5.1.2, the cohesive assumption underpins the model.

3.3.1 Two-Body Collisions

The frequency of collisions between two particles can be expressed by (Smoluchowski, 1917):

$$N_{im} = \alpha_a \beta_{im} n_i n_m \tag{3-5}$$

where

N_{im} = number of collisions between i and m class particles per unit time per unit volume,

α_a = aggregation efficiency factor, which differs from the similar α' term in Equation 2-1 and is discussed further in Section 3.5.1.2,

β_{im} = collision frequency function, dependent on particle diameters and system characteristics,

i, m = indices for i and m size classes, respectively, and

n_i, n_m = number concentration of i and m class particles, respectively.

The collision frequency function, β_{im}, can be calculated by a simple analysis of particle motions under the several modes of collision listed in the conceptual model of Section 3.1. The analysis begins with two idealized spherical particles as shown in Figure 3-4—one from the ith size class (the i particle) and one from the mth size class (the m particle). We surround the m particle with a collision sphere of diameter $D_{c,im} = F_c(D_i + D_m)$, where F_c = collision diameter function, with a value between 0 and 1, and D_i and D_m = diameter of the i and m particles, respectively. The two particles will experience a close encounter if their relative motion causes particle i to intrude within the collision sphere of particle m.

The parameter F_c does not appear explicitly in the aggregation literature, but it is implied by the "capture cross-section" concept of Adler (1981). It is needed because particles must mesh to at least some degree in order to collide; and nonspherical particles may be rotating, presenting a larger effective collision area. Section 3.5.1.2 develops a functional form of F_c based on fluid and particle behavior and modifies the concept of collision efficiency expressed in Equation 3-5.

Section 2.3.3 lists five processes as causing collisions in an estuarial sediment suspension. Only three are considered here —Brownian motion, flow shear, and differential settling. Biological filtering may be a potentially significant aggregation process in some estuarial waters, but is neglected here in favor of focusing on the basic physical processes.
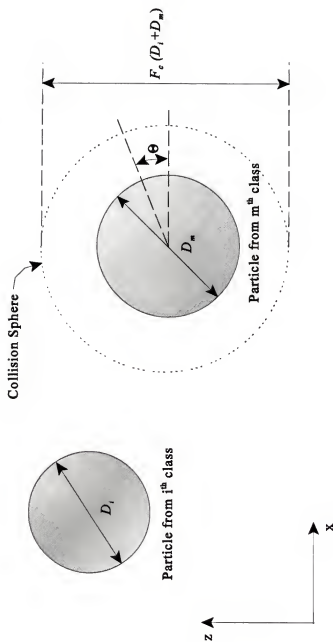
Figure 3-4. Definition of terms for two-body particle encounters.

3.3.1.1 Brownian motion

The collision frequency function for Brownian motion can be treated as a case of Fickian diffusion (Smoluchowski, 1917).

$$\beta_{B,im} = 4\pi E_{im} F_c (D_i + D_m) \tag{3-6}$$

where E_{im} = relative diffusion coefficient for the two particles, given by (Overbeek, 1952):

$$E_{im} = \frac{\overline{(x_i - x_m)^2}}{2t} = \frac{\overline{x_i^2}}{2t} - \frac{\overline{2x_i x_m}}{2t} + \frac{\overline{x_m^2}}{2t} \tag{3-7}$$

where x_i, x_m = displacement of particles i and m, respectively, in time t by Brownian motion. For random Brownian motion of approximately same-size particles, the term $\overline{2x_i x_m}$ is equal to zero, the remaining terms can be expressed as (Overbeek, 1952): $\frac{\overline{x_i^2}}{2t} = \frac{E_g D_g}{D_i}$, and Equation 3-7 becomes:

$$E_{im} = E_g D_g \left(\frac{1}{D_i} + \frac{1}{D_m} \right) \tag{3-8}$$

where

E_g = Brownian diffusion coefficient of the primary grain = $\kappa T / 3\pi\mu D_g$ (Einstein, 1905),

κ = Boltzman constant,

T = absolute temperature in deg. K,

μ = dynamic viscosity of the fluid, and

D_g = primary grain diameter.

Substituting Equation 3-8 and E_g into Equation 3-6 yields the two-body collision frequency function for Brownian motion:

$$\beta_{B,im} = \left[\frac{2}{3} \frac{\kappa T F_c}{\mu} \right] \frac{(D_i + D_m)^2}{D_i D_m}$$ (3-9)

which is the same as the Brownian portion of Equation 2-5 except for the collision diameter correction factor, F_c.

If the particles are nonspherical, such as the rods and plates typical of fine sediment mineral grains, their motion will be rotational as well as translational, and their collision diameter (a function of the maximum dimension) will be much larger than their nominal diameter while the diffusion coefficient (a function of mean dimension) remains nearly constant, so the Brownian motion collision frequency will increase relative to spherical particles. Experiments with rod-shaped particles compared with spheres have shown a fifty-fold increase in the probability of collision (Overbeek, 1952). This single grain phenomenon would seem to eliminate a reasonable upper bound of 1 for F_c, but single grains are comparatively rare in estuaries (Kranck et al., 1993), so the approximately spherical shape assumption and the range $0 < F_c < 1$ can be retained without undue error.

Equation 3-9 (with $F_c = 1$) has been shown to accurately describe the aggregation rate of uniform cohesive laboratory suspensions in which Brownian motion dominates aggregation (Overbeek, 1952), indicating that the assumptions underpinning it are reasonable for very small particles of uniform size. Using it for particles of unequal size introduces an error, but, as will be shown, except for the initial aggregation period in dispersed

suspensions, Brownian motion has a small effect on particles typical of estuaries, so the effect of the error will be small compared to the total collision function.

3.3.1.2 Flow shear

Taking the center of the m particle in Figure 3-4 as the coordinate origin moving at the flow speed in the x direction, the transport of i particles by flow into the m particle's collision sphere is (Saffman and Turner, 1956):

$$N_{im} = 2\,n_i \int\limits_0^{\pi/2} u_i \pi F_c^2 (D_i + D_m)^2 \cos\Theta \, d\Theta \qquad (3\text{-}10)$$

where

Θ = angle between x axis and a location on the sphere's surface, and

u_i = velocity of the i particle relative to center of the m particle, given by:

$$u_i = \frac{(D_i + D_m)}{2} \overline{\left| \frac{du}{dx} \right|} \qquad (3\text{-}11)$$

where it is assumed that the two particles are approximately the same size, they do not influence each other's motion, and energy is isotropically dissipated through eddies much smaller than $D_i + D_m$. If $\frac{du}{dx}$ is normally distributed, the mean of its absolute value in the equation above can be expressed[*] as:

---

[*] A personal communication with Hugo Rodriguez, University of Florida, confirmed that the Saffman and Turner (1956) paper has a typographical error—the π term in Equation 3-12 is omitted.

$$\overline{\left|\frac{du}{dx}\right|} = \sqrt{\frac{2\epsilon}{15\pi\nu}} \tag{3-12}$$

where:

ϵ = turbulent energy dissipation rate, and

ν = kinematic viscosity of the fluid.

Substituting Equations 3-11 and 3-12 into Equation 3-10, integrating it, and comparing the result with Equation 3-5 yields the flow shear collision frequency function:

$$\beta_{S,im} = \left[\frac{\pi F_c^2}{4}\sqrt{\frac{2}{15\pi}}\right]\sqrt{\frac{\epsilon}{\nu}}\,(D_i + D_m)^3 \tag{3-13}$$

Delachatosios and Probstein (1975) experimentally confirmed the form of this equation, and found the constant (in square brackets) to be 0.105, which implies that $F_c = 0.81$ in their experiments and supports the 0 to 1 range proposed above.

3.3.1.3 Differential settling

If the i and m particles in Figure 3-4 have different settling velocities, the number of i particles passing into the m particle collision sphere by differential settling alone is described by Equation 3-10 with the velocity being replaced by the difference in settling velocities between the two particles (McCave, 1984). Integrating that equation over the collision sphere surface yields the collision frequency function for differential settling:

$$\beta_{D,im} = \left[\frac{\pi F_c^2}{4}\right](D_i + D_m)^2\,|W_{s,i} - W_{s,m}| \tag{3-14}$$

where $W_{s,i}$ and $W_{s,m}$ = settling velocity of the i and m particles, respectively. This equation is equivalent to the differential settling part of Equation 2-5 if the settling velocity is assumed to follow Stokes Law and $F_c = 1$. Like Equation 3-13, it assumes the particles' motions are independent of each other (Overbeek, 1952), which is not strictly true. For example, a settling particle drags fluid along with it, inducing a following wake that will in turn accelerate following particles toward the settling particle (Daisley et al., 1964). However, the assumption is a necessary approximation compensated in part by use of the collision diameter function. (See Section 3.5.1.2.)

3.3.1.4 Net collision frequency function

All of the three primary collision processes can simultaneously contribute to aggregation; although it is clear that Brownian motion dominates at very small particle sizes and differential settling contributes only when at least one of the particles is large enough to settle faster than others. Swift and Friedlander (1964) found that linearly adding the collision frequency terms for Brownian motion and laminar shear gave predicted aggregation rates that matched experimental results for latex particles in a Couette mixing chamber. Here it is assumed that Brownian motion, turbulent shear, and differential settling effects can all be considered linearly additive in turbulent flows (Han, 1989; Lick et al., 1992), so that Equation 3-5 becomes:

$$N_{im} = \alpha_a (\beta_{B,im} + \beta_{S,im} + \beta_{D,im}) n_i n_m \tag{3-15}$$

Figure 3-5 illustrates each of the terms above for typical estuarial water column conditions. The differential settling function goes to zero for same-size particles (10 µm in Figure 3-5), and for particles larger than about 3 µm Brownian motion is seen to have at least an order of magnitude less effect than flow shear and differential settling. This dominance is explored further below by normalizing the contributions of each term.

Figures 3-6 and 3-7 illustrate the relative contributions (percent of total) of each component in Equation 3-15 for turbulent energy dissipation rates of 1×10^{-4} and 1 m^2/sec^3, respectively. The smaller value represents a energy dissipation rate characteristic of water column flow speeds less than about 0.5 m/sec, as shown in Table 3-1, and the larger value represents that occurring near the bed at the same flow speed, for flows which can be described by the law of the wall. For illustrative purposes F_c has been set to 0.75.

Table 3-1. Approximate shearing rates, shear stresses, and energy dissipation rates for a range of typical estuarial conditions.

Location	Mean Flow Speed (m/sec)	Shearing Rate[a] (sec^{-1})	Shear Stress[b] (Pa)	Order of Energy Dissipation Rate[c] (m^2/sec^3)
Average over Water Column	0.05	0.1	1×10^{-3}	10^{-7}
	0.5	4	4×10^{-2}	10^{-4}
	1.0	10	1×10^{-2}	10^{-3}
Near Bed	0.05	3	3×10^{-2}	10^{-4}
	0.5	200	0.2	1
	1.0	1000	1	10

Notes: [a] By Equation 5-4. [b] Shear stresses can be an order of magnitude greater in very energetic environments. [c] By Equation 3-12.
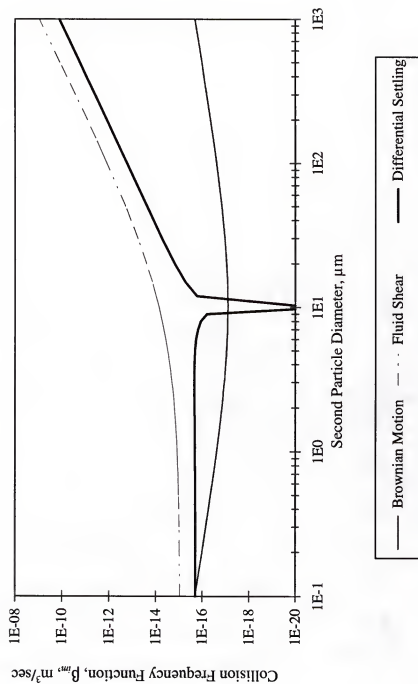
Figure 3-5. Collision Frequency Function for a 10 μm particle under typical estuarial flow conditions.

Figure 3-6. Relative contributions to Collision Frequency Function β_{im} for typical water column conditions of $\epsilon = 1 \times 10^{-4}$ m²/sec³.

a) First particle diameter = 1 μm; b) First particle diameter = 10 μm; c) First particle diameter = 100 μm.

a)

b)

c)
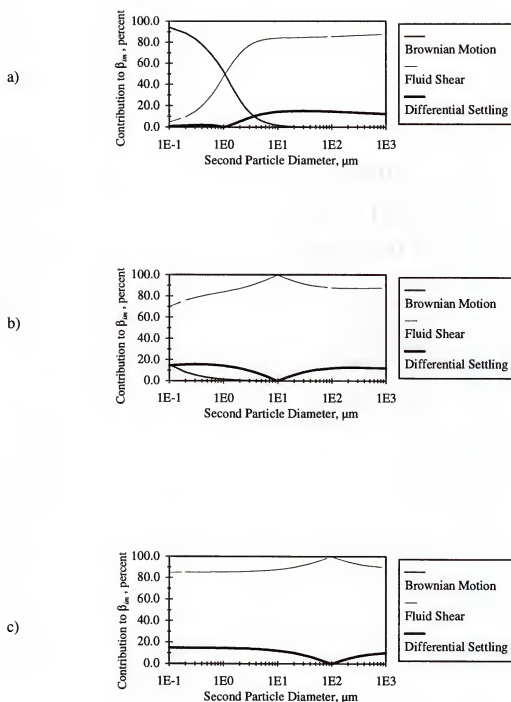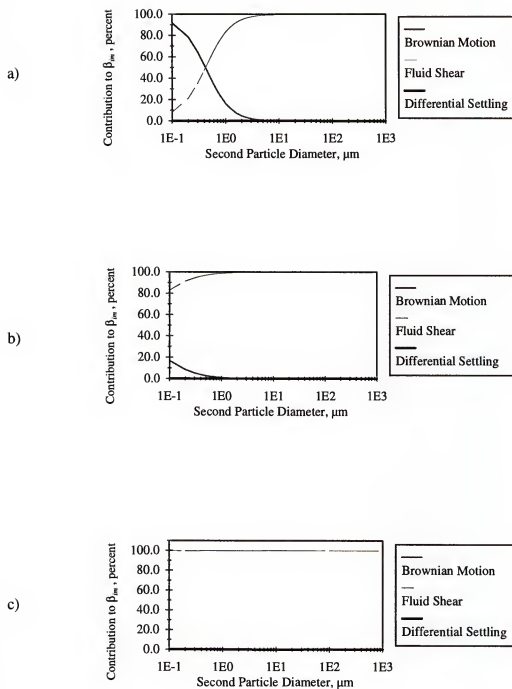
Figure 3-7. Relative contributions to collision frequency function β_{im} for typical near bed conditions of $\epsilon = 1$ m^2/sec^3.
  a) First particle diameter = 0.1 μm; b) First particle diameter = 1 μm; c) First particle diameter = 10 μm.

In Figure 3-6 the behavior of the differential settling term produces some odd effects in the curves. When the two particles are exactly the same size, $W_{s,i} = W_{s,m}$, the differential settling term goes from being a significant part of the total to zero, e.g., at 10 µm in Figure 3-6b and 100 µm in Figure 3-6c, and the flow shear term jumps to 100 percent, producing discontinuities in both curves. In Figure 3-7 the phenomenon isn't noticeable, since differential settling contributes a trivial relative number of collisions at the higher shear rate.

In Figure 3-6a, where the first (i) particle has a diameter of 1 µm, Brownian motion is seen to dominate for second (m) particle sizes less than 1µm, but shear overtakes it at about 1 µm and contributes more than 80 percent of the total collision frequency function for particle sizes exceeding 5 µm. Differential settling contributes 10 percent or more of the total for m particles larger than 5 µm. Figure 3-6b, with an i particle size of 10 µm, shows that flow shear is the dominant contributor for all m particle sizes, but with a still significant 10 to 20 percent contribution from differential settling at all sizes except $D_i \approx D_m$. For an i particle size of 100 µm, Figure 3-6c shows that Brownian motion has a negligible effect, with flow shear contributing 80 to 100 percent and differential settling contributing under 20 percent of the total.

Figures 3-7a through 3-7c show that at the higher energy dissipation rate of 1 m^2/sec^3 flow shear overwhelms differential settling for all particle sizes, and only when both particles are smaller than 1µm does Brownian motion make a significant contribution. Since near bed maximum energy dissipation rates are on the order of 10 to 30 m^2/sec^3 (corresponding to maximum flow speeds on the order of 1 m/sec) Figure 3-7 shows that in the near bed region

Brownian motion and differential settling can be neglected except for individual grains and near slack water.

Figures 3-8a and 3-8b illustrate the dependence of the combined collision frequency function on the sizes of the two colliding particles for an energy dissipation rate of 1×10^{-5} m^2/sec^3. Figure 3-8a covers the particle size range of 0.1 to 5 μm and shows the function to be a minimum at $D_i = D_m = 0.1$ μm, then increasing while either particle diameter is held constant and the other is increased. The local maxima along the side axes drops to a minimum between 0.1 and 1 μm, then rises montonically with increasing D_i and D_m. Figure 3-8b covers the size range of 5 to 1000 μm and exhibits a concave surface with the maximum collision frequency (about 2.5×10^{-9} m^3/sec) occurring when the two particles sizes are equal and at their largest plotted value of 1000 μm. The local minimum in Figure 3-8a is the result of Brownian motion effects declining more rapidly than the flow shear effect rises with increasing particle size. At larger sizes, the effect of flow shear is increased by the particles becoming larger targets, even to the point that the reduction of settling differential collisions from similar size particles (zero for same size) is offset.

3.3.2 Three-Body Collisions

Lick and coworkers (Burban et al., 1989; Lick et al., 1992) inferred the significance of three-body collisions from their aggregation chamber work (see Section 2.4.2.2.) and Clercx and Schram (1992) evaluated three-body hydrodynamic interactions in suspensions. Otherwise, the sedimentation literature is remarkably silent on the subject. Here a procedure from the gas dynamics literature is adapted to sediment particle collisions.
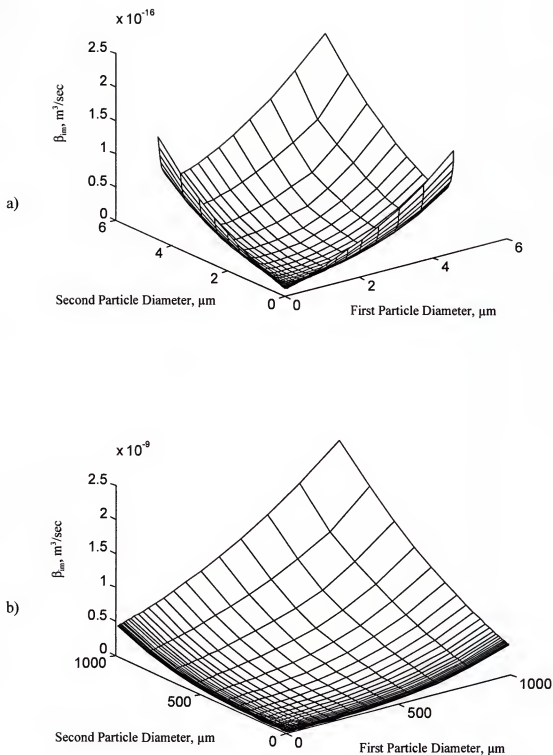
Figure 3-8. Total collision frequency function β_{im} for an energy dissipation rate typical of the estuarial water column. a) Particle size range of 0.1 to 5 µm; b) Particle size range of 0.1 to 1000 µm.

Following Rabinowitch (1937), the rate of three-body collisions is considered in terms of the probability of two essentially simultaneous two-body collisions—an i particle collides with a k particle and during that collision an m particle also collides with the same k particle. The two collisions are independent events. $EV(iK)$ is the event in which any i particle collides with a particular k particle, referred to as K, and $EV(Km)$ is the event in which the K particle collides with any m particle. The individual probabilities of those two events occurring in any given time interval t can be expressed as (Rabinowitch, 1937; Clarke and McChesney, 1964):

$$Pr[EV(iK)] = \frac{N_{ik}}{n_k} t \qquad (3\text{-}16)$$

The probability of a three-body collision is then the probability that a Km collision:

$$Pr[EV(Km)] = \frac{N_{km}}{n_k} t \qquad (3\text{-}17)$$

occurs in the time interval over which an iK collision occurs. Since events $EV(iK)$ and $EV(Km)$ statistically independent, the probability of their intersection—the probability of an iKm collision during the same time interval—is (Ochi, 1990):

$$Pr[EV(iKm)] = Pr[EV(iK) \cap EV(Km)]$$

$$= Pr[EV(iK)] \, Pr[EV(Km)]$$

$$= \frac{N_{ik} t_{ik}}{n_k} \frac{N_{km} t_{km}}{n_k} \qquad \textbf{(3-18)}$$

$$= \alpha_a^2 \beta_{ik} \beta_{km} n_i n_m t_{ik} t_{km}$$

where t_{ik}, t_{km} = duration of iK and Km collisions, respectively.

Equation 3-18 can be recast into collision frequency by:

$$N_{ikm} = Pr[EV(iKm)] \frac{n_k}{t_{ikm}}$$

$$= N_{ik} N_{km} \frac{t_{ik} t_{km}}{n_k t_{ikm}} \qquad \textbf{(3-19)}$$

$$= \alpha_a^2 \beta_{ik} \beta_{km} n_i n_k n_m \frac{t_{ik} t_{km}}{t_{ikm}}$$

where t_{ikm} = total duration of the three-body collision.

If the colliding particles were noncohesive inelastic bodies, the collision duration and the probability of a three-body collision would be essentially zero; however, porous cohesive aggregates will intermesh during a collision and thus experience a finite collision time between the moment of first contact and the moment at which enough grain-to-grain contact has been made to halt further interpenetration. Referring to Figure 3-9, if the two-body collision begins when the i particle first touches the k particle and ends when it has

a. Initial contact between i and k at t=0.

b. Collision complete at $t = t_{ik}$.

$$u_{ik} = \frac{u_i M_i}{M_i + M_k}$$
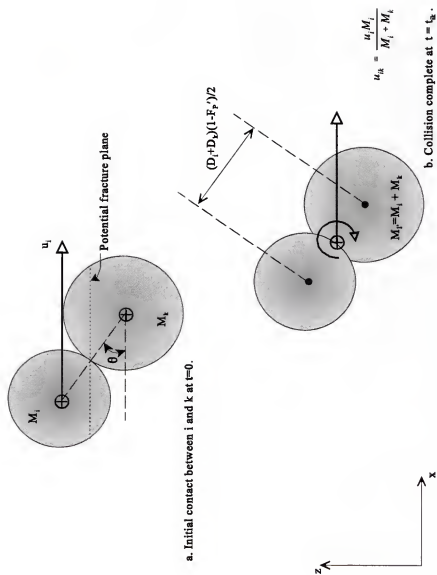
Figure 3-9. Schematic of two-particle collision.

penetrated some distance into the k particle, then an i-k collision duration will be approximately:

$$t_{ik} = \frac{(D_i + D_k)F_p}{2\,u_i} \tag{3-20}$$

where

$F_p = F_p{}'\cos\theta,$

$F_p{}'$ = coefficient representing the relative depth of interparticle penetration,

θ = angle between direction of u_i and the line connecting the i and k particle centers, and

u_i = velocity of i particle relative to the k particle, given by:

$$u_i = \begin{cases} \dfrac{\kappa T}{3\pi\mu D_i D_k} & \textit{Brownian Motion} \\[3mm] \dfrac{D_i + D_k}{2}\sqrt{\dfrac{2\epsilon}{15\pi\nu}} & \textit{Flow Shear} \\[3mm] \left|W_{s,i} - W_{s,k}\right| & \textit{Differential Settling} \end{cases} \tag{3-21}$$

The value of F_p in Equation 3-20 will be a function of particle momentum, particle density, and the number and strength of intraparticle bonds of the colliding particles; however, it must be greater than 0, and will be less than 0.5 unless significant crushing occurs within the colliding particles, which is unlikely since the strength of the particle will be exceeded and fragmentation could occur before that extent of crushing. An exact value

for F_p is unavailable, but for the present purposes, F_p is estimated to be about 0.1, following Krone (1963).

Considering now the three-body collision schematized in Figure 3-10, if the ik and km collisions are simultaneous, then the minimum value of t_{ikm} will be the larger of t_{ik} and t_{km} and will be best approximated over many collisions by $(t_{ik} + t_{km})/2$. The maximum possible value of t_{ikm} will occur if the two collisions are sequential, with the km collision beginning at the end of the ik collision, and $t_{ikm} = t_{ik} + t_{km}$. Assuming a normal distribution for both t_{ik} and t_{km}, the mean value of t_{ikm} can be estimated to be $3(t_{ik} + t_{km})/4$. Using these time values, the time ratio term of Equation 3-19 becomes:

$$\frac{t_{ik} \, t_{km}}{t_{ikm}} = \frac{2 F_p (D_i + D_k)(D_k + D_m)}{3 [u_m (D_i + D_k) + u_i (D_k + D_m)]} \tag{3-22}$$

where u_m = velocity of the m particle relative to the k particle. Substituting Equation 3-22 into Equation 3-19 and gathering terms yields the equation for three body collision frequency:

$$N_{ikm} = \alpha_{ikm} N_{ik} N_{km} \tag{3-23}$$

where α_{ikm} is the three-body collision efficiency parameter given by:

$$\alpha_{ikm} = \frac{2 F_p (D_i + D_k)(D_k + D_m)}{3 n_k [u_m (D_i + D_k) + u_i (D_k + D_m)]} \tag{3-24}$$

a. Initial contact between i and k at t=0, and between (i+k) and m between t=0 and t=t_{ikc}.

$$u_{ikm} = \frac{u_i M_i + u_m M_m}{M_i + M_k + M_m}$$

b. Collision complete at t = t_{ikm}.

$M_f = M_i + M_k + M_m$.
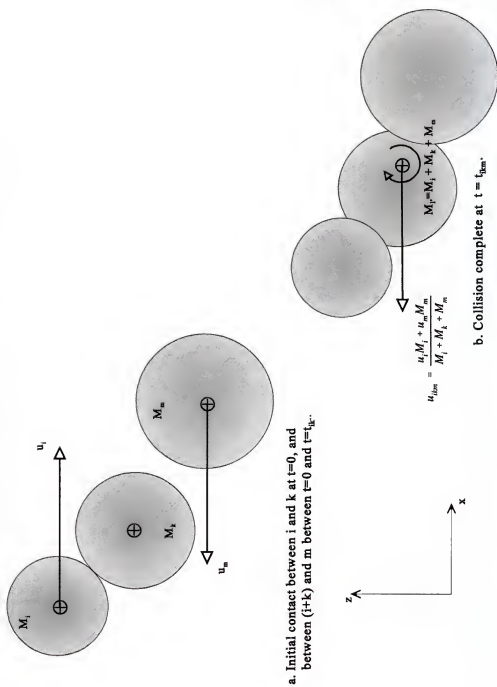
Figure 3-10. Schematic of three-particle collision.

Considering for illustrative purposes the flow shear mechanism alone, the expression for α_{ikm} can be simplified by substituting Equation 3-21 for the particle velocities, yielding:

$$\alpha_{ikm} = \frac{2F_p}{3n_k\sqrt{\dfrac{2\epsilon}{15\pi\nu}}} \tag{3-25}$$

Combining the flow shear term from Equation 3-25, Equation 3-5 for N_{ik} and N_{km}, and Equation 3-13 for β_{ik} and β_{im}, Equation 3-23 becomes:

$$\begin{aligned}
N_{ikm}(shear) &= N_{ik}N_{km}\frac{2F_p}{3n_k\sqrt{\dfrac{2\epsilon}{15\pi\nu}}} \\
&= \left[\frac{\alpha_a^2\pi^2}{24}\sqrt{\frac{2}{15\pi}}\,F_p F_c^4\right]\sqrt{\frac{\epsilon}{\nu}}\,(D_i+D_k)^3(D_k+D_m)^3 n_i n_m
\end{aligned} \tag{3-26}$$

The form of this equation is reasonable, in that the number of collisions increases with an increase in energy dissipation rate (square root), concentration (to the 3rd power), and particularly particle size (to the 6th power), which increases not only the target (collision sphere) size, but also the duration of collisions.

To further explore the nature of N_{ikm}, we can divide Equation 3-26 by the average number of i-k and k-m collisions to obtain:

$$\gamma_{ikm} = \frac{N_{ikm}}{(N_{ik}+N_{km})/2} = \left[\frac{\alpha_a\pi F_p F_c^2}{3}\right]\frac{(D_i+D_k)^3(D_k+D_m)^3 n_i n_m}{(D_i+D_k)^3 n_i + (D_k+D_m)^3 n_m} \tag{3-27}$$

which, for the simplest case where $D_i = D_k = D_m$ and $n_i = n_m$, reduces to:

$$\gamma_{ikm} = \left[\frac{4 \pi \alpha_a F_p F_c^2}{3} \right] D_k^3 n_k \tag{3-28}$$

This result is also reasonable, since the number of three-body collisions relative to the number of preceding two-body collisions will increase with increasing concentration and increasing particle size.

By the stated assumptions, every three-body collision must also be a two-body collision, so Equation 3-28 must always yield a result less than 1, i.e., $N_{ikm} < (N_{ik} + N_{km})/2$. Table 3-2 lists some example values of γ_{ikm} for a typical range of particle sizes and concentrations (using $\alpha_a = 1$, $F_c = 0.75$, $F_p = 0.1$, $D_i = D_k = D_m$, $n_i = n_m$, and values of $\Delta\rho$ as given in Figure 3-2 for San Francisco Bay sediment). As would be expected, the number of three-body collisions is a trivial fraction of the total number of collisions at concentrations on the order of 0.1 kg/m^3; whereas, at concentrations of 10 kg/m^3 they will constitute 1 to 2 percent of the two-body collisions. At 30 kg/m^3, they will constitute about 5 percent, and at 100 kg/m^3, a viscous slurry, about 18 percent, all well below the postulated maximum of 100 percent.

3.3.3 Four-Body Collisions

The logic used to derive Equation 3-19 can also be used to develop an expression for the number of four-body collisions:

$$N_{iklm} = \frac{t_{kl} t_{ikm}}{t_{iklm}} \frac{N_{kl} N_{ikm}}{n_k} \tag{3-29}$$

where t_{iklm} = duration of the four-body collision. The number of four-body collisions as a percentage of three-body collisions is shown in Table 3-2.

Table 3-2. Three-body and four-body collision ratios for representative ranges of concentration and particle size.

C_i kg/m³	D_i μm	n_i number/m³	γ_{ikm} percent	N_{iklm}/N_{ikm} percent
0.1	1	7.2×10^{13}	0.0084	0.0016
0.1	100	1.6×10^8	0.018	0.0036
10	1	7.2×10^{15}	0.84	0.16
10	100	1.6×10^{10}	1.8	0.36
10	1000	1.9×10^7	2.2	0.43
30	100	4.7×10^{10}	5.4	1.1
100	100	1.6×10^{11}	18	3.6

Based on these calculations, it appears that the number of three-body collisions will be make a minor contribution to the total number of flow-shear-induced collisions except at sediment concentrations of about 30 kg/m³ and higher. However, their net effect on aggregation processes may be more substantial than these numbers indicate, and that aspect is examined in Chapter 6. The results suggest that four-body collisions, which are a tiny fraction of the number of three-body collisions, will have a negligible effect on the total number of collisions at concentrations in the range expected for estuarial sediment suspensions.

3.3.4 Total Collision Frequency

The results of the preceding sections can be used to calculate the total number of collisions experienced by the model's k^{th} class as the sum of its two-body and three-body collisions:

$$\mathbb{N}_k = \sum_{i=1}^{s} N_{ik} + \sum_{i=1}^{s} \sum_{m=1}^{s} \alpha_{ikm} N_{ik} N_{km} \tag{3-30}$$

3.4 Shear Stresses on Aggregates

3.4.1 Two-Body Collision-Induced Stresses

Figure 3-9 illustrated the collision of two particles that bond during the collision. At time $t = 0$ a particle of mass M_i, moving at speed u_i relative to a particle of mass M_k, touches the k particle. At time $t = t_{ik}$ the combined particle has mass $M_{ik} = M_i + M_k$ and translational velocity u_{ik}, which by conservation of linear momentum is given by:

$$u_{ik} = \frac{u_i M_i}{M_i + M_k} \tag{3-31}$$

and by Newton's second law:

$$F_{ik} = \frac{u_{ik} M_k}{t_{ik}} \tag{3-32}$$

Combining the above two equations and using Equation 3-20 for t_{ik} yields an expression for the forces exerted on and by the particles during the collision:

$$F_{ik} = \frac{2u_i^2 M_i M_k}{F_p(D_i + D_k)(M_i + M_k)} \qquad \text{(3-33)}$$

If either particle fractures as a result of the applied force, the fracture plane will be the weakest surface between the point where the force is applied and the center of mass of that particle; however, for a given force the location of highest shear stress will be where the plane has the least area, which is between the applied force and the edge of the particle. Thus for a homogenous particle the probable fracture plane will intersect the contact point. While aggregates are not homogenous, the average fracture plane will lie at the most probable location, which is the point of contact, and run through the minimum area path of the particle as shown in Figure 3-9. Dividing Equation 3-34 by the area of the fracture surface identified in Figure 3-9 yields the critical shear stress experienced by the k aggregate.

$$\tau_{ik,k} = \frac{8u_i^2 M_i M_k}{\pi F_p D_k^2 (D_i + D_k)(M_i + M_k)} \qquad \text{(3-34)}$$

The shear stress experienced by the i particle is obtained by replacing the D_k^2 by D_i^2.

The equations for collisional shear stress from Brownian motion, turbulent shear, and differential settling can be obtained by substituting the respective velocity of particle approach into Equation 3-34. For the conservative (maximum) estimate of shear stress, the velocity of particle approach can be represented as the sum of those three velocities.

Equation 3-34 shows that the collision-induced shear stress increases linearly with energy dissipation rate. For the simplest case of equal size particles the shear stress is approximately proportional to the square of the particle diameter. The collision-induced shear stress will be smallest for two given particles when the collision velocity vector passes near the center of both particles, i.e., $\theta = 0$. The shear stress increases with the angle, as the same collision force is applied over a smaller shear surface. However, the present state of knowledge of particle strengths is insufficient to pursue the role of the angle θ further, and a reasonable approximation is to use the expected average of $\theta = \pi/4$.

3.4.2 Three-Body Collision-Induced Stresses

The collision of three bodies has more degrees of freedom than the two-body case just discussed, in part since the angle of approach of the second particle can vary through 360 degrees; however, if we consider only the most physically probable collision sequence, which is shown in Figure 3-10, the problem becomes more tractable. Following the same steps as in the two-body case, the shear stress experienced by the k particle is:

$$\tau_{ikm,k} = \frac{8}{\pi F_p D_k^2} \left\{ \frac{M_i M_k u_i^2}{(D_i + D_k)(M_i + M_k)} + \frac{(M_i + M_k) u_m}{(D_k + D_m)} \left[\frac{u_i M_i + u_m M_m}{M_i + M_k + M_m} - \frac{u_i M_i}{M_i + M_k} \right] \right\} \tag{3-35}$$

For the case of two or three same-size particles colliding, dividing Equation 3-35 by Equation 3-34 shows that three-body collisions produce shear stresses up to two thirds greater than two-body shear stresses; thus, even though Section 3.3.2 indicates that the

number of three-body collisions will be substantially smaller than the number of two-body collisions, their net effect on disaggregation may be more significant. This theoretical finding is consistent with the experimental inference of Burban et al. (1989) that three-body collisions were important for disaggregation, but less so for aggregation.

3.4.3 Flow-Induced Stresses

A suspended particle in a vertical velocity gradient will experience a net torque from differential drag on its top and bottom surfaces and rotate about its center until the rotational drag applied on the downstream and upstream surfaces balances the applied drag on the surfaces parallel to the flow. Assuming a linear velocity gradient across the diameter, Krone (1963) derived the maximum flow-induced shear stress in a spherical particle as:

$$\tau_u = \frac{\mu}{8} \frac{du}{dz} \tag{3-36}$$

where $\frac{du}{dz}$ = viscous flow velocity gradient across particle. The shearing rate near the bed, where $\frac{du}{dz}$ is greatest, can be adequately described by a viscous relationship such as Equation 3-36.

The relative importance of shear stresses imposed by two-body collisions to that imposed by flow shear alone can be examined by dividing $\tau_{ik,k}$ (Equation 3-35) by τ_u (Equation 3-36), with the following result for two same-size particles:

$$\frac{\tau_{kk,k}}{\tau_u} = \frac{4\rho_k D_k^2}{3\mu F_p \frac{du}{dz}} \left[\frac{2\epsilon}{15\pi\nu} \right] \tag{3-37}$$

The ratio of Equation 3-37 is plotted in Figure 3-11 for energy dissipation rates typical of estuarial waters. At the least value of $\epsilon = 1 \times 10^{-4}$ m²/sec³, flow-induced shear stresses dominate (by 10:1 or more) for particles smaller than about 100 µm, and reach approximate parity at about 300 µm. For $\epsilon = 1$ m²/sec³ approximate parity occurs at about 10 µm and for larger particles collisional stresses exceed flow-induced shear stresses, becoming hundreds of times greater for diameters larger than about 200 µm. At the near bed maximum of $\epsilon = 30$ m²/sec³ collisional stresses dominate for diameters over about 20 µm.

From this analysis it is concluded that both flow-induced shear stresses and collision-induced shear stresses can be important within the range of particle sizes and flow intensities typical of estuarial flows, with collision-induced shear being more important for larger particles and higher energy dissipation rates.

3.5 Aggregation and Disaggregation

Since the potential bonding forces between fine estuarial sediment grains are strong and the collision diameter function, F_c, excludes close encounters with a low potential for collision, it is assumed here that every true collision between cohesive particles (see Section 3.5.1.2) results in a bond. If the colliding particles are strong enough to remain intact through the collision, they will aggregate; whereas, if at least one of the colliding particles is not strong enough, both aggregation and disaggregation will result, with broken particle
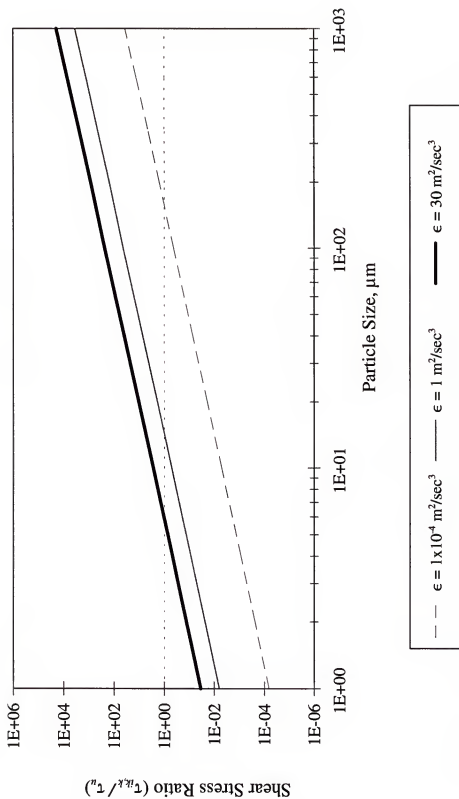
Figure 3-11. Ratio of collision-induced shear stress to flow-induced shear stress for two particles of the same size with energy dissipation rates typical of an estuarial water column and near-bed zone.

fragments bonding at the collision points. Disaggregation can occur without a collision if the strength of particles is less than the forces imposed by flow shear.

Disaggregation by shattering into many subparticles appears to be rare in the natural environment (Hogg et al., 1985), and the bonds between individual grains are much stronger than those between any two order 0 (or higher order) aggregates; therefore, it is assumed that few single grains are eroded from suspended aggregates and disaggregation primarily occurs by breakage along a single fracture surface within each aggregate.

As particles aggregate and disaggregate, the total mass concentration within each specified class in the distribution will (see Figure 3-1):

1.   Increase by aggregation of particles from smaller mass classes.

2.   Increase by disaggregation of particles from larger mass classes.

3.   Decrease by aggregation or disaggregation of particles within the class.

The mass and number concentrations of each of the classes can be updated for aggregation and disaggregation according to:

$$C_j(new) \ = \ C_j(old) \ + \ \dot{C}_j(sum)\Delta t \tag{3-38}$$

$$n_j(new) \ = \ \frac{C_j(new)}{M_j} \tag{3-39}$$

where $\dot{C}_j(sum)$ = sum of the mass change rates from flux and aggregation/disaggregation by the mechanisms described below, and

Δt = time interval over which aggregation/disaggregation rate is calculated.

3.5.1 Collisions

By the assumptions made thus far, every collision results in cohesion at the points of particle contact. If a fragment of a weaker particle breaks off while bonding to a nonbreaking particle, the nonbreaking particle will undergo aggregation while the weaker one undergoes disaggregation. For example, in a disaggregating collision between i class and k class particles, there are two possible outcomes—two new particles or three new particles as depicted in Figure 3-12. This logic dictates the number and configuration of a limited set of possible collision outcomes, which are listed by type below.

3.5.1.1 Collision outcomes

Collision outcomes are categorized below by the number of colliding particles (2 or 3), whether aggregation only (A) or both aggregation and disaggregation (D) occur, and the number of particles (1 to 4) resulting from the collision. In this discussion, the class subscript notation indicates the relative size of the colliding particles—subscript i denotes a colliding particle of a size class smaller than one with the subscript k, which is smaller than one with subscript m. Subscript j denotes the preselected size intervals and subscripts beginning with l denote a particle of any size.

Type 2A1. In a two-body collision of i and k particles in which both particles' shear strengths are greater than the collision-imposed shear stresses, one new particle of mass $M_{l'}$ is formed. This set of conditions is written as:

$$If \quad \begin{Bmatrix} \tau_i \ge \tau_{ik,i} \\ \tau_k \ge \tau_{ik,k} \end{Bmatrix} \quad M_i \to M_k \implies M_{l'} = M_i + M_k \tag{3-40}$$

a) Before Collision   After Collision

b) Before Collision   After Collision
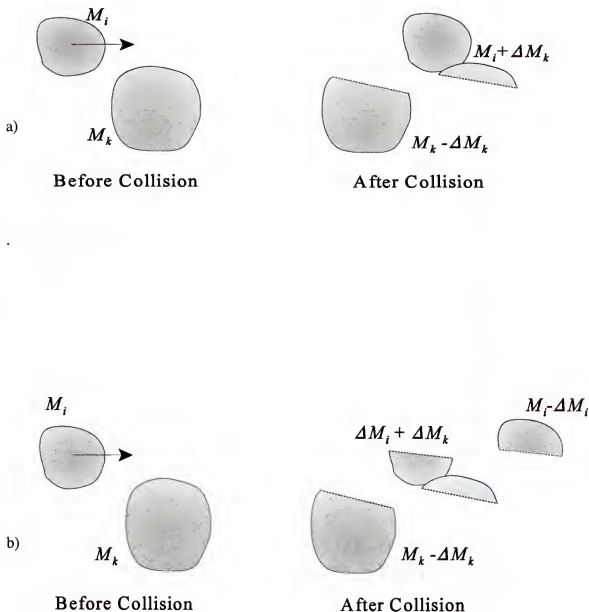
Figure 3-12. A disaggregating two-body collision will produce two or three particles depending on the strength of the particles compared with the collision-imposed forces.
a) Two particles result when the k particle is weaker and the i particle is stronger than the imposed stresses; b) Three particles result when both particles are weaker than the imposed stresses.

Since the mass of the l' particle will not necessarily be equal to one of the representative class masses, the new particle's class index $j=l$ is that for which $M_{i'}$ is greater than the class lower limit and less than the class upper limit, which is expressed as:

$$l = J\{i+k\} = CLASS\{M_j(lower) < (M_i + M_k) \le M_j(upper)\} \tag{3-41}$$

After the aggregating collision the i and k class particles will no longer exist, and the rate of mass concentration changes for the three affected classes can be computed as the mass change in each collision times the number of collisions per unit time per unit volume:

$$\dot{C}_{j=i}(ik) = -M_i N_{ik}$$
$$\dot{C}_{j=k}(ik) = -M_k N_{ik} \tag{3-42}$$

$$\dot{C}_{j=l}(ik) = +(M_i + M_k)N_{ik} \tag{3-43}$$

<u>Type 3A1</u>. In a three-body ikm collision where all three particles are strong enough to survive the collision one new particle of mass $M_{l'}$ is formed:

$$If \begin{Bmatrix} \tau_i \ge \tau_{ikm,i} \\ \tau_k \ge \tau_{ikm,k} \\ \tau_m \ge \tau_{ikm,m} \end{Bmatrix} M_i \to M_k \to M_m \Rightarrow M_{l'} = M_i + M_k + M_m \tag{3-44}$$

and so:

$$\dot{C}_{j=i}(ikm) = -M_i N_{ikm}$$
$$\dot{C}_{j=k}(ikm) = -M_k N_{ikm} \tag{3-45}$$
$$\dot{C}_{j=m}(ikm) = -M_m N_{ikm}$$

and:

$$\dot{C}_{j=i}(ikm) \;=\; +(M_i + M_k + M_m)N_{ikm} \qquad \textbf{(3-46)}$$

where l is defined by Equation 3-41.

    Type 2D2. As shown in Figure 3-12, two new particles result if the collisional shear stress from an ik collision exceeds the strength of only one colliding particle, which breaks into one free fragment and one fragment bonding with the other particle. Since a k particle is larger and thus weaker than an i particle, the k disaggregates and the i particle aggregates.

$$If \; \begin{Bmatrix} \tau_k < \tau_{ik} \\ \tau_i \ge \tau_{ik} \end{Bmatrix} \; M_i \to M_k \;\Rightarrow\; \begin{cases} M_{I1'} = M_k - \Delta M_k \\[2mm] M_{I2'} = M_i + \Delta M_k \end{cases} \qquad \textbf{(3-47)}$$

where ΔM_k = mass of the fragment which breaks from the k particle and bonds with the i particle.

    The angle θ in Figure 3-9 can vary from 0 to $\pi/2$. If we assume that the collision force is applied at the point of contact and the inertial resistance is applied at the center of the particles, then the maximum shear stress, and thus failure, will occur for $0 < \theta < \pi/2$. Thus ΔM_k may approach zero and fall into the smallest size class or be as large as $M_k/2$. Over many collisions the size will vary over that whole range and will average $\overline{\Delta M_k} = \dfrac{3}{16}M_k$, so the average mass change rates from Equation 3-47 will be:

$$\dot{C}_1' \;=\; +\left(M_k - \frac{3}{16}M_k \right)N_{ik}$$

$$\dot{C}_2' \;=\; +\left(M_i + \frac{3}{16}M_k \right)N_{ik} \qquad \textbf{(3-48)}$$

(The M_k terms within the brackets in the first equation are left unsimplified so that the mass bookkeeping is clear.)

The mass $M_{l1'}$ can be as small as $M_k/2$ and as large as M_k, so that a particle can fall into any class from $l_1 = J\{k/2\}^*$ to k. Mass $M_{l2'}$ will be larger than M_i and smaller than $(M_i + M_k/2)$, so $l2$, the class for particle $M_{l2'}$, can range from i to $J\{i+k/2\}$. Over many collisions the probability that either $M_{l1'}$ or $M_{l2'}$ will fall in any j^{th} class is assumed to be the result of a random distribution of fragment sizes over their possible ranges, so the mass concentration change rate for each of the involved classes will be given by Equation 3-42 plus:

$$\dot{C}_j(ik) = p_j(l=J\{\frac{k}{2}\}:k) \dot{C}_1' + p_j(l=i:J\{i+\frac{k}{2}\}) \dot{C}_2' \qquad j = 1 \ to \ s \tag{3-49}$$

where $p_j(l=i1:i2) = $ the probability mass function for the likelihood that $\dot{C}'$ will fall into a given class from $i1$ to $i2$, with $\sum_{j=i1}^{i2} p_j(l) = 1$. Derivation and tabulation of incremental probability mass function $p_j(l=i1:i2)$ are given in Appendix A.

Type 2D3. Three new particles are produced as shown in Figure 3-12 if the collisional shear stress exceeds the strength of both colliding particles. Two particles will consist of the free fragments of the i and k particles and a third will consist of the other fragments of each which have bonded at the point of impact, as indicated by Equation 3-50:

---

* In this case, Equation 3-41 is interpreted as: $J\{\frac{k}{2}\} = CLASS\{M_j(lower) < \left(\frac{M_k}{2}\right) \le M_j(upper)\}$.

$$If \ \begin{cases} \tau_i < \tau_{ik,i} \\ \tau_k < \tau_{ik,k} \end{cases} \ M_i \rightarrow M_k \ \Rightarrow \ \begin{cases} M_{l1'} = M_k - \Delta M_k \\ M_{l2'} = M_i - \Delta M_i \\ M_{l3'} = \Delta M_i + \Delta M_k \end{cases} \qquad \textbf{(3-50)}$$

Using the same logic as for the two particle outcome case, the concentration change rates will be:

$$\dot{C}_1' = +\left(M_k - \frac{3}{16}M_k\right)N_{ik}$$

$$\dot{C}_2' = +\left(M_i - \frac{3}{16}M_i\right)N_{ik} \qquad \textbf{(3-51)}$$

$$\dot{C}_3' = +\left(\frac{3}{16}M_i + \frac{3}{16}M_k\right)N_{ik}$$

The mass concentration change per class is then given by Equation 3-42 plus:

$$\dot{C}_j(ik) = p_j(l=J\{\frac{k}{2}\}:k)\,\dot{C}_1' + p_j(l=J\{\frac{i}{2}\}:i)\,\dot{C}_2'$$

$$+ p_j(l=1:J\{\frac{i}{2}+\frac{k}{2}\})\,\dot{C}_3' \qquad j = 1 \ to \ s \qquad \textbf{(3-52)}$$

<u>Type 3D2</u>. The outcomes of three-body *ikm* disaggregating collisions follow the same rules as two-body collisions except that there are more possible outcomes—two, three, or four new particles, depending on whether one, two, or three of the colliding particles' strengths are exceeded by the collisional shear stress—and the possible outcomes include variations on which particles share the fragments and how large the fragments are.

If only one particle (the m particle, which is largest and weakest of the three) is weaker than the imposed stresses there are two equally likely outcomes:

$$If \begin{Bmatrix} \tau_i \geq \tau_{ikm,i} \\ \tau_k \geq \tau_{ikm,k} \\ \tau_m < \tau_{ikm,m} \end{Bmatrix} M_i \rightarrow M_k \rightarrow M_m \Rightarrow \begin{cases} \begin{cases} M_{I1'} = M_i + \Delta M_m^0 \\ M_{I2'} = M_k + M_m - \Delta M_m^0 \end{cases} \\ or \\ \begin{cases} M_{I1'} = M_i + M_k + \Delta M_m \\ M_{I2'} = M_m - \Delta M_m \end{cases} \end{cases} \quad (3\text{-}53)$$

where ΔM_m^0 = the fragment of the m class particle, with the superscript 0 indicating the middle particle fragment, which can vary in size from $M \approx 0$ to M_m, since stresses are applied at the outer edges; thus: $\overline{\Delta M_m^0} = \frac{1}{2} M_m$

In the first case the m particle is between the i and k particles and in the second case it is not. Since either outcome is equally probable, the average mass change rate can be equally divided between the two possible configurations and:

$$\begin{aligned} C_1' &= + \left(M_i + \frac{1}{2} M_m \right) \frac{N_{ikm}}{2} \\ C_2' &= + \left(M_k + M_m - \frac{1}{2} M_m \right) \frac{N_{ikm}}{2} \\ C_3' &= + \left(M_i + M_k + \frac{3}{16} M_m \right) \frac{N_{ikm}}{2} \\ C_4' &= + \left(M_m - \frac{3}{16} M_m \right) \frac{N_{ikm}}{2} \end{aligned} \quad (3\text{-}54)$$

Equation 3-45 and Equation 3-55 describe the concentration changes by class:

$$
\begin{aligned}
\dot{C}_j(ikm) \;=\; & p(l=i:J\{i+m\})\,\dot{C}_1' + p(l=k:J\{k+m\})\,\dot{C}_2' \\
& + p(l=J\{i+k\}:J\{i+k+\tfrac{m}{2}\})\,\dot{C}_3' + p(l=1:J\{\tfrac{m}{2}\})\,\dot{C}_4' \qquad j=1\ to\ s
\end{aligned}
\tag{3-55}
$$

Type 3D3. If the k and m particles are weaker than the imposed stresses the collision can produce three possible sets of outcomes:

$$
If\;
\begin{Bmatrix}
\tau_i \geq \tau_{ikm,i} \\
\tau_k < \tau_{ikm,k} \\
\tau_m < \tau_{ikm,m}
\end{Bmatrix}
\; M_i \to M_k \to M_m \;\Rightarrow\;
\begin{cases}
\begin{cases}
M_{l1'} = M_i + \Delta M_k^0 \\
M_{l2'} = M_k - \Delta M_k^0 + \Delta M_m \\
M_{l3'} = M_m - \Delta M_m
\end{cases} \\
or \\
\begin{cases}
M_{l1'} = M_i + \Delta M_m^0 \\
M_{l2'} = M_m - \Delta M_m^0 + \Delta M_k \\
M_{l3'} = M_k - \Delta M_k
\end{cases} \\
or \\
\begin{cases}
M_{l1'} = M_k - \Delta M_k \\
M_{l2'} = M_i + \Delta M_k + \Delta M_m \\
M_{l3'} = M_m - \Delta M_m
\end{cases}
\end{cases}
\tag{3-56}
$$

Each case in Equation 3-56 is equally probable, so the collision number can be equally distributed among the three possible outcomes, producing:

$$
\begin{aligned}
C_1' &= +\left(M_i + \frac{1}{2}M_k\right)\frac{N_{ikm}}{3} \\
C_2' &= +\left(M_k - \frac{1}{2}M_k + \frac{3}{16}M_m\right)\frac{N_{ikm}}{3} \\
C_3' &= +2\left(M_m - \frac{3}{16}M_m\right)\frac{N_{ikm}}{3} \\
C_4' &= +\left(M_i + \frac{1}{2}M_m\right)\frac{N_{ikm}}{3} \\
C_5' &= +\left(M_m - \frac{1}{2}M_m + \frac{3}{16}M_k\right)\frac{N_{ikm}}{3} \\
C_6' &= +2\left(M_k - \frac{3}{16}M_k\right)\frac{N_{ikm}}{3} \\
C_7' &= +\left(M_i + \frac{3}{16}M_k + \frac{3}{16}M_m\right)\frac{N_{ikm}}{3}
\end{aligned}
\tag{3-57}
$$

The net mass change rates are given by Equation 3-45 plus:

$$
\begin{aligned}
C_j(ikm) &= p_j(l{=}i{:}J\{i{+}k\})\,C_1' + p_j(l{=}1{:}J\{k{+}\tfrac{m}{2}\})\,C_2' \\
&\quad + p_j(l{=}1{:}J\{\tfrac{m}{2}\})\,C_3' + p_j(l{=}i{:}J\{i{+}m\})\,C_4' \\
&\quad + p_j(l{=}1{:}J\{\tfrac{k}{2}{+}m\})\,C_5' + p_j(l{=}J\{\tfrac{k}{2}\}{:}k)\,C_6' \\
&\quad + p_j(l{=}i{:}J\{i{+}\tfrac{k}{2}{+}\tfrac{m}{2}\})\,C_7' \qquad\qquad j = 1\ to\ s
\end{aligned}
\tag{3-58}
$$

Type 3D4. If all three particles are weaker than the imposed stresses, there are six possible outcomes, of which three are unique:

$$
If \begin{cases} \tau_i < \tau_{ikm,i} \\ \tau_k < \tau_{ikm,k} \\ \tau_m < \tau_{ikm,m} \end{cases} M_i \rightarrow M_k \rightarrow M_m \Rightarrow \begin{cases} \begin{cases} M_{l1'} = M_i - \Delta M_i \\ M_{l2'} = \Delta M_i + \Delta M_k^0 \\ M_{l3'} = M_k - \Delta M_k^0 + \Delta M_m \\ M_{l4'} = M_m - \Delta M_m \end{cases} \\ or \\ \begin{cases} M_{l1'} = M_m - \Delta M_m \\ M_{l2'} = \Delta M_m + \Delta M_i^0 \\ M_{l3'} = M_i - \Delta M_i^0 + \Delta M_k \\ M_{l4'} = M_k - \Delta M_k \end{cases} \\ or \\ \begin{cases} M_{l1'} = M_k - \Delta M_k \\ M_{l2'} = \Delta M_k + \Delta M_m^0 \\ M_{l3'} = M_m - \Delta M_m^0 + \Delta M_i \\ M_{l4'} = M_i - \Delta M_i \end{cases} \end{cases} \quad \text{(3-59)}
$$

After combining similar terms, the mass change rates are given by:

$$\dot{C}_1' = +2\left(M_i - \frac{3}{16}M_i\right)\frac{N_{ikm}}{3}$$

$$\dot{C}_2' = +2\left(M_k - \frac{3}{16}M_k\right)\frac{N_{ikm}}{3}$$

$$\dot{C}_3' = +2\left(M_m - \frac{3}{16}M_m\right)\frac{N_{ikm}}{3}$$

$$\dot{C}_{4'} = +\left(\frac{3}{16}M_i + \frac{1}{2}M_k\right)\frac{N_{ikm}}{3}$$

$$\dot{C}_5' = +\left(\frac{1}{2}M_k + \frac{3}{16}M_m\right)\frac{N_{ikm}}{3} \qquad \textbf{(3-60)}$$

$$\dot{C}_6' = +\left(\frac{3}{16}M_k + \frac{1}{2}M_m\right)\frac{N_{ikm}}{3}$$

$$\dot{C}_7' = +\left(\frac{1}{2}M_m + \frac{3}{16}M_i\right)\frac{N_{ikm}}{3}$$

$$\dot{C}_8' = +\left(\frac{3}{16}M_m + \frac{1}{2}M_i\right)\frac{N_{ikm}}{3}$$

$$\dot{C}_9' = +\left(\frac{1}{2}M_i + \frac{3}{16}M_k\right)\frac{N_{ikm}}{3}$$

and mass change rates per class are given by Equation 3-45 plus:

$$\dot{C}_j(ikm) = p_j(l=J\{\frac{i}{2}\}{:}i)\,\dot{C}_1' + p_j(l=J\{\frac{k}{2}\}{:}k)\,\dot{C}_2'$$

$$+ p_j(l=J\{\frac{m}{2}\}{:}m)\,\dot{C}_3' + p_j(l=1{:}J\{\frac{i}{2}+k\})\,\dot{C}_4'$$

$$+ p_j(l=1{:}J\{k+\frac{m}{2}\})\,\dot{C}_5' + p_j(l=1{:}J\{\frac{k}{2}+m\})\,\dot{C}_6' \qquad \textbf{(3-61)}$$

$$+ p_j(l=1{:}J\{m+\frac{i}{2}\})\,\dot{C}_7' + p_j(l=1{:}J\{\frac{m}{2}+i\})\,\dot{C}_8'$$

$$+ p_j(l=1{:}J\{i+\frac{k}{2}\})\,\dot{C}_9' \qquad\qquad j = 1 \; to \; s$$

3.5.1.2 Collision efficiency and collision diameter function

An accurate determination of collision efficiency, α_a, in Equation 3-15 and collision diameter function, F_c, in Equations 3-9, 3-13, and 3-14 is integral to development of an algorithm that successfully describes observed aggregation rates. The aggregation literature includes two approaches to the challenge of finding collision efficiency—empirically fitting some version of Equation 2-1 to observations by adjusting α' (the apparent efficiency, which is not paired with F_c), or deriving a theoretical form for α' and empirically fitting that form to observations by adjusting secondary parameters. Both approaches are briefly described here and then an alternate method is proposed.

Empirical. The most straightforward method for estimating α' is to count the number of particles in an aggregating suspension at intervals and assume that every collision predicted by Equation 2-1 results in aggregation so that it can be solved for α'. Edzwald et

al. (1974) and Gibbs (1983) employed this laboratory method for stirred real sediment and clay mineral suspensions at various salinities, and the clay mineral results are plotted in Figure 3-13. Among the notable features of the plot are that: a) for kaolinite and illite there is a clear dependence of α' on salinity below 4 ppt, but less dependence above 4 ppt (consistent with Table 2-2); b) montmorillonite displays a continuing dependence of α' up to the maximum tested salinity of 17.5 ppt; and c) the results of Edzwald et al. (1974) versus Gibbs (1983) are inconsistent in both patterns and absolute values. Gibbs (1983) attributed the latter discrepancy to the likelihood of the pipette sampling of Edzwald et al. (1974) breaking aggregates before measurement, but the effects of other experimental conditions such as the ionic composition of the water (Edzwald et al. used a synthetic solution and Gibbs used diluted sea water) and apparatus operation may have also influenced the results.

<u>Theoretical</u>. Zeichner and Schowalter (1977) and Adler[*] (1981), among others, formulated theoretical collision efficiencies based on London-van der Waals attraction and flow field characteristics, producing integral expressions for α' based on the dimensionless parameter:

$$\Pi_A = \frac{2\pi\mu D_a^3 \dfrac{du}{dz}}{3A} \tag{3-62}$$

---

[*] Adler (1981) calculates the collision efficiency in terms of the "capture area" of two particles, which has the same conceptual basis as the collision diameter function, F_c, described in Section 3.3.1 and below.
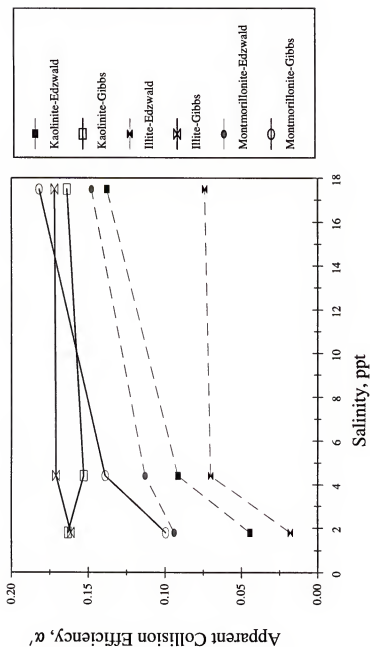
Figure 3-13. Apparent collision efficiency of clay mineral suspensions. Source of data: Edzwald et al. (1974) and Gibbs (1983). Lowest salinity points from Gibbs are interpolated from raw data.

where A = Hamaker constant, a proportionality factor in the London-van der Waals force, with a range of 0.1×10^{-19} to 6×10^{-19} joules (Kruyt, 1952). The resulting $\alpha' - \Pi_A$ expressions produce similar, but not identical results, and comparison of the predicted efficiency with observed data is usually unsatisfactory (Han, 1989; Adler, 1981). In particular, Adler (1981) observed that:

> . . . it is difficult to predict the behavior of colloidal suspensions. . . . Due to the multiplicity of parameters, it was not possible to represent the results by a single formula when colloidal forces were present; the behavior of colloidal suspensions can at times be quite puzzling. (Adler, 1981, page 114)

Theoretical and empirical difficulties. Adler's frustration has been widely shared. Gibbs (1983) noted that the characteristic collision efficiencies of pure clay minerals in shear flows cannot be combined in any rational way to yield the measured efficiencies of mixed estuarial sediments.[*]

The difficulties with the various approaches to determining collision efficiency are most obviously demonstrated by the fact that the literature reports values of α' ranging from 1×10^{-5} to 1 (Edzwald et al., 1974; Zeichner and Schowalter, 1977; Adler, 1981; McCave, 1984; O'Melia, 1985; Han, 1989; Lick et al., 1992). However, the analyses yielding the low end of that range of efficiencies have lumped a number of assumptions and effects (e.g., hydrodynamic effects, disaggregation, nonspherical shape, heterogenous sizes, and degree of sediment cohesion) into that single parameter, making it an extremely rough calibration coefficient for which there is no intuitive estimate and no consistent theoretical expression

---

[*] However, Whitehouse et al. (1960) found that settling velocities of many mixed mineral aggregates in quiescent water could be fairly accurately predicted by a simple ratio of the constituent minerals' individual settling velocities. The lone exceptions were some montmorillonite-illite mixtures.

of reasonable values. The more approximate the calculations, the wider range of efficiencies needed to reproduce the data.

The range of α' narrows in experiments with real sediments (as opposed to manufactured materials such as latex grains or single clay minerals such as kaolinite) and analyses which consider both aggregation and disaggregation. For example, collision efficiencies ranged from 0.04 to 0.22 in experiments with sediments from Pamlico Sound (Edzwald and O'Melia, 1975), and 0.02 to 0.5 for Detroit River sediments in seawater (Burban et al., 1989). Such results narrow the range; but even so, a revised approach is proposed here.

Proposed formulation. A proposed formulation of the collision efficiency and collision diameter function is based on the following assumptions:

1. In considering collisions, hydrodynamic and inertial forces must be treated separately from cohesion forces because of an order 3 disparity between spatial scales of the processes. Attractive and repulsive forces on cohesive particles are effective at maximum interparticle distances on the order of 1×10^{-3} μm (Hahn and Stumm, 1970); whereas, the hydrodynamic forces affecting aggregates act at distances on the order of aggregate diameters, i.e., order 1 to 1×10^3 μm, and the Kolmogorov microspace, which is order 1×10^4 μm in typical estuarial flows (Equation 2-6 and Table 3-1).

2. Data available in the literature on collision efficiency actually represent the net effect of separate collision, aggregation, and disaggregation efficiencies.

3. Collision efficiency, representing the fraction of near encounters of the first kind that result in collisions, is a function of fluid, flow, and sediment physical properties.

4. Aggregation efficiency, representing the fraction of collisions that result in bonding between the colliding particles, is a function only of degree of cohesion. For sub-20 μm mineral grains (see Table 2-1) with some organic material in suspension of at least 1 ppt salinity, aggregation efficiency can be considered to be equal to one.

5.   Disaggregation efficiency, representing the fraction of aggregating collisions that do not result in disaggregation of at least one of the colliding particles, is a function of the particle shear strength and the shearing forces imposed by the flow and collisions.

Assumption number 2 can be expressed as:

$$\alpha' = \alpha_a \alpha_c \alpha_d \tag{3-63}$$

where

α' = apparent collision efficiency of Equation 2-1;

α_c = modified collision efficiency, which by comparison of Equation 3-5 with Equations 3-9, 3-13, and 3-14 can be seen to be equal to F_c for Brownian motion and F_c^2 for flow shear and differential settling, and which is controlled by the factors listed in assumption 3;

α_d = disaggregation efficiency, controlled by the factors in assumption 5; and

α_a = aggregation efficiency as described in assumption 4 and used in Equation 3-15, given by:

$$\alpha_a = \begin{cases} f_g & S \geq S_0 \, ppt \\[2mm] f_g \dfrac{S}{S_0} & 0 < S < S_0 \, ppt \end{cases} \tag{3-64}$$

where

f_g = decimal fraction of material in the suspension that is strongly cohesive, i.e., with elemental grain diameter less than 20 µm (Table 2-2),

S = fluid salinity, and

S_0 = reference salinity.

The F_c term, and thus α_c, are assumed to vary smoothly over the range of 0 to 1 as discussed in Section 3.1.1. In a discrete, deterministic system with only two-body collisions, the disaggregation efficiency, α_d, can theoretically vary in a stepwise fashion from -1 (for all

Type 2D3 outcomes as described in Section 3.5.1.1) to 0 (all Type 2D2 outcomes) to +1 (all

Type 2A1 outcomes) as a function of shear strength versus imposed stresses. For three-body

collisions, it would vary from -1 to +2 (all Type 3A1 outcomes). In a probabilistic or

representative calculation that stepwise variation might be manifested as an asymptotic or

piecewise exponential-type function.

Inspection of the variables listed in assumptions 3-5 yields several nondimensional

parameters that may contribute to the probability of an aggregating collision between two

encountering particles. They can be expressed by Equation 3-64 plus[*]:

$$\alpha_c = \Pi_c\left[\left(\frac{\Delta\rho_i D_i^3}{\Delta\rho_m D_m^3}\right),\left(\frac{u_i(D_i + D_m)}{\nu}\right),\left(\frac{D_g}{D_1}\right),\left(\frac{S}{S_0}\right),\left(\frac{T_c}{T_0}\right),\left(\frac{CEC}{CEC_0}\right)\right] \quad \textbf{(3-65)}$$

and

$$\alpha_d = \Pi_d\left[\frac{\tau_m}{\tau_{im,m} + \tau_u}\right] \quad \textbf{(3-66)}$$

where

Π indicates some function of the bracketed nondimensional terms,

$\Delta\rho_i$, $\Delta\rho_m$ = incremental density (ρ_i - ρ, ρ_m - ρ) of the i and m class particles, respectively,

ρ_i, ρ_m = density of i and m class particles, respectively,

---

[*] The second and third terms contain a redundancy, in that rearranging yields the ratio D_i / D_m in both terms. Further, if Equation 3-3 for particle density is introduced, the ratio appears again. In the analysis culminating in Equation 3-71, a simplification of these terms to include only one diameter ratio was examined, but did not improve the fit to data. The form shown was selected as the best balance among degrees of freedom, simplicity of equation, and preservation of terms (such as particle mass) that provide an intuitive picture of particle dynamics.

ρ = fluid density,

D_i, D_m = diameter of i and m class particles, respectively,

u_i = i class particle velocity relative to second particle,

ν = kinematic viscosity of fluid,

D_g = diameter of primary grain,

D_1 = reference particle size,

S = fluid salinity,

S_0 = reference salinity,

T_c = fluid temperature, deg Celsius,

T_0 = reference temperature,

CEC = sediment cation exchange capacity,

CEC_0 = reference cation exchange capacity,

τ_m = shear strength of the larger particle,

$\tau_{im,m}$ = shear stress imposed on m particle by collision of i and m class particles, and

τ_u = shear stress imposed by flow velocity gradient.

The first term in Equation 3-65 expresses the relative masses of the two particles and thus their relative inertia. The second term is a particle Reynolds Number and characterizes inertial forces relative to viscous forces affecting the encountering particles. The third incorporates the fundamental grain size, which appears to affect equilibrium size and strength. The fourth through sixth terms are nondimensional forms of salinity, temperature, and cation exchange capacity (CEC), respectively, which affect cohesion but are here used to characterize fluid properties and flow behavior near the particles, since full cohesion is

assumed. The single term in Equation 3-66 represents the balance between particle strength and shear stresses imposed by the collision and velocity gradient.

The grain size and CEC of sediment samples can be measured, but often are not, so they can be estimated by the respective expressions:

$$D_g(sample) = 0.36f(K) + 0.062f(I) + 0.011f(M) + 0.062f(Ch)$$
$$CEC(sample) = 9f(K) + 25f(I) + 115f(M) + 34f(Ch)$$

(3-67)

where $f(K), f(I), f(M), f(Ch)$ = weight fractions of the sample composed of kaolinite, illite, montmorillonite, and chlorite, respectively, and the constants are representative values of equivalent grain diameter and CEC for the minerals indicated (Table 2-2). These calculations are approximate since the grain size and CEC for a given mineral may vary considerably from the nominal values employed, but they do provide some measure of the mineral-specific characteristics of the sediment.

Data to formulate the relationship indicated by Equations 3-65 and 3-66 are sparse and, as indicated by the above quote from Adler, more than a little confusing, at least in part because of differences in experimental conditions and methods, but primarily because of the diverse behaviors of seemingly similar cohesive sediment samples.

Data on collision efficiency for real sediments were compiled (see Appendix B) from the literature and the resulting 40 sets of useful data are listed in Table 3-3. Parameters listed in Table 3-3 include variables reported in the cited references and some computed variables as described below.

The data reported in Table 3-3 were obtained by experiments in two types of aggregation devices—Couette reactors and blade reactors. The Couette reactor, described

Table 3-3. Summary of collision efficiency experimental data and computed parameters.

Reference & Sediment Source	Shearing Rate 1/sec	Energy Dissipation Rate m²/sec³	Salinity ppt	Temperature deg C	Grain Size μm	CEC meg/100 g	Initial Median Diameter μm	Ending Median Diameter μm	Particle Size, D_m μm	Relative Density of m Particle kg/m³	Particle Size, D_i μm	Relative Density of i Particle kg/m³	Apparent Collision Efficiency α'
Burban-Detroit	600	8.48	35	21	0.25	32	3.9	32	18.0	375	9.0	458	0.17360
Burban-Detroit	400	3.77	35	21	0.25	32	3.9	32	18.0	376	9.0	458	0.19720
Burban-Detroit	200	0.94	35	21	0.25	32	3.9	84	44.0	291	22.0	355	0.12260
Burban-Detroit	600	8.48	35	21	0.25	32	3.9	15	9.5	451	4.7	550	0.27850
Burban-Detroit	100	0.24	35	21	0.25	32	3.9	172	88.0	239	44.0	291	0.08575
Burban-Detroit	200	0.94	35	21	0.25	32	3.9	148	76.0	249	38.0	304	0.09274
Burban-Detroit	400	3.77	35	21	0.25	32	3.9	125	64.5	261	32.2	318	0.10200
Burban-Detroit	400	3.77	35	21	0.25	32	3.9	19	11.5	427	5.7	521	0.24770
Burban-Detroit	200	0.94	35	21	0.25	32	3.9	32	18.0	376	9.0	458	0.19480
Burban-Detroit	100	0.24	35	21	0.25	32	3.9	40	22.0	355	11.0	432	0.17630
Burban-Detroit	100	0.24	35	21	0.25	32	3.9	90	47.0	286	23.5	348	0.11780
Burban-Detroit	200	0.94	35	21	0.25	32	3.9	25	14.5	400	7.2	487	0.22050

Table 3-3—(continued).

Reference & Sediment	Shearing Rate 1/sec	Energy Dissipation Rate m³/sec³	Salinity ppt	Temperature deg C	Grain Size μm	CEC meq/100 g	Initial Median Diameter μm	Ending Median Diameter μm	Particle Size, D_m μm	Relative Density of m Particle kg/m³	Particle Size, D_i μm	Relative Density of i Particle kg/m³	Apparent Collision Efficiency α'
Burban-Detroit	100	0.24	35	21	0.25	32	3.9	62	33.0	316	16.5	385	0.14110
Burban-Detroit	200	0.94	35	21	0.25	32	3.9	53	28.5	330	14.2	402	0.15230
Edzwald-Upper Pamlico	52	0.064	1.8	21	0.32	23	4.2	54	29.1	328	14.6	399	0.10000
Edzwald-Lower Pamlico	52	0.064	4.4	21	0.35	21	4.2	54	29.1	328	14.6	399	0.18000
Edzwald-Upper Pamlico	52	0.064	4.4	21	0.32	23	4.2	54	29.1	328	14.6	399	0.14000
Edzwald-Pamlico River	52	0.064	17.5	21	0.35	21	4.2	57	30.6	323	15.3	393	0.22000
Edzwald-Pamlico River	52	0.064	4.4	21	0.29	24	4.2	54	29.1	328	14.6	399	0.08000
Edzwald-Lower Pamlico	52	0.064	17.5	21	0.29	24	4.2	57	30.6	323	15.3	393	0.09500

Table 3-3—(continued).

Reference & Sediment	Shearing Rate 1/sec	Energy Dissipation Rate m²/sec³	Salinity ppt	Temperature deg C	Grain Size µm	CEC meg/100 g	Initial Median Diameter µm	Ending Median Diameter µm	Particle Size, D_m µm	Relative Density of m Particle kg/m³	Particle Size, D_i µm	Relative Density of i Particle kg/m³	Apparent Collision Efficiency α'
Edzwald-Upper Pamlico	52	0.064	17.5	21	0.32	23	4.2	57	30.6	323	15.3	393	0.16500
Edzwald-Pamlico River	52	0.064	1.8	21	0.35	21	4.2	54	29.1	328	14.6	399	0.13000
Edzwald-Lower Pamlico	52	0.064	1.8	21	0.29	24	4.2	54	29.1	328	14.6	399	0.04500
Gibbs-Delaware	55	0.071	1.1	21	0.18	19	3	38	20.5	362	10.3	441	0.07700
Gibbs-Amazon	11	0.0028	2	21	0.19	44	78	314	196.0	111	98.0	232	0.07200
Gibbs-Amazon	11	0.0028	2	21	0.19	44	3	78	40.5	298	20.3	363	0.69700
Gibbs-Yukon	11	0.0028	0.6	21	0.20	46	3	106	54.5	274	27.3	334	0.19800
Gibbs-Guiana	11	0.0028	0.9	21	0.15	61	3	106	54.5	274	27.3	334	0.21900
Gibbs-Delaware	55	0.071	4.4	21	0.18	19	3	38	20.5	362	10.3	441	0.17100

Table 3-3—(continued)

131

Reference & Sediment	Shearing Rate l/sec	Energy Dissipation Rate m³/sec³	Salinity ppt	Temperature deg C	Grain Size µm	CEC meg/100 g	Initial Median Diameter µm	Ending Median Diameter µm	Particle Size, D_m µm	Relative Density of m Particle kg/m³	Particle Size, D_i µm	Relative Density of i Particle kg/m³	Apparent Collision Efficiency α'
Gibbs-Delaware	55	0.071	17.5	21	0.18	19	3	37	20.0	364	10.0	444	0.20700
Tsai-Detroit	200	0.94	0.5	21	0.25	32	3.9	26	15.0	396	7.5	482	0.10640
Tsai-Detroit	100	0.24	0.5	21	0.25	32	3.9	105	54.5	274	27.2	334	0.05307
Tsai-Detroit	100	0.24	0.5	21	0.25	32	3.9	60	32.0	319	16.0	389	0.07207
Tsai-Detroit	400	3.77	0.5	21	0.25	32	3.9	50	27.0	335	13.5	408	0.07886
Tsai-Detroit	200	0.94	0.5	21	0.25	32	3.9	80	42.0	295	21.0	360	0.06292
Tsai-Detroit	400	3.77	0.5	21	0.25	32	3.9	20	12.0	422	6.0	514	0.11630
Tsai-Detroit	200	0.94	0.5	21	0.25	32	3.9	40	22.0	355	11.0	432	0.08876
Tsai-Detroit	200	0.94	0.5	21	0.25	32	3.9	100	52.0	278	26.0	338	0.05391
Tsai-Tanshui	100	0.24	35	21	0.22	42	5	80	42.5	294	21.3	358	0.04700
Tsai-Tanshui	100	0.24	0.05	21	0.22	42	5	400	202.5	107	101.3	228	0.00500

Sources: See Appendix B.

in detail by Tsai et al. (1987), consists of two concentric annuli and shearing is generated within the annular gap by rotation of one or both rings. An advantage of the Couette reactor is that the shear field is nearly uniform across the annulus. The blade reactor, described by Gibbs (1983), consists of a cylindrical cup in which two or more narrow blades are rotated about the central axis. The blade reactor has the advantage of generating a clearly turbulent flow; however, shear stresses near the blades will be substantially larger than the average across the cup, and the apparent efficiency should be less for similar shearing rates in a Couette reactor, since disaggregation occurring near the blades will artificially increase the number of particles in the suspension.

The experiments listed in Table 3-3 employed two methods to determine collision efficiency. In all cases samples were withdrawn from the reactor by pipette and then either the number of particles were counted or the size distribution was measured. Using the particle numbers method (Edzwald et al., 1974; Gibbs, 1983; Tsai and Hwang, 1995), the collision efficiency was then calculated by fitting Equation 2-1 to the data and assuming that every successful collision produced one particle from the two colliding particles (a Type 2A1 outcome in Section 3.5.1.1).

The experiments of Edzwald et al. (1974), Gibbs (1983), and Tsai and Hwang (1995) measured efficiencies for the earliest stages of the aggregation process, when particle sizes were small, but the former two did not measure particle sizes of the aggregated suspension. The median particle size for those experiments have been estimated here by: a) using Equation 2-10 to calculate an equilibrium particle size for the experimental conditions, b) using Equation 2-11 to approximate the time to achieve that equilibrium size; and c)

estimating the median particle size at the end of the measurement period by interpolation over time using the time history curves of Burban et al. (1989) as representative of the growth rate.

Tsai et al. (1987) and Burban et al. (1989) measured the grain size distribution of the samples and then fit Equation 2-4 to the measured sizes class by class to obtain two sets of collision efficiencies—one for aggregation (P_{aim}) and one for disaggregation (P_{dim})—which are functions of the grain sizes of the colliding i and m particles. For the purposes of this analysis, it has been assumed that α' is equal to the sum of P_{aim} and P_{dim}, since that is how it is expressed in Equation 2-6. The tabulated results of Tsai et al. (1987) and Burban et al. (1989) are thus based on a particle size distribution and vary with the size of the colliding particles plus other variables as discussed in Chapter 2. They are also representative of the whole aggregation process from dispersed suspension to near-equilibrium, where particle sizes are large and relatively stable.

The energy dissipation rates in the listed experiments ranged from a low of 0.0028 m^2/sec^3 to a high of 8.5 m^2/sec^3. Over that entire range flow shear dominates the collision process (see Figures 3-6 and 3-7), so the tabulated efficiencies apply strictly to shear-induced collisions only.

Table 3-4 presents the nondimensional parameters of Equations 3-65 and 3-66 for experiments listed in Table 3-3. Two particle sizes are tabulated. The larger diameter, D_m, represents a typical particle size during the period over which collision efficiency has been measured and has been specified in the table as the simple average of the initial and ending

Table 3-4. Nondimensional parameters for observed data of Table 3-3.

Reference-Sediment	$\Delta\rho_s D_s^3/\Delta\rho_w D_w^3$	$u_t(D_t+D_m)/\nu$	D_t/D_i	S/S_0	$\Phi/1.776$	CEC/CEC_0	$\tau_m/(\tau_{m,m}+\tau_u)$
Burban-Detroit River	3.43	0.0558	0.00417	17.5	0.62	3.5	334
Burban-Detroit River	3.85	0.250	0.00325	17.5	0.62	3.5	66
Burban-Detroit River	4.85	0.132	0.00168	17.5	0.62	3.5	309
Burban-Detroit River	4.63	0.199	0.00197	17.5	0.62	3.5	156
Burban-Detroit River	5.21	0.461	0.00124	17.5	0.62	3.5	86
Burban-Detroit River	5.29	0.262	0.00116	17.5	0.62	3.5	201
Burban-Detroit River	2.96	0.0732	0.00548	17.5	0.62	3.5	189
Burban-Detroit River	2.57	0.0780	0.00694	17.5	0.62	3.5	142
Burban-Detroit River	4.21	0.0608	0.00260	17.5	0.62	3.5	477
Burban-Detroit River	3.85	0.167	0.00325	17.5	0.62	3.5	113
Burban-Detroit River	3.85	0.0834	0.00325	17.5	0.62	3.5	266
Burban-Detroit River	5.73	1.34	0.000704	17.5	0.62	3.5	34
Burban-Detroit River	5.84	0.896	0.000606	17.5	0.62	3.5	79
Burban-Detroit River	5.60	1.94	0.000833	17.5	0.62	3.5	15
Edzwald-Lower Pamlico	4.55	0.0544	0.00323	0.90	0.62	2.7	741
Edzwald-Lower Pamlico	4.63	0.0599	0.00306	8.75	0.62	2.7	705
Edzwald-Lower Pamlico	4.55	0.0544	0.00323	2.20	0.62	2.7	741
Edzwald-Pamlico River	4.63	0.0599	0.00410	8.75	0.62	2.3	705
Edzwald-Pamlico River	4.55	0.0544	0.00433	2.20	0.62	2.3	741
Edzwald-Pamlico River	4.55	0.0544	0.00433	0.90	0.62	2.3	741
Edzwald-Upper Pamlico	4.63	0.0599	0.00358	8.75	0.62	2.5	705
Edzwald-Upper Pamlico	4.55	0.0544	0.00378	2.20	0.62	2.5	741
Edzwald-Upper Pamlico	4.55	0.0544	0.00378	0.90	0.62	2.5	741
Gibbs-Amazon Delta	2.57	0.444	0.000514	1.00	0.62	4.9	141
Gibbs-Amazon Delta	4.57	0.00599	0.00414	1.00	0.62	4.9	5068
Gibbs-Guiana	4.96	0.0101	0.00247	0.45	0.62	6.8	4000
Gibbs-Delaware Bay	4.49	0.0273	0.00474	8.75	0.62	2.1	1009
Gibbs-Delaware Bay	4.53	0.0286	0.00461	2.20	0.62	2.1	986
Gibbs-Delaware Bay	4.57	0.0299	0.00449	0.55	0.62	2.1	964
Gibbs-Yukon River	4.96	0.0101	0.00134	0.30	0.62	5.1	4000
Tsai-Detroit River	5.39	0.638	0.00104	0.25	0.62	3.5	66
Tsai-Detroit River	5.16	0.421	0.00130	0.25	0.62	3.5	92
Tsai-Detroit River	4.80	0.124	0.00174	0.25	0.62	3.5	320
Tsai-Detroit River	3.05	0.0790	0.00521	0.25	0.62	3.5	181
Tsai-Detroit River	3.50	0.0594	0.00401	0.25	0.62	3.5	322
Tsai-Detroit River	4.55	0.359	0.00208	0.25	0.62	3.5	66
Tsai-Detroit River	5.44	0.350	0.000992	0.25	0.62	3.5	165
Tsai-Detroit River	4.21	0.122	0.00260	0.25	0.62	3.5	213
Tsai-Tanshui Estuary	4.85	0.220	0.000866	17.5	0.62	4.7	224
Tsai-Tanshui Estuary	3.59	4.69	0.00173	0.03	0.62	4.7	3

Sources: See Appendix B.

particle sizes listed in Table 3-3. The second size, D_i, has been specified as the simple average of the initial particle size and D_m, representing a typical size involved in collisions with the m particle. Several other size combinations were tested, but within a reasonable range the choice did not have a major effect on the end result as long as the method was consistent.

Particle densities in Tables 3-3 and 3-4 were computed for the specified particle sizes using Equation 3-3 and, in the absence of site-specific data, coefficients from Figure 3-2. Shear strength of the particles was computed by Equation 3-4 with coefficients as given in Figure 3-3, and collision and flow-imposed shear stresses were computed by Equations 3-34 and 3-36, respectively. Temperature was expressed in terms of Φ, the nondimensional term defined by Equation 2-25.

The reference values in Equation 3-65 were set to be:

T_0 = 30 deg C, changed from 15 deg as in Equation 2-25,

S_0 = 2 ppt,

CEC_0 = 9 meq/100 g, and

D_I = the ending particle size in the suspension as given in Table 3-3.

A casual graphical inspection of α' versus the nondimensional parameters of Table 3-4 indicated obvious correlations for all parameters except CEC. (Temperature was not varied in the experiments cited and no evaluation was possible; so the form of Equation 2-25 was assumed.) The lack of an obvious CEC correlation agrees with observations that real sediments in estuarial waters exhibit a nearly uniform surface charge because of organic and oxide coatings (Hunter and Liss, 1982; Kranck et al., 1993; Gibbs, 1983). Nevertheless,

CEC was retained as a variable, since it slightly improved the fit to data when used in combination with the other variables.

As an initial test, the nondimensional terms of Table 3-4 were combined in a simple product form given by:

$$\Pi_\alpha = \frac{\left(\dfrac{D_g}{D_i}\right)\left(\dfrac{S}{S_0}\right)\left(1-0.875\dfrac{T_c}{T_0}\right)\left(\dfrac{CEC}{CEC_0}\right)\left(\dfrac{\tau_m}{\tau_{im,m}+\tau_u}\right)}{\left(\dfrac{\Delta\rho_i D_i^3}{\Delta\rho_m D_m^3}\right)\left(\dfrac{u_i(D_i+D_m)}{\nu}\right)} \qquad \textbf{(3-68)}$$

and plotted against the observed α' of Table 3-3. Figure 3-14 shows the result—a surprising degree of correlation for such a simple relationship. One data point, Gibbs (1983) Amazon sample value of 0.697 may either be an outlier or indicate a sharp upward inflection in the curve at higher values of Π_α. The blade reactor results from the Pamlico and Delaware systems tend to fall below the Couette reactor results, as would be expected from the nature of the devices as described above, but the agreement is nonetheless striking.

A least squares fit of a power law function to the points of Figure 3-14 yields:

$$\alpha' = 0.0848\,\Pi_\alpha^{0.163} \qquad \textbf{(3-69)}$$

Equation 3-69 fits the data with a correlation coefficient (R^2) of 0.59 and a standard error of α' estimate (Y_e) of 0.07 (0.71 and 0.04, respectively, if the Amazon outlier point is omitted).
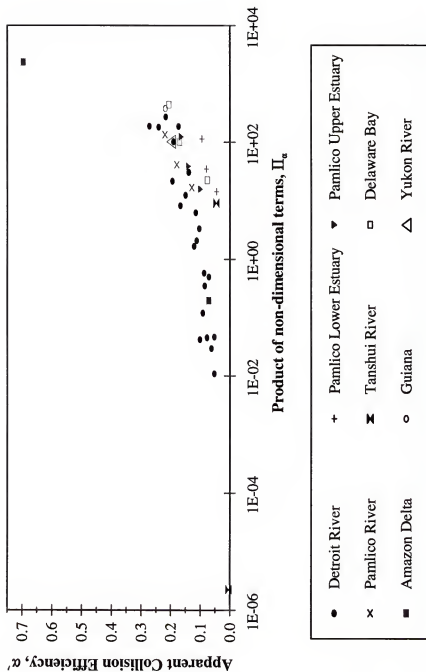
Figure 3-14. Comparison of observed apparent collision efficiency with product of non-dimensional terms of Equation 3-68. Sources of data: Edzwald et al. (1974); Gibbs (1983); Tsai et al. (1987); Burban et al. (1989); and Tsai and Hwang (1995).

Numerous regression trials[*] were performed on the sample set for α' versus the parameters of Table 3-4 in various combinations. The optimum mathematical relationship, selected on the criteria that it: a) be a product of terms and not a sum, b) vary between 0.05 and 0.7 over the measured range, c) exhibit no local maxima or minima over that range, d) maximize correlation coefficient, and e) minimize standard error of estimate, was:

$$\alpha' = \alpha_a \, 0.242 \, \Pi_c^{0.195} \, e^{\left(\frac{\Pi_d}{4670}\right)^2} \tag{3-70}$$

where $\alpha_a = 1$ and

$$\Pi_c = \left[\frac{\dfrac{D_g}{D_i}\dfrac{S}{S_0}\left(1 - 0.875\dfrac{T_c}{T_0}\right)\dfrac{CEC}{CEC_0}}{\dfrac{\Delta\rho_i D_i^3}{\Delta\rho_m D_m^3}\dfrac{u_i(D_i + D_m)}{\nu}}\right] \tag{3-71}$$

$$\Pi_d = \left[\frac{\tau_m}{\tau_{im,m} + \tau_u}\right] \tag{3-72}$$

Equation 3-70 yields an $R^2 = 0.91$ and $Y_e = 0.03$. Not only is the fit good, but the form agrees qualitatively with the relationships of Equation 3-68, and it expresses the effect

---

[*] Several hundred thousand equations were tested using: a) TableCurve3D software by Jandel Scientific, which fits more than 37,000 three-dimensional equations to a data set and then orders them according to user-specified criteria of best fit; and b) a standard regression for a four-dimensional power law using Corel Quattro Pro and MathWorks MATLAB software.

of Π_d in exponential form, consistent with the expected behavior of that term as discussed above.

Figure 3-15 displays the fit of Equation 3-70 to the observations in top, side, and isometric views. The comparison, like the goodness-of-fit statistics, shows that the equation represents the observations rather well over the range of measurements.

Figures 3-16a and 3-16b show the agreement between observed and calculated apparent collision efficiencies for Equations 3-69 and 3-70, respectively, along with the perfect fit 45 deg line. Equation 3-70 is clearly the better predictor, albeit with a more complex relationship. Equation 3-69 is an adequate interpolator for $0 < \alpha' < 0.25$, but fails to capture the high value of 0.697. If the 0.697 value is a valid point, and the theoretical upper limit of 1 on α' suggests that it may be, then Equation 3-69 is an unsatisfactory descriptor of the parameter. Visual inspection confirms that the functions are well-behaved over the range of independent parameter values given in Table 3-4. The goodness of fit appears to confirm at least the broad validity of assumptions 1 to 5 and the adequacy of the selected nondimensional terms to characterize the aggregation process. The remaining scatter, yielding a standard error of estimate of ± 4 percent of the full scale, is attributed to a) variations in experimental method among the data sources, b) inadequacy of using only two representative particle sizes to characterize a changing distribution of sizes, and c) incomplete incorporation of mineral composition effects. The latter deficiency can be seen most clearly in Figure 3-14, where sediments from three locations in the Pamlico River estuary, apparently differing mainly in mineral composition (although organic content and
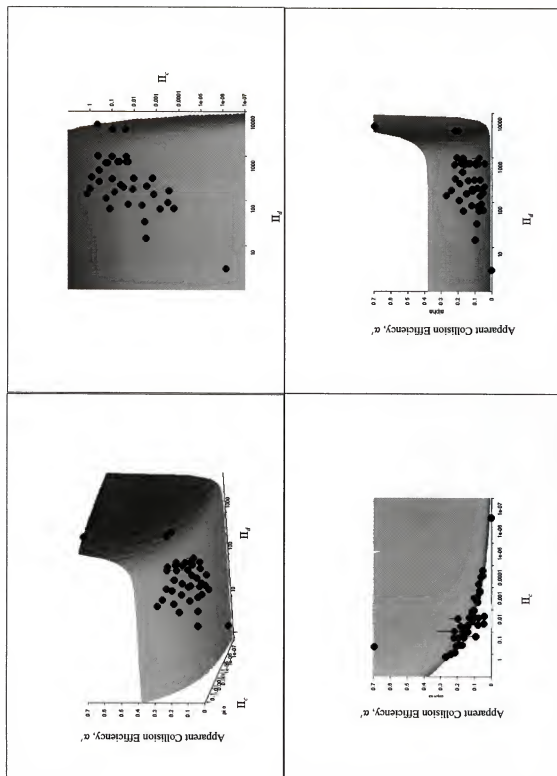
Figure 3-15. Four view comparison of observed apparent collision efficiencies with Equation 3-70.
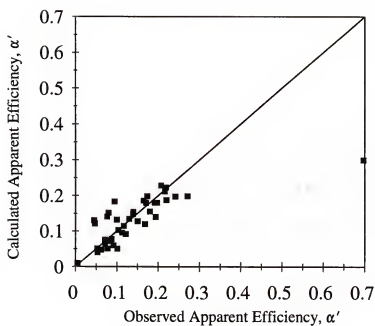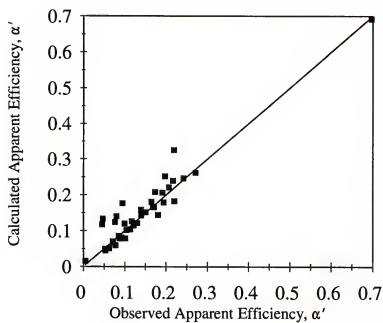
Figure 3-16. Observed versus calculated apparent effiency for two regression equations.
a) Equation 3-69; b) Equation 3-70.

grain size variability cannot be discounted) yield observed values of α' ranging from 0.095 to 0.165 for the same salinity (Table 3-3).

Given the success of the rationally based, but empirical, Equation 3-70, the remaining task is to separate the α_c and α_d parts of Equation 3-63. Given that $\alpha_t = F_c^2$ must fall between 0 and 1, and α_d can be assumed to lie between 0 and 1 for the parameter ranges shown in Table 3-4, Equation 3-70 can be set equal to Equation 3-63 and decomposed to yield:

$$\alpha_c = 0.805 \, \Pi_c^{0.195} \qquad\qquad 0 < \Pi_c < 3.04 \tag{3-73}$$

and

$$\alpha_d = 0.308 \, e^{\left(\frac{\Pi_d}{4670}\right)^2} \qquad\qquad 0 < \Pi_d < 5068 \tag{3-74}$$

and thus for flow-shear-induced collisions it can be concluded that:

$$F_c = 0.897 f_c \, \Pi_c^{0.0975} \tag{3-75}$$

where f_c is an as yet undefined term that accounts for the derivation of F_c using net aggregation results integrated over a period of time in which the size spectrum is changing. That is to say, if we look for some variation in F_c as the particle size spectrum evolves, the data of Table 3-4 will not show it since they represent the net effect over seconds to hours of aggregation. For the present f_c is considered to be a placeholder and taken to be equal to 1. In Chapter 6 it is evaluated by experiment.

The parameter α_a is given by Equation 3-64. The α_d term is not used in the proposed aggregation model, since Equations 3-40 to 3-61 explicitly account for disaggregation and it need not be artificially incorporated in the efficiency terms.

In the absence of experimental data for apparent efficiency of Brownian motion and differential settling collisions, Equation 3-75 is proposed for use with those processes as well, and the success of that proposal will be evaluated indirectly in subsequent analyses.

In summary, this development of a collision diameter function, F_c, provides what the limited data show to be a relatively well-behaved relationship between measurable parameters and the rate of successful interparticle collisions in the form of Equation 3-75. It is both heuristic and empirical, but is based on physical considerations and is clearly preferable to a tuned set of efficiencies covering four orders of magnitude.

3.5.2 Flow Shear-Induced Disaggregation

When the flow-induced shear stress exceeds the shear strength of the k class particle, it will shear along one surface and disaggregate into two smaller particles.

$$If \left\{ \tau_k < \tau_u \right\} \quad M_k \Rightarrow \quad \begin{cases} M_{l1'} = M_k - \Delta M_k^0 \\ M_{l2'} = \Delta M_k^0 \end{cases} \quad \textbf{(3-76)}$$

and the average mass change rates will be:

$$\dot{C}_1' = +\left(M_k - \frac{1}{2} M_k \right) n_k$$
$$\dot{C}_2' = +\frac{1}{2} M_k n_k \quad \textbf{(3-77)}$$

which says that two particles will be formed, their combined mass will be equal to the original particle's mass, and on average each one will have half the mass of the original. It

also points out that if the shear strength of the k particle is exceeded by the flow-imposed stresses at a point in space and time, <u>all</u> the k particles at that point will be disaggregated.

The distribution of mass change rates by class will be:

$$\dot{C_k}(shear) = -M_k n_k$$
$$\dot{C_j}(shear) = +p_j(l=1:k) M_k n_k \qquad j = 1\ to\ k$$

$$\text{(3-78)}$$

3.6 Size Distribution Changes Algorithm

The equations derived above can be used to calculate the overall changes in particle size distribution of a suspended fine sediment suspension by the aggregation and disaggregation that occur through collision and shear, given the following:

1. A particle size (mass) distribution model as defined in Section 3.2, giving lower limit and upper limit masses for $j = 1$ to s discrete size intervals, plus representations for particle density, strength, and settling velocity in terms of known quantities.

2. An initial mass concentration distribution for the sediment suspension, i.e., $C_j(t=0)$.

3. A description of conditions of the fluid (temperature, density, and viscosity) and flow (shearing rate or energy dissipation rate) as functions of space and time.

4. The particle concentration flux by size class from advection/diffusion and bed exchanges.

Then the following can be calculated:

1. The flow-induced shear stresses on each particle class by Equation 3-36.

2. The collision diameter function, F_c, by Equation 3-75.

3. Number of two-body collisions, N_{ik}, for i and $k = 1$ to s and the associated collision-induced shear stresses, τ_{ik}, by Equations 3-15 and 3-34, respectively.

4. Number of three-body collisions, N_{ikm}, for i, k, and $m = 1$ to s and the associated collision-induced shear stresses, τ_{ikm}, by Equations 3-23 and 3-35, respectively.

5. Aggregation/disaggregation mass concentration change rates from collisions, $\dot{C}_j(ik)$ and $\dot{C}_j(ikm)$, by appropriate equations from the Section 3.5.1 categories (Equations 3-40 to 3-61) selected on basis of comparison of imposed stresses with particle strengths.

6. Disaggregation mass concentration change rates from flow-induced stresses, $\dot{C}(shear)$, by Equation 3-78.

7. The rate of change of sediment mass concentration by size class then can be calculated from:

$$\dot{C}_j(sum) \; = \; \dot{C}_j(agg) \, - \, \dot{C}_j(shear) \, + \, \dot{C}_j(flux) \qquad i,k,m \; = \; 1 \; to \; s \qquad \textbf{(3-79)}$$

where $\dot{C}(flux)$ = rate of class j mass inflow from advection-diffusion and bed erosion/deposition as calculated by an external computation, and

$$\dot{C}_j(agg) \; = \; \frac{\dot{C}_j(ik)}{2} \, + \, \frac{\dot{C}_j(ikm)}{6} \qquad \textbf{(3-80)}$$

where division of the right hand side terms by 2 and 6 compensates for recounting of the same collisions by the permutations of i and k and i, k, and m, respectively.

8. Finally, the new size distribution is calculated by Equations 3-38 and 3-39.

Repetitive application of these steps will advance the particle size distribution through time.

The aggregation model proposed here is tested in Chapter 6.

CHAPTER 4
MULTI-CLASS DEPOSITION WITH AGGREGATION

4.1 Introduction

The preceding chapter presented a conceptual model and equations for fine sediment aggregation processes. This chapter combines those findings with a simple description for vertical transport and deposition of multiple size classes to produce an algorithm for computing a solution to the aggregation and deposition problem. Its purpose is to test basic concepts of aggregation and deposition in relation to the laboratory experiments presented in Chapter 5. It is limited to the case of cohesive sediment suspensions transported and deposited by steady, horizontally uniform flows.

4.2 Vertical Transport of Suspended Sediment

Transport of suspended sediment can be described by the three-dimensional unsteady advection-diffusion equation with appropriate source-sink terms representing exchanges between the flow and bed (e.g., Teisson, 1997; Teeter and Callegan, 1999). That approach can be simplified for some applications by assuming that flow and transport are steady and uniform in the lateral (y) direction and longitudinal (x) directions, producing a one-dimensional unsteady advection-diffusion equation in the vertical (z) direction. That

simplification is appropriate for examining the flume experiments of Chapter 5, where flow is steady, unidirectional, and nearly uniform in the flow direction.

Given the schematic sediment suspension and velocity profile shown in Figure 4-1 and following Mehta and Lott (1987) and Teeter (1999a), the suspended sediment transport equation for multiple sediment classes can be written as:

$$\frac{\partial C_i}{\partial t} = \frac{\partial}{\partial z}\left(E_z \frac{\partial C_i}{\partial z} + W_{s,i} C_i\right) \tag{4-1}$$

where

C_i = sediment mass concentration of ith class, with $i = 1$ to s,

t = time,

z = vertical dimension coordinate,

$W_{s,i}$ = settling velocity of ith class, and

E_z = vertical diffusion coefficient, assumed to be the same for all size classes and given by (Munk and Anderson, 1948):

$$E_z = \frac{E_{zn}}{\left(1 + B_E \mathbb{R}_g\right)^{m_E}} \tag{4-2}$$

where

E_{zn} = diffusion coefficient for nonstratified flows, given by Equation 4-4,

B_E and m_e = empirical coefficients, typically 0.5 and 0.33 (Ross, 1988), and

$\mathbb{R}_g$ = gradient Richardson Number, given by:

$$\mathbb{R}_g = \frac{-\dfrac{g}{\rho}\dfrac{\partial \rho}{\partial z}}{\left|\dfrac{\partial U}{\partial z}\right|^2} \tag{4-3}$$

where

g = acceleration of gravity,

ρ = fluid density, and

U = resultant horizontal flow velocity magnitude.
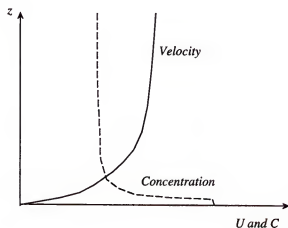
Figure 4-1. Schematic velocity and sediment concentration profiles.

The diffusion coefficient for nonstratified flows, E_{zn}, in Equation 4-2 can be expressed as (Jobson and Sayre, 1970):

$$E_{zn} = \begin{cases} B_{EI}\kappa_v u_* z\left(1 - \dfrac{z}{h}\right) + B_{E2}\left(\dfrac{1 - z/h}{0.9}\right)^3 & \dfrac{z}{h} \ge 0.1 \\[3mm] B_{EI}\kappa_v u_* z\left(1 - \dfrac{z}{h}\right) + B_{E2}\left(\dfrac{z/h}{0.1}\right)^3 & \dfrac{z}{h} < 0.1 \end{cases} \tag{4-4}$$

where

κ_v = von Karman coefficient,

h = flow depth,

u_* = shear velocity, given by:

$$u_* = \sqrt{\frac{\tau_b}{\rho}} \tag{4-5}$$

where

τ_b = bed shear stress, and

B_{EI} and B_{E2} = empirical coefficients, equal to 0.98 and 0.038, respectively, for fine sediment (Jobson and Sayre, 1970).

The von Karman coefficient, κ_v, is usually taken to be about 0.4, but its value in sediment suspensions has been the subject of much analysis and even more speculation. Yalin and Findlayson (1972) found that it may be affected by sediment at concentrations above 3 kg/m^3, but Partheniades (1962) found no evidence for an effect at concentrations up to 4 kg/m^3. In a series of experiments with detailed hot wire and hot film measurements in

the boundary layer, Gust (1976) and Gust and Southard (1983) found significant drag reduction in the presence of low sediment concentrations and inferred a reduced value of κ_v = 0.32. More recently, Mendoza and Zhou (1995) have formulated an apparent κ_v that can be larger or smaller than 0.4 for high or low sediment concentrations, respectively, but note that the experimental data can also be replicated by adding quadratic terms to the logarithmic velocity profile. For this effort, the traditional value of 0.4 has been used so as to leave the focus on the behavior of the aggregating sediment.

Initial conditions for Equation 4-1 consist of a specified distribution of C_i as a function of z at time t = 0. The boundary conditions are zero net sediment flux at the water surface and a calculated depositional flux at the bed, both given by:

$$E_z \frac{\partial C_i}{\partial z} + W_{s,i} C_i = \begin{cases} 0 & z = h \\ \dot{c}_i & z = 0 \end{cases} \tag{4-6}$$

where $\dot{c}_i$ = net rate at which particles of class i are deposited to the bed (Section 2.5.2), given by:

$$\dot{c}_i(z=0) = \begin{cases} 0 & \tau_b > \tau_{cd,i} \\ -W_{s,i} C_i(0+) \left(1 - \dfrac{\tau_b}{\tau_{cd,i}} \right) & \tau_b \le \tau_{cd,i} \end{cases} \tag{4-7}$$

where

$C_i(0+)$ = concentration of the i class just above the bed, and

$\tau_{cd,i}$ = critical shear stress for deposition of the i class.

Equation 4-7 has been limited to the case of deposition. Erosion and resuspension of sediment has been excluded from consideration, since the experiments described in Chapter 5 were limited to the deposition-only case. Addition of multi-class erosion to Equation 4-7 requires development of equations that account for the bed or fluid mud layer's structure, including the order of bonds among aggregates (Section 2.3.6.1) and the distribution of eroded/resuspended particle sizes.

Equations 4-1 through 4-6 require sediment characteristics to be defined for each class under consideration. Given a set of sediment classes based on size (either by diameter or by mass as described in Chapter 3), the class characteristics are settling velocity, $W_{s,i}$, given by Equation 4-8 below, and the critical shear stress for deposition, $\tau_{cd,i}$, assumed to be the shear strength of the next highest order aggregate (Section 2.3.6.1), and taken to be τ_{i+1}, as given by Equation 3-4.

The settling velocity is calculated by Equation 2-18 modified to account for hindered settling (Mehta and Li, 1997):

$$W_{s,i} = H \sqrt{\frac{4 g D_i}{3 C_{D,i}} \left(\frac{\Delta \rho_i}{\rho} \right)} \tag{4-8}$$

where H is the hindered settling factor, given by

$$H = \begin{cases} \left[1 - B_h \left(\sum_{i=1}^{s} C_i - C_2 \right) \right]^{m_h} & \sum_{i=1}^{s} C_i > C_2 \\ 1 & \sum_{i=1}^{s} C_i \le C_2 \end{cases} \qquad \textbf{(4-9)}$$

where

B_h = sediment specific coefficient,

C_2 = total concentration at the onset of hindered settling,

m_h = coefficient, typically = 5,

D_i = diameter of the i class particle,

$\Delta\rho_i$ = density difference of the i class particle, $\rho_i - \rho$, where ρ_i is given by Equation 3-3,

C_D = drag coefficient of the i class particle, as given by (Clift et al., 1978):

$$C_{D,i} = \begin{cases} \dfrac{24}{\mathbb{R}_{ep}} \left(1 + \dfrac{3}{16} \mathbb{R}_{ep} \right) & \mathbb{R}_{ep} \le 0.01 \\[2mm] \dfrac{24}{\mathbb{R}_{ep}} \left(1 + 0.1315 \mathbb{R}_{ep}^{(0.82 - 0.05 w)} \right) & 0.01 < \mathbb{R}_{ep} \le 20 \\[2mm] \dfrac{24}{\mathbb{R}_{ep}} \left(1 + 0.1935 \mathbb{R}_{ep}^{0.6305} \right) & 20 < \mathbb{R}_{ep} \le 260 \\[2mm] 10^{(1.6435 - 1.1242 w + 0.1558 w^2)} & 260 < \mathbb{R}_{ep} \le 1500 \\[2mm] 10^{(-2.4571 + 2.558 w - 0.9295 w^2 + 0.1049 w^3)} & 1500 < \mathbb{R}_{ep} \le 12,000 \end{cases} \qquad \textbf{(4-10)}$$

where $w = log_{10} \mathbb{R}_{ep}$, and

$\mathbb{R}_{ep}$ = particle Reynolds Number, given by:

$$\mathbb{R}_{ep} = \frac{W_{s,i} D_i}{\nu} \tag{4-11}$$

Equations 4-8 through 4-11 enable the calculations to encompass the Free Settling through Negligible Settling concentration-based zones of settling velocity given by Equation 2-22 and Figure 2-7, since the concentration-dependent aggregation that implicitly defines those zones is explicitly accounted for by the method described in the following section.

4.3 Aggregation Processes

Mass concentration of each class, C_i, changes as sediment deposits to the bed, given by Equation 4-7, and as aggregation processes shift sediment mass among the classes. Aggregation processes are calculated using the equations given in Chapter 3 with the following modification.

Equation 3-4 for particle shear strength, τ_k, and Equation 3-35 for three-body collision-induced shear stresses, $\tau_{ikm,k}$, yield deterministic results in which a given particle size has a single strength and experiences a finite set (1 to the number of classes) of collisional shear stresses. Thus, application of the collision outcome rules (e.g., Equation 3-50) will produce a particle size spectrum exhibiting an abrupt upper cutoff at a particular size k, where $\tau_k \leq \tau_{kkk,k}$. This deterministic result must be reconciled with the knowledge that both particle strength and collisional stresses will vary substantially, since the number, orientation, and strength of intra-aggregate bonds vary and turbulent flow fluctuations

affecting collisions have random components. For purposes of this calculation, randomness is accommodated in a highly simplified fashion by introducing modified collisional shear stresses:

$$\tau_{ik,k}^{*} = \tau_{ik,k}\left[1 + B_R(0.5 - N_R)\right]$$
$$\tau_{ikm,k}^{*} = \tau_{ikm,k}\left[1 + B_R(0.5 - N_R)\right]$$

(4-12)

where

$\tau_{ik,k}$ = shear stress imposed on a k class particle by an i-k collision, given by Equation 3-34,

$\tau_{ikm,k}$ = shear stress imposed on a k class particle by an i-k-m collision, as given by Equation 3-35,

B_R = coefficient modulating the degree of randomness assigned to the collisions, and

N_R = random number, 0 to 1.

A rigorous randomization procedure will require that the probability distribution for each term in the basic equations for shear stress be defined so that the overall distribution can be calculated. However, the simplified approach of Equation 4-12 will suffice to demonstrate the contribution of nondeterministic collision stresses.

In the aggregation processes portion of the calculation, the following are calculated:

1. The flow-induced shear stresses on each particle class by Equation 3-36.

2. The collision diameter function, F_c, by Equation 3-75.

3. Number of two-body collisions, N_{ik}, for i and $k = 1$ to s and the associated collision-induced shear stresses, $\tau_{ik,k}^{*}$, by Equations 3-15 and 4-12, respectively.

4. Number of three-body collisions, N_{ikm} for i, k, and $m = 1$ to s and the associated collision-induced shear stresses, $\tau_{ikm,k}^{*}$, by Equations 3-23 and 4-12, respectively.

5. Aggregation/disaggregation mass concentration change rates from collisions, $\acute{C}_j(ik)$ and $\acute{C}_j(ikm)$, by appropriate equations from the Section 3.5.1 categories (Equations 3-40 to 3-61) selected on basis of comparison of imposed stresses with particle strengths (e.g. by Equation 3-40, substituting imposed stresses from Equation 4-12).

6. Disaggregation mass concentration change rates from flow-induced stresses, $\acute{C}(shear)$, by Equation 3-78.

7. The rate of change of sediment mass concentration by size class from Equations 3-79 and 3-80.

8. Finally, the new size distribution is calculated by Equations 3-38 and 3-39.

4.4 Solution Method

A computer program to solve the combined transport and aggregation equations is given in Appendix C. Equations 4-1 through 4-6 for vertical transport are solved with an explicit finite difference routine adapted from Mehta and Li (1997) by modifying it to account for multiple sediment classes. The aggregation processes algorithm given in Section 4.3 is used to calculate the class-by-class sediment mass changes by aggregation and disaggregation while the mass loss from each class due to deposition is calculated by Equation 4-7.

The procedures given here and the implementing computer program given in Appendix C were tested against laboratory data as described in Chapter 6.

CHAPTER 5
SEDIMENT TRANSPORT AND DEPOSITION EXPERIMENTS

5.1 Introduction

Sediment transport and deposition experiments were conducted in a 100-m-long flume at the U.S. Army Engineer Waterways Experiment Station (WES). The objectives of the experiments described here were to provide data for: characterizing fine sediment aggregation and deposition, examining sorting of fine sediments during transport and deposition, and testing sedimentation models.

The experiments consisted of injecting a fine sediment slurry into a steady flow condition and measuring water levels, flow velocities and sediment concentration at cross sections along the flume length. This chapter describes the flume and experiments, presents experimental data, and provides a preliminary analysis. The following chapter provides analyses relative to the aggregation and deposition algorithms presented earlier.

5.2 The Experimental Facility

5.2.1 Flume

The WES 100 m flume, illustrated in Figure 5-1, was constructed of 6-mm-thick Lucite to dimensions of 99.7 m long, 0.46 m deep, and 0.23 m wide. It was elevated
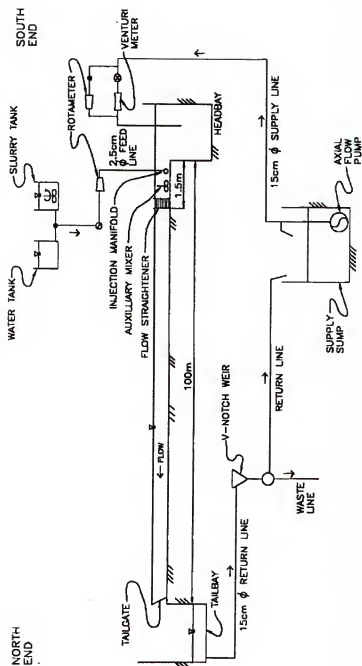
Figure 5-1. Schematic of 100 m flume.

above the floor of a laboratory hall and supported at 1.2 m intervals by steel crossbars and uprights. Lucite roughness elements 6.4 mm square and 30 cm long were mounted vertically on the flume sides at 51 mm on centers.

Each end of the flume connected to a 6.1-m-square and 1.5-m-deep basin. Periodic water level variations could be produced in the south end basin to create tidal effects, but in the tests described here, the south end basin was used as a steady-state inflow headbay. Water supply to the flume was pumped from a storage sump into the south end basin through either a 15 cm venturi meter or a rotameter, depending on the flow rate.

Station locations in the flume are here expressed as the distance in meters from the south (upstream) end of the flume. Thus Station 12.2 is 12.2 m from the south end.

A flow straightener was placed in the flume 1.5 m from the upstream end to damp turbulent eddies produced at the entrance section and sediment injection manifold. It consisted of a stack of 6-cm-diameter copper tubes, 102-mm-long, stacked in a close-packed arrangement.

At the north (downstream) end of the flume, an overflow tailgate controlled flow depth. From the overflow tailbay, a 15-cm-diameter pipe carried outflow by gravity to a collecting tank which emptied through a 60 degree v-notch weir. Overflow from the weir could be directed either back in to the supply sump for recirculation or into a waste line.

The flume had a Manning's roughness coefficient of 0.011 with no roughness strips and 0.022 with sidewall strips in place (CTH, 1955).

5.2.2 Injection Apparatus

The sediment injection apparatus consisted of a 0.1 m^3 water tank, a 4.5 m^3 slurry tank, a small paddle pump, a rotameter in a 2.5-cm-diameter slurry feed line, and an injection manifold. A quick action valve controlled the source of feed water between the water tank and slurry tank. The slurry tank was equipped with a mixing pump and four sets of 15 cm propellers driven at 945 rpm by an electric motor. Pre-experiment sampling showed that the sediment slurry in the tank was thoroughly mixed.

The injection manifold was placed across the flume 0.8 m from the upstream end. The manifold was constructed of a 22-cm-long, 2.5-cm-diameter plastic pipe with sealed ends and twenty-four 3-mm-diameter holes drilled in line along the pipe's length. The holes pointed downward and slightly downstream.

Between the injection manifold and flow straightener, a small motor-driven propeller was mounted in the flume to insure complete mixing of slurry and flume flow below the injection point and above the test sections.

5.2.3 Measurement Equipment

Water surface elevations were measured with Vernier point gages. These point gages were individually zeroed to a pooled water surface in the flume prior to each experiment.

Water velocities were measured with miniature Price-type current meters consisting of a vertical-axis bucket wheel mounted on point bearings. The five-cup

wheel was about 25 mm wide and 13 mm high. A perforated plastic disc above the cups alternately interrupted and passed a light beam to a photo cell and digital counter. Calibration to known flows related the number of light pulses to flow speed.

Water suspension samples of 118 ml were withdrawn from the flume. The sampling apparatus consisted of a vacuum chamber in which sample bottles were held beneath tubes leading from the sampling points. A vacuum pump reduced pressure in the chamber, drawing water through the tubes and into the bottles. The end of each sampling tube was turned so that a 32-mm-long tip pointed into the flow.

Up to 8 m of plastic tubing connected the sample intakes to the vacuum chamber, and more than 240 ml of water were withdrawn at the nearby locations while the samples from the furthest sampling points traveled to the chamber.

5.3 Experimental Procedures

5.3.1 Operation of the Flume

Operational procedures for the experiments were as follows:

1. Sediment and water were mixed in the slurry tank to obtain a slurry concentration of approximately 100 kg/m^3. Mixing propellers and pump were operated continuously for three hours prior to and during the test.

2. The nominal flume flow rate was introduced into the headbay by setting the supply line valve to obtain the specified flow as indicated by the venturi meter (higher flows) or the rotameter (lower flows), depending on flow rate. The tailgate was set to maintain a 15.2 cm water depth at Station 97.5.

3. Clear water from the water tank was pumped into the flume through the injection manifold at a flow rate equal to the slurry injection rate to be used. The slurry

injection flow rate was selected so as to obtain the desired sediment concentration in the flow.

4. Outflow from the flume was monitored at the v-notch weir, and water level profiles were taken along the flume to determine when steady-state conditions occurred.

5. Once steady conditions were obtained, the quick action valve was turned to change the injection from clear water to slurry. Simultaneously, the outflow was switched from recirculating to waste so that sediment was not recirculated.

6. Sediment slurry injection into the flume flow continued at a constant rate for one to three hours, long enough for measurable bed deposits to form. Suspension samples were taken at 15 min intervals.

7. The injection was switched back to clear water and continued until the sediment cloud had passed out of the flume.

8. Shutdown was accomplished by gradually slowing the inflow to a stop while maintaining full water depth in the flume.

9. Following shutdown the elevation of the deposited bed surface was estimated using the point gage at the water level measurement locations.

10. The flume was gradually drained to near the deposited bed surface by permitting slow release at the flume ends for 15 to 36 hours.

5.3.2 Measurements

Samples of the sediment slurry were analyzed for pH and cation exchange capacity.

Centerline suspension samples of 118 ml were withdrawn approximately 2 cm below the surface, at middepth, and approximately 2 cm above the bottom every 15 minutes every 6.1 m over the flume length. At stations 48.8 and 97.5, samples were also taken at the one-quarter and three-quarter depth locations. Samples were analyzed for

sediment concentration by a commercial laboratory service which filtered, dried, and weighed the samples.

Water surface elevations were recorded every 12.2 m along the flume for the steady clear water condition and every ten minutes during sediment injection. Elevation of the flume bottom was recorded at the start of each test at each location.

Vertical and horizontal velocity profiles were measured at Stations 12.2, 48.8, and 97.5 during stable clear water flow.

The depth of slurry in the mixing tank, temperature of the slurry, and temperature of water flowing into the flume were recorded at the beginning and end of each test.

Following shutdown, the point gage at each water level station was used to estimate the elevation of the deposited bed surface. After draining (the bed was not allowed to dry), bed samples were removed from 12.2 m intervals (centered at the water level measurement stations) by siphoning a section of bed deposit into a jar. Those samples were analyzed for dispersed median grain size and deposition characteristics as described later.

5.3.3 Measurement Error

Water surface elevation measurements using the point gages are accurate within 0.03 cm if the datum is properly set (Letter and McAnally, 1981). Errors in zeroing the gages can be substantially larger than that, but larger errors are usually obvious, and reading the datum plane can be considered to be of the same accuracy as the readings themselves, so a combined maximum error of ±0.06 cm is expected in the absolute water

level measurements on a stable water surface. Detecting a turbulent water surface with a point gage can be less accurate than that because of difficulty in determining the exact point at which the surface dimples. The bed elevation measurements with the point gages are considered approximate, for discerning when the gage point pierced the fluffy bed surface was not easily judged.

Velocity measurement accuracy with the miniature meters are ±0.03 cm/sec at speeds above 1.5 cm/sec (Letter and McAnally, 1981) except for a partially correctable bias that occurs in horizontal velocity gradients as discussed in Section 5.6.1.

Sediment concentration measurements can be affected by errors in sampling, alteration of the samples during transit and while awaiting analysis, and in the analysis itself. The samples taken in these experiments were analyzed for total suspended solids by a commercial laboratory using standard filtration, drying and weighing techniques, and such laboratories can be expected to exercise quality control to maintain a ±5 to 10 percent accuracy.[*] That cannot be considered an absolute accuracy, for it does not include the difficulties associated with pulling samples into vials over the 100-m-long flume in a consistent manner. Variability in concentration measurements is addressed again later in this chapter.

---

[*] Personal communication with A. M. Teeter of the USAE Waterways Experiment Station, Vicksburg, MS.

5.4 Experimental Conditions

A summary of sediment experimental conditions is given in Table 5-1. Commercial kaolinite (97% kaolin) from Edgar, Florida, was used in experiments W4 toW10, and Atchafalaya Bay, Louisiana, mud was used in experiment W11.

Table 5-1. Summary of experimental conditions.

Experiment Number[*]	Sediment	Nominal Initial Concentration kg/m³	Flow Rate m³/sec	Water Temperature deg C	Slurry Temperature deg C	Duration hr
W4	Kaolinite	10	0.0052	26	27	1.5
W5	Kaolinite	10	0.0070	24	27	1.0
W6	Kaolinite	10	0.0034	28	29	1.0
W9	Kaolinite	2	0.0034	26	27	1.25
W10	Kaolinite	5	0.0034	23	23	1.25
W11	Atchafalaya Bay mud	10	0.0017	12	13	1.25

Note:[*] Experiments W1 toW3 were flume and procedure shakedown tests. W7 and W8 were erosion experiments not reported here.

During a single experiment, water and slurry temperatures for the tests did not vary by more than 1 deg C from these shown in Table 5-1. Temperatures between experiments, however, varied substantially as they were conducted over several months.

Figure 5-2 shows the grain size distributions of the dispersed kaolinite and the Atchafalaya Bay mud. Median diameters were about 1 μm for the kaolinite and 15 μm for the Atchafalaya Bay mud. The Atchafalaya Bay sediment, as described below, included a significant fraction of silt and fine sand, and the clay fraction consisted predominantly of illite with some kaolinite and montmorillonite. It had a CEC of 11to
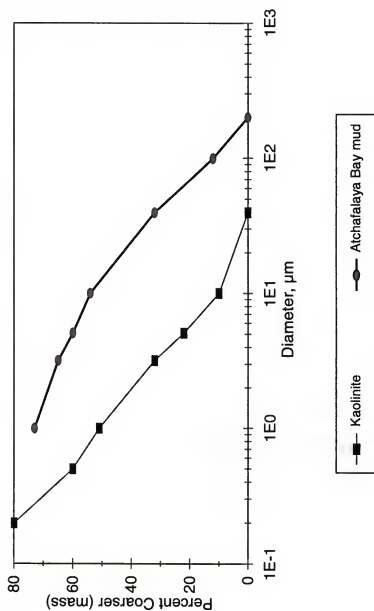
Figure 5-2. Dispersed grain size distribution of sediments used in experiments.

29 meq/100 g (Teeter and Pankow, 1989; Dixit et al., 1982). The kaolinite exhibited a CEC of approximately 6 meq/100 g.[*]

Tap water was used in the flume. It had a pH of 7.8, 18.3 ppm chlorides, 13.1 ppm sodium, and 1.9 ppm calcium, and an electrical conductivity of 0.19 μmho/cm (Dixit et al., 1982).

5.5 Atchafalaya Bay

Atchafalaya Bay, source of one of the tested sediments, is a shallow estuary on the Louisiana coast (see Figure 5-3), about 53 km wide and 13 km long with an average depth of only 1.5 m below National Geodetic Vertical Datum (NGVD). It was once sheltered from the Gulf of Mexico by extensive oyster reefs, which have been lost to subsidence and shell dredging. Extensive fresh and brackish marshes border the eastern and northern sides of the bay while the western end joins East Cote Blanche Bay, shown in Figure 5-4.

The bay receives the flow of the Atchafalaya River, which, in addition to draining the Atchafalaya and Red River Basins, serves as a major distributary of the Mississippi River. United States law mandates that the Atchafalaya River carry 30 percent of the combined Mississippi and Atchafalaya Rivers' total discharge at latitude 31 deg north. The U. S. Army Corps of Engineers, charged with enforcing that law, controls diversion of Mississippi River flows into the Atchafalaya at the Old River Control Structure and

---

[*] Specification sheet, Feldspar Corporation, Edgar, FL.
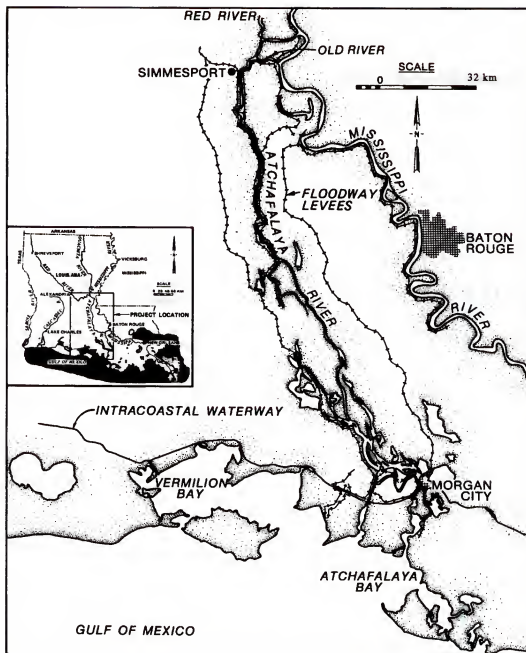
Figure 5-3. Atchafalaya River Basin. From: McAnally et al. (1985). Used with permission.
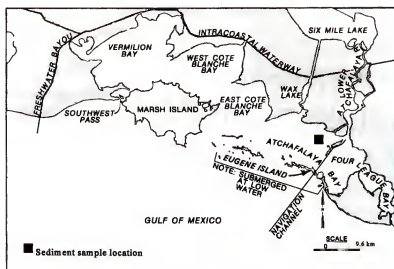
Figure 5-4. Atchafalaya Bay area and sediment sample location. From: Thomas et al. (1988). Used with permission.
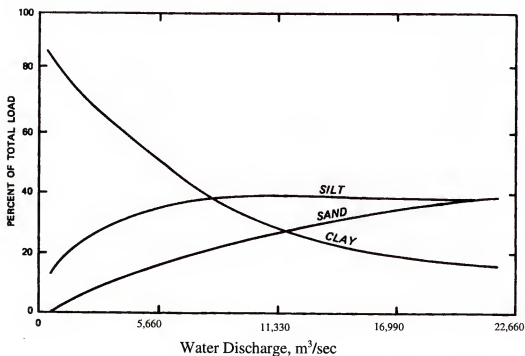
Figure 5-5. Distribution of total sediment load among three categories for Atchafalaya River at Simmesport, LA. From: Thomas et al. (1988). Used with permission.

Morganza Floodway, both near Vidalia, Louisiana. Total freshwater flows into the bay average about 5,600 m^3/sec, flowing through two outlets—the Lower Atchafalaya River and Wax Lake Outlet, the latter an artificial flood control channel dredged in 1941 (McAnally et al., 1985). During extreme Mississippi River floods, the Morganza Floodway just south of Old River is opened and the Atchafalaya basin can receive up to 42,000 m^3/sec, the project design flood (Thomas et al., 1988).

Tides in the bay can be either diurnal or mixed, with the K1 and O1 constituents dominating. Mean tide range at the location of the former oyster reefs is about 0.5 m. Net tidal and coastal currents sweep westward offshore and within the bays, with typical maximum velocities of less than 0.5 m/sec (Van Beek et al., 1977; Coleman et al., 1988). Winter storms can cause water level setdown of up to 0.6 m (Van Heerdon, 1980) and hurricane surges of 1 to 3 m have been recorded inside the bay (Ebersole, 1985).

Gulf of Mexico waves offshore of the bay can be as large as 3 m during hurricane passage, but are less than 1.2 m 95 percent of the time (Cratsley, 1975). Nonstorm Gulf waves attenuate sharply as they approach the shallow zone where the reefs used to lie and do not penetrate into the bay (Jensen, 1985). It is assumed that the very soft muds forming the bed there damp the wave energy. Locally generated waves within the bays can be a significant factor in sediment resuspension from the delta fringes (Letter, 1982).

About 1x10^{11} kg of sediment are transported into the bay annually by the river (Teeter and Pankow, 1989). That prodigious supply has filled what was once the upper estuary and is now the freshwater Grand and Six-Mile Lakes and has begun filling Atchafalaya Bay proper, building deltas at the mouths of the Lower Atchafalaya River

and Wax Lake Outlet. Delta growth has occurred despite an apparent subsidence (combined eustatic sea level rise, geologic subsidence and mud consolidation) rate of 1.0 to 1.6 cm/yr across the bay from 1962 to the present (Donnell et al., 1991).

Suspended sediment concentrations in river flows entering the bay typically range from 0.3 to 1.2 kg/m^3 with sizes distributed as shown in Figure 5-5 (Thomas et al., 1988). Bed sediments in the bay range in size from colloidal to about 1 mm, with the bay-wide D_{50} equal to 40 µm (Thomas et al., 1988).

The sediment sample tested here was taken from one of the delta lobes to the west of the primary delta at the mouth of the Lower Atchafalaya River. Figure 5-4 indicates the sample location.

5.6 Results

Data from the experiments are tabulated in Appendix D. Selected data and analyses are presented here, with additional analyses performed in Chapter 6, where the results of the experiments are compared with predicted values from the aggregation and deposition algorithms described in Chapters 3 and 4.

5.6.1 Hydraulics

Hydraulic parameters for the experiments are given in Table 5-2 as derived from the raw measurements in Appendix D. Manning's roughness coefficients shown in the table were computed from the mean velocity, slope, and hydraulic radius, and they are in agreement with the previously determined roughness value of 0.022, except for

experiment W11. The derived value of 0.031 for that experiment is believed to be the consequence of the Atchafalaya Bay silt and sand size particles (see Figure 5-2) depositing in the flume and establishing a hydraulically rough bed; whereas, the deposited kaolinite bed displayed a hydraulically smooth boundary comparable to the Lucite flume bottom.

Table 5-2. Hydraulic parameters for experiments.

Experiment Number	Mean Depth cm	Mean Velocity cm/sec	Water Surface Slope	Hydraulic Radius cm	Manning's Roughness Coefficient
W4	16.53	13.8	0.000282	6.76	0.020
W5	17.75	17.3	0.000459	6.95	0.021
W6	16.09	9.2	0.000142	6.68	0.021
W9	15.92	9.3	0.000151	6.65	0.022
W10	16.10	9.2	0.000161	6.68	0.023
W11	15.20	4.9	0.000085	6.52	0.031

Figures 5-6 and 5-7 display horizontal velocity profiles for two flow rates, 0.0033 m^3/sec and 0.0075 m^3/sec, that bracket the main experimental flow conditions. They show that velocities exhibited an apparent left to right skewness (more pronounced at the lower flow) that persisted over the length of the flume. Dye streams passing through the flow straightener and near the flume walls revealed no flow bias there, so the effect is attributed solely to the design of the flow meters, which biases readings in a velocity gradient as described below.
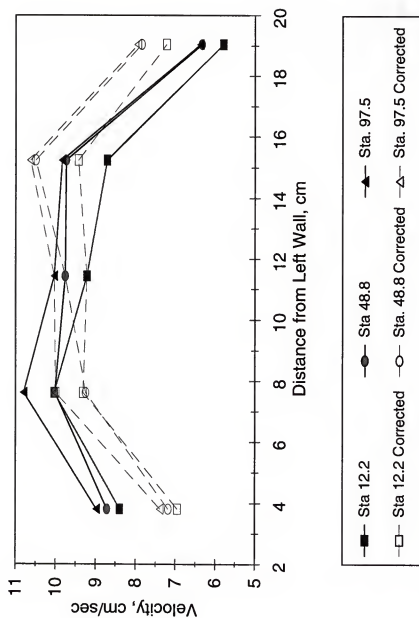
Figure 5-6. Transverse velocity profiles at three locations for a discharge of 0.033 m³/sec. Corrected profiles have been adjusted by Equation 5-5 and the meter calibration equation.
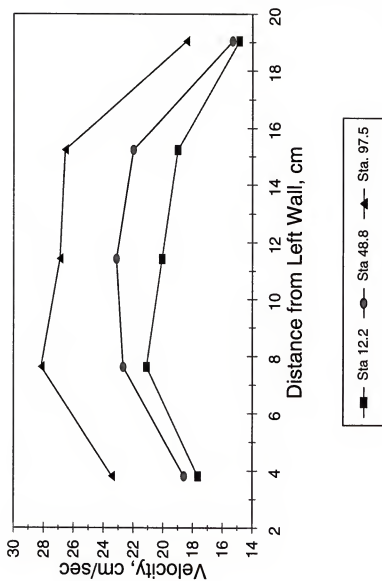
Figure 5-7. Transverse velocity profiles at three locations for a discharge of 0.075 m³/sec.

Figure 5-8 shows a schematic diagram of the miniature velocity meter. At steady state the net torque on the cup assembly is zero, so that:

$$\frac{1}{2}C_{DL}\rho(U_L + \omega a_w)^2 = \frac{1}{2}C_{DR}\rho(U_R + \omega a_w)^2 \qquad \textbf{(5-1)}$$

where

C_{DL} = drag coefficient for the rounded side of the left cup,

C_{DR} = drag coefficient for the open side of the right cup,

ρ = fluid density,

U_L = mean flow velocity acting on the left side cup,

U_R = mean flow velocity acting on the right side cup,

ω = angular speed of the cup assembly, and

a_w = radius of the cup wheel to center of cups.
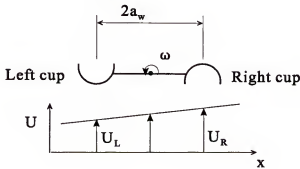
Figure 5-8. Schematic of velocity meter in a horizontal velocity gradient.

Approximating the mean flow speed across the meter as $\overline{U} = U_R - \Delta U/2 = U_L + \Delta U/2$ and rearranging Equation 5-1 yields the following expression for ω, which the meter senses and is translated into flow speed by a calibration curve:

$$\omega = \frac{\overline{U}}{a_w}\left(\frac{\sqrt{C_{DR}} - \sqrt{C_{DL}}}{\sqrt{C_{DR}} + \sqrt{C_{DL}}}\right) + \frac{\Delta U}{2a_w} \tag{5-2}$$

Equation 5-2 shows that if the velocity gradient is positive as in Figure 5-8, the meter spins faster than in a uniform flow of $\overline{U}$; whereas, if the gradient is negative it spins slower for the same mean velocity. Thus velocity measurements near the right wall of the flume, in a positive gradient, will be measured high, and those near the right wall, in a negative gradient, will be measured low, just as shown in Figures 5-6 and 5-7. Equation 5-2 can be used to correct the meter readings for the effect of velocity gradients by taking the second term on the right hand side as the error term. The meter readings can then be corrected[*] by $\Delta U/2$ if the velocity gradient across the meter is estimated by the law of the wall for fully rough turbulent flow (e.g., Daily and Harleman, 1973):

$$\frac{U}{u_*} = -5.76\log\left(\frac{k_s}{x_W}\right) + B_W \tag{5-3}$$

where

u_* = shear velocity, equal to $\sqrt{\tau_b/\rho}$,

---

[*] The meter calibration equation was $U = 0.733 + 0.1405\omega$ where ω is in radians per sec and velocity is in cm/sec.

τ_b = boundary shear stress,

k_s = roughness size, 6.4 mm for the flume sidewalls,

x_w = distance from the wall, and

B_w = constant.

Thus, after substituting for the shear velocity the velocity gradient can be calculated as:

$$\frac{dU}{dx} = \frac{\sqrt{g}\,n\,U_0}{R_h^{1/6}} \left(\frac{5.76 \log e}{x_w} \right)$$ (5-4)

where

g = acceleration of gravity,

n = Manning roughness coefficient,

U_0 = free-stream velocity, and

R_h = hydraulic radius.

The error correction can then be calculated as:

$$\Delta\omega = \frac{\Delta U}{2a_w} = \frac{dU}{dx}\frac{\Delta x}{2a_w} = \frac{dU}{dx}$$ (5-5)

Equation 5-5 has been applied to the raw velocities of Figure 5-6 and the corrected values are shown as hollow symbols connected by dashed lines. It can be seen that the equation slightly overcorrects the measured velocities, due to the simplifying assumptions of a linear velocity gradient and the log law profile in a narrow flume.

5.6.2 Sediment Concentration Vertical Profiles

Figures 5-9a, 5-9b, and 5-9c show the variation of sediment concentration with depth over the length of the flume (at 60 min after start of sediment injection) for experiments W5, W6, and W11, respectively. Experiment W5, with the highest flow rate and thus most vigorous mixing of the series, showed little to no stratification. In experiment W6, with a lower flow rate, the profile exhibited noticeable stratification (1 to 4 kg/m^3 difference between surface and bottom) between 30 and 70 m, but lost most of that stratification from 70 to 100 m. Experiment W11, with a substantial fraction of sand and silt sizes, displayed even greater stratification, up to 7 kg/m^3 difference between surface and bottom. At the higher flow rate, mixing was sufficient to keep the kaolinite sediment profile nearly homogenous, even though the gradual decline in concentration (discussed below) indicates that deposition was occurring.

5.6.3 Sediment Concentration Longitudinal Profiles

Figures 5-10 through 5-15 show the variation of depth-averaged concentration over the flume length for all six experiments and all measurement times. Experiment W4 (Figure 5-10) showed general consistency from one measurement time to the next, with some occasional suspect deviations (e.g., the jump in concentration at Station 42.7 at 15 min) from the overall trend of declining concentration. The trend clearly showed deposition occurring until after about Station 70, after which concentrations increased, implying either erosion of previously deposited bed, upward mixing of sediment passing
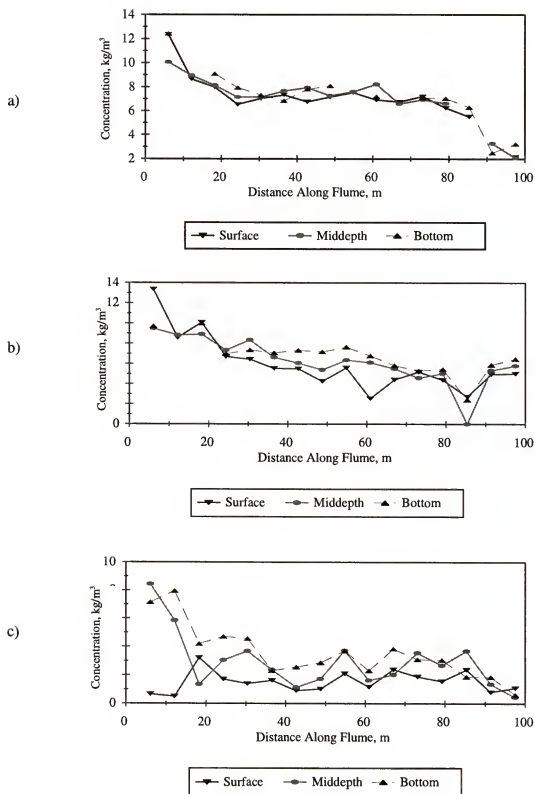
Figure 5-9. Variation of sediment concentration with depth over the length of the flume.
a) Experiment W5; b) Experiment W6; c) Experiment W11.

179
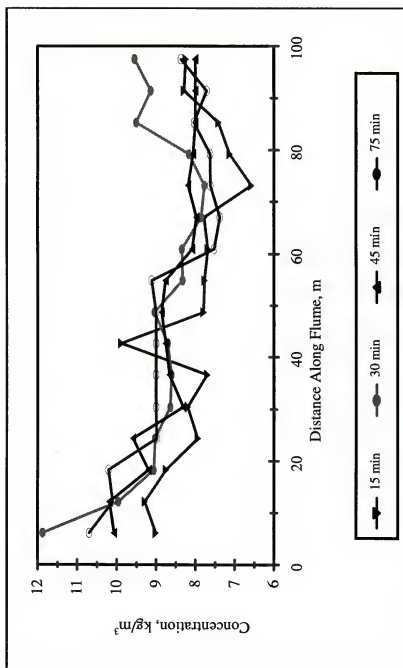
Figure 5-10. Longitudinal depth-averaged concentration profiles for experiment W4.
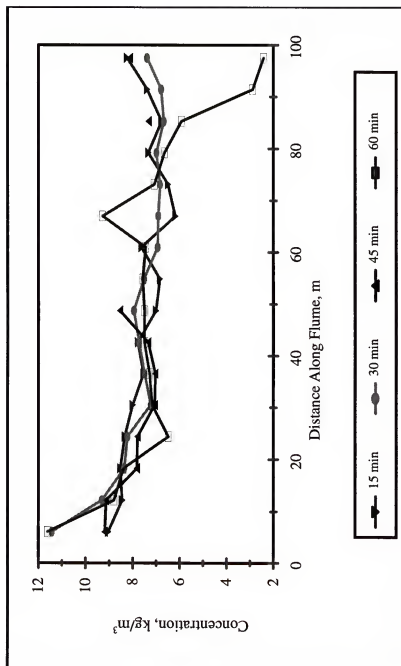
Figure 5-11. Longitudinal depth-averaged concentration profiles for experiment W5.
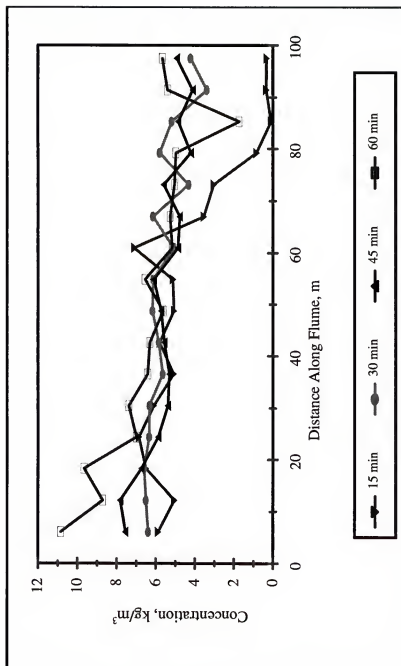
Figure 5-12. Longitudinal depth-averaged concentration profiles for experiment W6.
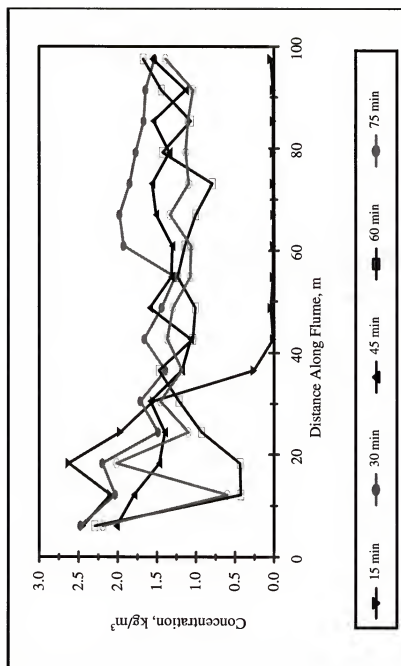
Figure 5-13. Longiudinal depth-averaged concentration profiles for experiment W9.
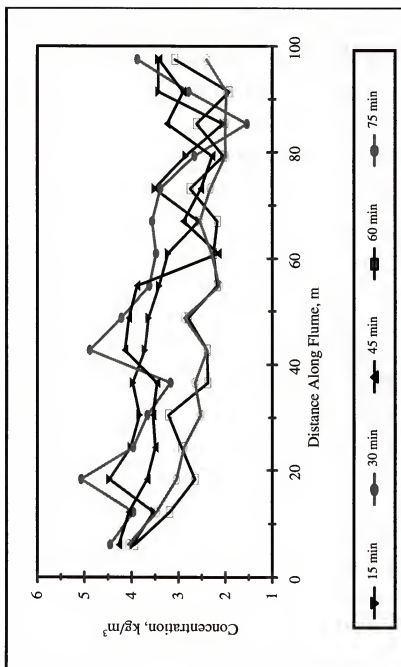
Figure 5-14. Longitudinal depth-averaged concentration profiles for experiment W10.

184
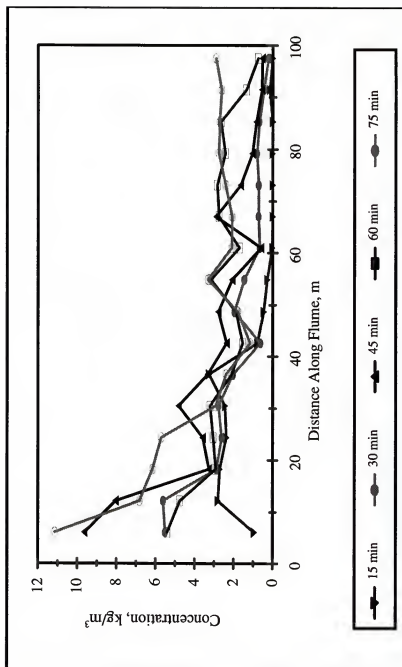
Figure 5-15. Longitudinal depth-averaged concentration profiles for experiment W11.

beneath the lowest sampling point at previous stations, or sampling of high concentrations from the near-bed zone. (These possible explanations are addressed below.) Experiment W5 (Figure 5-11) shows essentially the same trends, except at 60 min when the concentration falls off rather rapidly over the last 20 m of the flume. That decline was probably the result of the slurry tank delivering an unsteady or nonuniform sediment supply as the slurry level declined at the higher pumping rate, and should be disregarded. Experiment W6 (Figure 5-12) shows very consistent results with the exception of one suspiciously high measurement at Station 12.2 at 30 min. The apparent decline of concentration at 15 min in the last 40 m of the flume reflects the leading edge of the sediment plume not yet reaching the downstream stations within 15 min at the lower flow rate. The results of experiment W9 (Figure 5-13) were considerably more erratic than the other experiments, particularly in the first 30 m. As in W6, the 15 min measurement show that the plume has not yet progressed to the end of the flume. Experiment W10 (Figure 5-14) results showed considerable variation among the measurement times, and like W4, displays an increase in concentration at the end of the flume. Experiment W11 (Figure 5-15) showed a rapid initial decrease in concentration, reflecting settling out of the coarser fraction of the Atchafalaya Bay mud. The 15 min measurements again show the leading edge of the sediment plume still within the flume.

5.6.4 Profile Variability

Experiments W4 and W10 showed an increase in depth-averaged concentration near the downstream end of the flume, as did W5 and W9 to a lesser extent. As

mentioned above, this increase could have had several possible causes, including erosion of sediment deposited in the first few minutes of sediment injection, upward mixing of a high concentration layer traveling close to the bed, or a high concentration layer or deposited sediment clogging the near-bottom sampling tube. Each of these is considered in the following paragraphs.

5.6.4.1 Erosion

Erosion of sediment deposited prior to the 15 minute concentration measurement was possible, since the leading edge of the plume had somewhat lower concentrations and would have experienced less hindered settling effect than the fully developed concentration profile. That scenario requires that the initially deposited sediment have been erodible by the same flows that allowed it to deposit, which seems unlikely (Section 3.5.2) unless the higher sediment concentration at later times also increases the erosive power of the flow through modification of the boundary layer.

5.6.4.2 High concentration layer

The local increase in downstream concentration can also be interpreted to support the stirred layer concept proposed by Mehta (1991), since a disturbance of a near-bed, high concentration layer could inject a mass of sediment into the upper portion of the water column, as has been observed in wave-dominated flow by Cervantes et al. (1995). The possibility is reinforced by the previous observation that in Figure 5-9b the upstream stratification of experiment W6 disappears and concentration is nearly uniform with depth from Station 70 to 97.5.

If we assume that a perturbed stirred layer is the cause, then boundary layer growth might explain why it was perturbed at 50 to 70 m down the flume. If the flow is assumed to have had no boundary layer just downstream of the flow straightener, then a turbulent boundary layer could have grown away from the bed and side walls according to (Streeter, 1966):

$$\delta = 0.37 \left(\frac{\nu}{U_0} \right)^{1/5} x^{4/5} \qquad (5\text{-}6)$$

where

ν = kinematic viscosity of the fluid,

U_0 = free stream flow speed, and

x = distance downstream.

Solving Equation 5-6 for x where the boundary layer thickness is equal to the water depth or flume width yields an estimate of the distance to the location of a fully developed boundary layer profile in the flume. Solutions for each experiment are shown in Table 5-3. Clearly, none of the calculated distances are great enough to suggest that the initial boundary layer development is responsible for the rise in concentration at 70 to 80 m; however, the development length of 2 to 3 m could lead to turbulent structures of that order propagating down the flume and intermittently remixing a stirred layer, thus giving rise to the station to station concentration fluctuations apparent in Figures 5-10 through 5-15.

Table 5-3. Distance along flume to fully developed boundary layer.

Experiment Number	From Bottom m	From Sidewall m
W4	2.0	3.1
W5	2.3	3.2
W6	1.8	2.7
W9	1.8	2.7
W10	1.8	2.8
W11	1.4	2.4

The boundary layer development explanation for increased concentration near the end of the flume could be valid despite the results of Table 5-3, for Equation 5-6 assumes a zero pressure gradient. The flume's tailgate imposed an adverse pressure gradient near the downstream end of the flume, so the momentum of the boundary layer there would have been reduced and the net boundary stress increased (Daily and Harleman, 1973). Figure 5-16 shows the average water surface profiles for experiments W4, W5, W6, and W10. Those profiles do not particularly support the possibility for an adverse pressure gradient, for while W4 and W10 did indeed show a flatter slope in the downstream half of the flume, so did W6, which exhibited little or no concentration increase near the end. Likewise, W5, which did show a concentration increase near the end, did not display a significant reduction in slope.

Figure 5-17 shows the variation in mean water surface slope over the length of the flume during each experiment. The experiments exhibit only minor changes in slope,
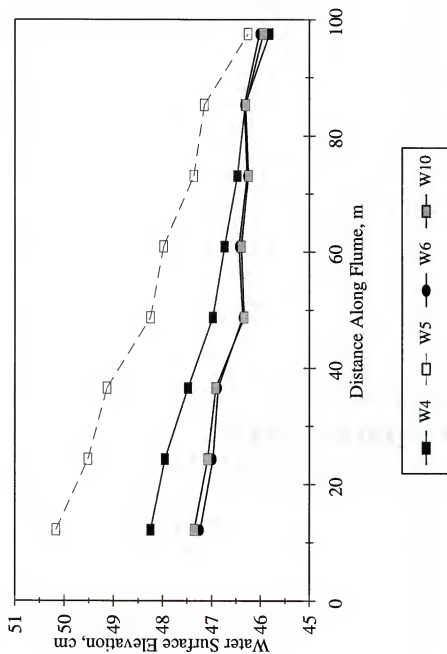
Figure 5-16. Average water surface elevation over length of flume.
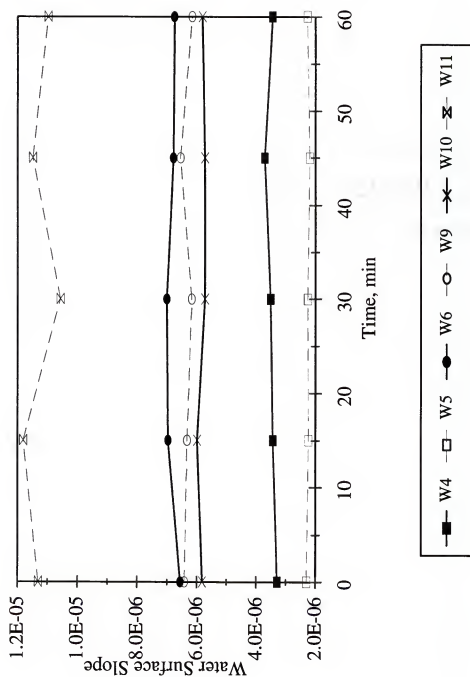
Figure 5-17. Variation of mean water surface slope over duration of experiments.

except for W11, which varies about 4 percent around its mean value. None of the slope changes were sufficient to produce the kinds of variability seen in Figures 5-10 through 5-15.

The above analyses provide hints, but certainly no proofs, of a reason for a near bed layer to be suddenly resuspended into the water column. It seems quite possible that the cause was a more prosaic geometric flaw in the 20-year-old flume. Warping was visible in some locations, and a subtle distortion of the bottom or sides could have produced a local acceleration sufficient to disturb a thin layer of high concentration sediment.

Intermittent or periodic turbulence bursts have been observed to eject sand-size sediment from the near-bed zone (e.g., Sumer and Diegaard, 1981) and that phenomenon could have occurred in the flume, mixing a high concentration layer upward, provided the layer was thin enough to pass beneath the near-bottom sampling point and so escape sampling until mixed upward.

The stirred layer, as proposed by Mehta (1991) is a thin near-bed zone where sediment is stirred by strong convection cells (Section 2.5.2). The concept is analogous to the oceanographic definition of a mixed layer, where wind and wave mixing at the air-sea boundary creates a zone of approximately constant temperature and salinity.

Newman (1990) employed a stirred-layer-type concept in describing an active interfacial layer between the water column and sediment bed in which agitated sediment accelerates the rate of particle removal from the water column. In her laboratory experiments the rate of tracer removal from the water column was an order of magnitude

faster if a high concentration interfacial layer were present. The interfacial layer in her experiments consisted of ". . . loosely bound (fluffy) aggregates . . ." on the order of 0.1 to 1 cm thick and agitated either by the water column or a mixing device.

Cervantes et al. (1995) inferred the height of the stirred layer as being about 5 percent of the water depth in sediment resuspension flume experiments in which short period waves were the source of resuspension. The flume flow depths ranged from 0.16 to 0.30 m, so λ_s was 0.8 to 1.5 cm. That was the only explicit attempt found in the literature to estimate that parameter.

The Kolmogorov and Taylor microscales may be helpful in estimating the stirred layer's thickness. The Kolmogorov microscales give the length and time scales, respectively, of the smallest turbulent structures as (Tennekes and Lumley, 1972):

$$
\lambda = \left[\frac{\nu^3}{\epsilon} \right]^{1/4}
$$
$$
\eta = \left[\frac{\nu}{\epsilon} \right]^{1/2}
$$

(5-7)

where

ν = dynamic viscosity of the fluid, and

ϵ = energy dissipation rate of the flow, given by Equation 3-12.

For typical estuarial flow conditions, λ ranges from about 10 to 300 μm, and η ranges from about 10^{-4} to 10^{-1} sec. The lower end of the above λ range is much too small for particles on the order of 100 μm to circulate, and the upper end would strain the

concept, so it is concluded that the stirred layer must be thicker than the Kolmogorov scale.

The Taylor microscale is related to the dimensions of the smallest correlated turbulent structures, and is given by (Tennekes and Lumley, 1972):

$$\lambda_T = \left[\frac{\overline{u'u'}}{\overline{\left(\frac{\partial u'}{\partial x}\right)^2}} \right]^{1/2} \tag{5-8}$$

where

u' = turbulent velocity fluctuation, and

x = length dimension.

For isotropic turbulence, Equation 3-12 can be used with Equation 5-8 to obtain:

$$\lambda_T = \left[\frac{10 \nu k_e}{\epsilon} \right]^{1/2} \tag{5-9}$$

where k_e = turbulent kinetic energy. If k_e is scaled by the square of the free-stream velocity, λ_T will be on the order of 0.6 to 14 mm for flows of 1 to 0.05 m/sec, respectively.

High resolution numerical experiments using direct numerical simulation of the Reynolds stress terms have shown that stretching of turbulent vortices creates long, coherent structures called "worms" with diameters 3 to 6 times that of the Kolmogorov turbulent microscale eddies (Jimenez et al., 1993), or about 30 to 1800 µm. Since larger

scale eddies occur in counter-rotating pairs (e.g., Daily and Harleman, 1973), a stack of worms can be envisioned, creating convection cells on the order of a few millimeters thick, the same order as the Taylor microscale.

Several investigators have used interfacial boundary layer concepts to characterize behavior near density (salt or sediment) interfaces. Among the measures employed are the shear layer (thickness defined as δ_s), the zone in which boundary shear effects are concentrated, as indicated by a steep velocity gradient, and the density interfacial layer (thickness defined as δ_d), the zone in which shear production and vorticity are concentrated, indicated by a steep density gradient. In salinity stratified flow Narimousa and Fernando (1987) found that δ_s had a mean value of 20 percent of the flow depth; whereas, Mehta and Srinivas (1993) found it varied only from about 4 to 15 percent of the depth in sediment stratification experiments. They attributed the difference to the stabilizing influence of settling sediment particles at an interface. The smaller δ_d was found by Narimousa and Fernando (1987) to be 7 percent of the depth and by Mehta and Srinivas (1993) to be 6 to 7 percent.

Thus, measurements of physical processes that can be intuitively or directly linked to the stirred layer range from a few millimeters to something less than 2 cm, with the only conscious efforts to detect it being the Cervantes et al. (1995) measurement showing it to be of order 1 cm in laboratory experiments with waves and the Newman (1990) assumption of 0.1 to 1 cm in laboratory mixing chambers. From these considerations it is reasonable to assume that the stirred layer thickness will be on the order of a centimeter, which would place it below the near-bottom sampling point.

The stirred layer hypothesis can be checked for physical realism by considering that the measured increase in depth-averaged concentration must be attributable to a layer sediment concentration less than that of deposited bed. Experiment W4 showed a 1.7 kg/m^3 increase, and that increase over a 16.53 cm depth would require a 1 cm thick stirred layer to have a concentration of about 28 kg/m^3, a reasonable concentration and certainly one capable of flowing.

<u>5.6.4.3 Bed or layer entrainment</u>

The maximum depth of deposit in the downstream half of the flume (values given in Section 5.6.3) ranged from nil to 0.94 cm, or up to about half the distance to the sample tube intake. Thus the sample tubes were not covered by the bed, but the possibility remains that the sample intake speed entrained material from the deposited bed or that a stirred layer traveling above the bed reached the sample intakes. To examine that possibility, Figure 5-18 shows longitudinal concentration profiles at 30 min for experiment W4, surface, middepth, and bottom plus depth averaged. This data set was selected because it had the most clearly defined downstream concentration increase. The mean concentration increased from 7.8 kg/m^3 at Station 73.2 to 9.5 kg/m^3 at Station 97.5. High concentration samples from the bed obviously did not cause the rise, since the near-bed sample concentrations were not significantly higher than those higher in the water column except at Station 73.2.

<u>5.6.4.4 Discussion</u>

These considerations are of the necessary but not sufficient category of proofs. They do not prove that a high concentration stirred layer at the bed occurred and caused
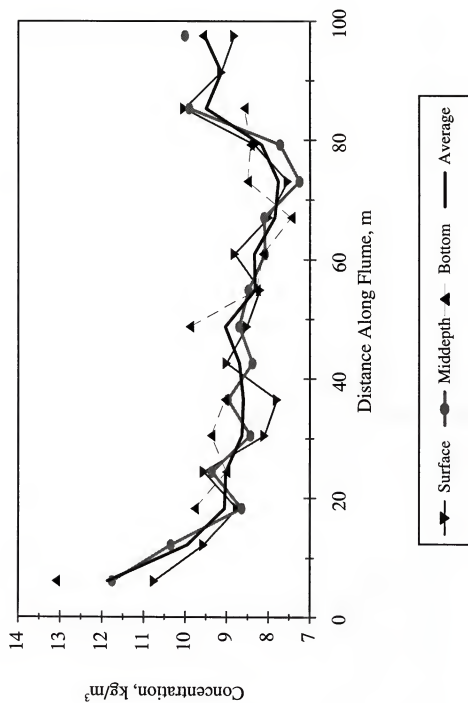
Figure 5-18. Longitudinal concentration profiles for experiment W4 at 30 min.

the apparent concentration increase in the downstream portion of the flume, but they do show that a stirred layer is one plausible explanation of that aspect of the flume results and arguably the most plausible of those considered. Experiments explicitly directed at finding a stirred layer will be required to fully assess the hypothesis.

5.6.5 Deposition Rate

Figure 5-19 shows the concentration profiles for all six experiments as an average of the 30, 45, 60, and 75 min profiles, each normalized by the average concentration at Station 6.1. It shows that experiments W9 (0.034 m^3/sec and 2 kg/m^3 initial condition) and W11 (Atchafalaya Bay mud) were clearly depositing at a different rate than the other experiments, but the other four display no readily discernable pattern other than that the concentration declined at roughly the same rate in all, indicating similar deposition rates.

The deposition rate as inferred from concentration decline can be examined more easily by fitting trend lines to the post-30-min concentrations and inferring deposition rates from the slopes of the trend lines. Table 5-4 shows the results of that calculation. The linear correlation coefficient reflects the scatter in the points along the profile, e.g., experiment W9 had a rather low correlation with distance and considerable variability, but it also reflects the fact that the concentration declined nonlinearly. The overall deposition rates show that deposition rate increased with increasing concentration and decreased with increasing velocity, qualitatively confirming Equation 2-34.
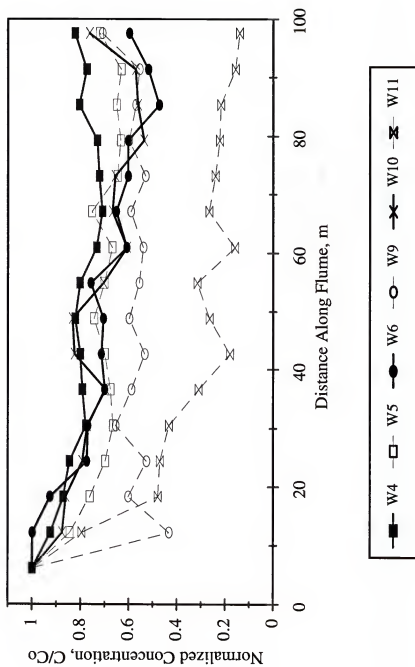
Figure 5-19. Normalized depth-averaged concentration over length of flume.

Table 5-4. Concentration profile slope and inferred deposition rate.

Experiment Number	Flow Rate m³/sec	Initial Concentration kg/m³	Correlation Coefficient (R²)	Concentration Profile Slope kg/m³-m	Overall Deposition Rate kg/m²-sec
W4	0.052	10.9	0.50	-0.0240	0.000547
W5	0.070	10.7	0.32	-0.0182	0.000559
W6	0.034	8.3	0.55	-0.0390	0.000577
W9	0.034	2.2	0.11	-0.00377	0.000056
W10	0.034	4.2	0.29	-0.0150	0.000222
W11[a]	0.017	7.9	0.49	-0.0533	0.000397

[a] Experiment W11 slope calculation excludes initial 12.2 m of the flume.

Figures 5-20 through 5-25 depict deposition rates as computed from two measurements—averaged concentrations and thickness of bed deposit. As described earlier, the deposited bed thickness was measured using a point gage and is considered an approximate measure because of the difficulty in judging when the point gage pierced the bed surface. Deposition rate in the figures (negative values indicate erosion) was computed as the product of depth and duration-averaged concentration differences between stations multiplied by the suspension discharge and divided by the area of the flume bottom between the stations.

Figures 5-20 to 5-25 show little apparent correlation between the computed deposition rate as it varies along the flume and the observed variation in deposit depth. Neither measure can be considered precise, and the inaccuracies in both make them of limited use.
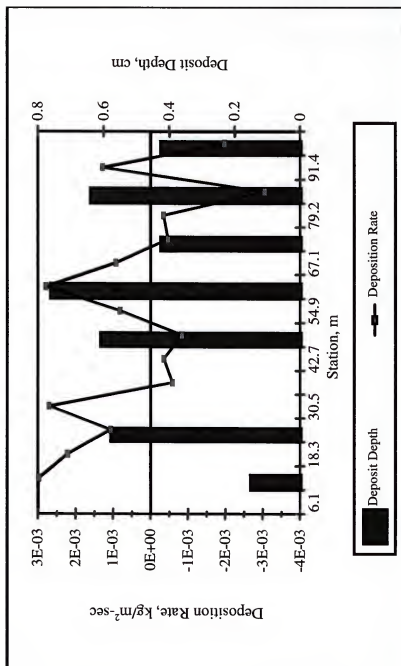
Figure 5-20. Deposition rate computed from concentration decline compared with measured bed thickness for experiment W4.

201
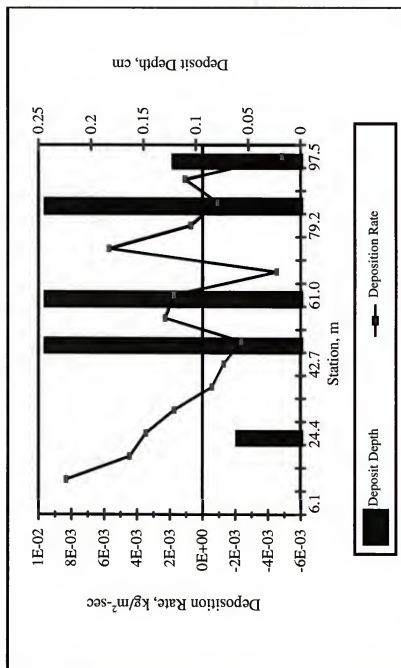
Figure 5-21. Deposition rate computed from concentration decline compared with measured bed thickness for experiment W5.

202
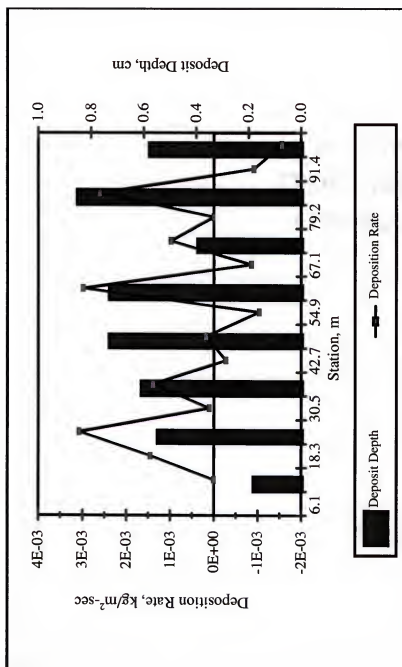
Figure 5-22. Deposition rate computed from concentration decline compared with measured bed thickness for experiment W6.
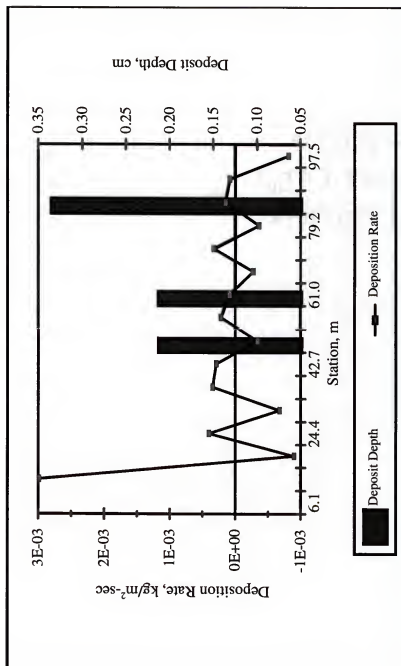
Figure 5-23. Deposition rate computed from concentration decline compared with measured bed thickness for experiment W9.
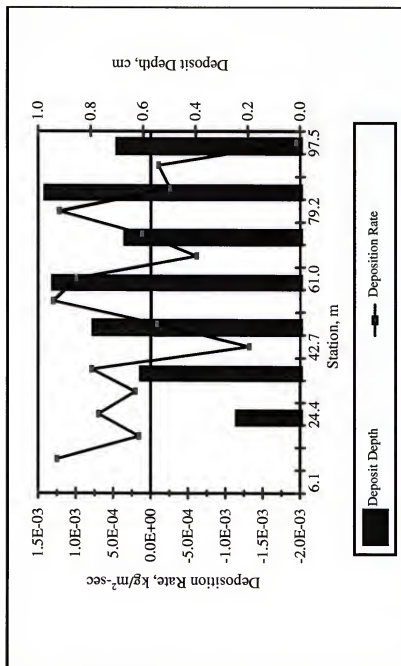
Figure 5-24 Deposition rate computed from concentration decline compared with measured bed thickness for experiment W10.
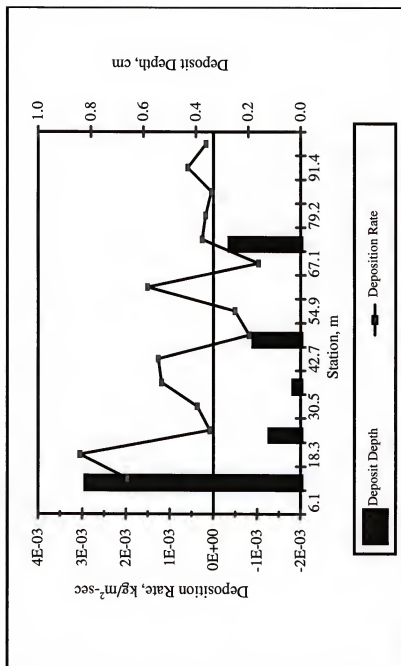
Figure 5-25. Deposition rate computed from concentration decline compared with measured bed thickness for experiment W11.

Bed samples from the flume at 12.2 m intervals were tested by Dixit et al. (1982) in an annular flume at the University of Florida. They concluded that the depositing sediments were sorted over the length of the flume by the settling velocity of the aggregates and shearing at the bed. Sorting was manifested in the deposition rate and apparent settling velocity and showed that aggregates containing the finest, and thus most cohesive, grains settled first. The data also showed that aggregate settling velocity increased with decreasing dispersed median grain size. The latter finding can be contrasted to Equation 2-9, which indicates that modal aggregate diameter (and by Equation 2-18, settling velocity) increases with increasing modal grain size. But Equation 2-9 was derived from suspended sediment samples; whereas, the bed samples tested by Dixit et al. were presorted by their own settling velocity and shear strength.

5.7 Summary

A series of kaolinite deposition experiments were conducted in a 100-m-long flume with initial sediment concentrations ranging from 2 to 10 kg/m^3 and mean flow speeds ranging from 9.2 to 17.3 cm/sec. One experiment tested 10 kg/m^3 Atchafalaya Bay mud at 4.9 cm/sec. Water surface, velocity, and vertical and longitudinal suspended sediment concentration profiles were measured, and bottom deposit thickness was estimated.

Significant variability in suspended sediment concentrations occurred in the experiments and is attributed in part to operational and measurement errors, but can also be plausibly explained as intermittent perturbation and upward mixing of a high

concentration layer flowing close to the bed, below the lowest sampling point. If such a layer occurred in the flume, it can be interpreted as a stirred layer (Section 2.5.1).

Deposition rate decreased with increasing concentration and increasing flow speed. The former can be attributed to an decrease in settling velocity associated with hindered settling and perhaps to decreased mean aggregate size, which is inversely proportional to concentration at the range of tested concentrations (Section 2.4.4.1). The latter can be attributed to higher bed shear stress and more vigorous mixing at higher flow speeds and also to decreased mean aggregate size, which is inversely proportional to shearing rate (Section 2.4.4.2).

Settling velocity of deposited sediment decreased over the length of the flume. Since concentration decreased, the hindered settling effect would have decreased also, so the diminution of settling velocity was the result of more rapid deposition of faster settling particles and thus sorting of the sediment.

CHAPTER 6
METHOD APPLICATION

6.1 Introduction

Chapter 3 proposes a method for calculating the aggregation rate of a fine sediment suspension by consideration of collisions among multiple size classes. Chapter 4 presents a simple method to calculate sediment deposition rates of multiple size classes with continuing aggregation as described in Chapter 3. This chapter applies those methods to experimental data in order to test their validity and to further explore aggregation processes.

The calculations were first tested against aggregation data from laboratory mixing chamber experiments. In these carefully controlled experiments aggregation results had been measured in terms of particle number concentration, median aggregate size, and/or aggregate size distribution. Comparison with these data permitted evaluation and adjustment of the basic aggregation calculations to ensure that they are an accurate and reliable representation of aggregation processes. Next, combined aggregation and deposition calculations were tested against flume data, including those presented in Chapter 5, to determine their suitability for application to conditions more closely approaching actual estuarine flows. Finally, calculated aggregation results were examined to identify significant processes.

6.2 Aggregation Chamber Calculations

A number of investigators have performed aggregation chamber experiments, some results of which are tabulated in Appendix B. From among them the freshwater experiments of Tsai et al. (1987) and the saltwater experiments of Burban et al. (1989), both performing identical experiments with Detroit River sediment in a Couette chamber, were reproduced. Also tested were one case from Edzwald et al. (1974) in which commercial kaolinite was aggregated in a paddle-stirred jar, and one from Gibbs (1983) in which Amazon River Delta sediment was aggregated in a Couette chamber. The experimental equipment and procedures for each are described in Section 3.5.1.2.

6.2.1 Laboratory Experimental Conditions

Table 6-1 lists the aggregation chamber experiments from which data were used and the pertinent conditions for each. Experimental conditions ranged from low to high shearing rates (with corresponding range of energy dissipation rates), low to high salinity, and low to high initial suspension concentration, in order to define the applicability of the aggregation model over a range of environments. Flow conditions for the G, T, and B series included shearing rates ranging from 11 to 600 sec^{-1}, well below the chamber's transition to turbulent flow at 900 sec^{-1} (Tsai et al., 1987). Flow in the chamber of experiment E1 was turbulent.

Figure 6-1 illustrates the average initial distribution of particle sizes by volume in the B and T series experiments as reported by Tsai et al. (1987).

Table 6-1 Aggregation Chamber Experimental Conditions.

Experiment Number[a]	Sediment	Initial Suspension Concentration kg/m^3	Mean Shearing Rate[b] 1/sec	Energy Dissipation Rate m^2/sec^3	Salinity ppt	Effective Gravity[c] g
E1	kaolinite	0.20	52.4	0.0641	2	1.00
G1	Amazon Delta	0.15	11	0.00282	2	1.01
T1	Detroit River	0.10	100	0.242	0.5	1.01
T2	Detroit River	0.80	200	0.942	0.5	1.14
T3	Detroit River	0.10	400	3.77	0.5	3.19
B1	Detroit River	0.10	100	0.242	17.5	1.01
B2	Detroit River	0.40	200	0.942	35	1.14
B3	Detroit River	0.40	600	8.48	35	12.1
B4	Detroit River	0.80	200	0.942	35	1.14
B5	Detroit River	0.1	200	0.942	35	1.14
B6	Detroit River	0.01	400	3.77	35	3.19
B7	Detroit River	0.1	400	3.77	35	3.19
B8	Detroit River	0.4	400	3.77	35	3.19
B9	Detroit River	0.4	100	0.242	35	1.10
B10	Detroit River	0.4	200	0.942	0.5	1.14
B11	Detroit River	0.4	200	0.942	17.5	1.14
B12	Detroit River	0.05	200	0.942	35	1.14
B13	Detroit River	0.1	200	0.942	17.5	1.14

Notes: [a] Experiment number prefix indicates data source by first letter of the primary author's family name—Edzwald et al. (1974), Gibbs (1983), Tsai et al. (1987), and Burban et al. (1989). [b] Calculated from shearing rate by Equation 3-12. [c] The Couette chamber created centrifugal accelerations which were represented by an increased gravitational acceleration.

The calculation procedure consisted of running program Danu (see Chapter 4 and Appendix C) in aggregation only mode (no transport or deposition), with initial mass concentrations as described below and chamber conditions as listed in Table 6-1.
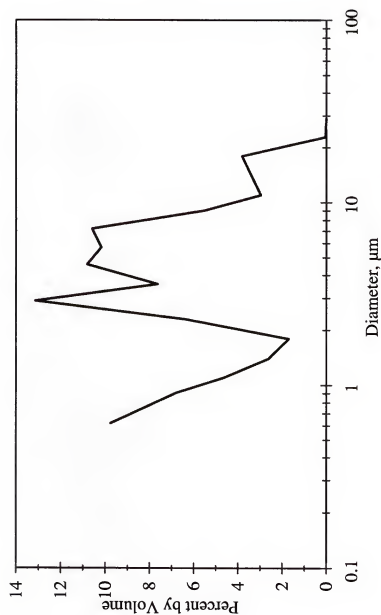
Figure 6-1. Initial size distribution of Detroit River sediment used in B and T series experiments. It is a dispersed size distribution, not the *in situ* distribution.

6.2.2 Calculations and Parameter Definitions

For initial concentrations in B and T series experiment calculations, the distribution shown in Figure 6-1 was assumed to apply for each experiment, since measurements by Tsai et al. (1987) showed that the distribution varied only slightly across the suspension concentration range. The E and G experiments used sediment with unspecified narrow distributions with all mass concentrated between 1 and 6 μm so arbitrary tapered distributions over that range were employed. Sensitivity calculations showed that only the initial period of aggregation was sensitive to the initial distribution, so the assumptions are reasonable for equilibrium calculations but suspect for the early period in each experiment.

6.2.2.1 Density and Strength

The aggregation processes scheme of Chapter 3 employs a size classification based on particle mass and a particle strength based on particle density; thus, selection of a particle class scheme affects both particle sizes and strengths. Of the references cited in Table 6-1, only Burban et al. (1989) provided density data and none reported particle strength, so an approach was used here which solved simultaneously for density and strength. Specifically, Equations 3-3 and 3-4 were combined to yield:

$$\tau_j = f_p \left(\frac{D_g}{D_j} \right)^2 \tag{6-1}$$

where

τ_j = shear strength of the j class particle,

D_g = grain diameter,

D_j = diameter of the j class particle, and

$f_p = B_\tau \, B_\rho^{2/(3-n_f)}$, where B_τ and B_ρ = shear strength and density coefficients, respectively.

The coefficients B_τ and B_ρ were assumed to depend on concentration, collision intensity, and salinity as described in Section 3.2. Program Danu was run for a selected set of Table 6-1 experiments (B2 to B6 and B8 to B11) spanning the range of concentrations, shearing rates, and salinities, and f_p was varied systematically until the correct median equilibrium size was computed for each. By regression analyses of those results the relationship between f_p and those parameters was found to be:

$$f_p = 0.422 \, C_r^{-1.66} \, G_{\epsilon gr}^{-0.169} \, (24.4 - S_r) \tag{6-2}$$

where

C_r = dimensionless sediment mass concentration = C/C_0,

C = total sediment mass concentration,

C_0 = reference sediment mass concentration, taken to be 0.8 kg/m³,

S_r = dimensionless salinity = S/S_0,

S = fluid salinity, ppt,

S_0 = reference salinity, taken to be 2 ppt, and

$G_{\epsilon gr}$ = dimensionless collision intensity function, given by:

$$G_{\epsilon gr} = \frac{\epsilon}{\epsilon_0} \frac{g_m}{g_{m0}} \tag{6-3}$$

where

ϵ = energy dissipation rate of the flow, given by Equation 3-12,

ϵ_0 = reference energy dissipation rate, taken to be 8.48 m²/sec³,

g_m = body acceleration force, and

g_{m0} = reference body acceleration force, taken to be 12.2g.

The reference values were selected so as to make the nondimensional terms vary between 0 and 1, except for S_0, which was set to conform with the corresponding salinity threshold value in Equation 3-68.

Results of the regression between values of f_p determined by numerical experiment are shown in Figure 6-2 along with a perfect fit 45 deg line. The correlation coefficient was 0.99.

Since this process yields an expression for f_p that does not distinguish between the values of B_p and B_τ, they were separated, with B_p = 16,500, so that the density curve most nearly represented the average density reported by Burban et al. (1989), and the remainder of Equation 6-2 was arbitrarily assigned to particle strength. Table 6-2 shows the resulting particle classification and properties scheme.

6.2.2.2 Collision time parameter

The derivation of Equation 3-75 for the collision diameter function included the assumption that the term f_c was needed to account for variation in collision efficiency over the period of aggregation. The density-strength calculations described above needed only to produce an equilibrium particle diameter, so that term was set to 1 for those calculations and examination of f_c was deferred until the following step.
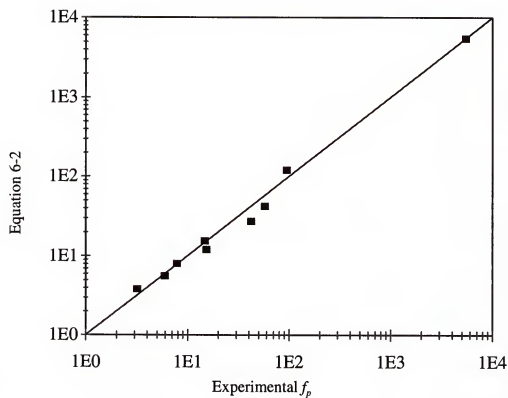
Figure 6-2. Comparison of regression-based Equation 6-2 density-strength function f_p with input values obtained by numerical experiments.

Table 6-2. Sediment classes and characteristics for aggregation chamber experiments.

Class Number	Representative Diameter μm	Minimum Mass kg	Representative Mass kg	Maximum Mass kg	Density kg/m³	Settling Velocity m/sec	Shear Strength Pa
1	0.563	0.00e+00	2.48e-16	3.31e-16	2650	3.15e-07	134
2	1.03	3.31e-16	1.52e-15	2.71e-15	2650	1.05e-06	134
3	1.57	2.71e-15	5.40e-15	8.09e-15	2650	2.45e-06	134
4	2.02	8.09e-15	1.14e-14	1.48e-14	2650	4.04e-06	134
5	2.54	1.48e-14	2.26e-14	3.05e-14	2650	6.37e-06	134
6	3.01	3.05e-14	3.80e-14	4.55e-14	2650	8.99e-06	134
7	3.89	4.55e-14	8.18e-14	1.18e-13	2650	1.50e-05	134
8	5.05	1.18e-13	1.69e-13	2.20e-13	2515	2.33e-05	108
9	6.48	2.20e-13	3.20e-13	4.20e-13	2245	3.14e-05	65.2
10	8.19	4.20e-13	5.85e-13	7.49e-13	2037	4.15e-05	40.9
11	10.7	7.49e-13	1.18e-12	1.60e-12	1843	5.70e-05	24.0
12	14.3	1.60e-12	2.54e-12	3.47e-12	1674	8.06e-05	13.5
13	19.4	3.47e-12	5.87e-12	8.27e-12	1532	1.17e-04	7.27
14	25.3	8.27e-12	1.22e-11	1.61e-11	1435	1.60e-04	4.27
15	37.6	1.61e-11	3.68e-11	5.75e-11	1324	2.57e-04	1.94
16	53.1	5.75e-11	9.83e-11	1.39e-10	1252	3.90e-04	0.971
17	71.4	1.39e-10	2.29e-10	3.19e-10	1204	5.53e-04	0.538
18	91.1	3.19e-10	4.63e-10	6.08e-10	1172	7.37e-04	0.330
19	111	6.08e-10	8.21e-10	1.03e-09	1151	9.26e-04	0.223
20	171	1.03e-09	2.90e-09	4.76e-09	1114	1.52e-03	0.0942
21	330	4.76e-09	2.03e-08	3.59e-08	1078	3.08e-03	0.0252
22	1270	3.59e-08	1.13e-06	2.23e-06	1043	9.34e-03	0.00169

To define the form of f_c, program Danu was again run repeatedly, this time for experiments B3, B4, B6, T1, and T3, with specified systematic variation of f_c until the rate of median diameter increase matched that of the laboratory experiments. Then those numerical-experiment-derived values were analyzed to establish a predictive relationship for f_c. Lick et al. (1993) found that the time to reach equilibrium diameter was an inverse power function of concentration and shearing rate (Equation 2-11) and these analyses confirmed that. The relationship found here took the form:

$$f_c = 0.081 \left(G_r C_r \right)^{-0.459} \tag{6-3}$$

where

G_r = nondimensional shearing rate, G/G_0,

G = fluid shearing rate, sec^{-1}, and

G_0 = reference shearing rate, taken to be 600 sec^{-1}.

Equation 6-4 is in qualitative agreement with Lick et al. (1993), who analyzed the same experiments for time to equilibrium and found the exponent to be -0.36 for fresh water and -0.44 for sea water. Figure 6-3 shows the regressions between calculated and measured f_c. The correlation coefficient for Equation 6-3 was 0.97.

6.2.3 Results

With f_p and f_c determined, program Danu was revised to incorporate Equations 6-3 and 6-4 and all the experiments of Table 6-1 were simulated by calculations. Table 6-3 summarizes the results, giving equilibrium sizes and times to reach size equilibrium. Times to equilibrium were estimated by inspection of median diameter time history plots. Note that only for Experiments E1, G1, T1 to T3, B1, B7, B12, and B13 were the calculated values completely independent predictions, since the other experiments were used to determine either or both f_p and f_c.

Table 6-3 calculated results for the T and B series are seen to be good approximate predictions of observed median particle size at equilibrium and the time required to reach it, including those experiments (T2, B1, B12, and B13) not used to fit Equations 6-2 and 6-4.
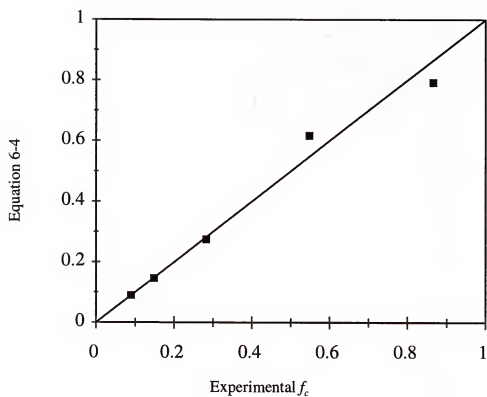
Figure 6-3. Comparison of regression result of Equation 6-4 for collision diameter adjustment, f_c, with input values obtained by numerical experiments.

Table 6-3 Aggregation Chamber Equilibrium Diameters.

Experiment Number	Measured		Calculated	
	Time to Equilibrium min	Median Diameter μm	Time to Equilibrium min	Median Diameter μm
E1	NA	NA	> 325	750
G1	NA	NA	120	120
T1[a]	90	110-119	99	116
T2	30	26-31	35	27
T3[a]	60	46-52	98	52
B1	NA	83	40	115
B2[a]	60	30-32	50	29
B3[a]	15	15	15	16
B4[a]	10	25	16	26
B5[a]	40	53-58	50	56
B6[a]	40-90	145-205	100	172
B7	50	32	35	35
B8[a]	30	18-20	32	24
B9[a]	40	39-41	26	48
B10[a]	50	38-40	80	37
B11[a]	NA	38	30	38
B12	45	80-89	50	84
B13	NA	69	50	74

Note: [a] Experiments used to define the constants in Equations 6-2 and 6-4.

Four aggregation chamber experiments—B4, B12, E1, and G1— are examined in more detail below in order to determine if the calculation method is realistic and to provide some insight into the significant processes.

6.2.3.1 Experiment B4

Figures 6-4 and 6-5 show the time history of median particle size (by volume) and number concentration, respectively, for Experiment B4. Comparison with laboratory observations shows that the calculated diameter grew somewhat too slowly but was in general agreement with observations. Particle number concentration, for which no laboratory data were available, increased in the first minute as larger particles disaggregated faster than smaller particles aggregated, then decreased as aggregation caught up. The plots indicate that median particle diameter reached equilibrium (confirmed by continuing the calculations to 30 min), but that the number concentration did not. Results presented below show why that was so.

Figure 6-6 shows the particle size distribution (by volume) at 15 min for Experiment B4. Equation 4-12 was employed to apply a random ±50 percent variation in the collision-induced shear stress at each time step. While the resulting calculated distribution exhibits a peak at the same diameter as the experimental peak, it is somewhat narrower than the observed distribution, falling off too sharply at larger sizes, suggesting that the simple randomness factor did not sufficiently capture the variability in collisions and particle strengths. Increasing the number of particle sizes did not significantly improve the agreement. Improvement in the calculated distribution may require the more rigorous probability treatment discussed in Chapter 4.

Figure 6-7 shows the particle number distribution, which is very different than the particle volume distribution of Figure 6-6. There are still very large numbers of particles at the smallest sizes, but they contribute relatively little mass or volume to the total suspension.
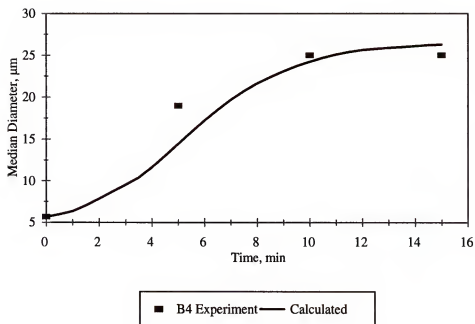
Figure 6-4. Observed and calculated time history of median diameter for Experiment B4.
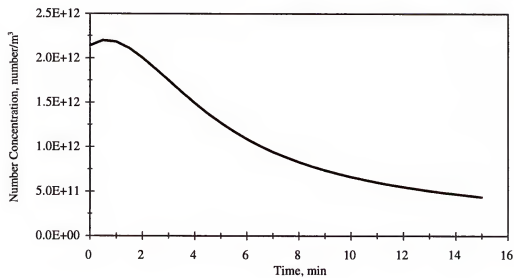
Figure 6-5. Calculated number concentration of particles for Experiment B4.
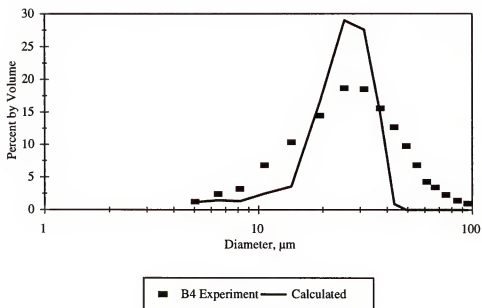
Figure 6-6. Measured and calculated particle size spectrum for Experiment B4 at 15 min.
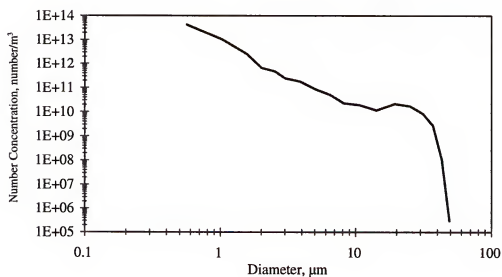
Figure 6-7. Calculated particle number spectrum for Experiment B4 at 15 min.

Figures 6-8 and 6-9 illustrate the comparative magnitude of mass change rates from two- and three-body collisions in Experiment B4. At 20 minutes (Figure 6-8) two-body collisions dominate, with one to two orders more mass change than from three-body collisions; however, at 180 minutes (Figure 6-9) the two-body and three-body rates are essentially the same magnitude but opposite sign. The relatively late occurrence of equality between the two forms of collision is consistent with the above observation that particle number equilibrium was not achieved as soon as median particle size equilibrium. Also noteworthy is that the equilibrium particle volume distribution peak (Figure 6-6) falls between 20 and 30 μm, coincident with the cross-over point for two- and three-body collision rates (Figure 6-9) at equilibrium. The significance of these results is discussed in Section 6.2.4.

6.2.3.2 Experiment B12

Results for Experiment B12, with the same hydrodynamic conditions but lower sediment concentration than B4 (0.05 to 0.8 kg/m^3), are given in Figures 6-10 to 6-15. In Figure 6-10 the calculated median diameter increases at first more slowly than the observed, then more rapidly, and reaches equilibrium size somewhat sooner than in the laboratory experiment. Figure 6-11 does not reveal the initial increase in particle numbers experienced in B4, perhaps because of a greatly diminished number of three-body collisions at the lower concentration. It does show that number concentration approaches equilibrium more rapidly than B4, which is attributed to the greater role of three-body collisions at the higher concentration.
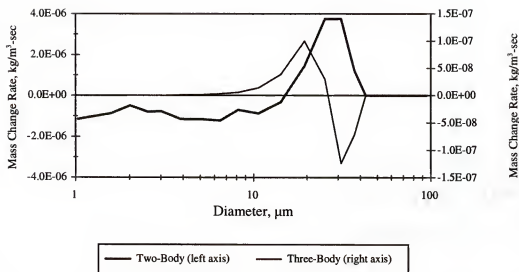
Figure 6-8. Experiment B4 mass change rates by two- and three-body collisions at 20 min.
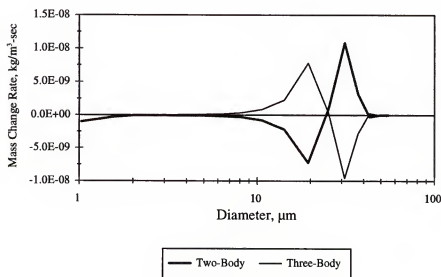
Figure 6-9. Experiment B4 mass change rates by two- and three-body collisions at 180 min.
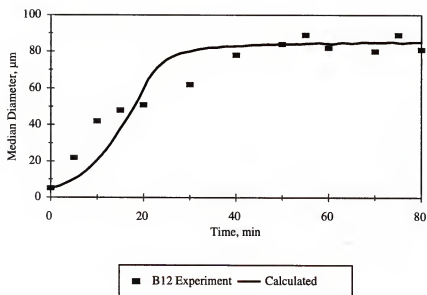
Figure 6-10. Observed and calculated median diameter time history for Experiment B12.
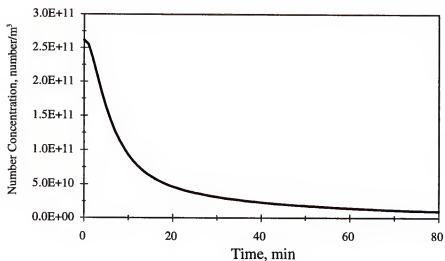
Figure 6-11. Calculated particle number concentration time history for Experiment B12.
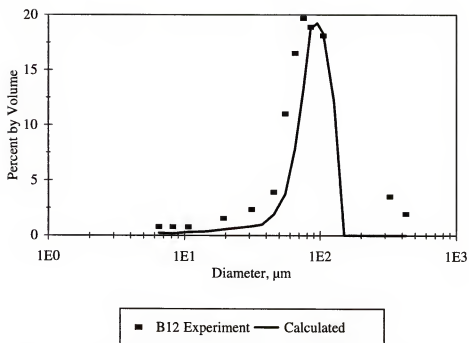
Figure 6-12. Experiment B12 observed and calculated particle size distribution at 80 min.
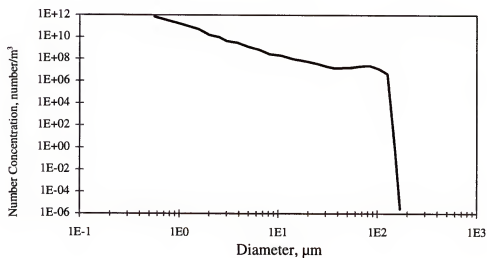
Figure 6-13. Experiment B12 calculated particle number distribution at 80 min.
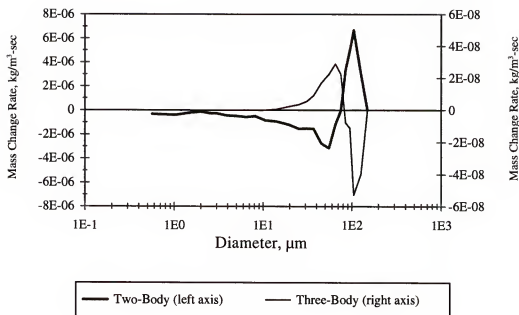
Figure 6-14. Experiment B12 mass change rate by two- and three-body collisions at 20 min.
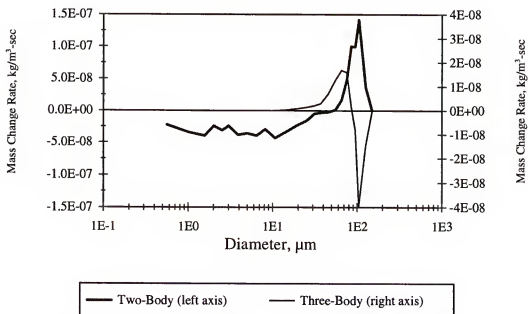
Figure 6-15. Experiment B12 mass change rate by two- and three-body collisions at 80 min.

Figures 6-12 and 6-13 show the particle size and number distributions for Experiment B12 at 80 min. The calculations reproduce the observed volume distribution much more closely than in Experiment B4, with the peaks agreeing in magnitude and nearly agreeing in location. However, as in B4, B12 falls off too sharply at the larger sizes.

Figures 6-14 and 6-15 compare two- and three-body collisions mass change rates at 20 min and 80 min. They repeat the trend noted in experiment B4—three-body collisions contributing orders of magnitude less mass change early in the experiment but increasing their relative contribution as time progresses. At size equilibrium they are roughly equal in magnitude and opposite in sign, with two-body collisions aggregating mass to 60 μm and larger sizes while three-body collisions are disaggregating those sizes and moving mass to smaller sizes. The difference in collision outcomes arises from the greater shear stresses imposed by three-body collisions for the same size particles (see Section 3.4.2).

6.2.3.3 Experiment E1

Figure 6-16 shows observed and calculated number concentration results for Experiment E1. Using values of the collision diameter function, F_c, as corrected by Equation 6-4, calculated aggregation was much too fast compared with the observed decline in concentration. Only when F_c was further reduced, to 20 percent of its calculated value, did the calculated aggregation rate approach the observed rate. The corresponding time history of median diameter is shown in Figure 6-17. The Detroit River expression for F_c (Equations 3-75 plus 6-4) drove the median size to an equilibrium diameter of about 120 μm in about 2 hr; however, using the reduced F_c slowed the growth dramatically, and the median diameter barely changed after 3 hr of aggregation. This result may be a reflection of the kaolinite's
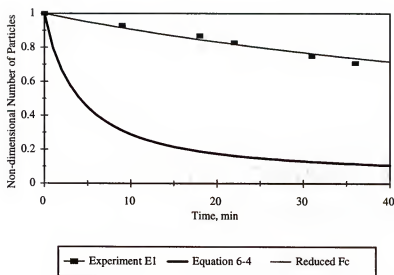
Figure 6-16. Experiment E1 particle number concentration history. Reduced F_c is 20 percent of Equation 6-4 value.
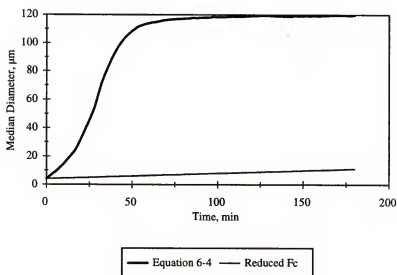
Figure 6-17. Experiment E1 median diameter growth history with F_c by Equations 3-75 and 6-4 and reduced to 20 percent of that value.

lower cohesion (indicated by lower CEC) compared with that of the Detroit River sediment. If so, a correction is needed to the aggregation efficiency, Equation 3-64, instead of F_c.

6.2.3.4 Experiment G1

Particle number concentration time history for Experiment G1 is shown for two time scales in Figures 6-18 and 6-19. Figure 6-18 compares 50 min of calculated number concentration with observations from the experiment, and it shows that the calculated aggregation rate is somewhat high when the Detroit River F_c is used, but approached the observed rate when F_c was reduced to 70 percent of the value obtained from Equations 3-75 and 6-4. At the longer time scale it can be seen that the suspension is not at equilibrium after 5 hr of calculations.

6.2.4 Discussion of Aggregation Chamber Results

The aggregation chamber results of the B, T, and G experiments suggest that the aggregation processes calculation method satisfactorily predicts the rate of aggregation and equilibrium median diameter for real mud in viscous flows such as are found in a Couette chamber, provided that the sediment can be adequately characterized as to density and strength. The E experiment showed very poor agreement, and that may be the effect of turbulent flow in the stirred chamber, error in initial distribution, or kaolinite's larger grain size and lower cohesion than other clay minerals.

In the chamber experiments equilibrium median diameter was reached well before particle number equilibrium occurred, since the volume contribution of the smallest particles was a tiny fraction of the largest particles.
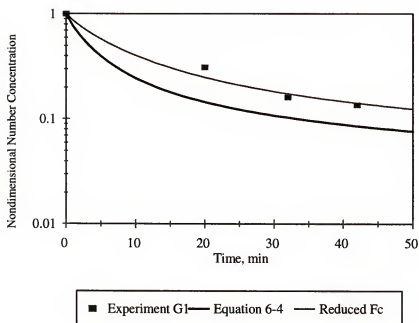
Figure 6-18. Observed and calculated particle number concentration history for Experiment G1 at 50 min. The reduced F_c is 70 percent of the value given by Equations 3-75 and 6-4.
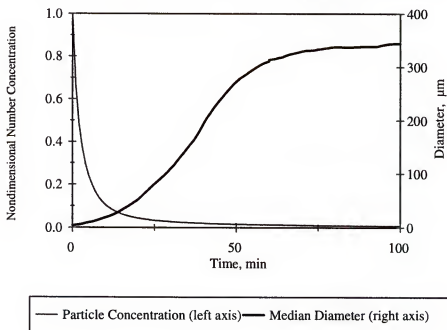
Figure 6-19. Calculated particle number concentration and median diameter for Experiment G1 at 5 hr.

The particle size distribution in these experiments lacked the larger sizes tail observed in the laboratory measurements. While adding a randomness factor to collision shear stresses improved the distribution shape, it was not sufficient to capture the variability in both collision forces and particle strengths. Adding more and smaller particle classes at the upper end might help, but at the expense of a greatly increased computational burden.

Applying Equation 6-4 as derived from Detroit River sediment experiments to kaolinite and Amazon Delta sediments was not a good approximation. Thus it seems that there is a sediment-specific aspect to the collision efficiency that is not captured by the variables of Equation 3-75. The results suggest that the sediment-specific aspect is exaggerated for kaolinite, or perhaps for any single mineral as opposed to natural muds (e.g., see Figure 3-13).

6.3 Flume Experiments

The method was tested against the kaolinite and Atchafalaya Bay mud depositional flume experiments' data described in Chapter 5, and against data from a San Francisco Bay mud flume experiment by Krone (1962). Experimental conditions for the calculations are summarized in Table 6-4.

Calculations were made with program Danu as described in the preceding section. Since the collision diameter function, F_c, required to calculate collision efficiency, is a function of equilibrium particle size in Equation 3-75, but affects aggregation rate and not the equilibrium size itself, the program was first run in aggregation-only mode (no deposition) to establish the equilibrium particle diameter for the experimental conditions,

which was then used in the depositional calculations to calculate the collision diameter

function, F_c. Equation 6-4 was used for f_c.

Table 6-4. Experimental conditions for flume calculations.

Number	Sediment	Initial Suspension Concentration kg/m³	Flow Depth m	Mean Velocity m/sec	Mean Shearing Rate sec⁻¹	Manning Bottom Roughness Coefficient	Mean Transit Time Through Flume min
W4	kaolinite	10.8	0.165	0.138	187	0.011	11
W5	kaolinite	11.4	0.178	0.173	313	0.011	8.8
W6	kaolinite	8.3	0.161	0.092	74.0	0.011	17
W9	kaolinite	2.2	0.159	0.093	98.5	0.011	17
W10	kaolinite	4.2	0.161	0.092	105	0.011	17
W11	Atchafalaya Bay mud	6.8	0.152	0.049	54.4	0.020	31
K	San Francisco Bay mud	0.78	0.304	0.113	52.8	0.011	4.0

6.3.1 Kaolinite Experiments

Initial conditions for this series consisted of the vertical sediment profiles for each

experiment as listed in Appendix D for Station 6.1 and the sediment size distribution given

in Figure 5-2.

Several particle density and strength equation combinations in the form of Equations

3-3 and 3-4 were tested. Equations 6-2 and 6-3 yielded a reasonably good comparison with

observed values for Experiment W4, so they were used for all five experiments.

Since program Danu calculates one-dimensional unsteady (z-t space) sediment concentration and deposition (Equations 4-1 through 4-7), the results were converted to the two-dimensional steady (z-x space) case by assuming that the coordinate system of Figure 4-1 moved down the flume at the mean flow speed of each experiment. Thus the time-varying results were converted to equivalent distances down the flume in order to directly compare observed and calculated values. This calculation assumes that the mean sediment velocity and mean water velocity are the same, which is a reasonably accurate approximation if the sediment is well mixed in the cross section and a rather poor one if it is not. The flume data showed little sediment stratification, but if a high concentration stirred layer did occur in the flume below the sampling points (Section 5.6.4), then the calculated concentration profiles will be artificially flattened. Further, if the stirred layer formed, dispersed, and reformed, the translation from time to space would be highly nonlinear.

Observed and calculated sediment concentration profiles over the length of the flume are shown for Experiments W4 to W10 in Figures 6-20 and 6-21, with time- and depth-mean laboratory observations depicted by solid squares and calculated depth-mean profiles by lines. Figure 6-20 shows the effect of flow speed, with roughly equal initial concentration Experiments W6, W4, and W5 shown in parts a, b, and c, respectively; and Figure 6-21 shows the effect of initial concentration, with roughly equal flow rate Experiments W6, W9, and W10 in parts a, b, and c, respectively.

Figures 6-20 and 6-21 show that the calculated curves lie above the observations and do not reproduce the observed nearly periodic variation with distance down the flume that was described in Chapter 5. Section 5.5.4 hypothesized that the observed concentration
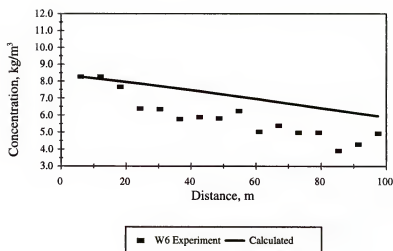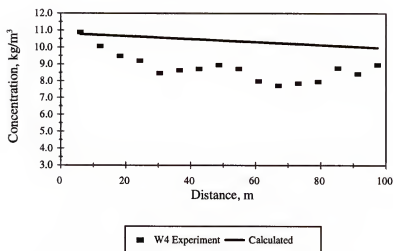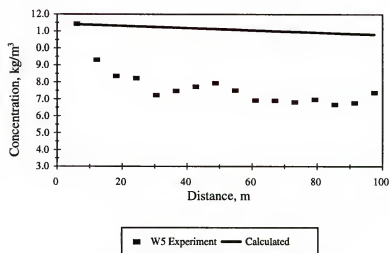
Figure 6-20. Observed and calculated concentration profiles along the flume.
a) Experiment W6; b) Experiment W4; c) Experiment W5.
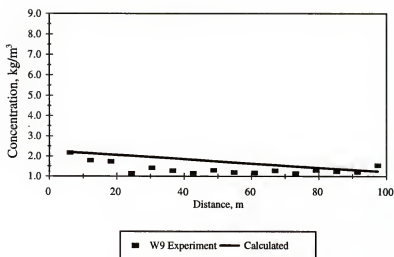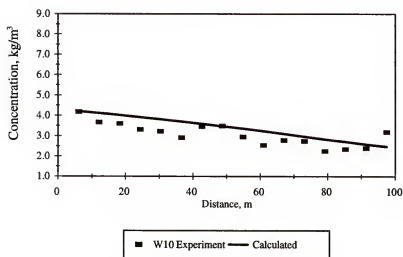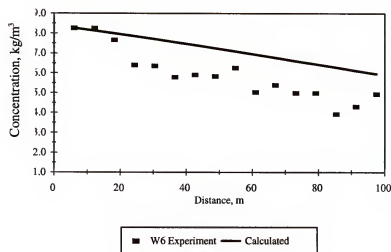
Figure 6-21. Observed and calculated longitudinal concentration profiles.
a) Experiment W9; b) Experiment W10; c) Experiment W6.

oscillations were spurious, an artifact of sampling points that did not capture a high concentration layer traveling near the bed and occasionally bursting up into the water column to be sampled. The calculated curves seem to parallel the observed values from about 20 m to the end of the flume, suggesting that the deposition rates are roughly equal after the first 20 m. If we assume that the 8 percent by mass of the kaolinite of size greater than 20 μm (Figure 5-2) is marginally cohesive and settles rapidly at the upper end of the flume, and shift the calculated concentration curves downward by that amount, they would skim slightly above and parallel to the observed points, consistent with the stirred layer hypothesis. However, the shift appears to increase for increasing flow rates (W4 and W5) and may reflect the inability of the time to space conversion (described above) to capture the true mean sediment travel speed in the presence of a stirred layer.

6.3.2 Atchafalaya Bay Mud

Figure 6-22 shows the longitudinal depth-mean concentration profile for Experiment W11, using Atchafalaya Bay mud. The mud had an initial size distribution (Figure 5-2) with a substantial (50 percent) fraction coarser than 20 μm that settled out in the first few feet of the flume, and the calculation captured at least a suggestion of that between 6 and 12 m; however, the calculation, like the kaolinite experiments above, did not assign an appropriate higher density to those larger particles, and they settled more slowly than their laboratory counterparts. In this case the deposition rate was less linear than in the kaolinite calculations, and the curve does not exactly parallel the observed concentration profile. In fact, the
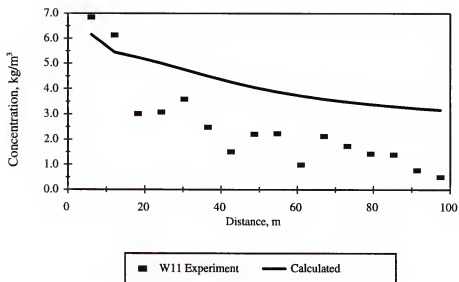
Figure 6-22. Observed and calculated longitudinal depth-mean concentration profile for Experiment W11, Atchafalaya Bay mud.
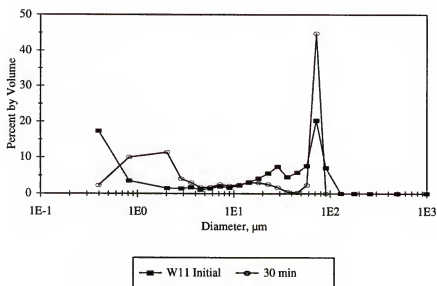
Figure 6-23. Initial and 30 min size distributions for Experiment W11, Atchafalaya Bay mud.

calculated profile flattens out toward the end of the flume, as opposed to the observed profile, which declines more rapidly toward the end.

Figure 6-23 shows the sediment size distribution at the beginning of the calculation and after 30 minutes, when a water-sediment parcel would have neared the end of the flume in Experiment W11. The distribution remains bimodal throughout the calculation, with the peak remaining at about 75 µm and the secondary peak moving toward larger sizes as ongoing aggregation pumps the smallest particles up the size distribution.

6.3.3 San Francisco Bay Mud

Experiment K was performed in a 30 m long and 1 m wide painted steel flume at the University of California, Berkeley (Krone, 1962). Water and sediment were recirculated by pumped flow through dual pipes, one 38 cm in diameter and one 30 cm in diameter.

The experimental procedure consisted of filling the flume to a depth of 0.3 m with water of 17 ppt salinity, then adding sediment as a slurry to a flow of about 1 m/sec until the concentration was about 1 kg/m^3. Once sediment addition was complete, the flow rate was reduced to the desired level and at intervals samples were taken from the return flow for analysis by filtration. In addition, graduated cylinder samples were dipped out of the one-third points of the flume for measurement of settling velocity.

The initial (dispersed) distribution of sediment sizes is shown in Figure 6-24. The sediment consisted predominantly of montmorillonite with illite and kaolinite and smaller amounts of halloysite and chlorite. It exhibited a CEC of 24 to 36 meq/100 gm (Krone, 1962; Mehta, 1973).
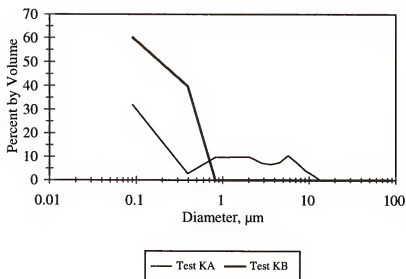
Figure 6-24. Assumed initial size distributions for tests KA and KB with San Francisco Bay mud. Test KA employed the original size distribution measured by Krone (1962).
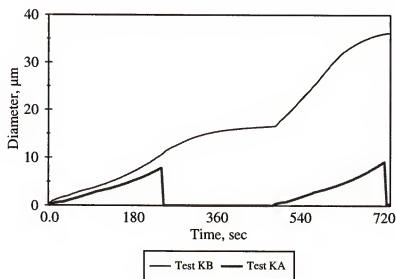
Figure 6-25. Median particle diameter evolution for test calculations KA and KB. The calculations were time-based, so can be considered to follow the flow as the suspension moves through the flume and recirculation pipe.

The calculation procedure consisted of two alternating hydrodynamic conditions: 243 sec (time of transit through the depositional length of the flume) of flow as listed in Table 6-4, followed by 236 sec of 0.17 m/sec return flow (through about 40 m of pipes). Wall shearing rates in the return flow pipe varied from 220 to 950 sec^{-1} (Krone, 1962), but will have been larger near the pump impellers. Two levels of shearing within the return flow were employed—in test calculation KA the return flow was assumed to exhibit a shearing rate of 950 sec^{-1} and in test KB the return flow was assumed to be sufficiently intense to completely disaggregate the sediment. Figure 6-24 shows the assumed initial distribution for test KB, and that distribution was reset for every period of return flow. Figure 6-25 illustrates the variation in median particle diameter that these two calculations produced.

The sequence of calculating with the flume flow condition, then the return flow condition as described above, was repeated for 170 hr, the length of the experiment. Particle density was calculated by Equation 3-3 with $B_p = 1650$ and $n_f = 2.6$ and particle strength by Equation 3-4 with $B_\tau = 200$ and $n_f = 2.2$.

Figure 6-26 shows the time history of observed and calculated depth-mean concentrations for Experiment K along with test calculations KA and KB. Test KA better reproduced the observed early period of rapid deposition, but in contrast to observations, continued that deposition rate until the sediment supply was virtually exhausted within 50 hr. Test KB deposited somewhat too slowly for the first few hours but then more closely reproduced the long, slow concentration decline observed in the laboratory experiment.
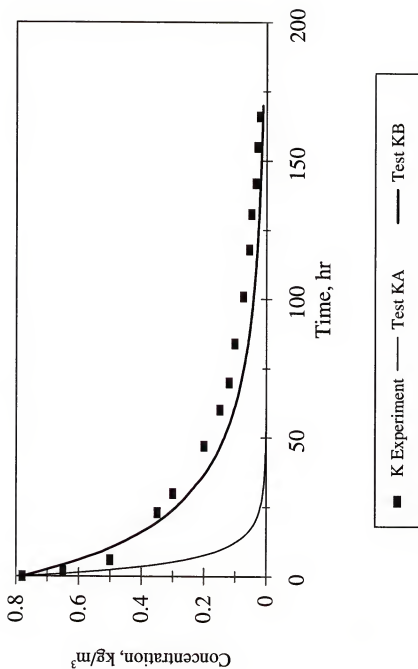
Figure 6-26. Observed and calculated time history of mean concentration in Experiment K, San Francisco Bay mud. Test KA was run with cyclic shear stresses representing flume flow and return flow beginning with the original size distribution shown in Figure 6-24. The test KB cycle consisted of the disaggregated distribution shown in Figure 6-24 at the flume inlet and then aggregation and deposition under flume flow conditions. Source of observed data: Krone (1962).

While both tests KA and KB used simplistic approximations to the return flow, they should have bracketed the effects of the return flow pump and pipes on aggregation processes. These results imply that either the calculated aggregation and deposition rates were too high or that the laboratory recirculation system thoroughly disaggregated the suspended sediment before reintroducing it into the flume. Since the calculation method seemed to under-predict Experiment W11 aggregation-deposition, the disaggregation explanation seems the more plausible for Experiment K. The remaining differences between observed and calculated concentration histories may be attributed to inaccuracy of the density and strength relationships at the smaller particle sizes (see Figures 3-2 and 3-3) or the simplifications involved in the one-dimensional deposition calculation.

Figure 6-27 illustrates the computed suspension mean settling velocity (mean of sum of the product of class settling velocity and class mass concentration over depth and classes) for the duration of test KB. It shows the instantaneous settling velocity ranged from 6.8×10^{-7} to 4.8×10^{-4} m/sec as the particles aggregated and disaggregated during the alternating flume and return flows, and the time-mean value gradually declined as the aggregation rate fell with declining concentration. These values bracket the 6.6×10^{-6} to 2.8×10^{-5} m/sec range calculated and inferred by Krone (1962) for flows similar to, but not exactly the same as those used in the calculations.

6.3.4 Discussion of Flume Results

Comparison of calculations with the flume experiment data provided mixed results. They clearly showed that the deposition algorithm needed a parallel noncohesive sediment
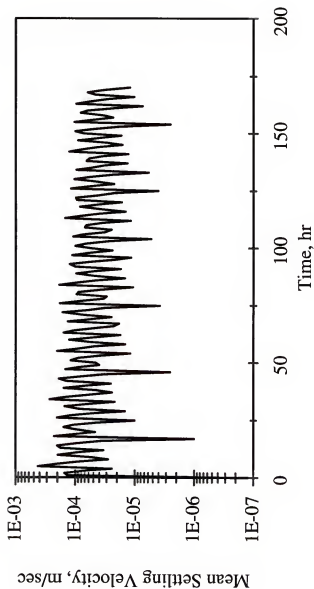
Figure 6-27. Variation of suspension mean settling velocity for test KB. The oscillations represent cyclic aggregation and disaggregation as the suspension moved through the flume and return flow pipes, respectively, but have been aliased to false frequencies by a 1 hr sampling interval in this plot.

calculation, in which the larger size classes had higher densities than the aggregates and were not subject to disaggregation. They indicate that the aggregation calculations improve the deposition calculations by moving sediment mass up into larger, more depositable size classes, but separating the effects of the deposition calculations from those of aggregation is not straightforward.

6.4 Exploratory Calculations

Calculations were performed to explore relationships among sediment concentration, flow shearing, equilibrium diameter, time to equilibrium, and particle size distribution. The test sediment was assumed to have characteristics of the San Francisco mud tested in the preceding section. Thirty-five sediment classes were employed as shown in Table 6-5.

6.4.1 Effect of Flow Intensity and Sediment Concentration

Calculations were made for a representative range of sediment concentrations and shearing intensities, the latter expressed as the energy dissipation rate, which can be related to shearing rate by Equation 3-12.

Figures 6-28 and 6-29 show time histories of the median particle diameter (by volume) and particle number concentration for a mass concentration of 1 kg/m^3 and energy dissipation rates of 100 and 2×10^{-4} m^2/sec^3, respectively. At the higher energy dissipation rate particle size equilibrium occurred within 30 min and number concentration equilibrium occurred within 4 hr; however, at the lower rate neither measure was in equilibrium at 10 hr.

Table 6-5. Sediment Classes and Characteristics for Exploratory Calculations.

Class Number	Representative Diameter μm	Minimum Mass kg	Representative Mass kg	Maximum Mass kg	Density kg/m³	Settling Velocity m/sec	Shear Strength Pa
1	0.0908	0.00e+00	1.04e-18	1.39e-18	2650	7.34e-09	672
2	0.392	1.39e-18	6.21e-17	1.23e-16	1965	8.01e-08	174
3	0.821	1.23e-16	4.98e-16	8.73e-16	1721	2.60e-07	83.1
4	2.02	8.73e-16	6.51e-15	1.21e-14	1506	1.10e-06	33.8
5	2.87	1.21e-14	1.79e-14	2.36e-14	1441	1.93e-06	23.8
6	3.62	2.36e-14	3.47e-14	4.59e-14	1403	2.79e-06	18.9
7	4.55	4.59e-14	6.76e-14	8.93e-14	1368	4.03e-06	15.0
8	5.73	8.93e-14	1.32e-13	1.74e-13	1337	5.82e-06	11.9
9	7.22	1.74e-13	2.57e-13	3.40e-13	1308	8.41e-06	9.46
10	9.10	3.40e-13	5.03e-13	6.66e-13	1282	1.22e-05	7.50
11	11.5	6.66e-13	9.85e-13	1.30e-12	1258	1.77e-05	5.96
12	14.4	1.30e-12	1.93e-12	2.56e-12	1236	2.55e-05	4.73
13	18.1	2.56e-12	3.79e-12	5.02e-12	1216	3.69e-05	3.76
14	22.8	5.02e-12	7.45e-12	9.87e-12	1198	5.32e-05	2.99
15	28.7	9.87e-12	1.47e-11	1.95e-11	1181	7.69e-05	2.37
16	36.2	1.95e-11	2.89e-11	3.83e-11	1166	1.11e-04	1.89
17	45.6	3.83e-11	5.71e-11	7.60e-11	1153	1.60e-04	1.50
18	57.4	7.60e-11	1.13e-10	1.49e-10	1140	2.33e-04	1.19
19	72.2	1.49e-10	2.22e-10	2.95e-10	1129	3.35e-04	0.945
20	90.9	2.95e-10	4.39e-10	5.83e-10	1118	4.81e-04	0.751
21	123	5.83e-10	1.08e-09	1.58e-09	1106	7.75e-04	0.554
22	162	1.58e-09	2.46e-09	3.34e-09	1096	1.19e-03	0.421
23	202	3.34e-09	4.70e-09	6.05e-09	1089	1.65e-03	0.338
24	242	6.05e-09	8.00e-09	9.95e-09	1083	2.16e-03	0.282
25	293	9.95e-09	1.42e-08	1.85e-08	1078	2.83e-03	0.233
26	341	1.85e-08	2.23e-08	2.62e-08	1074	3.50e-03	0.200
27	381	2.62e-08	3.10e-08	3.58e-08	1071	4.05e-03	0.179
28	455	3.58e-08	5.28e-08	6.97e-08	1067	5.08e-03	0.150
29	554	6.97e-08	9.48e-08	1.20e-07	1062	6.39e-03	0.123
30	714	1.20e-07	2.01e-07	2.83e-07	1057	8.44e-03	0.0956
31	911	2.83e-07	4.17e-07	5.51e-07	1053	1.09e-02	0.0749
32	1300	5.51e-07	1.20e-06	1.85e-06	1047	1.51e-02	0.0526
33	1780	1.85e-06	3.10e-06	4.36e-06	1043	1.99e-02	0.0382
34	2600	4.36e-06	9.51e-06	1.47e-05	1038	2.69e-02	0.0263
35	9570	1.47e-05	4.71e-04	9.28e-04	1027	6.27e-02	0.00713
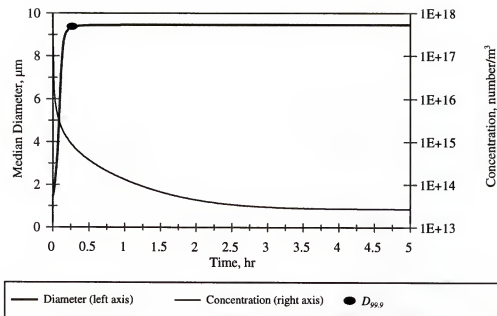
Figure 6-28. Median diameter and particle concentration time history for San Francisco Bay mud aggregating at 1 kg/m^3 and 100 m^2/sec^3.
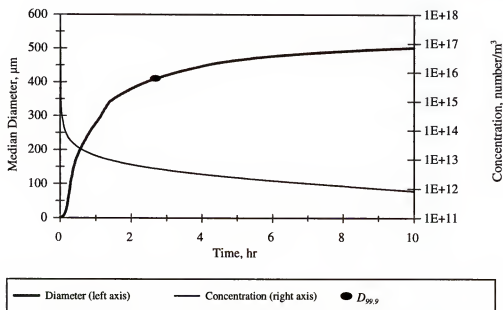
Figure 6-29. Median diameter and particle concentration time history for San Francisco Bay mud aggregating at 1 kg/m^3 and 2×10^{-4} m^2/sec^3.

In an estuarial environment, where flow conditions will change significantly within 2 hr, more than 10 hr to equilibrium is essentially meaningless; therefore, for present purposes a near-equilibrium size was arbitrarily defined as that diameter for which the change in one minute was less than 0.1 percent of the diameter. That value, designated as $D_{99.9}$, is plotted as a point on both Figures 6-28 and 6-29, and it is clearly a better approximation of the high energy dissipation rate equilibrium diameter than it is for the lower value. It is also dependent on the sediment size classification scheme. Despite these limitations, it is a useful indicator of aggregate size for a particular estuarial flow condition. The time required for the median diameter to reach $D_{99.9}$ is designated $T_{99.9}$.

The rate of aggregation is shown in size distribution form in Figure 6-30 for typical estuarial conditions of 0.1 kg/m^3 concentration and 0.01 m^2/sec^3 energy dissipation rate (shearing rate of about 21 sec^{-1}). Figure 6-30a displays the initial distribution for the sediment and the ensuing distribution at 0.25, 0.5 and 1 hr. The progression of the distribution moving to larger sizes and growing more peaked is essentially a more skewed version of Kranck's (1973) experimental portrayal of the process (Figure 2-2). As noted in the previous section, the randomness factor does not produce a symmetrical distribution. The skewness is consistent with the natural spectra of Figure 2-3, which also show a sharp drop off at larger sizes, but that may be due to deposition of larger particles, which was not calculated for the results shown in Figure 6-30.

Figure 6-30b continues the time progression for the example distribution, and it can be seen that the distribution changes very little after 1 hour. For this calculation $D_{99.9} = 211$ µm and $T_{99.9} = 1.4$ hr.

a)

Legend: t=0 hr, t=0.25 hr, t=0.5 hr, t=1 hr

b)

Legend: t=1 hr, t=2 hr, t=4 hr, t=8 hr
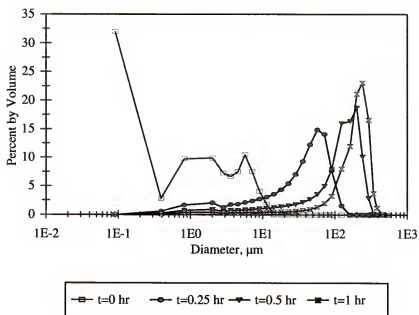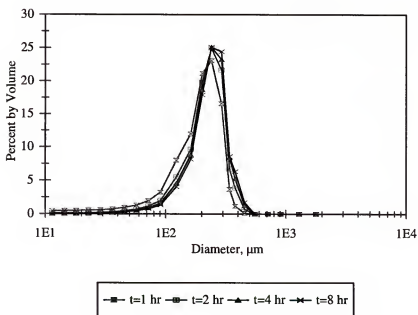
Figure 6-30. Time (t) evolution of size distribution for San Francisco Bay mud at C = 0.1 kg/m³ and ϵ = 0.01 m²/sec³. Compare with Figure 2-2.
a) Times t = 0 to 1 hr; b) Times t = 1 hr to 8 hr.

Figure 6-31 displays calculated results for a sediment concentration of 0.1 kg/m^3 and energy dissipation rate ϵ ranging from 1×10^{-6} to 100 m^2/sec^3, representing the range of typical flow conditions encountered in United States estuaries. Figure 6-31a shows the variation of $D_{99.9}$ with ϵ, and Figure 6-31b shows the variation of $T_{99.9}$ with ϵ. In Figure 6-31a $D_{99.9}$ is a maximum, about 500 μm, for the lowest value of energy dissipation, 1×10^{-6} m^2/sec^3(corresponding to a shearing rate of 0.2 sec^{-1} and a flow speed on the order of a few cm/sec), then decreases with increasing energy dissipation as a consequence of more forceful collisions disaggregating larger particles. For ϵ between 1×10^{-4} and 1×10^{-3} m^2/sec^3 $D_{99.9}$ plateaus and even rises slightly as a consequence of the competing contributions of shear-induced versus differential settling collisions and the competing disaggregating forces of two-body versus three-body collisions (see Section 3.4.2). For ϵ above 1×10^{-3} m^2/sec^3, $D_{99.9}$ decreases rapidly as shear-induced collision stresses dominate the process and limit the maximum particle size.

In Figure 6-31b the time to reach $D_{99.9}$ is seen to increase with energy dissipation increasing from 1×10^{-6} m^2/sec^3 as disaggregation begins to play a significant role and slows down the net aggregation rate, peaks at about 1×10^{-5} m^2/sec^3, and then declines as the effect of an increasing number of collisions and smaller equilibrium size overcomes the disaggregation effect. The break in slope at about 1×10^{-3} m^2/sec^3 corresponds to the size plateau noted in Figure 6-31b above and is attributable to the same causes. At the highest energy dissipation rate of 100 m^2/sec^3 (characteristic of near-bed flow speeds greater than 1 m/sec) the near-equilibrium size is small, about 10 μm, and is reached within 20 min.

a)

b)
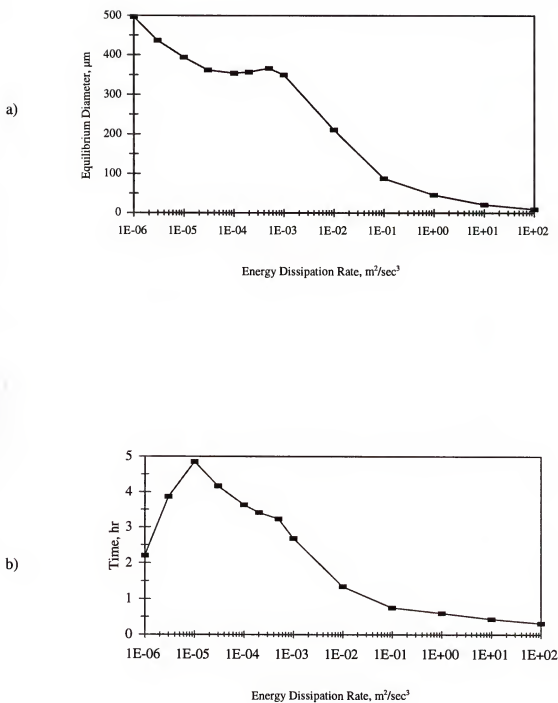
Figure 6-31. Aggregate near-equilibrium size and time variation for 0.1 kg/m^3 concentration. a) Near-equilibrium diameter, $D_{99.9}$; b) Time to near-equilibrium, $T_{99.9}$.

The combined effects of energy dissipation rate and sediment concentration on $D_{99.9}$ and $T_{99.9}$ are shown in Figures 6-32 and 6-33, respectively. Figure 6-32 shows that $D_{99.9}$ is only weakly dependent on concentration at lower energy dissipation rates and nearly independent of concentration at the highest energy dissipation rates, but, in general, $D_{99.9}$ increases with increasing concentration and decreasing flow intensity. Figure 6-33 displays the somewhat more complicated behavior of $T_{99.9}$, notably that a maximum occurs between $\epsilon = 1 \times 10^{-5}$ and 1×10^{-4} m²/sec³ (corresponding to shearing rates of about 0.6 to 2 sec⁻¹). For energy dissipation rates greater than that, $T_{99.9}$ decreases with increasing flow intensity. For energy dissipation rates lower than that, $T_{99.9}$ decreases with decreasing flow intensity. Over the tested range, $T_{99.9}$ decreases with increasing concentration, but the curve displays a saddle shape, with a plateau in the middle range of concentration caused by the increasing role of three-body collisions to the process with increasing concentrations.

Figure 6-34 displays the results of the preceding two figures in a slightly different manner, as a kind of aggregational speed given by $D_{99.9}$ divided by $T_{99.9}$. It shows that the speed at which aggregates grow increases slightly with increasing concentration at high flow intensities but sharply at low intensities where three-body collisions contribute more to aggregation than to disaggregation. It shows that aggregation speed is highest at low flow intensities where most or all collisions produce aggregation, decreases with increasing flow intensity as disaggregation begins to play a role, then rises to a local maximum at about 0.01 m²/sec³ (about 20 sec⁻¹ shearing rate) as the collision rate increases faster than the disaggregation rate, then falls once more as disaggregation becomes dominant.
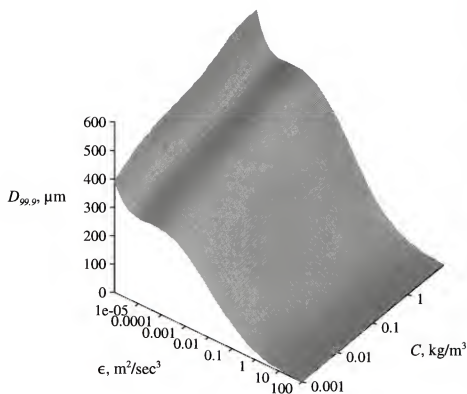
Figure 6-32. Near-Equilibrium Diameter, $D_{99.9}$, for San Francisco Bay mud as a function of flow energy dissipation rate, ϵ, and sediment concentration, C.
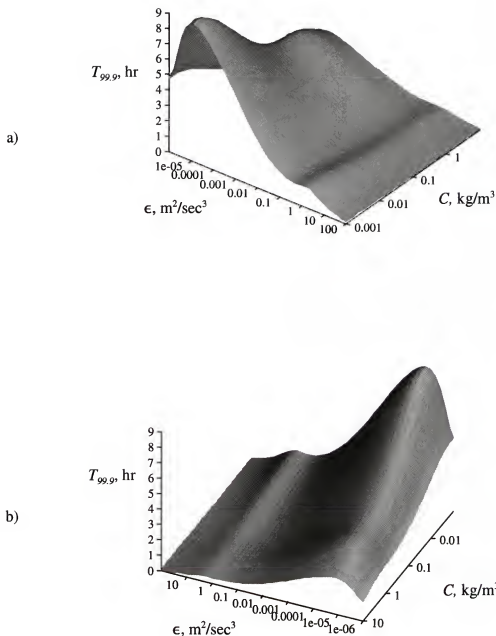
Figure 6-33. Time, $T_{99.9}$, to near-equilibrium diameter for San Francisco Bay mud as a function of energy dissipation rate, ϵ, and sediment concentration, C.
   a) View from negative C and positive ϵ quadrant; b)View from positive C and negative ϵ quadrant.
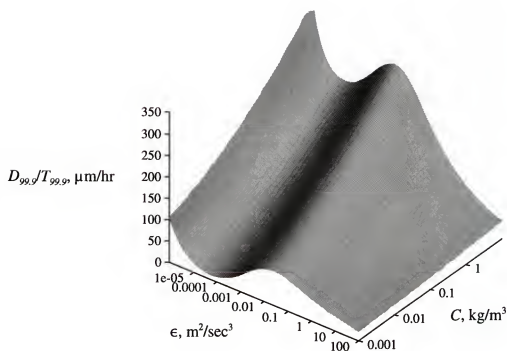
Figure 6-34. Aggregation speed, $D_{99.9}/T_{99.9}$, for San Francisco Bay mud as a function of flow energy dissipation rate, ϵ, and sediment concentration, C.

The results of Figures 6-30 through 6-34 show that for a sediment with the tested characteristics:

1. Near-equilibrium particle size, $D_{99.9}$, tended to be approximately proportional to mass concentration and inversely proportional to energy dissipation rate.

2. Time to near-equilibrium, $T_{99.9}$, had a local maximum at small, but nonvanishing energy dissipation rates. Below that flow intensity level, it was proportional to flow intensity and inversely proportional to concentration. Above that maximum it was inversely proportional to both flow intensity and concentration.

3. For $\epsilon > 0.01$ m^2/sec^3, equilibrium size was essentially independent of sediment concentration between 0.001 and 10 kg/m^3 .

4. For $\epsilon > 0.01$ m^2/sec^3 time to equilibrium is relatively insensitive to both energy dissipation rate and concentration.

Figure 6-32 does not wholly confirm Dyer's (1989) aggregate size plot (Figure 2-5). Like Figure 2-5, it shows the aggregate size rising to a maximum at low stresses and high concentrations, but does not show a relatively sharp drop at still lower stresses. The difference may lie in the way stresses are portrayed, for Figure 2-5 plots size against shearing rate alone; whereas, the results used for Figure 6-32 included shearing plus Brownian motion and differential settling, which become prominent at the lowest energy dissipation rates (see Figure 3-6).

6.4.2 Effect of Salinity

Aggregation-only calculations were performed for a constant sediment concentration of 0.1 kg/m^3, constant energy dissipation rate of 0.01 m^2/sec^3, and for salinities ranging from 0.25 ppt to 35 ppt. The near-equilibrium particle diameter, $D_{99.9}$, was about 212 μm for all

tested salinities greater than 0.5 ppt. At 0.25 ppt, it was 202 μm. Figure 6-35 shows the median diameter growth with time for three salinity values, and it appears that for the complete range of salinities $D_{99.9}$ converges on the same equilibrium diameter, albeit at different speeds.

Figure 6-36 shows the variation of $T_{99.9}$ with salinity, and it dramatically displays the strong effect of salinity on aggregation rate for salinities less than 2 ppt and the relative insensitivity of rate above 2 ppt. The curve has been plotted at two scales to show both the five-fold range of times and the more subtle salinity effect up to about 10 ppt. insensitivity of rate to salinities above 2 ppt. The curve has been plotted at two scales to show both the five-fold range of times and the more subtle salinity effect between 2 and 10 ppt.

The results of Figures 6-35 and 6-36 are not new information, but instead confirm prior observations (e.g., Krone, 1986) and reflect the assumptions made in Chapter 3. They do not preclude the possibility of a further salinity effect on particle strength or density.

6.4.3 Effect of Three-body and Four-Body Collisions

A set of aggregation-only calculations were performed for the same constant sediment concentration of 0.1 kg/m^3 and constant energy dissipation rate of 0.01 m^2/sec^3 described in the preceding section, with salinity of 35 ppt and with three-body collisions turned off. In Figure 6-37 the results are compared with the same calculations with three-body collisions turned on. It shows the two calculations with growth rates essentially identical during the first quarter-hour, then diverging. They approach the same equilibrium diameter of about 225 μm, but the two-body-only calculations approach equilibrium more rapidly, since the
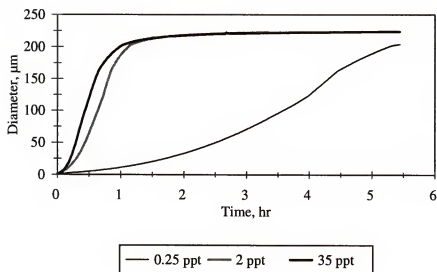
Figure 6-35. Time history of particle growth for three solution salinities.
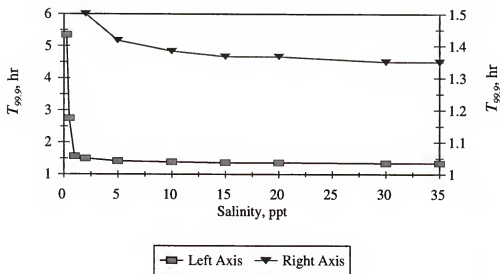
Figure 6-36. Time to near-equilibrium diameter as a function of salinity. The same curve is plotted twice, once against the left axis to show the complete range of values and again against the right axis to better display the effect near 5 ppt.
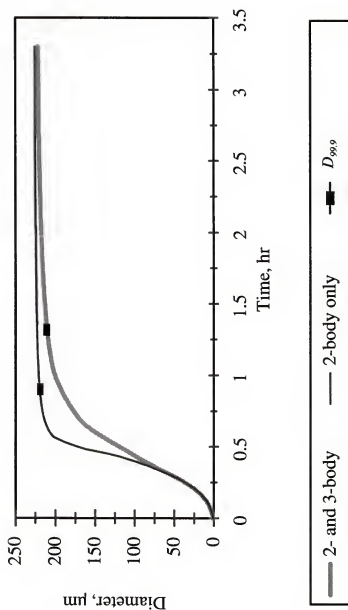
Figure 6-37. Median particle diameter history for $\epsilon = 1 \times 10^{-2}$ m^2/sec^3 and $C = 0.1$ kg/m^3 with and without considering three-body collisions. The solid square shows the value of $D_{99.9}$ for each—211 μm at 4860 sec with both two- and three-body collisions and 219 μm at 3120 sec with two-body collisions only.

more energetic three-body collisions contribute more to disaggregation than to aggregation, reaffirming the observations of Burban et al. (1989). The two-body-only calculations produced a near-equilibrium diameter of 219 µm while the two- and three-body calculations gave a value of 211 µm, both of which are indicated on the plot.

These results demonstrate that if the equilibrium diameter or the aggregation rate in the initial minutes of aggregation in a dispersed suspension is the desired result, the less computationally intensive two-body-only calculations will be suitable; however, if the rate of aggregation in a suspension approaching equilibrium is needed, the more rigorous two- and three-body collision calculations are needed.

Equation 3-29 and Table 3-2 showed that the number of four-body collisions will be a small fraction (1 percent or less) of the number of three-body collisions, which are themselves a small fraction (5 percent or less) of the number of two-body collisions in a sediment suspension. The mass change rate associated with four-body and higher order collisions was not calculated, but is expected to be a minor factor in the aggregation rate, for each successive increase in order will contribute progressively fewer collisions and bring proportionately less additional mass to the collision than the next lower order.

CHAPTER 7
CONCLUSIONS

7.1 Summary

Estuarial fine sediments make both positive and negative contributions to the coastal environment, and present significant challenges to conservation and management of water resources. As only one example of sediment challenges, the United States spends more than $500,000,000 annually in dredging excess sediment from navigable waterways, yet valuable wetlands are being lost to subsidence and erosion because of diminished sediment supply. (See Section 1.1.) Despite the economic and environmental importance of sediment transport, the tools available to water resource managers are seriously deficient in their ability to predict transport of fine sediments. Among those deficiencies is a limited understanding of the processes by which fine estuarial sediments aggregate and disaggregate as they are transported in suspension.

Estuarial sediments range in size from less than 1 μm to more than 4 mm, but the finer than 63 μm fraction dominates most estuaries. Fine sediments consist of mineral and nonmineral grains plus organic materials and demonstrate increasing interparticle cohesion with decreasing grain size below 40 μm. Individual grains are typically too small to settle under their own weight, and will remain suspended indefinitely unless they aggregate into larger particles.

261

Cohesion of individual grains, arising from molecular-scale physico-chemical attractive forces, causes colliding grains to bond and form aggregates and is a controlling factor in fine sediment transport, deposition, and erosion. Aggregation processes are affected primarily by sediment character (e.g., grain size and mineralogy), sediment concentration, fluid characteristics (e.g., salinity, temperature, and pH), and flow conditions (e.g., shearing rate). Colliding particles will bond and aggregate if their internal strength is greater than the forces imposed by the collision. Particle strength varies with density, and density varies inversely with size, since aggregates include substantial fluid-filled pore space.

As particles become larger by aggregating, they may attain settling velocities large enough to settle toward the bed. Settling leads to stratification of the suspension and high concentrations near the bed, where deposition may occur if the strength of the bonds within aggregates and between aggregates and the bed exceed the shearing stresses imposed by the flow. If flow-imposed stresses become large enough to exceed the strength of bonds among particles in the bed, erosion will occur.

The primary objective of this work is to develop an improved linkage between fine sediment aggregation and the sediment and flow characteristics that govern it. In pursuit of that objective, a combination statistical and deterministic, physics-based representation of fine sediment aggregation and deposition has been developed. The spectrum of particle sizes is represented by a discrete number of classes based on particle mass. Aggregation moves mass up through the classes, and disaggregation moves it down through the classes. Particle density and strength are expressed in terms of a fractal power law relationship to diameter. The number of particle collisions is expressed by simple statistical relationships, using a new

collision efficiency parameter that is defined by a number of nondimensional terms accounting for the physical and chemical forces that influence whether close encounters of particles become collisions. Particle collisions by Brownian motion, shearing, and differential settling may cause aggregation if the colliding particles' strength exceeds stresses imposed by the collision, or both aggregation and disaggregation if collision stresses exceed one or more of the particles' strengths. A small set of possible deterministic outcomes is defined on the basis of shear stresses and strengths and those outcome possibilities are used in concert with the collision theory to calculate the rate of change of sediment mass for each class.

Three aspects of the aggregation representation are new. First, the time-mean collision efficiency parameter, which has traditionally been a tuning factor varying by up to four orders of magnitude, has been shown to be a relatively well-behaved function of dimensionless terms employing particle mass, particle velocity, grain size, salinity, temperature, and cation exchange capacity. Second, the probability of three-body collisions has been explicitly formulated and included in the calculation method. Third, the outcomes of collisions have been defined as a set of mechanistic events which are converted to the probabilistic domain by a standard method.

A solution of the one-dimensional convection-diffusion equation for multiple grain sizes with class-by-class deposition calculations was combined with the new aggregation calculation method to provide a test vehicle for the method. In this approach, as large aggregates settle to the bed to deposit or disaggregate, new ones are created to replace them,

providing a continuous source of depositable particles. A simple computer program was written to make the combined aggregation and deposition calculations.

A series of kaolinite clay and Atchafalaya Bay mud deposition experiments were conducted in a 100-m-long flume with initial sediment concentrations ranging from 2 to 10 kg/m^3 and mean flow speeds ranging from 4.9 to 17.3 cm/sec. Water surface elevation, velocity, and vertical and longitudinal suspended sediment concentration profiles were measured, and bottom deposit thickness was estimated.

Significant variability in suspended sediment concentrations occurred in the experiments and is attributed in part to operational and measurement errors, but can also be plausibly explained as intermittent perturbation and upward mixing of a high concentration layer flowing close to the bed, below the lowest sampling point. If such a layer occurred in the flume, it can be interpreted as a stirred layer, a thin (order of mm) intense mixing zone of high sediment concentration (Section 2.5.1).

Deposition rate decreased with increasing concentration and increasing flow speed. The former is attributed to a decrease in settling velocity associated with hindered settling. The latter is attributed to higher bed shear stresses and more vigorous mixing at higher flow speeds and also to decreased mean aggregate size, which is inversely proportional to shearing rate (Sections 2.4.4.2 and 6.4).

The aggregation calculation method was applied to two categories of laboratory experiments—aggregation chamber experiments with no deposition, and flume experiments in which both aggregation and deposition were occurring. The method was tested for commercial kaolinite and mud from the Detroit River, Atchafalaya Bay, San Francisco Bay,

and the Amazon River Delta. The method was found to accurately predict the aggregation rate for Detroit River sediments, but to over-predict the aggregation rate of kaolinite and Amazon Delta mud. The method predicted the overall deposition rate reasonably well for the finest fraction of kaolinite, Atchafalaya Bay mud, and San Francisco Bay mud, but did not capture the deposition of silt-size particles in those suspensions. The experimental results suggest that the method better predicts the behavior of natural muds than that of kaolinite.

7.2 Conclusions

The following conclusions are drawn with respect to the fine sediment aggregation and deposition calculation method developed here:

1. The aggregation processes representation described in Chapter 3 offers three improvements over previous methods of calculating fine sediment aggregation—a deterministic functional parameterization of particle collision efficiency, an explicit statistical accounting for three-body collisions, and a set of mechanistic collision outcomes.

2. Replacing collision efficiency with two parameters—a new collision diameter function, F_c, given by Equations 3-75 and 6-4, and an aggregation efficiency, given by Equation 3-64, provides a rational method for calculating aggregation rates. However, Equation 6-4 may be sediment specific and not generally applicable.

3. Explicitly accounting for three-body collisions via Equation 3-23 provides a more realistic calculation of aggregation processes than if they are omitted, albeit at the cost of substantially increased calculation effort. Four-body and higher order collisions are not expected to play a substantial role in aggregation rate.

4. The finite set of collision outcomes and their criteria given by Equations 3-40 through 3-61 provide a reasonable simplification of the complex process of bonding and fragmenting aggregates while retaining a physical basis.

5.   The value of the proposed aggregation calculation method of Chapter 3 has been demonstrated by testing it against aggregation chamber experimental data for laminar shearing rates of 100 to 600 sec^{-1}, sediment concentrations of 0.1 to 0.8 kg/m^3, and salinities ranging from freshwater to ocean salinity.

6.   The value of the multi-class combined aggregation and deposition algorithm of Chapter 4 has been demonstrated by testing against flume experimental data for turbulent flow shearing rates of 50 to 300 sec^{-1}, sediment concentrations of 0.8 to 11 kg/m^3, and salinities of fresh water and 17 ppt. It did not accurately describe the deposition of the silt fraction in the tested muds.

7.   The aggregation processes calculation method presented here is suitable for use as a primary component of sediment transport computations via numerical modeling; however, it is computationally intensive. To avoid adding to the computational burden, it may be effectively used as an analytical tool to develop improved parametric models of aggregation processes and as a interpolative companion to laboratory and field investigations.

The following conclusions are drawn with respect to fine sediment aggregation processes in typical estuarial flow conditions:

1.   The aggregation rate for two specified particle sizes is proportional to the number concentration of both particles, elemental grain size, salinity, and cation exchange capacity; and inversely proportional to temperature, particle Reynolds Number, and the ratio of the larger to the smaller particle masses; and can be expressed by a power law relationship to parameters based on those variables.

2.   The number of three-body collisions is small with respect to two-body collisions at typical estuarial sediment concentrations, but they contribute significantly to aggregation processes in three ways:

    a.   Because they involve 50 percent more mass, on average, than two-body collisions, they contribute more to the aggregation process per collision than do two-body collisions.

    b.   In suspensions with a median particle diameter larger than about 100 μm they slow the aggregation process by disaggregating collisions among the largest particles.

    c.   In suspensions that are near an equilibrium between aggregation and disaggregation, the greater collisional stresses imposed by three-body collisions tend to disaggregate the largest particles and move mass downward

in the size spectrum, while two-body collisions move the mass upward in size. The balance between the two processes establishes the equilibrium size distribution, and the median size occurs near the size at which two-body and three-body collision mass change rates cross from negative to positive.

3. Aggregate median size generally approaches equilibrium more rapidly at higher rates of flow energy dissipation (and shearing) and higher fine sediment concentration, but at very low flow intensities the aggregation speed exhibits local maxima and minima. The particle concentration distribution itself approaches equilibrium more slowly than does the median diameter, because the smallest particles can be numerous yet aggregate slowly and make only a minor contribution to total volume concentration.

4. Equilibrium median aggregate size is proportional to sediment concentration and inversely proportional to flow shearing intensity.

5. The tested natural muds' behavior was more readily predictable than the single mineral kaolinite. Based on the experiences of other researchers (see Figure 3-13) the same might be said of other pure clays. A possible explanation of this phenomenon is that metal and oxide coatings on natural sediment grains produces more uniform cohesion (Section 3.5.1.2).

7.3 Recommendations

Several aspects of the aggregation processes description presented here need improvement through future research and development. Needs include:

1. An update of the collision diameter function, F_c, based on new laboratory data that fill the gaps in presently available data as shown in Figure 3-14.

2. A generalized, not sediment-specific version of the collision diameter function term f_c (Equation 6-3).

3. A density-based expression for particle interpenetration distance factor, F_p (Section 3.3.1).

4. General (not sediment-specific) statistical descriptors of aggregate density and strength (Equations 3-3 and 3-4), including an evaluation of the role of organic materials, and a statistical distribution of collision-imposed shear stresses.

5.　Evaluation and possible incorporation of particle collisions induced by filter-feeding organisms in estuarine waters.

6.　An explanation of the behavioral differences between single mineral sediment and estuarine muds.

7.　A computationally more efficient formulation of the calculations of the aggregation processes representation presented here.

8.　Implementation into a three-dimensional numerical transport model of the multi-class aggregation calculation method presented here.

The aggregation processes calculation method presented here will provide a significant improvement to the tools available to those charged with conserving and managing water resources where fine sediments constitute a significant challenge. A production-level application of the aggregation calculations will require that they be incorporated in a three-dimensional, coupled hydrodynamic and multi-grain-size sediment transport model. Such models (without the detailed aggregation computations) are available (e.g., Stronach et al., 1993; van Dam and Louwersheimer, 1995; Teeter and Callegan, 1999; Johnson et al., 1999) but rely on simplistic portrayals of continuing aggregation.

Potential applications that can benefit from this approach include designs to reduce channel and harbor sedimentation rates and tracking parcels of sediment so as to predict their path and fate.

PROBABILITY MASS FUNCTIONS FOR PARTICLE FRAGMENTS

Chapter 3 (Section 3.5.1.1) employs a probability mass function to distribute among size (mass) classes the sediment mass change occurring during particle-collision-induced fragmentation and formation of new particles. That probability mass function is derived and an example is tabulated below.

A probability distribution function may exist for the sizes of fragments produced by disaggregation, but it has not been measured. Here it is assumed that all particle sizes within the range of possible sizes are equally likely, so a simple objective probability (Lapin, 1990) of fragment sizes is calculated.

Given that the random variable of particle mass M_l is constrained to be:

$$M_l(\min) \leq M_l < M_l(\max) \tag{A-1}$$

where

$M_l(\min)$ = lower limit (inclusive) of particle mass, and

$M_l(\max)$ = upper limit of particle mass.

The probability of M_l falling within the certainty range is expressed as:

$$Pr[M_l(\min) \leq M_l < M_l(\max)] = 1 \tag{A-2}$$

269

By objective probability, for any two mass values M_1 and M_2, where $M_l(\min) \leq M_1 < M_2 \leq M_l(\max)$:

$$Pr[M_1 \leq M_l < M_2] = \frac{M_2 - M_1}{M_l(\max) - M_l(\min)} \tag{A-3}$$

In Section 3.5.1.1 the range of possible masses for given post-collision particle fragments is defined. For example, the k particle in Figure 3-12a breaks into two fragments, one with mass ΔM_k and the other with mass $M_k - \Delta M_k$. It naturally follows that ΔM_k can be no smaller than zero and no larger than M_k. Thus by Equation A-2:

$$Pr[0 \leq \Delta M_k < M_k] = 1 \tag{A-4}$$

If particle classes are defined by the intervals between upper and lower limits given in Section 3.2.1, then the probability that a particle of mass M_l will fall into a given class j is given by substituting the appropriate values into Equation A-3:

$$Pr[M_j(lower) \leq M_l < M_j(upper)] = \frac{M_j(upper) - M_j(lower)}{M_l(\max) - M_l(\min)} \tag{A-5}$$

Equation A-5 can be restated as a probability mass function for the discrete variable of sediment mass class index:

$$p(l=j) = \frac{M_j(upper) - M_j(lower)}{M_l(\max) - M_l(\min)} \tag{A-6}$$

Finally, Equation A-6 can be used to express the probability mass function used in Equations 3-49ff:

$$p_j(l=i1:i2) = \frac{M_j(upper) - M_j(lower)}{M_{i2}(max) - M_{i1}(min)} \qquad i1 \le j \le i2 \qquad \text{(A-7)}$$

which is to say that a particle of mass M_l, with a minimum possible size class $i1$ and a maximum possible size class $i2$, has a probability $p_j(l=i1:i2)$ of falling into sediment class j, and that probability is given by Equation A-7. Summation of Equation A-7 over the entire range of possible classes equals one, satisfying Equation A-2.

Application of Equation A-7 can be illustrated by use of the sediment mass classes shown in Table A-1. For that case of 30 sediment classes, Table A-2 shows the probability mass function $p_j(l=1:30)$. Because of the logarithmic expansion of the class intervals, the probability of a collisional fragment falling into class 1 is trivial compared with that of falling into class 30 when all 30 classes are possible; however, in several billion collisions at least some mass will land in class 1, so the small probabilities shown should be retained.

Table A-1. Example sediment classes definition.

Class	Representative Diameter μm	Minimum Mass kg	Representative Mass kg	Maximum Mass kg
1	0.7186	0.000E+00	3.767E-16	5.022E-16
2	0.9084	5.022E-16	7.370E-16	9.718E-16
3	1.144	9.718E-16	1.427E-15	1.882E-15
4	1.440	1.882E-15	2.766E-15	3.649E-15
5	1.812	3.649E-15	5.366E-15	7.083E-15
6	2.282	7.083E-15	1.042E-14	1.376E-14
7	2.873	1.376E-14	2.026E-14	2.677E-14
8	3.616	2.677E-14	3.944E-14	5.211E-14
9	4.553	5.211E-14	7.684E-14	1.016E-13
10	5.732	1.016E-13	1.498E-13	1.981E-13
11	7.216	1.981E-13	2.925E-13	3.869E-13
12	9.084	3.869E-13	5.715E-13	7.561E-13
13	11.44	7.561E-13	1.118E-12	1.479E-12
14	14.40	1.479E-12	2.188E-12	2.896E-12
15	18.13	2.896E-12	4.286E-12	5.676E-12
16	22.86	5.676E-12	8.405E-12	1.113E-11
17	28.77	1.113E-11	1.649E-11	2.185E-11
18	36.21	2.185E-11	3.239E-11	4.293E-11
19	45.58	4.293E-11	6.367E-11	8.441E-11
20	57.38	8.441E-11	1.252E-10	1.661E-10
21	72.22	1.661E-10	2.465E-10	3.270E-10
22	90.92	3.270E-10	4.856E-10	6.442E-10
23	114.5	6.442E-10	9.384E-10	1.233E-09
24	144.1	1.233E-09	1.804E-09	2.376E-09
25	181.3	2.376E-09	3.494E-09	4.612E-09
26	228.2	4.612E-09	6.807E-09	9.002E-09
27	287.2	9.002E-09	1.333E-08	1.765E-08
28	361.6	1.765E-08	2.619E-08	3.473E-08
29	455.3	3.473E-08	5.164E-08	6.855E-08
30	573.2	6.855E-08	1.021E-07	1.356E-07

Table A-2. Probability mass function values, $p_j(l=i1:i2)$, for $i1=1$.

j	1	2	3	4	5	6	7	8	9	10	11	12	13	14	15
1	1.00e+00	5.17e-01	2.67e-01	1.37e-01	7.08e-02	3.64e-02	1.87e-02	9.61e-03	4.93e-03	2.53e-03	1.29e-03	6.61e-04	3.38e-04	1.73e-04	8.80e-05
2		4.83e-01	2.50e-01	1.29e-01	6.62e-02	3.41e-02	1.75e-02	8.99e-03	4.61e-03	2.36e-03	1.21e-03	6.19e-04	3.16e-04	1.61e-04	8.24e-05
3			4.84e-01	2.49e-01	1.28e-01	6.61e-02	3.40e-02	1.74e-02	8.95e-03	4.58e-03	2.35e-03	1.20e-03	6.13e-04	3.13e-04	1.60e-04
4				4.84e-01	2.50e-01	1.28e-01	6.60e-02	3.39e-02	1.74e-02	8.90e-03	4.56e-03	2.33e-03	1.19e-03	6.08e-04	3.10e-04
5					4.85e-01	2.50e-01	1.28e-01	6.58e-02	3.38e-02	1.73e-02	8.86e-03	4.53e-03	2.32e-03	1.18e-03	6.03e-04
6						4.86e-01	2.50e-01	1.28e-01	6.57e-02	3.37e-02	1.72e-02	8.82e-03	4.50e-03	2.30e-03	1.17e-03
7							4.86e-01	2.50e-01	1.28e-01	6.56e-02	3.36e-02	1.72e-02	8.77e-03	4.48e-03	2.29e-03
8								4.87e-01	2.50e-01	1.28e-01	6.55e-02	3.35e-02	1.71e-02	8.74e-03	4.46e-03
9									4.87e-01	2.50e-01	1.28e-01	6.54e-02	3.34e-02	1.71e-02	8.70e-03
10										4.88e-01	2.50e-01	1.28e-01	6.52e-02	3.33e-02	1.70e-02
11											4.88e-01	2.50e-01	1.28e-01	6.51e-02	3.32e-02
12												4.89e-01	2.50e-01	1.27e-01	6.50e-02
13													4.89e-01	2.50e-01	1.27e-01
14														4.89e-01	2.50e-01
15															4.90e-01

Table A-2—continued.

The table below gives values indexed by row j (1–30) and column i_2 (16–30).

j	16	17	18	19	20	21	22	23	24	25	26	27	28	29	30
1	4.49e-05	2.28e-05	1.16e-05	5.91e-06	3.00e-06	1.53e-06	7.74e-07	4.04e-07	2.10e-07	1.08e-07	5.52e-08	2.82e-08	1.43e-08	7.25e-09	3.66e-09
2	4.20e-05	2.14e-05	1.09e-05	5.53e-06	2.81e-06	1.43e-06	7.24e-07	3.78e-07	1.96e-07	1.01e-07	5.17e-08	2.64e-08	1.34e-08	6.78e-09	3.43e-09
3	8.14e-05	4.15e-05	2.11e-05	1.07e-05	5.45e-06	2.77e-06	1.40e-06	7.34e-07	3.80e-07	1.96e-07	1.00e-07	5.11e-08	2.60e-08	1.32e-08	6.65e-09
4	1.58e-04	8.05e-05	4.10e-05	2.08e-05	1.06e-05	5.38e-06	2.73e-06	1.42e-06	7.38e-07	3.80e-07	1.95e-07	9.93e-08	5.04e-08	2.55e-08	1.29e-08
5	3.07e-04	1.57e-04	7.97e-05	4.05e-05	2.06e-05	1.05e-05	5.30e-06	2.77e-06	1.44e-06	7.39e-07	3.79e-07	1.93e-07	9.80e-08	4.97e-08	2.51e-08
6	5.98e-04	3.05e-04	1.55e-04	7.88e-05	4.00e-05	2.03e-05	1.03e-05	5.39e-06	2.79e-06	1.44e-06	7.36e-07	3.75e-07	1.91e-07	9.66e-08	4.88e-08
7	1.17e-03	5.93e-04	3.02e-04	1.54e-04	7.80e-05	3.96e-05	2.01e-05	1.05e-05	5.44e-06	2.80e-06	1.43e-06	7.31e-07	3.72e-07	1.88e-07	9.51e-08
8	2.27e-03	1.16e-03	5.89e-04	2.99e-04	1.54e-04	7.72e-05	3.92e-05	2.06e-05	1.06e-05	5.46e-06	2.80e-06	1.43e-06	7.24e-07	3.67e-07	1.85e-07
9	4.43e-03	2.26e-03	1.15e-03	5.84e-04	2.97e-04	1.51e-04	7.65e-05	3.99e-05	2.07e-05	1.07e-05	5.46e-06	2.78e-06	1.41e-06	7.16e-07	3.62e-07
10	8.66e-03	4.41e-03	2.24e-03	1.14e-03	5.80e-04	2.94e-04	1.49e-04	7.80e-05	4.04e-05	2.08e-05	1.07e-05	5.44e-06	2.76e-06	1.40e-06	7.07e-07
11	1.69e-02	8.62e-03	4.39e-03	2.23e-03	1.13e-03	5.76e-04	2.92e-04	1.53e-04	7.91e-05	4.07e-05	2.09e-05	1.06e-05	5.40e-06	2.74e-06	1.38e-06
12	3.31e-02	1.69e-02	8.59e-03	4.37e-03	2.22e-03	1.13e-03	5.72e-04	2.99e-04	1.55e-04	7.97e-05	4.08e-05	2.08e-05	1.06e-05	5.35e-06	2.71e-06
13	6.49e-02	3.31e-02	1.68e-02	8.56e-03	4.35e-03	2.21e-03	1.12e-03	5.85e-04	3.06e-04	1.56e-04	8.00e-05	4.08e-05	2.07e-05	1.05e-05	5.30e-06
14	1.27e-01	6.48e-02	3.30e-02	1.68e-02	8.52e-03	4.33e-03	2.20e-03	1.15e-03	5.94e-04	3.06e-04	1.57e-04	7.99e-05	4.06e-05	2.06e-05	1.04e-05
15	2.50e-01	1.27e-01	6.47e-02	3.29e-02	1.67e-02	8.49e-03	4.31e-03	2.23e-03	1.17e-03	6.00e-04	3.08e-04	1.57e-04	7.96e-05	4.03e-05	2.04e-05
16	4.90e-01	2.50e-01	1.27e-01	6.46e-02	3.28e-02	1.67e-02	8.46e-03	4.42e-03	2.29e-03	1.18e-03	6.04e-04	3.08e-04	1.56e-04	7.92e-05	4.00e-05
17		4.91e-01	2.50e-01	1.27e-01	6.45e-02	3.28e-02	1.66e-02	8.68e-03	4.50e-03	2.32e-03	1.19e-03	6.05e-04	3.07e-04	1.56e-04	7.87e-05
18			4.91e-01	2.50e-01	1.27e-01	6.44e-02	3.27e-02	1.71e-02	8.85e-03	4.56e-03	2.33e-03	1.19e-03	6.04e-04	3.06e-04	1.55e-04
19				4.92e-01	2.50e-01	1.27e-01	6.43e-02	3.36e-02	1.74e-02	8.97e-03	4.59e-03	2.34e-03	1.19e-03	6.03e-04	3.05e-04
20					4.92e-01	2.50e-01	1.27e-01	6.62e-02	3.43e-02	1.77e-02	9.05e-03	4.61e-03	2.34e-03	1.19e-03	6.00e-04
21						4.92e-01	2.50e-01	1.27e-01	6.62e-02	3.43e-02	1.78e-02	9.09e-03	4.62e-03	2.34e-03	1.18e-03
22							4.93e-01	2.57e-01	1.33e-01	6.87e-02	3.52e-02	1.79e-02	9.11e-03	4.61e-03	2.33e-03
23								4.93e-01	2.48e-01	1.28e-01	6.53e-02	3.33e-02	1.69e-02	8.57e-03	4.33e-03
24									4.82e-01	2.48e-01	1.27e-01	6.48e-02	3.29e-02	1.67e-02	8.42e-03
25										4.85e-01	2.48e-01	1.27e-01	6.43e-02	3.26e-02	1.65e-02
26											4.88e-01	2.49e-01	1.27e-01	6.40e-02	3.23e-02
27												4.90e-01	2.49e-01	1.26e-01	6.38e-02
28													4.92e-01	2.49e-01	1.26e-01
29														4.93e-01	2.49e-01
30															4.95e-01

COMPILATION OF APPARENT COLLISION EFFICIENCY DATA

The data in the following tables were compiled from the cited sources to provide input to the analysis of the collision diameter function performed in Chapter 3, Section 3.5.1.2, and to test the aggregation algorithm as described in Chapter 6.

Table B-1. Experimental collision efficiency data from Edzwald et al. (1974).

Sediment Source	Experiment	Mineral Content[a] %				Shear Rate 1/sec	Sediment Concentration kg/m³	Salinity ppt	Temperature deg C	Initial Median Particle Diameter µm	Ending Median Particle Diameter[b] µm	Collision Efficiency α'
		K	I	Ch	M							
Pamlico River	Pipette sample from blade reactor	58	0	40	2	52	0.2	1.8	21[c]	4.2	54	0.13
								4.4			54	0.18
								17.5			57	0.22
Upper Pamlico Estuary		48	10	40	2			1.8			54	0.10
								4.4			54	0.14
								17.5			57	0.165
Lower Pamlico Estuary		38	20	40	2			1.8			54	0.045
								4.4			54	0.08
								17.5			57	0.095

Notes:

a. K=kaolinite; I=illite; Ch=chlorite; M=montmorillonite.

b. Diameter not given in reference. Values estimated from Equation 2-10 and rate of growth curves of Burban et al. (1989).

c. Temperature not given. Estimated.

Table B-2. Experimental collision efficiency data from Gibbs (1983).

Sediment Source	Experiment	Mineral Content[a] % K	I	Ch	M	Shear Rate[b] 1/sec	Sediment Concentration kg/m³	Salinity ppt	Temperature deg C	Initial Median Particle Diameter[c] μm	Ending Median Particle Diameter[c] μm	Collision Efficiency α'
Delaware Bay	2 mm pipette sample from blade reactor	38	62			55	0.15-0.16	1.1	21[d]	3	38	0.077
								4.4			38	0.171
								17.5			37	0.207
Amazon Delta	2 mm pipette sample	38	24	27		11		2			78	0.072
											78	0.697
Yukon River	from Couette reactor		29	45	20			0.6			106	0.198
Atlantic shelf, Guiana		30	18		45			0.9			106	0.219

Notes:

a. K=kaolinite; I=illite; Ch=chlorite; M=montmorillonite.

b. Shearing rate not given in reference. Values shown were back-calculated from other data given.

c. Diameter not given. Values estimated from Equation 2-10 and rate of growth curves of Burban et al. (1989).

d. Temperature not given. Estimated.

Table B-3. Experimental collision efficiency data from Tsai et al. (1987).

Sediment Source	Experiment	Mineral Content[a] %				Temperature deg C	Salinity ppt	Sediment Concentration kg/m³	Shear Rate l/sec	Initial Median Particle Diameter µm	Ending Median Particle Diameter µm	Aggregation Factor, P_a[b]	Disaggregation Factor, P_d[b]
		K	I	Ch	M								
Detroit River	3 mm pipette sample from Couette reactor	2	1	3	4	19-23	0.5	0.4	400	3.9	20	0.15	0.0072
								0.4	100		60	0.15	0.0018
								0.4	200		40	0.15	0.0036
								0.8	200		26	0.15	0.006
								0.1	400		50	0.15	0.0024
								0.1	100		105	0.15	0.0006
								0.1	200		80	0.15	0.0012
								0.05	200		100	0.15	0.0006

Notes:

a. K=kaolinite; I=illite; Ch=chlorite; M=montmorillonite. Only relative abundance given in reference. Most abundant = 1. According to Salim et al. (1996) the relative abundance of clays in the region are 60 percent illite, 12 percent kaolinite, and 9 percent chlorite.

b. Efficiency for aggregation expressed as $P_{aim} = P_a \sqrt{2D_0/(D_i+D_j)}$ and for disaggregation as $P_{dim} = P_d (D_i+D_j)/(2D_0)$ where D_0 is a reference diameter = 4 µm.

Table B-4. Experimental collision efficiency data from Burban et al. (1989).

Sediment Source	Experiment	Mineral Content[a] %				Shear Rate 1/sec	Sediment Concentration kg/m³	Salinity ppt	Temperature deg C	Initial Median Particle Diameter µm	Ending Median Particle Diameter µm	Aggregation Factor, P_a[b]	Disaggregation Factor, P_d[b]
		K	I	Ch	M								
Detroit River	3 mm pipette sampling from Couette reactor	3	2	1	4	600	0.4	35	19-23	3.9	15	0.30	0.03
						400	0.4				19		0.02
						100	0.4				40		0.0069
						200	0.8				25		0.014
						200	0.4				32		0.0093
						100	0.1				62		0.0033
						400	0.1				32		0.01
						200	0.1				53		0.0042
						200	0.05				84		0.0022
						100	0.05				90		0.0019
						400	0.01				125		0.0013
						600	0.01				75		0.0028
						200	0.01				148		0.00093
						100	0.01				172		0.00072

Notes:

a. K=kaolinite; I=illite; Ch=chlorite; M=montmorillonite. Only relative abundance given in reference. Most abundant = 1. According to Salim et al. (1996) the relative abundance of clays in the region are 60 percent illite, 12 percent kaolinite, and 9 percent chlorite.

b. Efficiency for aggregation expressed as $P_{aim} = P_a (2D_i/(D_i+D_j))$ and for disaggregation as $P_{dim} = P_d (D_i+D_j)/(2D_o)$ where D_o is a reference diameter = 4 µm.

Table B-5. Experimental collision efficiency data from Tsai and Hwang (1995).

| Sediment Source | Experiment | Mineral Content[a] % | | | | Shear Rate 1/sec | Sediment Concentration kg/m³ | Salinity ppt | Temperature deg C | Initial Median Particle Diameter μm | Ending Median Particle Diameter μm | Collision Efficiency α' |
		K	I	Ch	M							
Tanshui Estuary	2 mm pipette sample from Couette reactor	4	2	1	3	100		0.05	21[b]	5	400	0.005
								35			80	0.047

Notes:

a. K=kaolinite; I=illite; Ch= chlorite; M=montmorillonite.   Only relative abundance given in reference.   Most abundant = 1.

b. Temperature not given in reference.   Estimated.

Chapter 4 presents an algorithm for calculating suspended multi-class fine sediment deposition with continuing aggregation. This appendix presents the computer program Danu[*], which implements that algorithm.

The program, listed beginning on the following page, was written in FORTRAN77 and organized into five functional blocks—main program, input routines, setup routines to calculate unchanging variables, calculation routines, and output routines. Some subroutines, noted by comment lines, were either adopted or adapted from the single particle size one-dimensional deposition and erosion program Vest (Mehta and Li, 1997). Danu was compiled and built under Microsoft Power Station FORTRAN Development System, Version 4. The executable code ran as a MSDOS program under Windows95 and WindowsNT.

Danu runs in two modes, one in which only the aggregation calculations are made, and one in which both aggregation and deposition are calculated. Erosion and resuspension are not calculated, but since program Vest included those calculations, the code structure is

---

[*] Danu is a river goddess in the traditions of India and of the ancient Celtic peoples in Ireland. In the Celtic tradition she was also known as the universal earth mother. (Triple E, 1999).

in place to make those calculations once an appropriate multi-class erosion algorithm is devised.

The program was initially run for a number of simple test cases to ensure that it conserved sediment mass and generated results that were both consistent with the original equations and within reasonable bounds. Finally, the program was run to replicate laboratory test cases and to perform calculations that explored aggregation processes, both of which are described in Chapter 6.

Program Listing

```
      Program DANU
C
C     Computes deposition and aggregation
C
C     Deposition and erosion components based on program VEST, written
C     by Mehta and Li (1997) and modified for unsteady waves Jan 1998,
C     multiple grain sizes plus incorporating aggregation by WHM 10/98.
C
C     Ver 1.0    1998
C
C     W. H. McAnally
C
      INCLUDE 'PATHOSCOM.FOR'
      INCLUDE 'VESTCOM.FOR'
C
C     INITIALIZE
C
      NKMAX=1001
      PI=3.14159
      G=9.80665
      KONCE=0
      VKK=0.4
      OPEN(33,FILE='ASCRTCH')
C
      CALL INPUT1()
C
      CALL SETUP()
C
C     INPUT FIRST STEP EULERIAN RESULTS
C
      CALL INPUTH1()
C
C     CHOOSE METHOD OF COMPUTATIONS
C
```

```
      IF(ITYPE.LE.0)THEN
        CALL ACALC00()
      ELSE
        IF(ITYPE.EQ.1)THEN
          CALL ACALC01()
C         CALL ACALCSF()
        ELSE
          IF(IOPTPATH.EQ.1) THEN
            IF(IOPTPROB.EQ.0) CALL ACALC10()
            IF(IOPTPROB.EQ.1) CALL ACALC11()
          ELSE
            IF(IOPTPATH.EQ.2)THEN
              IF(IOPTPROB.EQ.0) CALL ACALC20()
              IF(IOPTPROB.EQ.1) CALL ACALC21()
            ELSE
              CALL TILT(ITYPE,IOPTPATH,IOPTPROB)
            ENDIF
          ENDIF
        ENDIF
      ENDIF
C
C     WRITE FINAL RESULTS AND CLOSE
C
      CALL OUTPUTCLOSE()
C
      STOP
      END
C*******************************************************************
C     END OF MAIN
C*******************************************************************
C     PRIMARY TIME-STEPPING BLOCK
C*******************************************************************
C
      SUBROUTINE ACALC00()
C
C     PERFORMS AGGREGATION CHAMBER COMPUTATIONS
C
C
      INCLUDE 'PATHOSCOM.FOR'
      INCLUDE 'VESTCOM.FOR'
C
      T=T0
      CALL SETUP00()
      CALL UPDATE()
      CALL OUTPUT00(T)
      DO WHILE(T.LE.TLAST)
        IF(T.GE.T2)THEN
          CALL INPUTH2(T)
        ENDIF
        CALL UPDATE()
        CALL AGGREGATION00(T)
        IF(T-TOUT.GE.TSKIP.OR.T.GE.TLAST)THEN
          CALL OUTPUT00(T)
          IF(IKMON.NE.2)IKMON=1
        ENDIF
        T=T+DTL
      ENDDO
      CALL OUTPUT00(T)
```

```
      RETURN
      END
C
C*******************************************************************
C
      SUBROUTINE ACALC01()
C
C     CALCULATES DEPOSITION WITH CONTINUING AGGREGATION
C
      INCLUDE 'PATHOSCOM.FOR'
      INCLUDE 'VESTCOM.FOR'
C
      TT=T0
      T=TT
      CALL SETUP00()
      CALL UPDATE()
      CALL OUTPUT00(T)
      NCL=JCLASSES+1
      CALL INPUTVEST()
      CALL SETUPVEST(T)
      LOOP=TAGDUR/DTL
      CTT=-DT
      DO WHILE(TT.LE.TLAST)
        IAGG=0
        IF(TT.EQ.0.)IAGG=1
        IF(TT-TAGLAST.GE.TAGSKIP)THEN
          IAGG=1
          TAGLAST=TT
        ENDIF
        IF(TT.GE.T2)THEN
          CALL INPUTH2(T)
        ENDIF
        CALL VEST(TT)
        T=TT
        IF(IAGG.EQ.1)THEN
          DO I=1,NGRIDS
            DO JC=1,NCL
              CJ(JC)=0.
              IF(C(I,JC).GT.1.E-6) CJ(JC)=C(I,JC)
            ENDDO
            DO L=1,LOOP
              CALL UPDATE()
              CALL AGGREGATION00(T)
              IF(TT-TOUT.GE.TSKIP)THEN
                CALL OUTPUT01(TT,I)
                IF(IKMON.NE.2)IKMON=1
              ENDIF
              T=T+DTL
            ENDDO
            T=TT
            DO JC=1,NCL
              C0(I,JC)=CJ(JC)
            ENDDO
          ENDDO
        ENDIF
        TT=TT+DT
        CTT=CTT+DT
      ENDDO
```

```
      RETURN
      END
C
C
********************************************************************
C
      SUBROUTINE ACALCSF()
C
C     CALCULATES DEPOSITION & CONTINUING AGGREGATION FOR KRONE '62 FLUME
C     EXPERIMENT WITH SAN FRANCISCO BAY MUD
C
      INCLUDE 'PATHOSCOM.FOR'
      INCLUDE 'VESTCOM.FOR'
C
      TT=T0
      T=TT
      CALL SETUP00()
      CALL UPDATE()
      CALL OUTPUT00(T)
      NCL=JCLASSES+1
      CALL INPUTVEST()
      CALL SETUPVEST(T)
      LOOP=DT/DTL
      CTT=-DT
      TSTARTLOOP=T0
      TIMETOTAL=TIME1+TIME2
      LOOPSF=(TLAST-T0)/TIMETOTAL
      DO LSF=1,LOOPSF
       UU=UUU1
       EPS=EPS1
       DV=DV1
       CALL SETUP00()
       TSTARTLOOP=TT
       DO WHILE(TT-TSTARTLOOP.LE.TIME1)
         CALL VEST(TT)
         T=TT
          DO I=1,NGRIDS
            DO JC=1,NCL
              CJ(JC)=0.
              IF(C(I,JC).GT.1.E-6) CJ(JC)=C(I,JC)
            ENDDO
            DO L=1,LOOP
              CALL UPDATE()
              CALL AGGREGATION00(T)
              IF(TT-TOUT.GE.TSKIP)THEN
                CALL OUTPUT01(TT,I)
                IF(IKMON.NE.2)IKMON=1
              ENDIF
              T=T+DTL
            ENDDO
            T=TT
            DO JC=1,NCL
              C0(I,JC)=CJ(JC)
            ENDDO
          ENDDO
        TT=TT+DT
        CTT=CTT+DT
       ENDDO
```

```
      UU=UUU2
      EPS=EPS2
      DV=DV2
      CALL SETUP00()
      DO WHILE(TT-TSTARTLOOP.LE.TIMETOTAL)
       CALL VEST(TT)
        T=TT
         DO I=1,NGRIDS
           DO JC=1,NCL
             CJ(JC)=0.
             IF(C(I,JC).GT.1.E-6) CJ(JC)=C(I,JC)
           ENDDO
           DO L=1,LOOP
             CALL UPDATE()
             CALL AGGREGATION00(T)
             IF(TT-TOUT.GE.TSKIP)THEN
               CALL OUTPUT01(TT,I)
               IF(IKMON.NE.2)IKMON=1
             ENDIF
             T=T+DTL
           ENDDO
           T=TT
           DO JC=1,NCL
             C0(I,JC)=CJ(JC)
           ENDDO
         ENDDO
        TT=TT+DT
        CTT=CTT+DT
      ENDDO
      ENDDO
      RETURN
      END
C
C*****************************************************************
C
      SUBROUTINE ACALC10()
C
C     PERFORMS TRACKING COMPUTATIONS USING QUICKEST OPTIONS--
C     BINARY PROBABILTY OUTCOMES AND SIMPLE PARTICLE VELOCITY.
C
      INCLUDE 'PATHOSCOM.FOR'
      INCLUDE 'VESTCOM.FOR'
C
      WRITE(*,*)'OPTION NOT YET AVAILABLE FOR PATH= 1 AND',
     &          ' PROBABILITY= 0.'
      RETURN
      END
C
C*****************************************************************
C
      SUBROUTINE ACALC11()
C
C     PERORMS COMPUTATIONS USING ...
C
      INCLUDE 'PATHOSCOM.FOR'
      INCLUDE 'VESTCOM.FOR'
C
      WRITE(*,*)'OPTION NOT YET AVAILABLE FOR PATH= 1 AND',
```

```
      &             ' PROBABILITY= 1'
      STOP
      RETURN
      END
C
C*****************************************************************
C
      SUBROUTINE ACALC20()
C
C     PERORMS COMPUTATIONS USING ...
C
      INCLUDE 'PATHOSCOM.FOR'
      INCLUDE 'VESTCOM.FOR'
C
      WRITE(*,*)'OPTION NOT YET AVAILABLE FOR PATH= 2',
      &             ' PROBABILITY= 0'
      STOP
      RETURN
      END
C
C*****************************************************************
C
      SUBROUTINE ACALC21()
C
C     PERORMS COMPUTATIONS USING ...
C
      INCLUDE 'PATHOSCOM.FOR'
      INCLUDE 'VESTCOM.FOR'
C
      WRITE(*,*)'OPTION NOT YET AVAILABLE FOR PATH= 2 AND',
      &             ' PROBABILITY= 1'
      STOP
      RETURN
      END
C
C*****************************************************************
C     ## END OF CALCULATION SEPARATION & PRIMARY TIME LOOPING BLOCK
C*****************************************************************
C     BEGIN INPUT BLOCK
C*****************************************************************
C
      SUBROUTINE INPUT1()
C
C     READ RUN CONTROL AND INITIAL CONDITION DATA
C
      INCLUDE 'PATHOSCOM.FOR'
      INCLUDE 'VESTCOM.FOR'
C
      CHARACTER*4 DUM
      CHARACTER*16 RUNCTL
      CHARACTER*16 KERNIN,DIAMOUT,SEDFILE,EULERFILE,GEOFILE,SPECTRA,
     & BEDFILE,CHIST,KERNOUT1,KERNOUT2,HOTCON,HOTCLASS
      CHARACTER*60 RUNLABEL,KERNLABEL,EULERLABEL,SEDLABEL,BEDLABEL,
     & OLDRUNLABEL,FILENAMES,DUMCHAR
C
C     READ RUN CONTROL
C
      WRITE(*,*)'PROGRAM DANU'
```

```
      WRITE(*,*)'  '
      WRITE(*,*)'PLEASE GIVE RUN CONTROL INPUT FILE NAME '
      READ(*,*)RUNCTL
      OPEN(1,FILE=RUNCTL,STATUS='OLD')
      READ(1,*)DUM,RUNLABEL
      READ(1,*)DUM,ITYPE,IOPTPROB,IOPTPATH,JEULER,JGEO,IHOT,IRHO
      READ(1,*)DUM,KERNIN,EULERFILE,GEOFILE,SEDFILE,BEDFILE,
     & HOTCON,HOTCLASS
      READ(1,*)DUM,DIAMOUT,SPECTRA,CHIST,KERNOUT1,KERNOUT2,FILEOUT
      READ(1,*)DUM,T0,TLAST,DTL,TSKIP,FPIN,TAGSKIP,TAGDUR
      READ(1,*)DUM,XNU,XMU,RHO,GMULT
      READ(1,*)DUM,RHOG,D1,R1,ER1,D2,R2,ER2,D3,RHOMULT
      READ(1,*)DUM,B11,EM7,RANMULT
      READ(1,*)DUM,S2MULT,S3MULT,X3MULT,X2MULT,TAUMULT,DV,EPS,SUMCONC,S
C
C     SPECIAL READ FOR SFB MUD EXPERIMENT
C
C     READ(1,*)DUM,UUU1,DV1,EPS1,TIME1
C     READ(1,*)DUM,UUU2,DV2,EPS2,TIME2
C
      IF(ITYPE.EQ.0)CLOSE(1)
      IF(XNU.EQ.0)THEN
        XNU=1.E-6
      ENDIF
      IF(XMU.EQ.0)THEN
        XMU=1.E-3
      ENDIF
      IF(RHO.EQ.0)THEN
        RHO=1000.
      ENDIF
      G=GMULT*G
      R1=R1*RHOMULT
      R2=R2*RHOMULT
C
      IF(ITYPE.GT.0)THEN
        OPEN(44,FILE=CHIST,STATUS='UNKNOWN')
        WRITE(44,*)'       TIME(MIN)            CBAR, KG/M^3',
     & '        DEPOSITION RATE, KG/SEC'
      ENDIF
C
C     READ KERNEL DATA
C
      IF(ITYPE.EQ.2)THEN
        OPEN(321,FILE='KERNOUT1.TXT')
        OPEN(322,FILE='KERNOUT2.TXT')
        OPEN(2,FILE=KERNIN,STATUS='OLD')
        READ(2,*)DUM,KERNLABEL
        READ(2,*)DUM,OLDRUNLABEL,FILENAMES
        READ(2,*)DUM,NK
        IF(NK.GT.NKMAX)THEN
          WRITE(*,*)'ERROR: MORE THAN ',MAXK,' KERNELS. STOP IN INPUT1'
          STOP
        ELSE
          DO K=1,NK
            READ(2,*)DUM,KID(K),KBED(K),KLASS0(K),AMASSK0(K),DK0(K),
     &             RHOK(K),WSK(K),(VPK(I,K),I=1,3),
     &             (X0K(I,K),I=1,3)
            IF(DK0(K).EQ.0.)THEN
```

```
              CALL DIAMETER(AMASSK0(K),DK0(K),RHOK(K))
            ELSE
              DK0(K)=DK0(K)*1.E-6
            ENDIF
            DK(K)=DK0(K)
            IF(RHOK(K).EQ.0)THEN
              CALL DENSITY(DK(K),RHOK(K))
            ENDIF
            IF(AMASSK0(K).EQ.0.)THEN
              AMASSK0(K)=PI*RHOK(K)*DK(K)**3./6.
            ENDIF
            AMASSK(K)=AMASSK0(K)
            KLASS(K)=KLASS0(K)
            IF(WSK(K).EQ.0)THEN
              CALL SETTLVEL(DK(K),RHOK(K),WSK(K))
            ENDIF
            CALL STRENGTH(RHOK(K),TAUSK(K))
            DO I=1,3
              X1K(I,K)=X0K(I,K)
            ENDDO
          ENDDO
        ENDIF
        CLOSE(2)
      ENDIF
C
C     READ GEOMETRY DATA
C
      IF(JGEO.EQ.1)THEN
        OPEN(11,FILE=GEOFILE,STATUS='OLD',FORM='BINARY')
        CALL INPUTGEO(11)
        CLOSE(11)
      ENDIF
C
C     READ EULERIAN DATA
C
      IF(JEULER.EQ.1)THEN
        OPEN(12,FILE=EULERFILE,STATUS='OLD',FORM='BINARY')
        EULERLABEL='TABS10 RESULTS'
C
C       INSERT READ HEADER AND HYDRO DATA FROM TABS FILE
C
C         OPEN(13,FILE=BEDFILE,STATUS='OLD',FORM='BINARY')
C         BEDLABEL='TABS10 BED RESULTS'
C
C       INSERT READ HEADER AND BED DATA FROM TABS FILE
C
C         CLOSE(13)
      ENDIF
C
      IF(JEULER.EQ.2)THEN
        OPEN(12,FILE=EULERFILE,STATUS='OLD')
        READ(12,*)DUM,EULERLABEL
      ENDIF
C
      IF(JEULER.NE.1)THEN
C
C       READ ASCII SEDIMENT BED DATA
C
```

```
C       OPEN(3,FILE=BEDFILE,STATUS='OLD')
C       READ(3,*)DUM,BEDLABEL
C       READ(3,*)DUM,NLAYERS,RHOCRIT,RICRIT
C       DO I=1,NLAYERS
C         READ(3,*)DUM,L,TAUCM(L),TAUCE(L)
C       ENDDO
C       CLOSE(3)
      ENDIF
C
C     READ BASIC SEDIMENT CHARACTERISTICS
C
      OPEN(4,FILE=SEDFILE,STATUS='OLD')
      READ(4,*)DUM,SEDLABEL
      READ(4,*)DUM,DG,CEC,ALPHAA,PERCOH,PERKAO,PERILL,PERMONT,PERCHL
      IF(DG.EQ.0)THEN
        DG=(0.36*PERKAO+0.062*PERILL+0.011*PERMONT+0.062*PERCHL)/100.
      ENDIF
      IF(CEC.EQ.0)THEN
        CEC=(9.*PERKAO+25.*PERILL+115.*PERMONT+34.*PERCHL)/100.
      ENDIF
      IF(ALPHAA.EQ.0)THEN
        ALPHAA=PERCOH/100.
      ENDIF
      READ(4,*)DUM,JCLASSES,JSTART
      IF(IHOT.EQ.0)THEN
          AMIN(1)=0.
          TOTAL0=0.
          READ(4,*)DUM,DJMAX(1),CJ(1)
          TOTAL0=TOTAL0+CJ(1)
          DJMAX(1)=DJMAX(1)*1.E-6
          CALL DENSITY(DJMAX(1),RHOP)
          AMAX(1)=(PI*RHOP*DJMAX(1)**3.)/6.
          AMASSJ(1)=(AMAX(1)+AMIN(1))*0.75
          CALL DIAMETER(AMASSJ(1),DJ(1),RHOJ(1))
          CALL SETTLVEL(DJ(1),RHOJ(1),WSJ(1))
          CALL STRENGTH(RHOJ(1),TAUSJ(1))
          TAUSJ(1)=TAUMULT*TAUSJ(1)
          XNJ(1)=(CJ(1)/AMASSJ(1))
          AMIN(2)=AMAX(1)
          DO I=2,JCLASSES
            READ(4,*)DUM,DJMAX(I),CJ(I)
            TOTAL0=TOTAL0+CJ(I)
            DJMAX(I)=DJMAX(I)*1.E-6
            CALL DENSITY(DJMAX(I),RHOP)
            AMAX(I)=(PI*RHOP*DJMAX(I)**3.)/6.
            AMASSJ(I)=(AMAX(I)+AMIN(I))/2.D0
            CALL DIAMETER(AMASSJ(I),DJ(I),RHOJ(I))
            IF(I.LT.JCLASSES)THEN
              AMIN(I+1)=AMAX(I)
            ENDIF
            CALL SETTLVEL(DJ(I),RHOJ(I),WSJ(I))
            CALL STRENGTH(RHOJ(I),TAUSJ(I))
            TAUSJ(I)=TAUMULT*TAUSJ(I)
            XNJ(I)=(CJ(I)/AMASSJ(I))
          ENDDO
          I=JCLASSES+1
          DJMAX(I)=4.*DJMAX(JCLASSES)
          CALL DENSITY(DJMAX(I),RHOP)
```

```
            AMIN(I)=AMAX(JCLASSES)
            AMAX(I)=(PI*RHOP*DJMAX(I)**3.)/6.
            AMASSJ(I)=(AMAX(I)+AMIN(I))/2.D0
            CALL DIAMETER(AMASSJ(I),DJ(I),RHOJ(I))
            CALL SETTLVEL(DJ(I),RHOJ(I),WSJ(I))
            CALL STRENGTH(RHOJ(I),TAUSJ(I))
            TAUSJ(I)=TAUSJ(I)*TAUMULT
            CJ(I)=0.
            XNJ(I)=0.
            TOTAL2=TOTAL0
            CLOSE(4)
            IF(ITYPE.LT.0)THEN
              DO J=1,JCLASSES
                CJ(J)=CJ(J)*SUMCONC/TOTAL0
              ENDDO
            ENDIF
        ELSE
C
C     READ HOTSTART CONCENTRATION DISTRIBUTION
C
        OPEN(4,FILE=HOTCON,STATUS='OLD')
  909   READ(4,*,END=910)DUM
        GO TO 909
  910   DO I=1,JCLASSES+IHOT
          BACKSPACE(4)
        ENDDO
        READ(4,44)DUMCHAR
   44   FORMAT(A60)
        WRITE(*,44)DUMCHAR
        BACKSPACE(4)
        READ(4,*)TIME,IDUM,JC,DUM,CJ(1),DUM,DUM,DUM,DUM,DUM
        TOTAL0=CJ(1)
        WRITE(*,*)'READING HOTSTART FILES',HOTCON,HOTCLASS
        WRITE(*,*)'TIME ',TIME,' CLASS = ',JC,' CONCENTRATION ',CJ(JC)
        DO J=2,JCLASSES+1
          READ(4,*)TIME,IDUM,JC,DUM,CJ(JC),DUM,DUM,DUM,DUM,DUM
          TOTAL0=TOTAL0+CJ(JC)
        ENDDO
        WRITE(*,*)'TIME ',TIME,' CLASS = ',JC,' CONCENTRATION ',CJ(JC)
        TOTAL2=TOTAL0
        CLOSE(4)
C
C     READ HOTSTART CLASSES
C
        OPEN(4,FILE=HOTCLASS,STATUS='OLD')
        READ(4,*)DUM
        READ(4,*)DUM
        READ(4,*)DUM
        DO J=1,JCLASSES+1
          READ(4,*)I,DJ(I),AMIN(I),AMASSJ(I),AMAX(I),
     &       RHOJ(I),WSJ(I),TAUSJ(I)
        ENDDO
        READ(4,*,END=1001)I
        GOTO 1001
 1000   WRITE(*,*)'ERROR:DIFFERENT NUMBER OF CLASSES IN HOTSTART.'
        STOP
 1001   CONTINUE
        TOTAL0=0.
```

```
      DO J=1,JCLASSES+1
        DJ(J)=DJ(J)*1.E-6
        XNJ(J)=(CJ(J)/AMASSJ(J))
        TOTAL0=TOTAL0+CJ(J)
      ENDDO
      CLOSE(4)
      WRITE(*,*)'HOTSTART READ COMPLETE'
    ENDIF
C
C     START RESULTS FILES & ECHO PRINT INPUT DATA
C
    AA=-9999999999.
    IA=999
    IF(ITYPE.LT.2)THEN
        OPEN(21,FILE=SPECTRA)
        WRITE(21,1)RUNLABEL
        WRITE(21,*)T0,TLAST,DTL,JSTART
        WRITE(21,*)XNU,XMU,RHO
        WRITE(21,*)RHOG,D1,R1,ER1,D2,R2,ER2,D3
        WRITE(21,*)B11,EM7
        WRITE(21,2)KERNIN,KERNLABEL
        WRITE(21,3)SEDFILE,SEDLABEL
        WRITE(21,4)BEDFILE,BEDLABEL
        WRITE(21,5)GEOFILE,EULERFILE,EULERLABEL
        WRITE(21,9)
        WRITE(21,11)AA,IA,AA,AA,AA,AA,AA,AA,AA
    ELSE
        OPEN(321,FILE=KERNOUT1)
        WRITE(321,1)RUNLABEL
        WRITE(321,*)T0,TLAST,DTL,JSTART
        WRITE(321,*)XNU,XMU,RHO
        WRITE(321,*)RHOG,D1,R1,ER1,D2,R2,ER2,D3
        WRITE(321,*)B11,EM7
        WRITE(321,2)KERNIN,KERNLABEL
        WRITE(321,3)SEDFILE,SEDLABEL
        WRITE(321,4)BEDFILE,BEDLABEL
        WRITE(321,5)GEOFILE,EULERFILE,EULERLABEL
        WRITE(321,6)
        WRITE(321,11)AA,IA,AA,AA,AA,AA,AA,AA,AA
        OPEN(322,FILE=KERNOUT2)
        WRITE(322,1)RUNLABEL
    ENDIF
    OPEN(22,FILE=DIAMOUT)
    OPEN(23,FILE='CLASSES.TXT')
    WRITE(22,1)RUNLABEL
    WRITE(23,1)RUNLABEL
    WRITE(23,*)'SIZE CLASSES'
    WRITE(22,1)RUNLABEL
    WRITE(22,2)KERNIN,KERNLABEL
    WRITE(22,3)SEDFILE,SEDLABEL
    WRITE(23,7)
    DO J=1,JCLASSES+1
      DJMICRO=DJ(J)*1.E6
      WRITE(23,8)J,DJMICRO,AMIN(J),AMASSJ(J),AMAX(J),RHOJ(J),WSJ(J),
&                TAUSJ(J)
    ENDDO
    CLOSE(23)
    WRITE(22,10)
```

```
    1 FORMAT('TRUN',2X,A40)
    2 FORMAT('TKER',2X,A16,2X,A40)
    3 FORMAT('TSED',2X,A16,2X,A40)
    4 FORMAT('TBED',2X,A16,2X,A40)
    5 FORMAT('TEUL',2X,A16,2X,A16,2X,A40)
    6 FORMAT(1X,'  TIME      K     KID    KBED     DIAM         X',
     & '           Y           Z          VX          VY',
     & '          VZ')
    7 FORMAT(' CLASS DIAMETER    MIN MASS     MASS        MAX MASS',
     & '     DENSITY    SETTLING VEL.  STRENGTH')
    8 FORMAT(1X,I5,F12.6,3(E12.6,1X),3(E12.6,1X))
    9 FORMAT(10X,'  J      DIAMETER     MASS CONC. NUMBER CONC.' ,
     & '   DCSHEAR    DC 2-BODY    DC 3-BODY PARTICLE NO. %')
   10 FORMAT(1X,'     TIME        D50      D MEDIAN   D MED (MEAS)'
     & '  TOTAL MASS   MASS CHANGE NO. MASS LIMITS  3 BODY ON/OFF')
   11 FORMAT(G12.6,I5,1X,2(G12.6,1X),5(E12.6,1X))
C
      RETURN
      END
C
C*****************************************************************
C
      SUBROUTINE INPUTGEO(IGEO)
C
C     READ GEOMETRY FILE
C
C     ADAPTED FROM TABS-10.  AUG 98
C
      INCLUDE 'PATHOSCOM.FOR'
      INCLUDE 'VESTCOM.FOR'
C
      READ (IGEO) NPGEO, NEGEO, NPM, NES,
     *            ((CORD(J,K),SPEC(K),K=1,3),
     *            ALFA, NFIX, AO,
     *            NSURF, J = 1,NPGEO),
     *            (NDEP(J), NREF, J = 1, NPM),
     *            ((NOP(J,K),K=1,20),
     *            NCORN, IMAT(J),
     *            TH, NFIXH, J = 1, NEGEO),
     *            (WIDTH, J = 1, NPGEO)
      NE = NEGEO
      NP = NPGEO
      IF(NPGEO.GT.2000.OR.NEGEO.GT.600)THEN
        WRITE(*,*)'ERROR: MORE NODES AND ELEMENTS THAN DIMENSIONED.',
     &            'STOP IN INPUTGEO.'
        STOP
      ENDIF
      RETURN
      END
C
C*****************************************************************
C
      SUBROUTINE INPUTH1()
C
C     FIRST PASS READ EULERIAN RESULTS FILE, EITHER TABS-10 OR ASCII,
C     OR GENERATE HYDRO & SED RESULTS
C
```

```
      INCLUDE 'PATHOSCOM.FOR'
      INCLUDE 'VESTCOM.FOR'
      CHARACTER DUM*4
C
      TIME2=1.E8
      IF(JEULER.GT.0)THEN
        IF(JEULER.EQ.1)THEN
C
C          READ(12) TABS HYDRO & BED ,TIME2 ETC
C
        ELSE
          IF(JEULER.EQ.2)THEN
C
            READ(12,*)DUM,T1,S1,TEMP1,EPS1,DV1,XV1,YV1,ZV1,IKMON
            READ(12,*)DUM,T2,S2,TEMP2,EPS2,DV2,XV2,YV2,ZV2,DUM
C
          ENDIF
        ENDIF
      ELSE
        T1=T0
        T2=T0+DTL
        IF(IOPTPATH.GT.0)THEN
C
C        GENERATE ARTIFICIAL HYDRO AND SEDIMENT INPUT
C
          XV=1.
          YV=1.
          ZV=0.01
          S=30.
          TEMP=20.
          DO I=1,JCLASSES
            CJ(I)=1.
          ENDDO
          TAUBED=1.
          EPS=1.
          BEDELEV=100.
          DV=10.
          LAYERTOP=1
          RHOLAYER(1)=1100.
        ELSE
C
C        FOR AGGREGATION CHAMBER
C
          EPS=1.
          DV=10.
          S=30.
          TEMP=20.
        ENDIF
      ENDIF
C
      RETURN
      END
C
C
C******************************************************************
C
      SUBROUTINE INPUTH2(T)
C
```

```
C     READ EULERIAN INPUT FILE OR GENERATE INPUT
C
      INCLUDE 'PATHOSCOM.FOR'
      INCLUDE 'VESTCOM.FOR'
      CHARACTER DUM*4
C
C     SET ALL TIME2 VARIABLES TO TIME1
C
      T1=T2
      S1=S2
      TEMP1=TEMP2
      EPS1=EPS2
      DV1=DV2
      XV1=XV2
      YV1=YV2
      ZV1=ZV2
C
C     READ TIME 2
C
      T2=1.E18
      IF(JEULER.GT.0)THEN
        IF(JEULER.EQ.1)THEN
C
C          READ(12) TABS HYDRO & BED ,TIME2 ETC
C
        ELSE
          IF(JEULER.EQ.2)THEN
C
            READ(12,*)DUM,T2,S2,TEMP2,EPS2,DV2,XV2,YV2,ZV2,IKMON
C
          ENDIF
        ENDIF
      ELSE
        TZ=T
        T2=T1+DTL
C
C       GENERATE ARTIFICIAL HYDRO AND SEDIMENT INPUT
C
        IF(IOPTPATH.GT.0)THEN
          XV=1.
          YV=1.
          ZV=0.01
          S=30.
          TEMP=20.
          TAUBED=1.
          EPS=1.
          BEDELEV=100.
          DV=10.
          LAYERTOP=1
          RHOLAYER(1)=1100.
          DO I=1,JCLASSES
            CJ(I)=1.
          ENDDO
        ELSE
          S=30.
          TEMP=20.
          EPS=1.
          DV=10.
```

```
      ENDIF
      ENDIF
C
      RETURN
      END
C
C
C     ********************************************************************
C
      SUBROUTINE INPUTVEST()
C
C     READ DEPOSITION CALCULATION RUN CONTROL
C     ADAPTED FROM PROGRAM VEST BY MEHTA AND LI, 1997
C
      INCLUDE 'PATHOSCOM.FOR'
      INCLUDE 'VESTCOM.FOR'
      DIMENSION CII(ND,MAXC)
      CHARACTER DUMFILEOUT*16
C
      IFILE=1
      READ(1,*)
      READ(1,*)
      READ(1,*) DUMFILEOUT
      WRITE(*,*)FILEOUT
      READ(1,*)
      READ(1,*) FILEGRA
      WRITE(*,*) FILEGRA
      OPEN(42,FILE=FILEOUT,STATUS='UNKNOWN')
      OPEN(43,FILE=FILEGRA,STATUS='UNKNOWN')
C      OPEN(44,FILE='ACONC.TXT',STATUS='UNKNOWN')
C
C     MOD TO VARY WAVE HEIGHT WHM JAN 98
      IF(MODE.EQ.2.OR.MODE.EQ.3)THEN
        OPEN(10,FILE='FILEWAVE.INP',STATUS='UNKNOWN')
        OPEN(11,FILE='RESULTS1.OUT',STATUS='UNKNOWN')
        OPEN(12,FILE='RESULTS2.OUT',STATUS='UNKNOWN')
        WRITE(11,101)
        WRITE(12,102)
  101   FORMAT(5X,'   TIME    WAVE HT WAVE PERIOD CBAR',/
     1       5X,'  (SEC)      (M)     (SEC)    MG/L')
  102   FORMAT(5X,'   TIME    WAVE HT WAVE PERIOD ABOVE BED   CONC',/
     1       5X,'  (SEC)      (M)     (SEC)      (M)    MG/L')
      ENDIF
      READ(1,*)
      READ(1,*) DESCR
      WRITE(*,*) DESCR
      READ(1,*)
      READ(1,*) H0, M0, NGRIDS               !DISCRETIZATION PARAMETERS
      WRITE(*,*) H0, M0, NGRIDS
      READ(1,*)
      READ(1,*) STT,DTRUN,DT,DTOUT           !TIME PARAMETERS
      WRITE(*,*) STT,DTRUN,DT,DTOUT
      IF(DTOUT.LE.0.000001) THEN
         READ(1,*)
         READ(1,*) IDT
         WRITE(*,*) IDT
         READ(1,*)
```

```
        READ(1,*) (DDTOUT(I),I=1,IDT)
        WRITE(*,*) (DDTOUT(I),I=1,IDT)
      END IF
      READ(1,*)
      READ(1,*)
C     FOLLOWING TWO LINES FOR SINGLE GRAIN CLASS WS
C     READ(1,*) WSC0, WS0, WSA, WSB, WSM, WSN !SETTLING VELOCITY
PARAMETERS
      WRITE(*,*) WSC0, WS0, WSA, WSB, WSM, WSN
      READ(1,*) HK2, BETAH , WSB
      WRITE(*,*) HK2, BETAH, WSB
      READ(1,*)
      READ(1,*)
      READ(1,*) DSK1, DSK2                  !STABILIZED DIFFUSION
CONSTANTS.
C     READ(1,*) DPS                         !DEPOSITION RATE
      WRITE(*,*) DSK1, DSK2
      DPS=1.0
C
      READ(1,*)
      READ(1,*)
      READ(1,*) MODE                        !DEFINE: PROGRAM LOGIC
      WRITE(*,*) MODE
      IF(MODE.EQ.1) THEN
        READ(1,*)
        READ(1,*) UU, QN                    !CURRENT HYDRODYNAMICS
      WRITE(*,*) UU, QN
      ELSE IF(MODE.EQ.2) THEN
        READ(1,*)
        READ(1,*) WHEIGHT,WPERIOD,WDIFFK    !WAVE HYDRODYNAMICS
      WRITE(*,*) WHEIGHT,WPERIOD,WDIFFK
      ELSE IF(MODE.EQ.3) THEN
        READ(1,*)
        READ(1,*) UU, QN                    !CURRENT HYDRODYNAMICS

      WRITE(*,*) UU, QN
        READ(1,*)
        READ(1,*) WHEIGHT,WPERIOD,WDIFFK    !WAVE HYDRODYNAMICS
      WRITE(*,*) WHEIGHT,WPERIOD,WDIFFK
C     ELSE IF(MODE.EQ.4) THEN
C        READ(1,*) UMAX, PTIDE, QQN         !TIDAL HYDRODYNAMICS
      ELSE
         WRITE(*,*) '"MODE" INPUT IS WRONG! "MODE" MUST 1, 2 OR 3'
         STOP
      END IF
C
      READ(1,*)
      READ(1,*) RHOSED, RHOM, RHOW          !DENSITY
      WRITE(*,*) RHOSED, RHOM, RHOW
      READ(1,*)
      READ(1,*)
      READ(1,*)MCHOO
      WRITE(*,*) MCHOO
      IF(MCHOO.EQ.1) THEN
        READ(1,*)
C        READ(1,*) RIC, ENT0, ENN           !ENTRAINMENT PARAMETER
        READ(1,*) RIC, ENT0                 !ENTRAINMENT PARAMETER
      WRITE(*,*) RIC, ENT0
```

```
      ENN=1.0
      READ(1,*)
      READ(1,*)
      READ(1,*) GG1,GG2,UU2              !MUD REOLOGY
     WRITE(*,*) GG1, GG1, UU2
     ELSE IF(MCHOO.EQ.2) THEN
      READ(1,*)
      READ(1,*) TAUDEP                   !CRITICAL STRESS OF
DEPOSITION
      WRITE(*,*) TAUDEP
     READ(1,*)
      READ(1,*) WFRIC                    !WAVE FRICTION COEFFICIENT
      WRITE(*,*) WFRIC
     READ(1,*)
      READ(1,*) BDP1, BDP2, RHBBAR       !BED DENSITY PARAMETERS
      WRITE(*,*) BDP1, BDP2, RHBBAR
     READ(1,*)
      READ(1,*) PHIC, TCP1, TCP2         !CRITICAL STRESS PARAMETERS
      WRITE(*,*) PHIC, TCP1, TCP2
     READ(1,*)
      READ(1,*) ERSMAX, ERP1, ERP2       !EROSION RATE COEF PARAMETERS
     WRITE(*,*) ERSMAX, ERP1, ERP2
     ELSE
      WRITE(*,*)'INAPPROPRIATE CHOICE FOR BOTTOM SEDIMENT!'
      STOP
     END IF
C
     READ(1,*)
     READ(1,*) JN,JCN                    !INITIAL CONCENTRATION
POINTS
     WRITE(*,*) JN,JCN
     DO I =1,JN
      READ(1,*)
      READ(1,*)
C
     J=1
C
     READ(1,*) ZI(I),(CII(I,JC),JC=1,JCN)  !INITIAL CONCENTRATION
PROFILE
      WRITE(*,*) ZI(I),(CII(I,JC),JC=1,JCN)
     END DO
C
     IF(JCN.EQ.1.AND.NCL.GT.1)THEN
       DO I=1,JN
         DO JC=1,NCL
           CI(I,JC)=CII(I,JCN)*CJ(JC)*S2MULT/TOTAL0
C     WRITE(33,1000)I,JC,CJ(JC),CII(I,JCN),CI(I,JC)
C 1000 FORMAT(2I5,3E12.6)
         ENDDO
       ENDDO
     ELSE
       DO I=1,JN
         DO JC=1,NCL
           CI(I,JC)=CII(I,JC)*S2MULT
         ENDDO
       ENDDO
     ENDIF
```

```
      CLOSE(1)
CCC
      WRITE(43,*) H0, NGRIDS
      WRITE(*,*) H0, NGRIDS
      IF(DTOUT.LE.0.000001) THEN
          III=IDT+1
          WRITE(43,*)III,DTOUT
          WRITE(*,*)III,DTOUT
      ELSE
          III=INT((DTRUN-STT)/DTOUT)+1
          WRITE(43,*) III,DTOUT
      END IF
      RETURN
      END
C
C*****************************************************************
C     ## END OF INPUT BLOCK
C*****************************************************************
C     BEGIN SETUP BLOCK
C*****************************************************************
C
C*****************************************************************
C
      SUBROUTINE SETUP()
C
C     DEFINE CONSTANTS AND BASIC TERMS
C
      INCLUDE 'PATHOSCOM.FOR'
      INCLUDE 'VESTCOM.FOR'
C
      BOLTZ=1.3805E-23
      TO15PINU=2./(15.*PI*XNU)
      BROWNCONST=2.D0*BOLTZ/(3.*XMU)
      SHEARCONST=(PI*TO15PINU**0.5)/4.
      DIFFSCONST=PI/4.
      LAMBDAS=0.001
      BOLTZ=1.3805E-23
      RETURN
      END
C
C
C*****************************************************************
C
      SUBROUTINE SETUP00()
C
C     PRE-CALCULATE OFTEN-USED PARAMETERS
C
      INCLUDE 'PATHOSCOM.FOR'
      INCLUDE 'VESTCOM.FOR'
C
      KEEPON=0
      SUMVOL=0.
      TOTALVOL=0.
      DO J=JSTART,JCLASSES
        TOTALVOL=TOTALVOL+XNJ(J)*DJ(J)**3
      ENDDO
      J=JSTART-1
      DO WHILE(KEEPON.LT.1)
```

```
       J=J+1
       IF(J.GT.JCLASSES)KEEPON=1
         SUMVOL=SUMVOL+XNJ(J)*DJ(J)**3
         FRAC=SUMVOL/TOTALVOL
         IF(FRAC.GE.0.5)THEN
           F1=(SUMVOL-XNJ(J)*DJ(J)**3)/TOTALVOL
           F=FRAC-F1
           IF(F.NE.0)THEN
             DMED=DJ(J-1)+(0.5-F1)*(DJ(J)-DJ(J-1))/(F)
           ELSE
             DMED=DJ(J)
           ENDIF
           FRAC=0.
           TOTALVOL=0.
           KEEPON=KEEPON+1
         ENDIF
       ENDDO
C
C      INTERPOLATE HYDRO
C
       TT=0.
       IF(ITYPE.GE.0)THEN
         CALL INTERPOLATE00(TT)
       ELSE
         DV=SQRT(2.*EPS*1.E6/(15.*3.1416))
       ENDIF
C
       IF(S.GE.1)THEN
         ALPHAAA=ALPHAA
       ELSE
         ALPHAAA=S*ALPHAA
       ENDIF
       TR=1.-0.875*TEMP/30.
       SR=S/2.D0
       CECR=CEC/9.
       DGR=DG/(X3MULT)
       DMED0=DMED
C
       DO K=1,JCLASSES
         DCSHEAR(K)=0.
C
C        DENSITY-DEPENDENT FP
C
         FP(K)=FPIN*(1-((RHOJ(K)-RHO)/1650.))
         IF(FP(K).LT.0.01)FP(K)=0.01
         IF(FPIN.LT.0.)FP(K)=DABS(FPIN)
C
         DO I=1,JCLASSES
           DIK(I,K)=DJ(I)+DJ(K)
           DD(I,K)=DJ(I)*DJ(K)
           AMIK(I,K)=AMASSJ(I)+AMASSJ(K)
           AMM(I,K)=AMASSJ(I)*AMASSJ(K)
           AMR=RHOJ(I)/RHOJ(K)
           AMR=AMR*(DJ(I)/DJ(K))**3.
           IF(AMR.LT.1.AND.AMR.NE.0.)THEN
             AMR=1./AMR
           ENDIF
           PI00(I,K)=XNU/(AMR*DIK(I,K))
```

```
          PI0(I,K)=DGR*SR*TR*CECR*PI00(I,K)
       ENDDO
      ENDDO
      DO K=1,JCLASSES
       DO I=1,JCLASSES
         UIB=BOLTZ*(TEMP+273.15)/(3.*PI*XMU*DD(I,K))
         UIS=DIK(I,K)*SQRT(TO15PINU*EPS)/2.D0
         UID=DABS(WSJ(I)-WSJ(K))
         UISUM=UIB+UIS+UID
         IF(UISUM.NE.0.)PIC=PI0(I,K)/UISUM
C          IF(UISUM.NE.0.)PIC=PI0(I,K)/DMAX1(UIB,UIS,UID)
C          UI(I,K)=DMAX1(UIB,UIS,UID)
         UI(I,K)=(UIB*UIB+UIS*UIS+UID*UID)**0.5
         UI(K,I)=UI(I,K)
         FC=0.897*PIC**0.0975
         IF(FC.GT.1.)FC=1.
         IF(X2MULT.GT.0)FC=FC*X2MULT*0.0806*
     &     (SUMCONC*DV/(0.8*600.))**(-.4592)
         IF(X2MULT.LT.0.)FC=FC*DABS(X2MULT)
         BETABROWN=BROWNCONST*(TEMP+273.15)*FC*DIK(I,K)*DIK(I,K)
         BETABROWN=BETABROWN/DD(I,K)
         BETASHEAR=SHEARCONST*FC*FC*SQRT(EPS)*DIK(I,K)**3
         BETADIFFS=DIFFSCONST*FC*FC*DIK(I,K)*DIK(I,K)
         BETADIFFS=BETADIFFS*DABS(WSJ(I)-WSJ(K))
         BETA=BETABROWN+BETASHEAR+BETADIFFS
         XNIK(I,K)=ALPHAAA*BETA
         STAI=16./(PI*0.707*(FP(I)+FP(K))*(0.707*DJ(I))**2.)
         STAK=16./(PI*0.707*(FP(K)+FP(I))*(0.707*DJ(K))**2.)
         TAUIKC(K,I)=STAI*UI(K,I)**2*AMM(I,K)/(DIK(I,K)*AMIK(I,K))
         TAUIKC(I,K)=STAK*UI(I,K)**2*AMM(I,K)/(DIK(I,K)*AMIK(I,K))
         TAUIKC(K,I)=S2MULT*TAUIKC(K,I)
         TAUIKC(I,K)=S2MULT*TAUIKC(I,K)
       ENDDO
      ENDDO
      DO K=1,JCLASSES
       DO I=1,K
         DO M=K,JCLASSES
           AMIKM(I,K,M)=AMASSJ(I)+AMASSJ(K)+AMASSJ(M)
           FPIK=(FP(I)+FP(K))/2.
           FPKM=(FP(K)+FP(M))/2.
           FPMI=(FP(M)+FP(I))/2.
           STA=UI(I,K)*UI(K,M)*AMASSJ(K)/AMIKM(I,K,M)
           STA=STA*DABS(UI(I,K)*AMASSJ(I)+UI(M,K)*AMASSJ(M))
           STA=STA/(UI(M,K)*FPIK*DIK(I,K)+UI(I,K)*FPKM*DIK(K,M))
           TAUIKMC(I,K,M)=S3MULT*STA*64./(3.*PI*(0.707*DJ(K))**2.)
           TAUIKMC(K,I,M)=S3MULT*STA*64./(3.*PI*(0.707*DJ(I))**2.)
           TAUIKMC(I,M,K)=S3MULT*STA*64./(3.*PI*(0.707*DJ(M))**2.)
           TAUIKMC(M,K,I)=TAUIKMC(I,K,M)
           TAUIKMC(M,I,K)=TAUIKMC(K,I,M)
           TAUIKMC(K,M,I)=TAUIKMC(I,M,K)
         ENDDO
       ENDDO
      ENDDO
C
C     CALCULATE PROBABILITY DISTRIBUTION FUNCTION FOR FRAGMENTS
C
      DO I1=1,JCLASSES
       DO I2=I1,JCLASSES
```

```
          DO J=I1,I2
             PF(J,I1,I2)=(AMAX(J)-AMIN(J))/(AMAX(I2)-AMIN(I1))
          ENDDO
        ENDDO
      ENDDO
      RETURN
      END
C
C     *****************************************************************
C
      SUBROUTINE SETUPVEST(TT)
C
C     EXTRACTED AND ADAPTED FROM PROGRAM VEST BY MEHTA AND LI, 1997
C
      INCLUDE 'PATHOSCOM.FOR'
      INCLUDE 'VESTCOM.FOR'
C
      IF(WHEIGHT.LT.1E-10) THEN
         WHEIGHT=1E-10
      END IF
      DZ=H0/FLOAT(NGRIDS)
      ST=STT*60.0
      MMC=DTOUT*60.0
      MMT=DTRUN*60.0
C*    INITIAL DATA **
      DO 1 I=1,NGRIDS
         Z(I)=(FLOAT(I)-0.5)/FLOAT(NGRIDS)*H0
1     CONTINUE
C
      IF(JN.EQ.1) THEN
        DO JC=1,NCL
          DO 2 I=1,NGRIDS
             C0(I,JC)=CI(1,JC)
2         CONTINUE
        ENDDO
      END IF
C
      IF(JN.GT.1.AND.JN.LT.NGRIDS) THEN
        DO I=1,JN-1
          IF(ZI(I+1).LE.ZI(I)) THEN
            WRITE(*,*)
     &      'INCORRECT SELECTION FOR INITIAL CONCENTRATION INPUT.'
            WRITE(*,*)'THE ZI(I) IS NOT IN AN INCREASING ORDER.'
            STOP
          END IF
        END DO
        DO JC=1,NCL
          DO 3 JI=1,JN-1
            DO 4 I=1,NGRIDS
              SS=(FLOAT(I)-0.5)*DZ
              IF(Z(I).LE.ZI(1)) THEN
                C0(I,JC)=CI(1,JC)
              ELSE IF(Z(I).GE.ZI(JN)) THEN
                C0(I,JC)=CI(JN,JC)
              ELSE
                IF(Z(I).GT.ZI(JI).AND.Z(I).LT.ZI(JI+1)) THEN
                  C0(I,JC)=CI(JI,JC)+(CI(JI+1,JC)-CI(JI,JC))
     *                    *(Z(I)-ZI(JI))/(ZI(JI+1)-ZI(JI))
```

```
                  ELSE IF(Z(I).EQ.ZI(JI)) THEN
                     C0(I,JC)=CI(JI,JC)
                     ELSE IF(Z(I).EQ.ZI(JI+1)) THEN
                        C0(I,JC)=CI(JI+1,JC)
                  END IF
               END IF
4            CONTINUE
3         CONTINUE
       ENDDO
       END IF
C
       IF(JN.EQ.NGRIDS) THEN
          DO JC=1,NCL
             DO 5 I=1,NGRIDS
                C0(I,JC)=CI(I,JC)
5         CONTINUE
       ENDDO
       END IF
C
       EROMAS=0.0
C
       DO I=1,NGRIDS
          DO JC=1,NCL
             C(I,JC)=C0(I,JC)
          ENDDO
       END DO
C
       RETURN
       END
C
C****************************************************************
C     ## END SETUP BLOCK
C****************************************************************
C     BEGIN CALCULATION BLOCK
C****************************************************************
C
       SUBROUTINE AGGREGATION00(T)
C
C     CALCULATES AGGREGATION/DISAGGREGATION OF COHESIVE PARTICLES
C     FOR ALL CLASSES IN AN AGGREGATION CHAMBER
C
       INCLUDE 'PATHOSCOM.FOR'
       INCLUDE 'VESTCOM.FOR'
       CHARACTER LOC*4
C
       DO K=1,JCLASSES+1
          DCI(K)=0.D0
          DCK(K)=0.D0
          DCM(K)=0.D0
          DCC2(K)=0.D0
          DCC3(K)=0.D0
          DCX(K)=0.D0
       ENDDO
C
C     SHEAR-INDUCED BREAKAGE
C
       TAUU=XMU*DV/8.
       DO K=1,JCLASSES+1
```

```
        IF(XNJ(K).GT.1.)THEN
          IF(TAUU.GT.TAUSJ(K))THEN
            DCSHEAR(K)=-AMASSJ(K)*XNJ(K)/2.D0
            ANEWMASS=AMASSJ(K)/2.D0
            CALL CLASS(ANEWMASS,KJ)
            DCSHEAR(KJ)=DCSHEAR(KJ)+AMASSJ(K)*XNJ(K)/2.D0
            CJ(K)=CJ(K)+DCSHEAR(K)
            XNJ(K)=CJ(K)/AMASSJ(K)
            CJ(KJ)=CJ(KJ)+DCSHEAR(K)
            XNJ(KJ)=CJ(KJ)/AMASSJ(KJ)
          ENDIF
        ENDIF
      ENDDO
C
C     THREE-BODY COLLISIONS
C
      IF(IKMON.EQ.1.OR.IKMON.EQ.2)THEN
        DO K=1,JCLASSES
          IF(XNJ(K).GT.1.)THEN
            DO I=1,K
              IF(XNJ(I).GT.1)THEN
                DO M=K,JCLASSES
                  IF(XNJ(M).GT.1)THEN
C                   OMIT NEXT LINE FOR SIMPLE CASE
C                   CALL COLLISIONS300(I,K,M,ST)
                    FPIK=(FP(I)+FP(K))/2.
                    FPKM=(FP(K)+FP(M))/2.
                    FPMI=(FP(M)+FP(I))/2.
                    TIK=DIK(I,K)*FPIK/(2.*UI(I,K))
                    TKM=DIK(K,M)*FPKM/(2.*UI(M,K))
                    TMI=DIK(I,M)*FPMI/(2.*UI(M,I))
                    TIKM=2.*3.*(TIK+TKM+TMI)/(4.*3.)
                    XN=(XNIK(I,M)*XNIK(I,K)*TIK*TMI
     &                  +XNIK(K,I)*XNIK(K,M)*TKM*TIK
     &  +XNIK(M,K)*XNIK(M,I)*TMI*TKM)*XNJ(I)*XNJ(K)*XNJ(M)/(TIKM)
                    IF(RANMULT.GT.0)THEN
                      CALL RANDOM_NUMBER(RNO)
                      RMULT=1.+RANMULT*(0.5-RNO)
                      IF(RMULT.LT.0)RMULT=-RMULT
                    ELSE
                      RMULT=1.
                    ENDIF
                    TAUK=TAUIKMC(I,K,M)*RMULT
                    TAUI=TAUIKMC(K,I,M)*RMULT
                    TAUM=TAUIKMC(I,M,K)*RMULT
                    SI=TAUSJ(I)
                    SK=TAUSJ(K)
                    SM=TAUSJ(M)
                    FNI=1.
                    FNK=1.
                    FNM=1.
                    CIA=AMASSJ(I)*XN*DTL
                    IF(CJ(I)-CIA.LT.0.)THEN
                      FNI=0.9D0*CJ(I)/CIA
                      NLIMIT=NLIMIT+1
                    ENDIF
                    CK=AMASSJ(K)*XN*DTL
                    IF(CJ(K)-CK.LT.0.)THEN
```

```
                        FNK=0.9D0*CJ(K)/CK
                        NLIMIT=NLIMIT+1
                      ENDIF
                      CM=AMASSJ(M)*XN*DTL
                      IF(CJ(M)-CM.LT.0.)THEN
                        FNM=0.9D0*CJ(M)/CM
                        NLIMIT=NLIMIT+1
                      ENDIF
                      XN=DMIN1(FNI,FNK,FNM)*XN
                      DCCI=AMASSJ(I)/AMASSJ(K)
                      DCCK=1.
                      DCCM=AMASSJ(M)/AMASSJ(K)
                      DCM(I)=DCM(I)-DCCI
                      DCM(K)=DCM(K)-DCCK
                      DCM(M)=DCM(M)-DCCM
                      IF(SI.GE.TAUI.AND.SK.GE.TAUK.AND.SM.GE.TAUM)THEN
C                       TYPE 3A1
                        CALL CLASS(AMIKM(I,K,M),NJC)
                        DCM(NJC)=DCM(NJC)+DCCI+DCCK+DCCM
                      ELSE
                        IF(SI.GE.TAUI.AND.SK.GE.TAUK.AND.SM.LT.TAUM)THEN
C                         TYPE 3D2
                          XF=0.5D0
                          XMASS=AMASSJ(I)+AMASSJ(M)
                          CALL CLASS(XMASS,I2)
                          I2=MAX(1,I,I2-1)
                          DO J=I,I2
                            DCM(J)=DCM(J)+(DCCI+0.5D0*DCCM)*XF*PF(J,I,I2)
                          ENDDO
                          XMASS=AMASSJ(K)+AMASSJ(M)
                          CALL CLASS(XMASS,I2)
                          I2=MAX(1,K,I2-1)
                          DO J=K,I2
                            DCM(J)=DCM(J)+(DCCK+0.5D0*DCCM)*XF*PF(J,K,I2)
                          ENDDO
                          XMASS=AMASSJ(I)+AMASSJ(K)
                          CALL CLASS(XMASS,I1)
                          XMASS=AMASSJ(I)+AMASSJ(K)+AMASSJ(M)*0.5D0
                          CALL CLASS(XMASS,I2)
                          I2=MAX(1,I1,I2-1)
                          DO J=I1,I2
                            DCM(J)=DCM(J)+(DCCI+DCCK+3.D0*DCCM/16.D0)
     &                        *XF*PF(J,I1,I2)
                          ENDDO
                          XMASS=AMASSJ(M)*0.5D0
                          CALL CLASS(XMASS,I2)
                          I2=MAX(1,I2-1)
                          DO J=1,I2
                            DCM(J)=DCM(J)+(13.D0*DCCM/16.D0)*XF*PF(J,1,I2)
                          ENDDO
                        ELSE
                          IF(SI.GE.TAUI.AND.SK.LT.TAUK.AND.SM.LT.TAUM)THEN
C                           TYPE 3D3
                            XF=1.D0/3.D0
                            XMASS=AMASSJ(I)+AMASSJ(K)
                            CALL CLASS(XMASS,I2)
                            I2=MAX(1,I,I2-1)
                            DO J=I,I2
```

```
                  DCM(J)=DCM(J)+(DCCI+0.5D0*DCCK)*XF*PF(J,I,I2)
                ENDDO
                XMASS=AMASSJ(K)+AMASSJ(M)*0.5D0
                CALL CLASS(XMASS,I2)
                I2=MAX(1,I2-1)
                DO J=1,I2
                  DCM(J)=DCM(J)+(0.5D0*DCCK+3.D0*DCCM/16.D0)
     &             *XF*PF(J,1,I2)
                ENDDO
                XMASS=AMASSJ(M)*0.5D0
                CALL CLASS(XMASS,I2)
                I2=MAX(1,I2-1)
                DO J=1,I2
                  DCM(J)=DCM(J)+2.D0*(13.D0*DCCM/16.D0)
     &             *XF*PF(J,1,I2)
                ENDDO
                XMASS=AMASSJ(I)+AMASSJ(M)
                CALL CLASS(XMASS,I2)
                I2=MAX(1,I,I2-1)
                DO J=I,I2
                  DCM(J)=DCM(J)+(DCCI+0.5D0*DCCM)*XF*PF(J,I,I2)
                ENDDO
                XMASS=AMASSJ(K)*0.5D0+AMASSJ(M)
                CALL CLASS(XMASS,I2)
                I2=MAX(1,I2-1)
                DO J=1,I2
                  DCM(J)=DCM(J)+(3.D0*DCCK/16.D0+0.5D0*DCCM)
     &             *XF*PF(J,1,I2)
                ENDDO
                XMASS=AMASSJ(K)*0.5D0
                CALL CLASS(XMASS,I1)
                I2=MAX(1,I1,K-1)
                DO J=I1,I2
                  DCM(J)=DCM(J)+2.D0*(13.D0*DCCK/16.D0)
     &             *XF*PF(J,I1,I2)
                ENDDO
                XMASS=AMASSJ(I)+(AMASSJ(K)+AMASSJ(M))
     &           *0.5D0
                CALL CLASS(XMASS,I2)
                I2=MAX(1,I,I2-1)
                DO J=I,I2
                  DCM(J)=DCM(J)+(DCCI+3.D0*(DCCK+DCCM)/16.D0)
     &             *XF*PF(J,I,I2)
                ENDDO
              ELSE
C               TYPE 3D4
                XF=1.D0/3.D0
                XMASS=AMASSJ(I)*0.5D0
                CALL CLASS(XMASS,I1)
                I2=MAX(1,I-1,I1)
                DO J=I1,I2
                  DCM(J)=DCM(J)+2.D0*(13.D0*DCCI/16.D0)
     &             *XF*PF(J,I1,I2)
                ENDDO
                XMASS=AMASSJ(K)*0.5D0
                CALL CLASS(XMASS,I1)
                I2=MAX(1,K-1,I1)
                DO J=I1,I2
```

```fortran
                  DCM(J)=DCM(J)+2.D0*(13.D0*DCCK/16.D0)
     &              *XF*PF(J,I1,I2)
                ENDDO
                XMASS=AMASSJ(M)*0.5D0
                CALL CLASS(XMASS,I1)
                I2=MAX(1,M-1,I1)
                DO J=I1,I2
                  DCM(J)=DCM(J)+2.D0*(13.D0*DCCM/16.D0)
     &              *XF*PF(J,I1,I2)
                ENDDO
                XMASS=AMASSJ(I)*0.5D0+AMASSJ(K)
                CALL CLASS(XMASS,I2)
                I2=MAX(1,I2-1)
                DO J=1,I2
                  DCM(J)=DCM(J)+(3.D0*DCCI/16.D0+0.5D0*DCCK)
     &              *XF*PF(J,1,I2)
                ENDDO
                XMASS=AMASSJ(M)*0.5D0+AMASSJ(K)
                CALL CLASS(XMASS,I2)
                I2=MAX(1,I2-1)
                DO J=1,I2
                  DCM(J)=DCM(J)+(3.D0*DCCM/16.D0+0.5D0*DCCK)
     &              *XF*PF(J,1,I2)
                ENDDO
                XMASS=AMASSJ(K)*0.5D0+AMASSJ(M)
                CALL CLASS(XMASS,I2)
                I2=MAX(1,I2-1)
                DO J=1,I2
                  DCM(J)=DCM(J)+(3.D0*DCCK/16.D0+0.5D0*DCCM)
     &              *XF*PF(J,1,I2)
                ENDDO
                XMASS=AMASSJ(I)*0.5D0+AMASSJ(M)
                CALL CLASS(XMASS,I2)
                I2=MAX(1,I2-1)
                DO J=1,I2
                  DCM(J)=DCM(J)+(3.D0*DCCI/16.D0+0.5D0*DCCM)
     &              *XF*PF(J,1,I2)
                ENDDO
                XMASS=AMASSJ(M)*0.5D0+AMASSJ(I)
                CALL CLASS(XMASS,I2)
                I2=MAX(1,I2-1)
                DO J=1,I2
                  DCM(J)=DCM(J)+(3.D0*DCCM/16.D0+0.5D0*DCCI)
     &              *XF*PF(J,1,I2)
                ENDDO
                XMASS=AMASSJ(K)*0.5D0+AMASSJ(I)
                CALL CLASS(XMASS,I2)
                I2=MAX(1,I2-1)
                DO J=1,I2
                  DCM(J)=DCM(J)+(3.D0*DCCK/16.D0+0.5D0*DCCI)
     &              *XF*PF(J,1,I2)
                ENDDO
              ENDIF
            ENDIF
          ENDIF
        ENDIF
        DO J=1,JCLASSES+1
          DCX(J)=DCM(J)*XN+DCX(J)
          DCM(J)=0.D0
```

```
                       ENDDO
                         XN3(K)=XN3(K)+XN
                     ENDIF
                   ENDDO
                   DO J=1,JCLASSES+1
                     DCI(J)=DCI(J)+DCX(J)
                     DCX(J)=0.D0
                   ENDDO
                 ENDIF
               ENDDO
             DO J=1,JCLASSES+1
               DCK(J)=DCK(J)+DCI(J)*AMASSJ(K)
               DCI(J)=0.D0
             ENDDO
           ENDIF
         ENDDO
         DO J=1,JCLASSES+1
           DCC3(J)=DCC3(J)+DCK(J)*DTL
           CJ(J)=CJ(J)+DCC3(J)
           DCK(J)=0.D0
         ENDDO
       ENDIF
C
C      TWO-BODY COLLISIONS
C
       DO K=1,JCLASSES
         IF(XNJ(K).GT.1)THEN
           DO I=1,K
             IF(XNJ(I).GT.1.)THEN
C            OMIT NEXT LINE FOR SIMPLE CASE
C            CALL COLLISIONS200(I,K)
             XNJ(I)=(CJ(I)/AMASSJ(I) )
             XNJ(K)=(CJ(K)/AMASSJ(K))
             XN=XNIK(I,K)*(XNJ(I)-XN3(I))*(XNJ(K)-XN3(K))
             IF(XN.LT.0.)XN=0.1D0
             XN2(K)=XN2(K)+XN
             FNI=1.
             FNK=1.
             CIA=AMASSJ(I)*XN*DTL
             IF(CJ(I)-CIA.LT.0.)THEN
               FNI=0.9*CJ(I)/CIA
               NLIMIT=NLIMIT+1
             ENDIF
             CK=AMASSJ(K)*XN*DTL
             IF(CJ(K)-CK.LT.0.)THEN
               FNK=0.9*CJ(K)/CK
               NLIMIT=NLIMIT+1
             ENDIF
             XN=DMIN1(FNI,FNK)*XN
             DCCI=AMASSJ(I)/AMASSJ(K)
             DCCK=1.
             DCI(I)=DCI(I)-DCCI
             DCI(K)=DCI(K)-DCCK
             IF(RANMULT.GT.0)THEN
               CALL RANDOM_NUMBER(RNO)
               RMULT=1.+RANMULT*(0.5-RNO)
               IF(RMULT.LT.0)RMULT=-RMULT
             ELSE
```

```
               RMULT=1.
             ENDIF
             TAUK=TAUIKC(I,K)*RMULT
             TAUI=TAUIKC(K,I)*RMULT
             IF(TAUSJ(I).GE.TAUI.AND.TAUSJ(K).GE.TAUK)THEN
C              TYPE 2A1
               CALL CLASS(AMIK(I,K),NJC)
               DCI(NJC)=DCI(NJC)+DCCI+DCCK
             ELSE
               IF(TAUSJ(I).GE.TAUI.AND.TAUSJ(K).LT.TAUK)
     &              THEN
C                TYPE 2D2
                 CALL CLASS((AMASSJ(K)/2.D0),I1)
                 I2=MAX(1,I1,K-1)
                 DO J=I1,I2
                   DCI(J)=DCI(J)+13.D0*DCCK*PF(J,I1,I2)/16.D0
                 ENDDO
                 CALL CLASS((AMASSJ(I)+AMASSJ(K)/2.D0),I2)
                 I2=MAX(1,I,I2-1)
                 DO J=I,I2
                   DCI(J)=DCI(J)+(DCCI+3.D0*DCCK/16.D0)*PF(J,I,I2)
                 ENDDO
               ELSE
C                TYPE 2D3
                 CALL CLASS((AMASSJ(K)/2.D0),I1)
                 I2=MAX(1,I1,K-1)
                 DO J=I1,I2
                   DCI(J)=DCI(J)+(13.D0*DCCK/16.D0)*PF(J,I1,I2)
                 ENDDO
                 I2=I1
                 CALL CLASS((AMASSJ(I)/2.D0),I1)
                 I2=MAX(1,I1,I-1)
                 DO J=I1,I2
                   DCI(J)=DCI(J)+(13.D0*DCCI/16.D0)*PF(J,I1,I2)
                 ENDDO
                 CALL CLASS(((AMASSJ(I)+AMASSJ(K))/2.D0),I2)
                 I2=MAX(1,I2-1)
                 DO J=1,I2
                   DCI(J)=DCI(J)+(3.D0*(DCCI+DCCK)/16.D0)*PF(J,1,I2)
                 ENDDO
               ENDIF
             ENDIF
             DO J=1,JCLASSES+1
               DCK(J)=DCK(J)+DCI(J)*AMASSJ(K)*XN*DTL
               DCI(J)=0.D0
             ENDDO
           ENDIF
         ENDDO
       ENDIF
     ENDDO
C
C     CALCULATE TOTALS
C
     TOTAL1=TOTAL2
     TOTAL2=0.D0
     DCGROSS=0.D0
     DC3GROSS=0.D0
     DO J=1,JCLASSES+1
```

```
      DCC2(J)=DCC2(J)+DCK(J)
      DCK(J)=0.D0
      CJ(J)=CJ(J)+DCC2(J)
      XNJ(J)=CJ(J)/AMASSJ(J)
      TOTAL2=TOTAL2+CJ(J)
      IF(CJ(J).LT.0.)THEN
        NLIMIT=NLIMIT+1
        NWRITE=NWRITE+1
        IF(NWRITE.LE.100)
     &    WRITE(22,23)T,J,CJ(J)
   23    FORMAT(' ERROR:NEGATIVE MASS: T,J,CJ = ',E12.6,I5,E12.6)
        CJ(J)=0.D0
        XNJ(J)=0.D0
      ENDIF
      DCGROSS=DCGROSS+DABS(DCC2(J)+DCC3(J))
      DC3GROSS=DC3GROSS+DABS(DCC3(J))
      ENDDO
      CHANGE12=TOTAL2-TOTAL1
      CUMCHANGE=DABS(TOTAL2-TOTAL0)/TOTAL0
      IF(CUMCHANGE.GT.0.1.AND.ITYPE.EQ.0)THEN
        CALL OUTPUT00(T)
        WRITE(21,1)T,CUMCHANGE
        WRITE(22,1)T,CUMCHANGE
        WRITE(*,1)T,CUMCHANGE
    1   FORMAT(1X,'COMPUTATION STOPPED AT T ',G12.6,
     &  ' FRACTIONAL TOTAL MASS CHANGE OF ',G12.3)
        STOP
      ENDIF
      IF(IKMON.NE.0.AND.DCGROSS.NE.0.)THEN
        IF(DABS(DC3GROSS/DCGROSS).LT.0.01.AND.IKMON.NE.2)IKMON=0
      ENDIF
      RETURN
      END
C
C*******************************************************************
C
      SUBROUTINE AGGREGATION10(K)
C
C     CALC AGGREGATION/DISAGGREGATION OF COHESIVE PARTICLES FOR TRACKING
C
      INCLUDE 'PATHOSCOM.FOR'
      INCLUDE 'VESTCOM.FOR'
C
C     NOT YET IMPLEMENTED
C
      RETURN
      END
C
C*******************************************************************
C
      SUBROUTINE BED01(K)
C
C     CALCULATE EROSION OF KERNEL
C
      INCLUDE 'PATHOSCOM.FOR'
      INCLUDE 'VESTCOM.FOR'
C
C      NOT YET IMPLEMENTED
```

```
C
      RETURN
      END
C
C
C******************************************************************
C
         SUBROUTINE BEDFLUX1(WSBB,C0BB,JCC,USTAR,FS,ERCONST)
C
C        BEDFLUX SUB FOR FLUID MUD
C        ADOPTED FROM PROGRAM VEST BY MEHTA AND LI, 1997
C
      INCLUDE 'PATHOSCOM.FOR'
      INCLUDE 'VESTCOM.FOR'
      DIMENSION FS(MAXC)
C
      IF(RIG.GE.RIC) THEN
          FEN=0.0
      ELSE
          FEN=RHOM*USTAR*ENT0*(RIC*RIC/RIG-RIG)**ENN
      END IF
      FSE=-1.0*DPS*WSBB*C0BB
      FS(JCC)=FEN+FSE
      RETURN
      END
C
C
C******************************************************************
C
         SUBROUTINE BEDFLUX2(WSBB,C0BB,JCC,FS,ERCONST)
C
C        BEDFLUX SUB FOR BED
C        ADAPTED FROM PROGRAM VEST BY MEHTA AND LI, 1997
C
      INCLUDE 'PATHOSCOM.FOR'
      INCLUDE 'VESTCOM.FOR'
      DIMENSION FS(MAXC)
C
C*       BED DENSITY              *****
      IF(DZB.GE.M0) THEN
        WRITE(*,*)'ALL THE SEDIMENT AT THE BOTTOM IS ERODED!'
        WRITE(*,*)'BED DEPTH IS INCORRECT OR TIME STEP IS TOO LARGE!'
        STOP
      ELSE IF(DZB.LT.0.0) THEN
          RHOB=RHBBAR*BDP1
      ELSE
          RHOB=RHBBAR*BDP1*((M0-DZB)/M0)**BDP2
      END IF
C
C*       EROSION SHEAR STRENGTH       *****
C
      TAUERO=TCP1*(RHOB/RHOSED-PHIC)**TCP2
      ERCONST=ERSMAX*EXP(-ERP1*TAUERO**ERP2)
C
C*       EROSION OR DEPOSITION RATE        *****
C
      IF(TAUDEP.GT.0.)THEN
        IF(TAUBED.LT.TAUDEP)THEN
```

```
            FS(JCC)=-1.0*WSBB*C0BB*(1.0-TAUBED/TAUDEP)
          ELSE
            IF(TAUBED.GE.TAUERO) THEN
              FS(JCC)=ERSMAX*EXP(-ERP1*TAUERO**ERP2)*(TAUBED-TAUERO)
            ELSE
              FS(JCC)=0.
            ENDIF
          ENDIF
        ELSE
          IF(TAUBED.LE.TAUSJ(JCC+1))THEN
            FS(JCC)=-1.0*WSBB*C0BB*(1.0-TAUBED/TAUSJ(JCC+1))
C         THERE MUST BE SOME CLASS JCC MATERIAL IN THE BED BEFORE IT CAN
ERODE
C         NOT YET IMPLEMENTED
C         TAUERO=TAUSJ(JCC)
          ELSE
C           IF(TAUBED.GT.TAUERO)THEN
C             FS(JCC)=ERSMAX*EXP(-ERP1*TAUSJ(JCC)**ERP2)*
C    &                           (TAUBED-TAUSJ(JCC))
C           ELSE
              FS(JCC)=0.
C           ENDIF
          ENDIF
        END IF
C
C*        BED CHANGE          ********
C
      DZBT=DZB+DT*FS(JCC)/RHOB
      IF(DZBT.LE.M0) THEN
        DZB=DZBT
      ELSE
        FS(JCC)=(M0-DZB)*RHOB/DT
        DZB=M0
      END IF
      RETURN
      END
C
C*****************************************************************
C
      SUBROUTINE CLASS(XMASS,NCLASS)
C
C     CALCULATE CLASS OF NEW PARTICLE
C
      INCLUDE 'PATHOSCOM.FOR'
      INCLUDE 'VESTCOM.FOR'
C
      I=1
      DO WHILE(XMASS.GT.AMAX(I))
        I=I+1
      ENDDO
      NCLASS=I
      IF(NCLASS.EQ.0)NCLASS=1
      IF(NCLASS.GT.MAXC)THEN
        NCLASS=MAXC-1
        WRITE(21,1)XMASS
  1     FORMAT('WARNING: PARTICLE OF MASS = ',E12.6,'FORMED;',
     &         'EXCEEDING MAXIMUM SIZE CLASS.')
        IF(NCLASS.GT.JCLASSES.OR.NCLASS.LT.1)WRITE(33,*)'CLASS',
```

```
      &   XMASS,NCLASS
        ENDIF
        RETURN
        END
C
C*************************************************************************
C
        SUBROUTINE COLLISIONS200(I,K)
C
C       COMPUTES NUMBER OF 2-BODY COLLISIONS AND COLLISION STRESSES
C       IN AGGREGATION CHAMBER
C
        INCLUDE 'PATHOSCOM.FOR'
        INCLUDE 'VESTCOM.FOR'
C
C       NOT YET IMPLEMENTED
C
        RETURN
        END
C
C
C*************************************************************************
C
        SUBROUTINE COLLISIONS300(I,K,M,STR)
C
C       COMPUTES NUMBER OF 3-BODY COLLISIONS AND COLLISION STRESSES
C       IN AGGREGATION CHAMBER
C
        INCLUDE 'PATHOSCOM.FOR'
        INCLUDE 'VESTCOM.FOR'
C
C       NOT YET IMPLEMENTED
C
        RETURN
        END
C
C*************************************************************************
C
        SUBROUTINE DENSITY(D,RHOP)
C
C       COMPUTES PARTICLE DENSITY
C
        INCLUDE 'PATHOSCOM.FOR'
        INCLUDE 'VESTCOM.FOR'
C
        DDD=D*1.E6
        IF(IRHO.EQ.1)THEN
C         BURBAN EQN
          XTERM=(1-TOTAL0)*(1-DV*1.E-3)
          RHOP=RHO+1650.*(4/DDD)**XTERM
        ELSE
          IF(IRHO.EQ.2)THEN
C           MCCAVE & KRANCK FORM
            IF(DDD.LE.D1) THEN
              RHOP=RHO+RHOG
            ELSE
              IF(DDD.LE.D2) THEN
                RHOP=RHO+R1*DDD**ER1
```

```fortran
            ELSE
              IF(DDD.LE.D3) THEN
                RHOP=RHO+R2*DDD**ER2
              ELSE
                RHOP=RHO+R2*1000**ER2
              ENDIF
            ENDIF
          ENDIF
        ELSE
          IF(IRHO.EQ.3.OR.IRHO.EQ.4)THEN
C           KRANENBURG FRACTAL EQN
            RHOP=RHO+(R1*(DG/DDD)**(3.-ER1))
          ENDIF
        ENDIF
      ENDIF
      IF(RHOP.GT.RHOG)RHOP=RHOG
      RETURN
      END
C
C
C****************************************************************************
C
      SUBROUTINE DENSITYPL(D,RHOP)
C
C     COMPUTES PARTICLE DENSITY USING POWER LAW
C
      INCLUDE 'PATHOSCOM.FOR'
      INCLUDE 'VESTCOM.FOR'
C
C     CONVERT DIAMETERS BACK TO MICRONS AND THEN
C     APPLY COEFFICIENTS ACCORDING TO PARTICLE SIZE
C
      DDD=D*1.E6
      IF(DDD.LE.D1) THEN
        RHOP=RHO+RHOG
      ELSE
        IF(DDD.LE.D2) THEN
          RHOP=RHO+R1*DDD**ER1
        ELSE
          IF(DDD.LE.D3) THEN
            RHOP=RHO+R2*DDD**ER2
          ELSE
            RHOP=RHO+R2*1000**ER2
          ENDIF
        ENDIF
      ENDIF
      RETURN
      END
C
C****************************************************************************
C
      SUBROUTINE DEPOSITION01(K)
C
C     COMPUTES DEPOSITION PROBABILITY
C
      INCLUDE 'PATHOSCOM.FOR'
      INCLUDE 'VESTCOM.FOR'
C
```

```fortran
C     NOT YET IMPLEMENTED.
C
      RETURN
      END
C
C******************************************************************
C
      SUBROUTINE DIAMETER(XMASS,DIAM,RHOP)
C
C     CALCULATES PARTICLE DIAMETER(M)& DENSITY (KG/CU M) FROM MASS(KG)
C
      INCLUDE 'PATHOSCOM.FOR'
      INCLUDE 'VESTCOM.FOR'
C
      IF(RHOP.EQ.0.)THEN
        ERROR=1.
        RHONEW=1100.
        DO WHILE(ERROR.GT.0.005)
          RHOOLD=RHONEW
         IF(RHOOLD.EQ.0.)RHOOLD=1.
          DIAM=(6.*XMASS/(PI*RHOOLD))**(1./3.)
          CALL DENSITY(DIAM,RHONEW)
          ERROR=DABS(RHONEW-RHOOLD)/RHOOLD
        ENDDO
        RHOP=RHONEW
      ELSE
        IF((PI*RHOP).EQ.0)WRITE(22,1)
    1 FORMAT(' ERROR IN DIAMETER. DIVIDE BY ZERO.')
        DIAM=(6.*XMASS/(PI*RHOP))**(1./3.)
        CALL DENSITY(DIAM,RHOP)
      ENDIF
      RETURN
      END
C
C************************************************************************
C
      SUBROUTINE HYDROFLOW2()
C
C     HYDRODYNAMICS SUB--FLOW FOR BED
C     ADAPTED FROM PROGRAM VEST BY MEHTA AND LI, 1997
C
      INCLUDE 'PATHOSCOM.FOR'
      INCLUDE 'VESTCOM.FOR'
C
      KKSS=3.15*100000.0*9.8*3.0*QN**6.0
      Y0=KKSS/30.1
      FF=8.0*9.8*QN**2.0/H0**(1.0/3.0)
      TAUBED=RHOW*FF*UU**2.0/8.0
C     FOLLOWING LINE HARDWIRED FOR WES FLUME
      USTAR0=SQRT(G)*(UU*QN)/(H0*.229/(2.*H0+.229))**0.1667
      DO 2 I=2,NGRIDS+1
        ZZ=(FLOAT(I-1))*DZ
        DVEL(I)=UU/ZZ/(LOG(H0/Y0)-1.0)
        KN(I)=(VKK*VKK*UU)/(LOG(H0/Y0)-1.0)*ZZ*(H0-ZZ)/H0
C     FOLLOWING LINES HARDWIRED FOR WES FLUME. ORIG LINE ABOVE.
C       KN(I)=5.*VKK*USTAR0*ZZ*(H0-ZZ)/H0
    2 CONTINUE
      RETURN
```

```
      END
C
C***********************************************************************
C
C
      SUBROUTINE HYDROWAVE1(RD)
C
C     HYDRODYNAMICS SUB--WAVE FOR FLUID MUD
C     ADOPTED FROM PROGRAM VEST BY MEHTA AND LI, 1997
C
      INCLUDE 'PATHOSCOM.FOR'
      INCLUDE 'VESTCOM.FOR'
C
      SIG=2.0*3.14159265/WPERIOD
      QKK=(SIG*SIG)/9.8
1     QK=SIG**2.0/(9.8*TANH(QKK*H0))
      IF(ABS(QK-QKK).GT.0.000001) THEN
        QKK=0.5*(QK+QKK)
        GOTO 1
      END IF
      WNU=0.5*(QK+QKK)
      WLENGTH=2.0*3.14159265/WNU
      WFR=2.0*PI/WPERIOD
      DO 2 I=2,NGRIDS+1
        ZZ=(FLOAT(I-1))*DZ
        DVEL(I)=WHEIGHT/2.0*WFR*WNU
     *          *SINH(WNU*ZZ)/SINH(WNU*H0)
C     KN(I)=WDIFFK*WFR*WHEIGHT**2.0*(SINH(WNU*Z))**2.0
C     *                          /(2.0*(SINH(WNU*H0))**2.0)
      KN(I)=WDIFFK*WFR*WHEIGHT**2.0*SINH(WNU*H0/(H0+RD)*(ZZ+RD))
     *          *COSH(WNU*ZZ)/(2.0*(SINH(WNU*H0))**2.0)
2     CONTINUE
      RIG=G*(XNU*WPERIOD)**0.5*(RHOM-RHOW)/RHOW/(DUDB*DUDB)
      UB=SIG/2.0*WHEIGHT/(SINH(WNU*H0))
      RETURN
      END
C
C
C***********************************************************************
C
      SUBROUTINE HYDROWAVE2()
C
C     HYDRODYNAMICS SUB--WAVE FOR BED
C     ADOPTED FROM PROGRAM VEST BY MEHTA AND LI, 1997
C
      INCLUDE 'PATHOSCOM.FOR'
      INCLUDE 'VESTCOM.FOR'
C
      SIG=2.0*3.14159265/WPERIOD
      QKK=(SIG*SIG)/9.8
1     QK=SIG**2.0/(9.8*TANH(QKK*H0))
      IF(ABS(QK-QKK).GT.0.000001) THEN
        QKK=0.5*(QK+QKK)
        GOTO 1
      END IF
      WNU=0.5*(QK+QKK)
      WLENGTH=2.0*3.14159265/WNU
      WFR=2.0*PI/WPERIOD
```

```
      DO 2 I=2,NGRIDS+1
        ZZ=(FLOAT(I-1))*DZ
        DVEL(I)=WHEIGHT/2.0*WFR*WNU*SINH(WNU*ZZ)/SINH(WNU*H0)
        KN(I)=WDIFFK*WFR*WHEIGHT**2.0*(SINH(WNU*ZZ))
     *        *COSH(WNU*ZZ)/(2.0*(SINH(WNU*H0))**2.0)
2     CONTINUE
      TAUBED=RHOW*WFRIC/2.0*(WHEIGHT/2.0*WFR/SINH(WNU*H0))**2.0
      RETURN
      END
C
C*****************************************************************************
C
      SUBROUTINE INTERPOLATE(X1,X2,X3,T)
C
C     INTERPOLATE HYDRO & SED RESULTS FOR NEW TIME POINT
C
      INCLUDE 'PATHOSCOM.FOR'
      INCLUDE 'VESTCOM.FOR'
C
C     NOT YET IMPLEMENTED
C
      TZ=X1+X2+X3+T
      RETURN
      END
C
C*****************************************************************************
C
      SUBROUTINE INTERPOLATE00(T)
C
C     INTERPOLATE HYDRO & SED RESULTS FOR NEW TIME POINT IN CHAMBER
C
      INCLUDE 'PATHOSCOM.FOR'
      INCLUDE 'VESTCOM.FOR'
C
      IF((T2-T1).EQ.0)WRITE(*,1)
    1 FORMAT('ERROR: T2-T1=0 IN INTERPOLATE00')
      S=S1+(S2-S1)*(T-T1)/(T2-T1)
      TEMP=TEMP1+(TEMP2-TEMP1)*(T-T1)/(T2-T1)
      EPS=EPS1+(EPS2-EPS1)*(T-T1)/(T2-T1)
      DV=DV1+(DV2-DV1)*(T-T1)/(T2-T1)
      XV=XV1+(XV2-XV1)*(T-T1)/(T2-T1)
      YV=YV1+(YV2-YV1)*(T-T1)/(T2-T1)
      ZV=ZV1+(ZV2-ZV1)*(T-T1)/(T2-T1)
      TAUU=DV*XMU/8
      RETURN
      END
C
C*****************************************************************************
C
      SUBROUTINE SETTLVEL(D,RHOP,WSS)
C
C     CALCULATES SETTLING VELOCITY BY MODIFIED STOKES LAW
C
      INCLUDE 'PATHOSCOM.FOR'
      INCLUDE 'VESTCOM.FOR'
C
      ERROR=1.
      CONST=4.*G*(RHOP-RHO)/(3*RHO)
```

```fortran
      CD=10.
      WSOLD=.01
      DO WHILE(DABS(ERROR).GT.0.01)
        WSNEW=(CONST*D/CD)**0.5
        RE=WSNEW*D/XNU
        IF(RE.EQ.0.)RE=0.1
        W=LOG10(RE)
        RE24=24/RE
        IF(RE.LE.0.01) THEN
          CD=RE24*(1+3*RE/16.)
        ELSE
          IF(RE.LE.20) THEN
            CD=RE24*(1+0.1315*RE**(0.82-0.05*W))
          ELSE
            IF(RE.LE.260) THEN
              CD=RE24*(1+0.1935*RE**0.6305)
            ELSE
              IF(RE.LE.1500) THEN
                CD=10**(1.6435-1.1242*W+0.1558*W**2)
              ELSE
                CD=10**(-2.4571+2.558*W-0.9295*W**2+0.1409*W**3)
              ENDIF
            ENDIF
          ENDIF
        ENDIF
        ERROR=(WSOLD-WSNEW)/WSOLD
        WSOLD=WSNEW
      ENDDO
      WSS=WSNEW
      RETURN
      END
C
C****************************************************************************
C
      SUBROUTINE STRENGTH(RHOP,TAUS)
C
C     CALCULATE AGGREGATE STRENGTH
C
      INCLUDE 'PATHOSCOM.FOR'
      INCLUDE 'VESTCOM.FOR'
C
      IF(IRHO.EQ.1)THEN
        TAUS=B11*(RHOP-RHO)**EM7
      ELSE
        IF(IRHO.EQ.2)THEN
          TAUS=B11*(RHOP-RHO)**EM7
        ELSE
          IF(IRHO.EQ.3)THEN
            TAUS=B11*((RHOP-RHO)/(RHO))**(2./(3.-EM7))
          ELSE
            IF(IRHO.EQ.4)THEN
              TERM1=24.42-S/2.
              TERM2=(EPS*GMULT/(8.48*12.1))**(-0.1691)
              TERM3=(SUMCONC/0.8)**(-1.657)
              BTAU=0.2561*(TERM1*TERM2*TERM3)
              TAUS=BTAU*((RHOP-RHO)/(RHO))**(2./(3.-EM7))
              WRITE(*,*)'BTAU = ',BTAU
              WRITE(33,*)'BTAU = ',BTAU
```

```fortran
            ELSE
              TAUS=B11*((RHOP-RHO)/(RHO))**(2./(3.-EM7))
            ENDIF
          ENDIF
        ENDIF
      ENDIF
C
      RETURN
      END
C
C     ****************************************************************
C
      SUBROUTINE STM(N,X,Z,A,B,C)
C
C     SOLVES TRI-DIAGONAL MATRIX EQUATIONS **
C     ADOPTED FROM PROGRAM VEST BY MEHTA AND LI, 1997
C
C       DIMENSION X(N),Z(N),A(N),B(N),C(N)
C       DIMENSION Y(500),P(500),Q(500),R(500)
      REAL*8 X(N),Z(N),A(N),B(N),C(N)
      REAL*8 Y(500),P(500),Q(500),R(500)
      Q(1)=A(1)
      DO 1 I=1,N-1
        R(I)=B(I)
        P(I)=C(I)/Q(I)
        Q(I+1)=A(I+1)-P(I)*B(I)
1     CONTINUE
      Y(1)=Z(1)
      DO 2 I=1,N-1
        Y(I+1)=Z(I+1)-Y(I)*P(I)
2     CONTINUE
      X(N)=Y(N)/Q(N)
      DO 3 I=N-1,1,-1
        X(I)=(Y(I)-R(I)*X(I+1))/Q(I)
3     CONTINUE
      RETURN
      END
C
C***************************************************************************
C
      SUBROUTINE SUSPENSION10(K,T)
C
C     CALCULATES PATH, AGGREGATION, AND DEPOSITION OF
C     PARTICLES IN SUSPENSION BY DETERMINISTIC, SIMPLE PATH METHOD.
C
      INCLUDE 'PATHOSCOM.FOR'
      INCLUDE 'VESTCOM.FOR'
C
C     NOT YET IMPEMENTED
C
      RETURN
      END
C
C***************************************************************
C
      SUBROUTINE TRAJECTORY01(K)
C
C     CALCULATE PARTICLE TRAJECTORY BY SIMPLE VECTOR SUM
```

```
C
      INCLUDE 'PATHOSCOM.FOR'
      INCLUDE 'VESTCOM.FOR'
C
C     NOT YET IMPLEMENTED
C
      RETURN
      END
C
C******************************************************************
C
      SUBROUTINE TWOBODY01(I,K)
C
C     CALCULATES TWO-BODY COLLISIONS
C
      INCLUDE 'PATHOSCOM.FOR'
      INCLUDE 'VESTCOM.FOR'
C
C     CALCULATE COLLISION EFFICIENCY
C
      DSUM=DJ(I)+DK(K)
      TR=1-0.875*TEMP/30.
      SR=S/2.D0
      CECR=CEC/9.
      AMR=RHOJ(I)/RHOK(K)
      AMR=AMR*(DJ(I)/DK(K))**3
      DGR=DG/DK(K)
      IF(AMR.LT.1.AND.AMR.NE.0.)THEN
        AMR=1./AMR
      ENDIF
C     FIXX
      UI(I,K)=DSUM*SQRT(EPS*TO15PINU)/2.D0
      REP=UI(I,K)*DSUM/XNU
       IF(REP.NE.0.AND.AMR.NE.0.)THEN
          PIC=DGR*SR*TR*CECR/(AMR*REP)
       ELSE
          PIC=DGR*SR*TR*CECR
       ENDIF
      FC=0.805*PIC**0.195
      IF(S.GE.1)THEN
        ALPHAAA=ALPHAA
      ELSE
        ALPHAAA=S*ALPHAA
      ENDIF
      IF(FC.EQ.0.)THEN
        WRITE(21,1)I,K
    1   FORMAT('WARNING: ONE OF THE DIMENSIONLESS TERMS IN FC IS ZERO',
     &           ' IN SUBROUTINE TWOBODY01, I&K= ',2I5)
      ENDIF
C
C     CALCULATE COLLISION FREQUENCY FUNCTIONS
C
      BETABROWN=BROWNCONST*(TEMP+273.15)*FC*DSUM*DSUM
      BETABROWN=BETABROWN/(DJ(I)*DK(K))
      BETASHEAR=SHEARCONST*FC*FC*SQRT(EPS/XNU)*DSUM**3
      BETADIFFS=DIFFSCONST*FC*FC*DSUM*DSUM*DABS(WSJ(I)-WSK(K))
      BETA=BETABROWN+BETASHEAR+BETADIFFS
C
```

```
C      CALCULATE NUMBER AND PROBABILITY OF COLLISIONS
C
       XNIK(I,K)=ALPHAAA*BETA*XNJ(I)*XNJ(KLASS(K))
       IF(XNJ(KLASS(K)).NE.0.)THEN
          PROBIK(I)=XNIK(I,K)*DTL/XNJ(KLASS(K))
       ELSE
          PROBIK(I)=0.
       ENDIF
       RETURN
       END
C
C********************************************************************
C
       SUBROUTINE UPDATE()
C
C      UPDATES PARAMETERS
C
       INCLUDE 'PATHOSCOM.FOR'
       INCLUDE 'VESTCOM.FOR'
C
       TAUU=DV*XMU/8.
       NLIMIT=0
C
C      CALCULATE D MEDIAN MASS AND VOLUME FOR SUSPENSION
C
       SUMCONC=0.
       SUMVOL=0.
       TOTCONC=0.
       FRACTION=0.
       TOTVOL=0.
       SUMNUM=0.
       SUMDIM=0.
       DO J=1,JCLASSES+1
         TOTCONC=TOTCONC+CJ(J)
         TOTVOL=TOTVOL+XNJ(J)*DJ(J)**3.
         XNJ(J)=(CJ(J)/AMASSJ(J))
         DCSHEAR(J)=0.
         XN3(J)=0.
       SUMNUM=SUMNUM+XNJ(J)
       SUMDIM=SUMDIM+DJ(J)*XNJ(J)
       ENDDO
       DBAR=SUMDIM/SUMNUM
       SUMSQR=0.
       DO J=1,JCLASSES+1
          SUMSQR=SUMSQR+(XNJ(J)*DJ(J)-DBAR*SUMNUM)**2.
       ENDDO
       STDDEV=SQRT(SUMSQR/SUMNUM)
       KEEPON=0
       J=0
       DO WHILE(KEEPON.LT.1)
         J=J+1
         IF(J.GT.JCLASSES)KEEPON=1
         SUMCONC=SUMCONC+CJ(J)
         IF(TOTCONC.GT.0)FRACTION=SUMCONC/TOTCONC
         IF(FRACTION.GE.0.5)THEN
            F1=(SUMCONC-CJ(J))/TOTCONC
            F=FRACTION-F1
            IF(F.NE.0.)THEN
```

```
         D50=DJ(J-1)+(0.5-F1)*(DJ(J)-DJ(J-1))/(F)
       ELSE
         D50=DJ(J)
       ENDIF
       FRACTION=0.
       TOTCONC=0.
       KEEPON=1
     ENDIF
   ENDDO
   KEEPON=0
   SUMVOL=0.
   J=0
   DO WHILE(KEEPON.LT.1)
     J=J+1
     IF(J.GT.JCLASSES)KEEPON=1
     SUMVOL=SUMVOL+XNJ(J)*DJ(J)**3
     FRAC=SUMVOL/TOTVOL
     IF(FRAC.GE.0.5D0)THEN
       F1=(SUMVOL-XNJ(J)*DJ(J)**3)/TOTVOL
       F=FRAC-F1
       IF(F.NE.0)THEN
         DMED=DJ(J-1)+(0.5D0-F1)*(DJ(J)-DJ(J-1))/(F)
       ELSE
         DMED=DJ(J)
       ENDIF
       FRAC=0.
       TOTVOL=0.
       KEEPON=KEEPON+1
     ENDIF
   ENDDO
   IF(S.GE.1)THEN
     ALPHAAA=ALPHAA
   ELSE
     ALPHAAA=S*ALPHAA
   ENDIF
   TR=1.-0.875*TEMP/30.
   SR=S/2.D0
   CECR=CEC/9.
   IF(DMED.EQ.0.)THEN
     WRITE(*,7)
 7   FORMAT(' ERROR: DMED = 0 IN UPDATE.')
     DMED=DG
   ENDIF
   DGR=DG/DMED
   DO I=1,JCLASSES
    DO K=1,JCLASSES
      PI0(I,K)=DGR*SR*TR*CECR*PI00(I,K)
    ENDDO
   ENDDO
   RETURN
   END
C
C
C    ****************************************************************
C
     INCLUDE 'WAVEROUTINES.FOR'
C
C    ****************************************************************
C
```

```
      SUBROUTINE VEST(TT)
C
C     ADAPTED FROM PROGRAM VEST BY MEHTA AND LI, 1997
C
      INCLUDE 'PATHOSCOM.FOR'
      INCLUDE 'VESTCOM.FOR'
      DIMENSION C0OT(ND),CSTM(ND),FS(MAXC)
C
      DO 6 I=1,NGRIDS
        DO JC=1,NCL
          IF(C0(I,JC).LT.0.0000001) THEN
            C0(I,JC)=0.0000001
          END IF
        ENDDO
   6  CONTINUE
C
      IF(MODE.EQ.2.OR.MODE.EQ.3)READ(410,*)WHEIGHT,WPERIOD
      IF(MODE.EQ.1) THEN
      IF(MCHOO.EQ.1) THEN
         WRITE(*,*)'FOR ENTRAINMENT OF FLUID MUD UNDER CURRENT,'
         WRITE(*,*)'THIS CASE IS NOT APPROPRIATE FOR PRACTICAL USE.'
         WRITE(*,*)'SORRY!!!'
         STOP
C        CALL HYDROFLOW1(DVEL,KN)
C        USTAR=UU
      ELSE IF(MCHOO.EQ.2) THEN
         CALL HYDROFLOW2()
      ELSE
      END IF
      END IF
C
      IF(MODE.EQ.2) THEN
C     CALL PROWMITA(PWD1,PWD2,PDEN1,PDEN2,PWP,PAMP1,
C    *                    PMU1,PUU,PGG1,PGG2,IP,RRR,RR2)
        IF(MCHOO.EQ.1) THEN
          PMU1=XNU*RHOW
          IP=10
          CALL PROWMITA(H0,M0,RHOW,RHOM,WPERIOD,WHEIGHT,
     *                    PMU1,UU2,GG1,GG2,IP,RRR,RR2)
          DUDB=RRR
          CALL HYDROWAVE1(RR2)
          USTAR=UB
        ELSE IF(MCHOO.EQ.2) THEN
          CALL HYDROWAVE2()
        ELSE
        END IF
        END IF
        IF(MODE.EQ.3) THEN
          IF(MCHOO.EQ.1)THEN
            PMU1=XNU*RHOW
            IP=10
            CALL PROWMITA(H0,M0,RHOW,RHOM,WPERIOD,WHEIGHT,
     *                    PMU1,UU2,GG1,GG2,IP,RRR,RR2)
            DUDB=RRR
            CALL WAVECURRENT1(RR2)
            USTAR=UB
          ELSE IF(MCHOO.EQ.2) THEN
            RR2=0.0
```

```
      CALL  WAVECURRENT2()
   ELSE
   END IF
 END IF
C  IF(MODE.EQ.4) THEN
C     CALL HYDROTIDE(DVEL,KN,TT,USTAR)
C  END IF
 TOTALC(1)=0.
 DO JC=1,NCL
   TOTALC(1)=TOTALC(1)+C0(1,JC)
 ENDDO
 HINDER=1.
 IF(TOTALC(1).GT.WSB)HINDER=(1.D0-HK2*TOTALC(1))**BETAH
 DO JC=1,NCL
   WS(1,JC)=WSJ(JC)*HINDER
 ENDDO
 DO 12 I=2,NGRIDS
   C0LO=0.
   C0UP=0.
   DO JC=1,NCL
     C0LO=C0LO+C0(I-1,JC)
     C0UP=C0UP+C0(I,JC)
   ENDDO
C
C
   CCC=ABS((C0UP-C0LO)/(C0UP+C0LO))
   IF(CCC.GT.0.7) THEN
     CC=C0UP
   ELSE
     CC=(C0UP+C0LO)/2.0
   END IF
C
C     SET SETTLING VEL BY CLASS, MOD FOR HINDERED SETTLING AS NEEDED
C
   TOTALC(I)=0.
   DO JC=1,NCL
     TOTALC(I)=TOTALC(I)+C0(I,JC)
   ENDDO
   HINDER=1.
   IF(TOTALC(I).GT.WSB)HINDER=(1.D0-HK2*TOTALC(I))**BETAH
   DO JC=1,NCL
     WS(I,JC)=WSJ(JC)*HINDER
   ENDDO
C
C     DIFFUSION COEFFICIENT      *****
C
   IF(MODE.EQ.1) THEN
     VCC=0.01
   ELSEIF (MODE.EQ.2.) THEN
     VCC=0.0001
   ELSEIF (MODE.EQ.3) THEN
     VCC=0.01
   END IF
   VCC=0.001
   IF(CC.LT.VCC.OR.DVEL(I).LE.0.0)THEN
     RI=0.0
   ELSE
     IF((-C0UP+C0LO).LT.0.0) THEN
```

```
                RI=-0.5/DSK1
          ELSE
                RI=(G/CC)*((-C0UP+C0LO)/DZ)/(DVEL(I))**2.0
          END IF
        END IF
        KS(I)=KN(I)/(1.0+DSK1*RI)**DSK2
  12  CONTINUE
C
C*        BOTTOM BOUNDARY CONDITION            **********
C
      DO JC=1,NCL
        WSBB=WS(1,JC)
        IF(MCHOO.EQ.1) THEN
              CALL BEDFLUX1(WSBB,C0(1,JC),JC,USTAR,FS,ERCONST)
        ELSE
              CALL BEDFLUX2(WSBB,C0(1,JC),JC,FS,ERCONST)
        END IF
        IF(FS(JC).GT.0.)EROMAS=EROMAS+FS(JC)*DT
      ENDDO
C*          INITIAL CONDITIONS                 **********
        IF(ABS(TT).LE.(ST+1.0E-6)) THEN
          CALL OUTPUTVEST(TT,FS,ERCONST)
        END IF
C*    IMPLICIT CALCULATION                     **********
      DO JC=1,NCL
        R(1)=-DT/(DZ*DZ)*KS(2)
        P(1)=1.0-R(1)
        C0T(1,JC)=C0(1,JC)+DT/DZ*FS(JC)
        C00T(1)=C0T(1,JC)
        DO 13 I=2,NGRIDS
          Q(I-1)=R(I-1)-DT/DZ*WS(I,JC)
          R(I)=-DT/(DZ*DZ)*KS(I+1)
          P(I)=1.0-Q(I-1)-R(I)
          C00T(I)=C0(I,JC)
  13    CONTINUE
        CALL STM(NGRIDS,CSTM,C00T,P,Q,R)
        DO I=1,NGRIDS
          C(I,JC)=CSTM(I)
          IF(C(I,JC).LT.0.D0)C(I,JC)=1.D-07
        ENDDO
      ENDDO
C*    OUTPUT RESULTS                           *************
      IF(MMC.GT.0.0001) THEN
        IF(ABS(CTT-MMC).LE.0.00001.AND.TT.GT.0.00001) THEN
          CALL OUTPUTVEST(TT,FS,ERCONST)
          CTT=CTT-MMC
        END IF
      ELSE
        DO I=1,IDT
          IF(ABS(TT/60.0-DDTOUT(I)).LT.0.001) THEN
          CALL OUTPUTVEST(TT,FS,ERCONST)
          END IF
        END DO
      END IF
      DO JC=1,NCL
        DO 14 I=1,NGRIDS
          C0(I,JC)=C(I,JC)
  14    CONTINUE
```

```
        ENDDO
C       IF(TT.LT.MMT) THEN
C         GOTO 999
C       END IF
C       MOD TO VARY WAVE. WHM JAN 98
        IF(MODE.EQ.2.OR.MODE.EQ.3)THEN
          CLOSE(410)
          CLOSE(411)
          CLOSE(412)
        ENDIF
C     ENDMOD
C     STOP
      RETURN
      END
C
C**********************************************************************
C     ## END CALCULATION BLOCK
C**********************************************************************
C     BEGIN OUTPUT BLOCK
C**********************************************************************
C
      SUBROUTINE OUTPUT00(T)
C
C     WRITE RESULTS FILE
C
      INCLUDE 'PATHOSCOM.FOR'
      INCLUDE 'VESTCOM.FOR'
C
      TOTALVOL=0.
      SUMN=0.
      DO J=1,JCLASSES+1
        SUMN=SUMN+XNJ(J)
      ENDDO
      DO J=JSTART,JCLASSES+1
        TOTALVOL=TOTALVOL+XNJ(J)*DJ(J)**3.
      ENDDO
      KEEPON=0
      SUMVOL=0.
      J=JSTART-1
      DOLD=DPRIME
      DO WHILE(KEEPON.LT.1)
        J=J+1
        IF(J.GT.JCLASSES)KEEPON=1
          SUMVOL=SUMVOL+XNJ(J)*DJ(J)**3
          FRAC=SUMVOL/TOTALVOL
        IF(FRAC.GE.0.5)THEN
          F1=(SUMVOL-XNJ(J)*DJ(J)**3)/TOTALVOL
          F=FRAC-F1
          IF(F.NE.0)THEN
            DPRIME=1.D06*(DJ(J-1)+(0.5-F1)*(DJ(J)-DJ(J-1))/(F))
          ELSE
            DPRIME=DJ(J)*1.D06
          ENDIF
          FRAC=0.
          KEEPON=KEEPON+1
        ENDIF
      ENDDO
      D50MICRO=D50*1.D06
```

```
      RAT=DOLD/DPRIME
      DMEDMIC=DMED*1.D06
      RATT=DPRIME/X3MULT
      WRITE(22,2)T,SUMN,D50MICRO,DMEDMIC,DPRIME,TOTAL2,CHANGE12,
     & NLIMIT,EPS,DV,RAT,RATT
      WRITE(*,2) T,SUMN,D50MICRO,DMEDMIC,DPRIME,TOTAL2,CHANGE12,
     & NLIMIT,EPS,DV,RAT,RATT
    2 FORMAT(1X,7(G10.4,1X),I5,4G10.4)
      SUM2=0.
      SUM3=0.
      DO J=1,JCLASSES+1
        SUM2=SUM2+DCC2(J)
        SUM3=SUM3+DCC3(J)
        DJMICRO=DJ(J)*1.E6
        PERCENT=100.*XNJ(J)*DJ(J)**3./TOTALVOL
        WRITE(21,1)T,J,J,DJMICRO,CJ(J),XNJ(J),DCSHEAR(J),DCC2(J),DCC3(J)
     &             ,PERCENT,XN2(J),XN3(J)
    1   FORMAT(G12.6,2I5,1X,2(G12.6,1X),7(E12.6,1X))
      ENDDO
      WRITE(21,3)DCGROSS,DC3GROSS
      WRITE(21,3)SUMN,SUM2,SUM3
    3 FORMAT(30X,E12.4,18X,2E12.6)
      TOUT=T
      RETURN
      END
C***********************************************************************
C
      SUBROUTINE OUTPUT01(TT,IGRID)
C
C     WRITE RESULTS FILE
C
      INCLUDE 'PATHOSCOM.FOR'
      INCLUDE 'VESTCOM.FOR'
C
      TOTALVOL=0.
      DO J=JSTART,JCLASSES+1
        TOTALVOL=TOTALVOL+XNJ(J)*DJ(J)**3.
      ENDDO
      KEEPON=0
      SUMVOL=0.
      J=JSTART-1
      DO WHILE(KEEPON.LT.1)
        J=J+1
        IF(J.GE.JCLASSES)KEEPON=1
        SUMVOL=SUMVOL+XNJ(J)*DJ(J)**3
        FRAC=SUMVOL/TOTALVOL
        IF(FRAC.GE.0.5)THEN
          F1=(SUMVOL-XNJ(J)*DJ(J)**3)/TOTALVOL
          F=FRAC-F1
          IF(F.NE.0)THEN
            DPRIME=1.D06*(DJ(J-1)+(0.5-F1)*((DJ(J)-DJ(J-1))/(F)))
          ELSE
            DPRIME=DJ(J)*1.D06
          ENDIF
          FRAC=0.
          KEEPON=KEEPON+1
        ENDIF
      ENDDO
```

```fortran
      D50MICRO=D50*1.D06
      DMEDMIC=DMED*1.D06
      WRITE(22,2)TT,IGRID,D50MICRO,DMEDMIC,DPRIME,TOTAL2,NLIMIT,IKMON,
     &            TOTALC(IGRID),UU
      WRITE(*,2) TT,IGRID,D50MICRO,DMEDMIC,DPRIME,TOTAL2,NLIMIT,IKMON,
     &            TOTALC(IGRID),UU
    2 FORMAT(1X,G10.4,I5,4(G10.4,1X),2I5,2G10.4)
      SUM2=0.
      SUM3=0.
      DO J=1,JCLASSES+1
        SUM2=SUM2+DCC2(J)
        SUM3=SUM3+DCC3(J)
        DJMICRO=DJ(J)*1.E6
        PERCENT=100.*XNJ(J)*DJ(J)**3./TOTALVOL
        WRITE(21,1)TT,IGRID,J,DJMICRO,CJ(J),XNJ(J),DCSHEAR(J),DCC2(J),
     &            DCC3(J),PERCENT
    1   FORMAT(G12.6,2I5,1X,2(G12.6,1X),5(E12.6,1X))
      ENDDO
C       WRITE(21,3)DCGROSS,DC3GROSS
      WRITE(21,3)SUM2,SUM3
    3 FORMAT(70X,2E12.6)
      TOUT=TT
      RETURN
      END
C***********************************************************************
C
      SUBROUTINE OUTPUT10(K,T)
C
C     WRITE RESULTS FILE
C
      INCLUDE 'PATHOSCOM.FOR'
      INCLUDE 'VESTCOM.FOR'
C
      DKMICRO=DK(K)*1.E6
      WRITE(321,1)T,K,KID(K),KBED(K),DKMICRO,
     &      (X1K(I,K),I=1,3),(VPK(I,K),I=1,3)
      WRITE(322,2)KID(K),KBED(K),KLASS(K),AMASSK(K),DKMICRO,
     &            RHOK(K),WSK(K),(VPK(I,K),I=1,3),
     &            (X2K(I,K),I=1,3)
    1 FORMAT(F10.5,1X,3(I5,1X),7(E12.6,1X))
    2 FORMAT('KID ',3(I5,1X),11(E12.6,1X))
      RETURN
      END
C
C
C
C***********************************************************************
C
      SUBROUTINE OUTPUTCLOSE()
C
C     WRITE AND CLOSE RESULTS FILE
C
      INCLUDE 'PATHOSCOM.FOR'
      INCLUDE 'VESTCOM.FOR'
C
      WRITE(21,1)TLAST
C       WRITE(22,1)T
    1 FORMAT('RUN COMPLETE AT TIME =',F12.6)
```

```
        CLOSE(21)
        CLOSE(22)
        CLOSE(23)
        CLOSE(33)
C
        RETURN
        END
C
C
C
C       *********************************************************************
C
        SUBROUTINE OUTPUTVEST(TT,FS,ERCONST)
C
C       ADAPTED FROM PROGRAM VEST BY MEHTA AND LI, 1997
C
        INCLUDE 'PATHOSCOM.FOR'
        INCLUDE 'VESTCOM.FOR'
        DIMENSION FS(MAXC)
C
        IF(ABS(TT-STT*60.0).GT.0.01) GOTO 30
        WRITE(42,'(A30)') DESCR
        WRITE(42,*) 'INPUT FILENAME IS: ', FILEIN
        WRITE(42,*) 'MODE =',MODE, ' (1=CURRENT, 2=WAVE, 3=WAVE+CUR)'
        WRITE(42,*) 'THE TIME STEP USED IS: ', DT, ' (SEC)'
        WRITE(42,*) 'DISCRETIZATION PARAMETERS FOLLOW'
        WRITE(42,*) 'NGRIDS=',NGRIDS,' DTSEC=',DT,'(SEC) DZ=',DZ,'(M)'
        WRITE(42,*) 'DEPTH    OF    WATER    (M)    IS:', H0
        WRITE(42,*) 'DEPTH OF BOTTOM SEDIMENT(M) IS:', M0
        WRITE(42,*) 'FLUID MUD DENSITY (KG/M^3)   IS:',RHOM
        WRITE(42,*) 'WATER      DENSITY      (KG/M^3) IS:',RHOW
        WRITE(42,*) 'SEDIMENT GRANULAR DENSITY(KG/M^3) IS:',RHOSED
        WRITE(42,*) 'SETTLING VELOCITY PARAMETERS FOLLOW'
C       WRITE(42,*) '   WSC0        WS0        WSA        WSB     · WSM'
C
C       *    WSN'
C       WRITE(42,'(6(1X,E10.3))') WSC0,WS0,WSA,WSB,WSM,WSN
        WRITE(42,*) '   HK2        BETAH        WSB'
        WRITE(42,'(6(1X,E10.3))') HK2,BETAH,WSB
        WRITE(42,*) 'STABILIZED DIFFUSION PARAMETERS FOLLOW'
        WRITE(42,*) '     ALPHA0          BETA0'
        WRITE(42,'(2(2X,E12.4))') DSK1, DSK2
        IF(MODE.EQ.1.OR.MODE.EQ.3) THEN
        WRITE(42,*) 'FLOW HYDRODYNAMIC PARAMETERS FOLLOW'
        WRITE(42,*) 'FLOW AVE. VELO.(M/S) , MANNING`S COEFFICIENT'
        WRITE(42,'(2(10X,F10.4))') UU, QN
        END IF
        IF(MODE.EQ.2.OR.MODE.EQ.3) THEN
        WRITE(42,*) 'WAVE HYDRODYNAMIC PARAMETERS FOLLOW'
        WRITE(42,*)'WHEIGHT(M),WPERIOD(S),WLENGTH(M),WDIFFCOEF,WFRIC COEF'
        WRITE(42,'(5(E10.4,1X))')WHEIGHT,WPERIOD,WLENGTH,WDIFFK,WFRIC
        END IF
C       IF(MODE.EQ.3) THEN
C        WRITE(42,*) 'TIDAL HYDRODYNAMIC PARAMETERS FOLLOW'
C        WRITE(42,*) 'MAX. TIDAL VELOCITY, TIDAL PERIOD,  MANNING`S COEF'
C        WRITE(42,'(3(1X,E10.4))') UMAX, PTIDE, QQN
C       END IF
        IF(MCHOO.EQ.1) THEN
        WRITE(42,*) 'FLUID MUD PARAMETERS FOLLOW'
```

```
      WRITE(42,*) 'MUD REOLOGICAL PARAMETERS'
      WRITE(42,*) '  GG1    ,   GG2    ,   UU2    ,   DUDB   '
      WRITE(42,'(4(1X,E10.4))') GG1,GG2,UU2,DUDB
      WRITE(42,*) 'ENTRAINMENT RATE COEFFICIENT PARAMETERS FOLLOW'
      WRITE(42,*) '  ENT0    ,   ENN    ,   ENTAD'
      WRITE(42,'(3(1X,E10.4))') ENT0, ENN, RIC*RIC
      WRITE(42,*) 'CRITICAL GLOBAL RICHARSON NUMBER IS:',RIC
      ELSE IF(MCHOO.EQ.2) THEN
      WRITE(42,*) 'BED PARAMETERS FOLLOW'
      WRITE(42,*) 'BED DENSITY PARAMETERS FOLLOW'
      WRITE(42,*) '  BDP1,      BDP2,      RHBBAR'
      WRITE(42,'(3F10.4)') BDP1,BDP2,RHBBAR
      WRITE(42,*) 'BED SHEAR STRENGTH'
      WRITE(42,*) '  PHIC ,   TCP1 ,    TCP2 '
      WRITE(42,'(3F10.4)') PHIC, TCP1, TCP2
      WRITE(42,*) 'EROSION RATE PARAMETERS FOLLOW'
      WRITE(42,*) '  ERSMAX  ,   ERP1  ,    ERP2  '
      WRITE(42,'(3F10.4)') ERSMAX, ERP1, ERP2
      WRITE(42,*) 'TAUDEP = ', TAUDEP, '(PA)'
      ELSE
      END IF
30    SUSPMAS = 0.0
      WSSUM=0.
      WRITE(*,*) 'PROGRAM IN PROGRESS: TIME=',TT/60.0,'(MIN)'
      WRITE(42,*)
      WRITE(42,*) 'CONCENTRATIONS (G/L) FOR TIME=',TT/60.0, '(MIN)'
C     MOD TO VARY WAVE. WHM JAN 98
      IF(MODE.EQ.2.OR.MODE.EQ.3)THEN
        WRITE(42,*) 'WAVE HEIGHT = ', WHEIGHT,
     1 ' (M)  WAVE PERIOD = ',WPERIOD, ' (SEC)'
      ENDIF
      WRITE(42,*)'EROSION RATE CONSTANT = ', ERCONST
C     ENDMOD
      WRITE(42,1001)
 1001 FORMAT('ELEVATION FROM BED       DIFFUSION COEF M^2/SEC',
     1 '    CONCENTRATION (G/L)   SETTLING VEL (M/SEC) ')
      DO 11 I=NGRIDS,1,-1
        ZZ=(FLOAT(I)-0.5)*DZ
        WSBAR=0.
        DO JC=1,NCL
         WSBAR=WSBAR+WS(I,JC)*C0(I,JC)
        ENDDO
        WSBAR=WSBAR/TOTALC(I)
        WRITE(42,'(4(4X,G15.6))') ZZ,KN(I),TOTALC(I),WSBAR
        WRITE(43,902) ZZ,TOTALC(I),WSBAR
 902    FORMAT(3(4X,G15.6))
C       DO JC=1,NCL
C         WRITE(44,901)TT/60.D0,ZZ,I,JC,C0(I,JC),WS(I,JC)
C 901    FORMAT(' B',(4X,2G15.6,2I5,2G15.6))
C       ENDDO
      IF(MODE.EQ.2.OR.MODE.EQ.3)
     & WRITE(412,102)TT,WHEIGHT,WPERIOD,ZZ,1000*C(I,JC)
        DO JC=1,NCL
         SUSPMAS=SUSPMAS+C0(I,JC)*DZ
         WSSUM=WSSUM+WS(I,JC)*C0(I,JC)
        ENDDO
11    CONTINUE
C     MOD BY WHM JAN 98
```

```
102    FORMAT(5X,4(G10.4),G12.6)
       CBAR=SUSPMAS/H0
C      WSBAR=WSSUM/NGRIDS
       WSBAR=WSSUM/(SUSPMAS)
       FSSUM=0.
       DO JC=1,NCL
         FSSUM=FSSUM+FS(JC)
       ENDDO
       IF(MODE.EQ.2.OR.MODE.EQ.3)
     & WRITE(411,101)TT,WHEIGHT,WPERIOD,1000*CBAR
101    FORMAT(5X,3(G10.4),G12.6)
       WRITE(42,*)
       WRITE(*,*)'DEPTH-AVERAGED CONCENTRATION & UU: ',CBAR, ' (KG/M^3) '
     & ,UU
       WRITE(42,*)'DEPTH-AVERAGED CONCENTRATION: ',CBAR, ' (KG/M^3)'
       WRITE(42,*)'DEPTH-AVERAGED SETTLING VELOCITY: ',WSBAR, ' (M/SEC)'
       WRITE(42,*) 'DEPOSITION(-)/EROSION(+) RATE: ,FSSUM, '(KG/SEC)'
C      MOD END
       WRITE(42,*)'TOTAL SEDIMENT NOW IN SUSPENSION:',SUSPMAS,' (KG/M^2)'
       WRITE(42,*)'TOTAL SEDIMENT ADDED FROM BED EROSION: ',EROMAS,
     *' (KG/M^2)'
       IF(MCHOO.EQ.1) THEN
         WRITE(42,*) 'GLOBAL RICHARDSON NUMBER :', RIG
       ELSE IF(MCHOO.EQ.2) THEN
         WRITE(42,*)'TOTAL SEDIMENT LOST FROM BED DEPOSITION:', DZB, '(M)'
C        WRITE(44,903)TT/60.,CBAR,WSBAR,DZB,(C0(I,JC),JC=1,NCL)
         WRITE(44,903)TT/60.,CBAR,WSBAR,DZB
  903    FORMAT((G15.6,50(1X,G15.6)))
         WRITE(42,*) 'TAUBED = ', TAUBED, '(PA), '
         WRITE(42,*) 'TAUERO = ', TAUERO, '(PA)'
       ELSE
       END IF
       DUM=TT
9999   RETURN
       END
C
C****************************************************************
C
       SUBROUTINE TILT(IT,IPA,IPR)
C
C
       WRITE(*,*)'ERROR IN INPUT'
       WRITE(*,*)'OPTIONS INVALID: ITYPE = ',IT,' IOPTPROB = ',IPR,
     &          ' IOPTPATH = ',IPA
       STOP
       RETURN
       END


C      PATHOSCOM.FOR
       IMPLICIT DOUBLE PRECISION(A-H,O-Z)
       PARAMETER (ND=50,MAXC=40,MAXK=2,N21=2,N9=2,NLAY=1)
C      ALL BLOCK
       COMMON/FLUID/XNU,XMU,RHO,EPS,EPS1,EPS2,DV,TEMP,S,TAUU
       COMMON/AGGREGATION/DG,DGR,CEC,CECR,SR,TR,ALPHAAA,ALPHAA,
       COMMON/BED/RHOBED(NLAY),RHOCRIT,RICRIT,TAUCM(NLAY),TAUCE(NLAY),
     & LAYERTOP,RHOLAYER(NLAY),BEDELEV,TAUBED
       COMMON/CLASSES/JCLASSES,RHOJ(MAXC),DJ(MAXC),AMASSJ(MAXC),
```

```fortran
     & CJ(MAXC),XNJ(MAXC),TAUCD(MAXC),D50,DMED,TAUSJ(MAXC),MAXCLASS,
     & AMIN(MAXC),UI(MAXC,MAXC),XNIK(MAXC,MAXC),XNIKM(MAXC,MAXC,MAXC),
     & JSTART,TOTALNUMBER,TOTAL0,PF(MAXC,MAXC,MAXC),DJMAX(MAXC),
     & AMAX(MAXC),WSJ(MAXC),SUMCONC,DMED0
      COMMON/FLAGS/ITYPE,IOPTPROB,IOPTPATH,JEULER,JGEO,NWRITE,IRHO
      COMMON/RUNCTL/T0,TLAST,DTL,KONCE,TSKIP,TOUT,T1,T2,TAGSKIP,TAGDUR
      COMMON/CONSTANTS/TO15PINU,BROWNCONST,SHEARCONST,
     & DIFFSCONST,LAMBDAS,BOLTZ,PI,G,B11,GMULT,RANMULT,
     & EM7,R1,R2,ER1,ER2,D1,D2,D3,RHOG,FPIN
C     CHAMBER BLOCK
      COMMON/CHAMBER/PI0(MAXC,MAXC),PI00(MAXC,MAXC),DIK(MAXC,MAXC),
     & ALPHAIKM0(MAXC,MAXC,MAXC),ST0(MAXC),TAUIKC(MAXC,MAXC),
     & TAUIKMC(MAXC,MAXC,MAXC),AMIK(MAXC,MAXC),DD(MAXC,MAXC),XN2(MAXC),
     & AMM(MAXC),DCSHEAR(MAXC),DCC2(MAXC),DCC3(MAXC),IKMON,
     & TOTAL2,CHANGE12,NLIMIT,DCGROSS,DC3GROSS,XN3(MAXC),FP(MAXC),
     & DCI(MAXC),DCK(MAXC),DCM(MAXC),DCX(MAXC),AMIKM(MAXC,MAXC)
C     & DIV1(MAXC,MAXC,MAXC),DIV2(MAXC,MAXC,MAXC),DIV3(MAXC,MAXC,MAXC)
C     KERNEL BLOCK
      COMMON/KERNEL/NK,NKMAX,KID(MAXK),KBED(MAXK),KLASS0(MAXK),
     & KLASS(MAXK),AMASSK(MAXK),AMASSK0(MAXK),DK(MAXK),RHOK(MAXK),
     & WSK(MAXK),X0K(3,MAXK),X1K(3,MAXK),X2K(3,MAXK),VPK(3,MAXK),
     & KELEM(MAXK),DK0(MAXK),TAUSK(MAXK),TAUIK(MAXC)
C     COLLISION BLOCK
      COMMON/COLLISION/PROBIK(MAXC),PROBIKM(MAXC,MAXC)
C     EULERIAN BLOCK
      COMMON/HYDRO/XVEL(N21,N9,2),YVEL(N21,N9,2),ZVEL(N21,N9,2),
     & SAL(N21,N9,2),CONC(N21,N9,2,MAXC),EPSI(N21,N9,2),
     & XV,XV1,XV2,YV,YV1,YV2,ZV,ZV1,ZV2,S1,S2,C1(MAXC),C2(MAXC),
     & TEMP1,TEMP2,DV1,DV2,TIME1,TIME2
      COMMON/MESH/NE,NP,CORD(N21,3),NDEP(N21),BEDEL(N21),
     & NOP(N21,N21),IMAT(N21),SPEC(3)
C     NONCOHESIVE BLOCK
C
      COMMON/NONCO/CJN(MAXC),WSJN(MAXC),TOTALN

C     VESTCOM.FOR
      COMMON/CHAR/DESCR,FILEIN,FILEOUT,FILEGRA
      COMMON/CON/ C0T(ND,MAXC),DVEL(ND),C0(ND,MAXC),C(ND,MAXC),Z(ND),
     * WS(ND,MAXC),KN(ND),KS(ND),ZI(500),CI(500,MAXC),DDTOUT(500),
     * P(ND),Q(ND),R(ND),WSBAR,IDT,ST
      COMMON/COMX/H0,M0,VKK,RHOW,KKSS,CTT,JN,
     * MMT,MMC,MODE,NGRIDS,DZ,DTRUN,DTOUT,DT,STT,DPS,MCHOO
      COMMON/WAVE/WHEIGHT,WPERIOD,WDIFFK,WLENGTH,UB,WFRIC
      COMMON/FLOW/UU,QN,UUU1,UUU2
      COMMON/TIDE/QQN,UMAX,PTIDE
      COMMON/MUD/RHOSED,RHOM,RIC,RIG,DUDB,ENT0,ENN
      COMMON/MR/GG1,GG2,UU2
      COMMON/OUT/WSC0,WS0,WSA,WSB,WSM,WSN,DSK1,DSK2
      COMMON/CAL/SUSPMAS,EROMAS
      COMMON/BED/ DZB,TAUDEP,BDP1,BDP2,RHBBAR,PHIC,TCP1,TCP2,
     *            ERSMAX,ERP1,ERP2,TAUERO
      COMMON/CLASSES/NCL,TOTALC(ND)
      COMMON/MULT/S2MULT,S3MULT,X3MULT,X2MULT,RHOMULT,STDDEV
      REAL M0, KKSS
      REAL*8 MMC,MMT,CTT
      REAL KS, KN
      CHARACTER DESCR*60,FILEIN*30,FILEOUT*30,FILEGRA*30
```

APPENDIX D
FLUME EXPERIMENT DATA

Data from the flume experiments described in Chapter 5 are given in Tables D-1 through D-10. Table D-1 lists water surface elevations, Tables D-2 and D-3 list flow speeds, and Tables D-4 through D-9 provide suspended sediment concentration measurements. Table D-10 lists bed thickness measurements. Unless otherwise stated, measurements were made along the flume centerline.

Table D-1. Water surface elevations from flume experiments, cm.

Experiment No.	Time after injection start, min	Station: Distance Along Flume, m							
		12.2	24.4	36.6	48.8	61.0	73.2	79.2	97.5
W4	0	48.43	48.07	--	46.88	46.76	46.48	46.36	45.84
	10	48.16	48.01	--	47.15	46.73	46.45	46.33	45.84
	20	48.40	48.01	--	46.79	46.76	46.48	46.33	45.84
	30	48.16	48.04	--	46.79	46.73	46.45	46.33	45.84
	40	48.16	48.04	--	47.09	46.76	46.54	46.33	45.83
	50	48.16	47.67	--	47.09	46.73	46.45	46.30	45.83
	60	48.16	48.04	--	47.09	46.70	46.45	46.27	45.78
W5	0	50.11	49.68	49.13	48.31	48.04	47.49	47.27	46.33
	10	50.51	49.68	49.23	48.46	48.10	47.49	47.27	46.33
	20	50.08	49.47	49.07	48.25	48.01	47.40	47.21	46.27
	30	50.20	49.38	48.92	48.16	47.88	47.34	47.06	46.21
	40	50.20	49.47	49.07	48.16	47.88	47.34	47.12	46.21
	50	49.99	49.44	49.35	48.16	47.98	47.12	46.94	46.18
	60	50.11	49.53	49.19	48.25	47.98	47.40	47.18	46.27
W6	0	47.24	47.03	46.91	46.42	46.42	46.24	46.30	45.99
	10	47.24	47.00	46.91	46.39	46.48	46.33	46.36	46.02
	20	47.24	47.00	46.85	46.39	46.48	46.33	46.36	46.06
	30	47.24	46.97	46.85	46.36	46.48	46.30	46.36	46.06
	40	47.24	46.94	46.85	46.36	46.42	46.27	46.33	46.02
	50	47.24	46.97	46.85	46.36	46.39	46.24	46.33	46.02
	60	47.21	46.94	46.85	46.30	46.42	46.24	46.33	46.02
W9	0	47.09	46.79	46.70	46.18	46.24	46.02	46.12	45.81
	15	47.12	46.85	46.70	46.18	46.24	46.06	46.21	45.84
	30	47.12	46.85	46.70	46.18	46.21	45.99	46.15	45.84
	45	47.15	46.85	46.73	46.24	46.30	46.12	46.18	45.87
	60	47.18	46.94	46.76	46.27	46.30	46.06	46.15	45.87
W10	0	47.52	47.24	47.09	46.51	46.57	46.39	46.48	46.12
	15	47.40	47.09	46.94	46.39	46.42	46.33	46.36	46.02
	30	47.30	47.03	46.85	46.27	46.33	46.18	46.24	45.87
	45	47.30	47.03	46.85	46.27	46.33	46.18	46.24	45.87
	60	47.27	47.03	46.85	46.27	46.33	46.18	46.21	45.87
W11	0	46.02	45.81	45.75	45.42	45.57	45.51	45.63	45.51
	15	45.99	45.81	45.78	45.42	45.57	45.54	45.63	45.51
	30	46.02	45.84	45.81	45.45	45.63	45.57	45.72	45.63
	45	46.02	45.84	45.81	45.45	45.63	45.57	45.69	45.57
	60	46.02	45.84	45.81	45.45	45.66	45.57	45.72	45.60

Note: Flume floor elevation was 30.48 cm.

Table D-2. Flow speeds, cm/sec, for a flume flow rate of 0.0033 m³ /sec.

Station 12.2					
Distance Above Bottom, cm	Distance from Left Wall, cm				
	3.81	7.62	11.43	15.24	19.05	Mean
15.54	7.5	9.5	9.5	8.0	6.3	8.2
11.92	9.5	11.3	10.2	9.9	6.3	9.4
8.29	8.9	11.4	10.3	9.1	5.6	9.1
4.66	9.0	10.2	9.2	9.1	6.0	8.7
1.07	7.1	7.8	6.9	7.5	4.8	6.8
Mean	8.4	10.0	9.2	8.7	5.8	8.4

Station 48.8					
Distance Above Bottom, cm	Distance from Left Wall, cm				
	3.81	7.62	11.43	15.24	19.05	Mean
14.78	7.8	9.3	9.7	9.1	5.8	8.3
11.34	9.4	11.0	10.5	10.5	6.9	9.7
7.92	9.7	11.5	11.0	11.2	7.3	10.1
4.48	9.2	10.5	10.0	10.5	6.9	9.4
1.07	7.5	7.8	7.6	7.4	4.8	7.0
Mean	8.7	10.0	9.8	9.7	6.3	8.9

Station 97.6					
Distance Above Bottom, cm	Distance from Left Wall, cm				
	3.81	7.62	11.43	15.24	19.05	Mean
14.23	7.7	10.6	10.4	9.2	5.6	8.7
10.94	9.8	11.4	11.0	10.9	7.4	10.1
7.65	10.2	12.0	11.5	11.0	7.3	10.4
4.36	9.4	11.7	10.1	10.3	6.2	9.5
1.07	7.8	8.3	7.2	7.8	5.4	7.3
Mean	9.0	10.8	10.0	9.8	6.4	9.2

Table D-3. Flow speeds, cm/sec, for a flume flow rate of 0.0074 m³ /sec.

Station 12.2						
Distance Above Bottom, cm	Distance from Left Wall, cm					
	3.81	7.62	11.43	15.24	19.05	Mean
18.87	15.3	17.7	17.3	16.6	12.9	16.0
14.42	18	21.7	20.4	18.5	14.2	18.6
9.97	17.2	21.5	20.8	16.6	11.2	17.5
5.52	16.6	20.5	18.8	16.3	10.2	16.5
1.07	14.3	15.4	14.6	14.7	9.5	13.7
Mean	16.3	19.4	18.4	16.5	11.6	16.4

Station 48.8						
Distance Above Bottom, cm	Distance from Left Wall, cm					
	3.81	7.62	11.43	15.24	19.05	Mean
16.67	15.1	18.9	18.9	16.4	13.1	16.1
12.1	19.5	23.1	22.4	22.8	15.3	20.6
8.87	19.8	23.5	23.9	22.9	14.9	21.0
4.97	18	21.7	20.8	21.3	14.3	19.2
1.07	15.8	17.1	16.2	16.8	10.4	15.3
Mean	17.6	20.9	20.4	20.0	13.2	18.4

Station 97.6						
Distance Above Bottom, cm	Distance from Left Wall, cm					
	3.81	7.62	11.43	15.24	19.05	Mean
13.47	12.5	21.3	20.6	19.6	14.6	17.7
10.36	22.4	26.9	26.7	26.6	17.7	24.1
7.25	22.2	28.6	27.1	26.2	17.6	24.3
4.15	22	26.1	24.2	24.6	15.1	22.4
1.07	20.6	22.7	17.5	20.9	14.5	19.2
Mean	19.9	25.1	23.2	23.6	15.9	21.6

Table D-4. Centerline sediment concentration profiles for experiment W4, kg/m^3.

Station Number	Time, min	Sample Depth					
		Surface	Quarter Depth	Middepth	Three-Quarter Depth	Bottom	Mean
6.1	15	8.706		8.736		9.583	9.008
6.1	30	10.748		11.754		13.103	11.868
6.1	45			10.070			10.070
6.1	60	9.849				12.867	11.358
6.1	75	10.244		11.150			10.697
12.2	15	9.286					9.286
12.2	30	9.566		10.344			9.955
12.2	45	8.951		11.419			10.185
12.2	75	10.350		9.850			10.100
18.3	15					8.747	8.747
18.3	30	8.759		8.643		9.775	9.059
18.3	45			9.190			9.190
18.3	75	10.588		9.837			10.213
24.4	15		8.171	7.715			7.943
24.4	30	9.554	8.130	9.363	9.077	9.020	9.029
24.4	45	9.330	9.093	9.395	10.315	9.808	9.588
24.4	75	9.176	8.975	8.812			8.988
30.5	15					8.197	8.197
30.5	30	8.098		8.436		9.379	8.638
30.5	45	8.264		8.301		8.379	8.315
30.5	75						0.000
36.6	15	7.485		7.923			7.704
36.6	30	7.796		8.976		9.050	8.607
36.6	45	8.234		8.871		8.867	8.657
36.6	75						
42.7	15					9.885	9.885
42.7	30	9.011		8.389			8.700
42.7	45	8.749		8.566		8.948	8.754
42.7	75						0.000
48.8	15					7.792	7.792
48.8	30	8.524		8.706		9.894	9.041
48.8	45	8.305		9.580		8.699	8.861
48.8	75						
54.9	15	7.430		7.786		8.092	7.769
54.9	30	8.207		8.484		8.289	8.327
54.9	45	9.083		8.488		8.703	8.758

Table D-4—continued.

Station Number	Time, min	Sample Depth					
		Surface	Quarter Depth	Middepth	Three-Quarter Depth	Bottom	Mean
54.9	75	8.932		8.800		9.609	9.114
61.0	15	7.922		7.375		7.774	7.690
61.0	30	8.811		8.083		8.135	8.343
61.0	45	8.345		7.915		7.990	8.083
61.0	75	6.968		7.013		8.589	7.523
67.1	15	7.908		8.038		7.395	7.780
67.1	30	7.997		8.105		7.456	7.853
67.1	45	7.307		7.785		8.818	7.970
67.1	75	7.095		8.012		7.034	7.380
73.2	15	6.574					6.574
73.2	30	7.541		7.258		8.506	7.768
73.2	45	8.108		8.453		7.996	8.186
73.2	75	7.412		7.537		7.918	7.622
79.2	15	6.991				7.268	7.130
79.2	30	8.339		7.716		8.437	8.164
79.2	45	7.204		7.774		9.212	8.063
79.2	75	7.045		7.073		8.758	7.625
85.3	15	7.274		7.472		7.491	7.412
85.3	30	10.030		9.907		8.585	9.507
85.3	45						
85.3	75	7.758		8.470		7.868	8.032
91.4	15	7.422		7.973		9.477	8.291
91.4	30	9.137					9.137
91.4	45						
91.4	75	6.871		7.865		8.403	7.713
97.5	15	6.537	13.737	5.728		6.986	8.247
97.5	30	8.828	9.753	10.007		9.585	9.543
97.5	45						
97.5	75			8.089	8.239	8.774	8.367

Table D-5. Centerline sediment concentration profiles for experiment W5, kg/m³.

Station Number	Time, min	Surface	Quarter Depth	Middepth	Three-Quarter Depth	Bottom	Mean
6.1	15	8.308		8.463		10.367	9.046
6.1	30	11.145		11.530		11.613	11.429
6.1	45	8.950		9.655		8.964	9.190
6.1	60	12.356		10.061		12.429	11.615
12.2	15	8.694		8.202			8.448
12.2	30	9.305		9.315			9.310
12.2	45	9.355		8.925			9.140
12.2	60	8.648		8.954			8.801
18.3	15	8.095		8.715		8.774	8.528
18.3	30	7.984		8.370		8.730	8.361
18.3	45	7.474		7.323		8.685	7.827
18.3	60	7.982		8.125		9.090	8.399
24.4	15	8.148	7.499	7.967	8.662	9.435	8.342
24.4	30	8.746	8.931	7.967	7.424	8.050	8.224
24.4	45	7.768	6.815	7.427	8.148	8.856	7.803
24.4	60	6.536	6.895	7.138	3.923	7.930	6.484
30.5	15	7.549		8.431		8.026	8.002
30.5	30	6.585		7.238		7.872	7.232
30.5	45	7.442		6.925		6.835	7.067
30.5	60	7.041		7.165		7.317	7.174
36.6	15	7.025		7.528		8.071	7.541
36.6	30	6.757		8.261		7.476	7.498
36.6	45	6.737		7.153		7.212	7.034
36.6	60	7.337		7.656		6.847	7.280
42.7	15	7.593		7.787		7.976	7.785
42.7	30	7.342		7.987		7.872	7.734
42.7	45	6.847		7.526		7.654	7.342
42.7	60	6.764		7.942		7.810	7.505
48.8	15	6.292		6.731		8.022	7.015
48.8	30	7.885		8.150		7.814	7.950
48.8	45	8.653		8.446		8.534	8.544
48.8	60	7.161		7.259		8.084	7.501
54.9	15	7.310		5.213		7.999	6.841
54.9	30	6.262		7.701		8.607	7.523
54.9	45						

Table D-5—continued.

Station Number	Time, min	Sample Depth					
		Surface	Quarter Depth	Middepth	Three-Quarter Depth	Bottom	Mean
54.9	60	7.539		7.595			7.567
61.0	15	7.195		7.942		7.749	7.629
61.0	30	6.564		6.953		7.287	6.935
61.0	45						
61.0	60	6.919		8.228		7.204	7.450
67.1	15	6.637		5.729			6.183
67.1	30	6.874		6.519		7.343	6.912
67.1	45						
67.1	60	6.752		6.607		14.482	9.280
73.2	15	6.645		6.753		6.083	6.494
73.2	30	6.603		6.519		7.377	6.833
73.2	45						0.000
73.2	60	7.215		6.943		7.094	7.084
79.2	15	8.458		6.709		6.848	7.338
79.2	30			6.633		7.335	6.984
79.2	45						
79.2	60	6.271		6.623		7.041	6.645
85.3	15	6.971		6.553		6.769	6.764
85.3	30			6.678			6.678
85.3	45	8.043		6.429		7.475	7.316
85.3	60	5.535				6.316	5.926
91.4	15			7.166		7.608	7.387
91.4	30					6.784	6.784
91.4	45						
91.4	60			3.269		2.503	2.886
97.5	15		8.243				8.243
97.5	30	6.365	7.379	7.990		7.822	7.389
97.5	45			7.904		8.316	8.110
97.5	60	2.161	2.187	2.085	2.425	3.243	2.420

Table D-6. Centerline sediment concentration profiles for experiment W6, kg/m^3.

Station Number	Time, min	Sample Depth					
		Surface	Quarter Depth	Middepth	Three-Quarter Depth	Bottom	Mean
6.1	15	6.104		5.853		5.701	5.886
6.1	30	8.028		7.762		3.386	6.392
6.1	45	8.145		8.691		5.808	7.548
6.1	60	13.344		9.481		9.711	10.845
12.2	15	4.576		5.516			5.046
12.2	30	16.632					16.632
12.2	45	7.563		8.068			7.816
12.2	60	8.592		8.815			8.703
18.3	15	6.167		6.480		6.869	6.506
18.3	30	6.673		6.306		6.800	6.593
18.3	45	7.691		5.862		6.640	6.731
18.3	60	10.089		8.891		10.013	9.664
24.4	15	6.307	6.314	6.659	7.995	7.015	6.858
24.4	30	6.052	5.203	7.135	6.751	6.530	6.334
24.4	45	5.609	5.396	5.934	5.784	6.667	5.878
24.4	60	6.722	6.868	7.351	7.009	6.990	6.988
30.5	15	6.059		6.093		6.124	6.092
30.5	30	5.692		6.671		6.585	6.316
30.5	45	4.918		5.343		5.881	5.381
30.5	60	6.430		8.336		7.359	7.375
36.6	15	2.190		6.213		6.835	5.080
36.6	30	4.721		5.913		6.286	5.640
36.6	45	4.576		5.313		6.029	5.306
36.6	60	5.543		6.628		7.073	6.415
42.7	15	5.200		6.268		5.953	5.807
42.7	30	5.246		5.896		6.387	5.843
42.7	45	4.886		5.712		6.067	5.555
42.7	60	5.520		6.061		7.329	6.304
48.8	15	4.683		5.012		5.479	5.058
48.8	30	5.472		5.964		7.042	6.159
48.8	45	5.127		5.589		6.432	5.716
48.8	60	4.258		5.403		7.186	5.616
54.9	15	4.406		5.048		5.909	5.121
54.9	30	5.377		5.880		7.141	6.133
54.9	45	5.141		5.349		7.790	6.093
54.9	60	5.611		6.358		7.664	6.544

Table D-6—continued.

Station Number	Time, min	Sample Depth					
		Surface	Quarter Depth	Middepth	Three-Quarter Depth	Bottom	Mean
61.0	15	6.559		2.684		12.066	7.103
61.0	30	4.801		5.183		5.273	5.086
61.0	45	4.599		5.113		4.858	4.857
61.0	60	2.554		6.127		6.787	5.156
67.1	15	3.053		4.017			3.535
67.1	30			5.861		6.407	6.134
67.1	45	4.380		4.630		5.285	4.765
67.1	60	4.426		5.514		5.844	5.262
73.2	15	2.194		2.874		4.039	3.035
73.2	30	3.068		4.334		5.566	4.323
73.2	45	4.532		4.449		7.796	5.592
73.2	60	5.208		4.601		5.305	5.038
79.2	15	0.498		0.794		1.229	0.840
79.2	30			5.575		6.010	5.793
79.2	45	3.919		4.089		4.597	4.202
79.2	60	4.409		5.029		5.458	4.966
85.3	15	0.079		0.098		0.120	0.099
85.3	30	4.586		5.012		5.938	5.179
85.3	45	4.396		4.772		5.365	4.844
85.3	60	2.735		0.024		2.435	1.731
91.4	15	0.012		1.008		0.015	0.345
91.4	30	0.074		4.819		5.257	3.383
91.4	45	5.055		3.878		3.375	4.103
91.4	60	4.960		5.343		5.886	5.396
97.5	15	1.560	0.007	0.012	0.011	0.027	0.323
97.5	30	3.117	4.460	4.383	4.327	4.816	4.221
97.5	45	4.304	4.625	4.984	5.324	5.380	4.923
97.5	60	5.037	5.145	5.801	5.871	6.466	5.664

Table D-7. Centerline sediment concentration profiles for experiment W9, kg/m³.

Station Number	Time, min	Sample Depth					
		Surface	Quarter Depth	Middepth	Three-Quarter Depth	Bottom	Mean
6.1	15	2.356		2.571		2.405	2.444
6.1	30	2.377		2.469		2.582	2.476
6.1	45	1.972		2.063		2.016	2.017
6.1	60	1.842		2.745			2.293
6.1	75	2.184		2.206		2.181	2.190
12.2	15	2.230		2.179		1.880	2.096
12.2	30	2.058		2.186		1.858	2.034
12.2	45	1.792		2.159		1.422	1.791
12.2	60	0.011		0.011		1.256	0.426
12.2	75	1.772		0.019		0.009	0.600
18.3	15	2.119		3.181		2.581	2.627
18.3	30	3.248		1.659		1.683	2.197
18.3	45	1.559		1.387		1.463	1.470
18.3	60	0.024		0.849			0.436
18.3	75			2.662		1.369	2.015
24.4	15	1.918	1.862	1.889	1.654	2.512	1.967
24.4	30	1.300	1.216	1.454	1.522	1.939	1.486
24.4	45	1.365	1.242	1.422	1.559	1.406	1.399
24.4	60	1.000	1.071	0.739	0.794	1.030	0.927
24.4	75	0.989	1.018	1.086	1.103	1.291	1.097
30.5	15	1.321				1.776	1.549
30.5	30	1.721		1.630		1.781	1.711
30.5	45	1.566		1.602		1.580	1.583
30.5	60	1.259		1.289		1.106	1.218
30.5	75	1.454		1.425		1.491	1.457
36.6	15	0.154		0.225		0.402	0.260
36.6	30	1.331		1.489		1.354	1.392
36.6	45	1.362		1.041		1.140	1.181
36.6	60	1.284		1.706		1.427	1.472
36.6	75	1.171		1.177		1.187	1.178
42.7	15	0.006		0.011		0.017	0.011
42.7	30	1.660		1.603		1.722	1.662
42.7	45	1.045		1.090		1.068	1.068
42.7	60	0.986		0.997		1.137	1.040
42.7	75	1.373		1.350		1.375	1.366

continued

Table D-7—continued.

Station Number	Time, min	Sample Depth					
		Surface	Quarter Depth	Middepth	Three-Quarter Depth	Bottom	Mean
48.8	15	0.009		0.009		0.107	0.042
48.8	30	1.151		1.528		1.636	1.438
48.8	45	1.556		1.653		1.563	1.591
48.8	60	1.103		1.004		0.914	1.007
48.8	75			1.253		1.336	1.295
54.9	15	0.000		0.018		0.023	0.014
54.9	30	1.074		1.297		1.433	1.268
54.9	45	1.263		1.355		1.331	1.316
54.9	60	1.161		1.294		1.247	1.234
54.9	75	0.971		1.052		1.195	1.073
61.0	15	0.013		0.008		0.010	0.010
61.0	30	1.489		1.861		2.422	1.924
61.0	45	1.060		1.291		1.562	1.304
61.0	60	1.306		0.893		1.230	1.143
61.0	75	1.003		1.082		1.108	1.064
67.1	15	0.020		0.004		0.006	0.010
67.1	30	1.880		1.959		2.094	1.978
67.1	45	1.586		1.362		1.587	1.512
67.1	60	0.433		1.233		1.347	1.004
67.1	75	1.340		1.299		1.363	1.334
73.2	15	0.009		0.011		0.023	0.014
73.2	30	1.755		1.828		1.968	1.850
73.2	45	1.387		1.599		1.704	1.563
73.2	60	0.323		0.474		1.576	0.791
73.2	75	0.954		1.324		1.002	1.093
79.2	15	0.002		0.012		0.025	0.013
79.2	30	1.664		1.840		1.804	1.769
79.2	45	1.241		1.409		1.370	1.340
79.2	60	1.325		1.436		1.523	1.428
79.2	75	0.900		1.152		1.338	1.130
85.3	15	0.006		0.016		0.012	0.011
85.3	30	1.479		1.754		1.770	1.668
85.3	45	1.501		1.600		1.531	1.544
85.3	60	1.117		1.056		1.031	1.068
85.3	75	0.988		1.194		1.128	1.103

Table D-7—continued.

Station Number	Time, min	Sample Depth					
		Surface	Quarter Depth	Middepth	Three-Quarter Depth	Bottom	Mean
91.4	15	0.002		0.012		0.025	0.013
91.4	30	1.442		1.741		1.756	1.646
91.4	45	1.199		0.955		1.242	1.132
91.4	60	1.389		1.470		1.471	1.444
91.4	75	0.925		1.004		1.185	1.038
97.5	15	0.005	0.030	0.026	0.051	0.096	0.042
97.5	30	1.464	1.411	1.464	1.645	1.678	1.533
97.5	45	1.438	1.300	1.318	1.822	1.890	1.554
97.5	60	1.561	1.667	1.633	1.572	1.941	1.675
97.5	75	1.427	1.351	1.333	1.379	1.453	1.389

Table D-8. Centerline sediment concentration profiles for experiment W10, kg/m³.

Station Number	Time, min	Sample Depth					
		Surface	Quarter Depth	Middepth	Three-Quarter Depth	Bottom	Mean
6.1	15	3.451		4.165		4.324	3.980
6.1	30	4.586				4.328	4.457
6.1	45	4.069		4.139		4.602	4.270
6.1	60	3.505		4.111		4.193	3.936
6.1	75	4.057		3.986		4.181	4.075
12.2	15	3.048		3.682		3.871	3.533
12.2	30	4.157		4.117		3.634	3.969
12.2	45	4.045		4.140		4.001	4.062
12.2	60	3.783		3.071		2.708	3.187
12.2	75	3.554		3.598		3.254	3.469
18.3	15	3.939		5.353		4.131	4.474
18.3	30	5.583		5.536		4.095	5.071
18.3	45	4.004		3.168		3.844	3.672
18.3	60	2.482		2.392		3.067	2.647
18.3	75	2.763		3.235		3.120	3.039
24.4	15	4.040	3.481	4.225	4.236	4.134	4.023
24.4	30	3.878	3.846	3.946	3.832	4.329	3.966
24.4	45		3.343	3.613	3.543		3.500
24.4	60	2.713	2.923	2.789	3.049	3.201	2.935
24.4	75	2.999	2.878	2.521	2.828	3.189	2.883
30.5	15	3.790		3.694		4.019	3.834
30.5	30	3.845		3.576		3.574	3.665
30.5	45	3.393		3.587		3.660	3.546
30.5	60	3.739		3.038		2.863	3.213
30.5	75	3.042		2.728		1.807	2.526
36.6	15	3.687		3.840		4.397	3.975
36.6	30	2.867		2.951		3.704	3.174
36.6	45	3.471		3.675		3.233	3.460
36.6	60	1.938		2.465		2.728	2.377
36.6	75	2.345		2.684		2.915	2.648
42.7	15	3.040		3.825		4.294	3.720
42.7	30	6.579		4.418		3.677	4.891
42.7	45	5.153		3.596		3.690	4.146
42.7	60	2.717		2.096		2.357	2.390
42.7	75	2.704		2.139		2.327	2.390

continued

Table D-8—continued.

Station Number	Time, min	Sample Depth					
		Surface	Quarter Depth	Middepth	Three-Quarter Depth	Bottom	Mean
48.8	15	3.833		3.602		3.485	3.640
48.8	30	3.074		4.462		5.118	4.218
48.8	45	3.560		3.904		4.724	4.062
48.8	60	2.342		2.758		3.290	2.796
48.8	75	2.790		2.744		3.090	2.875
54.9	15	3.671		2.843		3.733	3.416
54.9	30	3.297		3.196		4.382	3.625
54.9	45	4.592		3.257		3.814	3.888
54.9	60	1.860		2.240		2.419	2.173
54.9	75	1.657		2.559		2.178	2.132
61.0	15	3.161		3.353		3.164	3.226
61.0	30	2.917				4.047	3.482
61.0	45			4.217		0.086	2.151
61.0	60	2.180		2.005		2.580	2.255
61.0	75	2.144		2.078		2.662	2.295
67.1	15	0.008		4.143		3.564	2.572
67.1	30			3.653		3.479	3.566
67.1	45	2.705		3.084		2.902	2.897
67.1	60	2.160		2.282		2.076	2.173
67.1	75	3.030		1.941		2.685	2.552
73.2	15	3.321		3.343		3.865	3.510
73.2	30	3.421		3.485		3.261	3.389
73.2	45	2.637		2.413			2.525
73.2	60	1.701		1.826		4.735	2.754
73.2	75	1.750		2.457		2.774	2.327
79.2	15	3.131		1.026		4.397	2.851
79.2	30	2.703		2.376		2.899	2.659
79.2	45	1.760		2.811			2.285
79.2	60	1.929		1.747		2.455	2.044
79.2	75	1.502		1.968		2.534	2.001
85.3	15	0.347		2.719		3.096	2.054
85.3	30			0.037		3.053	1.545
85.3	45	4.061		2.747		2.930	3.246
85.3	60	2.607		2.406		2.839	2.617
85.3	75	1.642		1.787		2.585	2.005

continued

Table D-8—continued.

Station Number	Time, min	Sample Depth					
		Surface	Quarter Depth	Middepth	Three-Quarter Depth	Bottom	Mean
91.4	15			3.241		3.622	3.431
91.4	30	2.566		2.504		3.280	2.783
91.4	45			2.731		3.069	2.900
91.4	60			1.892		1.952	1.922
91.4	75			2.105		1.850	1.978
97.5	15	2.789	3.422	3.325	3.799	3.847	3.436
97.5	30	3.230	4.138	3.743	4.303	3.987	3.880
97.5	45	3.236	1.877	3.395	4.495	4.078	3.416
97.5	60	2.479	2.738	3.134	3.327	3.707	3.077
97.5	75	2.221	2.379	2.154	2.268	2.985	2.402

Table D-9. Centerline sediment concentration profiles for experiment W11, kg/m^3.

Station Number	Time, min	Sample Depth					
		Surface	Quarter Depth	Middepth	Three-Quarter Depth	Bottom	Mean
6.1	15	0.041		0.198		2.623	0.954
6.1	30	0.467		4.383		11.678	5.509
6.1	45	0.655		9.146		10.111	6.637
6.1	60	0.658		8.441		7.126	5.408
6.1	75	7.669		10.612		15.132	11.138
12.2	15	0.074		0.373		7.988	2.812
12.2	30	1.188		5.825		9.811	5.608
12.2	45	1.411		8.836		13.870	8.039
12.2	60	0.502		5.828		7.950	4.760
12.2	75	4.294		6.695		9.450	6.813
18.3	15	0.474		0.265		7.394	2.711
18.3	30	2.361		0.660		5.626	2.882
18.3	45	3.348		1.219		5.220	3.262
18.3	60	3.208		1.353		4.188	2.916
18.3	75	9.072		2.250		7.110	6.144
24.4	15	0.256	0.543	1.013	0.734	9.336	2.376
24.4	30	0.343	0.800	0.933	4.680	6.314	2.614
24.4	45	0.600	1.769	4.020	5.561	5.918	3.574
24.4	60	1.710	2.090	3.050	3.692	4.698	3.048
24.4	75	0.485	6.370	7.366	6.282	8.038	5.708
30.5	15	0.389		0.497		6.434	2.440
30.5	30	0.655		1.093		6.591	2.780
30.5	45	0.731		6.641		7.067	4.813
30.5	60	1.406		3.672		4.547	3.208
30.5	75	0.590		5.196		3.016	2.934
36.6	15	0.564		0.859		8.381	3.268
36.6	30	0.181		1.129		4.754	2.022
36.6	45	1.038		2.734		6.193	3.322
36.6	60	1.628		2.376		2.317	2.107
36.6	75	0.688		2.806		3.677	2.390
42.7	15	0.782		0.667		0.911	0.787
42.7	30	0.636		0.637		0.642	0.638
42.7	45	1.131		1.548		4.394	2.358
42.7	60	0.921		1.135		2.563	1.540
42.7	75	1.056		0.635		1.803	1.165

Table D-9—continued

Station Number	Time, min	Sample Depth					
		Surface	Quarter Depth	Middepth	Three-Quarter Depth	Bottom	Mean
48.8	15	0.347		0.506		0.519	0.457
48.8	30	0.540		0.700		4.636	1.959
48.8	45	1.584		2.179		4.590	2.784
48.8	60	1.035		1.733		2.867	1.878
48.8	75	0.701		2.306		2.334	1.780
54.9	15	0.277		0.261		0.305	0.281
54.9	30	0.653		0.628		3.094	1.458
54.9	45	1.458		1.200		3.566	2.075
54.9	60	2.102		3.720		3.701	3.174
54.9	75	1.889		5.328		2.732	3.316
61.0	15	0.029		0.032		0.002	0.021
61.0	30	0.562		0.656		0.766	0.661
61.0	45	0.688		0.720		0.380	0.596
61.0	60	1.177		1.637		2.318	1.711
61.0	75	1.415		2.072		2.812	2.100
67.1	15	0.007		0.007		0.012	0.009
67.1	30	0.682		0.750		0.744	0.725
67.1	45	1.478		0.120		7.111	2.903
67.1	60	2.394		2.033		3.839	2.755
67.1	75	1.660		2.251		2.318	2.077
73.2	15	0.008		0.012		0.008	0.009
73.2	30	0.636		0.733		0.783	0.717
73.2	45	1.275		1.414		2.232	1.640
73.2	60	1.899		3.554		3.101	2.851
73.2	75	1.962		2.512		2.761	2.412
79.2	15	0.020		0.011		0.013	0.015
79.2	30	0.591		0.874		0.957	0.807
79.2	45	0.741		1.198		1.176	1.038
79.2	60	1.574		2.674		3.055	2.434
79.2	75	2.499		2.740		3.048	2.762

continued

Table D-9—continued.

Station Number	Time, min	Sample Depth					
		Surface	Quarter Depth	Middepth	Three-Quarter Depth	Bottom	Mean
85.3	15	0.009		0.008		0.005	0.007
85.3	30	0.741		0.726		0.583	0.683
85.3	45	0.745		0.662		1.092	0.833
85.3	60	2.379		3.685		1.898	2.654
85.3	75	2.754		2.716		2.705	2.725
91.4	15	0.463		0.008		0.014	0.162
91.4	30	0.424		0.428		0.476	0.443
91.4	45	0.212		0.861		0.573	0.549
91.4	60	0.814		1.369		1.871	1.351
91.4	75	2.832		2.476		2.568	2.625
97.5	15	0.011	0.002	0.005	0.011	0.009	0.008
97.5	30	0.200	0.188	0.227	0.248	0.240	0.221
97.5	45	0.635	0.295	0.771	0.296	0.689	0.537
97.5	60	1.104	0.893	0.454	0.657	0.632	0.748
97.5	75	2.750	2.941	2.628	3.201	3.038	2.911

Table D-10. Sediment Bed Deposition Thickness, cm

Station Number m	Experiment Number					
	W4	W5	W6	W9	W10	W11
12.2	0.15	--	0.18	--	--	0.82
24.4	0.58	0.06	0.55	--	0.24	0.12
36.6	--	--	0.61	--	0.61	0.03
48.8	0.61	0.24	0.73	0.21	0.79	0.18
61.0	0.76	0.24	0.73	0.21	0.94	--
73.2	0.43	--	0.40	--	0.67	0.27
85.3	0.64	0.24	0.85	0.34	0.98	--
97.5	0.43	0.12	0.58	--	0.70	--

LIST OF REFERENCES

Adler, P. M. (1981). "Heterocoagulation in shear flow." *J. Colloid Interface Sci.*, 83(1), 106-115.

Argaman, Y., and Kaufman, W. J. (1970). "Turbulence and flocculation." *J. San. Engrg.*, ASCE, 96(SA2), 223-241.

Ariathurai, R., MacArthur, R. C., and Krone, R. B. (1977). "Mathematical model of estuarial sediment transport." *T.R. D-77-12*, USAE Waterways Exp. Sta., Vicksburg, MS.

Boesch, D. F., Josselyn, M. N., Mehta, A. J., Morris, J. T., Nuttle, W. K., Simenstad, C. A., and Swift, D. J. P. (1994). "Scientific assessment of coastal wetland loss, restoration and management in LA." *J. Coastal Rsch.*, Special Issue 10, 1-103.

Burban, P. Y., Lick, W., and Lick, J. (1989). "The flocculation of fine-grained sediments in estuarine waters." *J. Geophys. Rsch.*, 94(C6), 8323-8330.

Burt, T. N. (1986). "Field settling velocities of estuary muds." *Estuarine Cohesive Sediment Dynamics*, Vol 14 Coastal and Estuarine Studies, A. J. Mehta, ed., Springer-Verlag, New York, 126-150.

Cervantes, E. E., Mehta, A. J., and Li, Y. (1995). "A laboratory-based examination of episodic resuspension of fine-grained sediments by waves and currents." *Proc. COPEDEC IV*, 4th Int. Conf. on Coastal and Port Engrg. in Dev. Countries, Brazilian Wat. Resrcs. Assn., Rio de Janeiro, Brazil, 1-13.

Clarke, J. F., and McChesney, M. (1964). *The Dynamics of Real Gases*. Butterworth, Washington, DC.

Clercx, H. J. H., and Schram, P. P. J. M. (1992). "Three particle hydrodynamic interactions in suspensions." *J. Chem. Physics*, 96(43), 3137-3151.

Clift, R., Grace, R., Jr., and Weber, M. E. (1978). *Bubbles, drops, and particles*. Academic Press, New York.

Coleman, C. J., Teeter, A. M., Donnell, B. P., Fisackerly, G. M., Crouse, D. A., and Parman, J. W. (1988). "The Atchafalaya River delta, report 2: field data, section 1: Atchafalaya Bay program description and data, volume 1: main text." *T.R. HL-82-15, No. 2,* USAE Waterways Exp. Sta., Vicksburg, MS.

Cratsley, D. W. (1975). "Recent deltaic sedimentation, Atchafalaya Bay, Louisiana." M.S. thesis, Louisiana State University, Baton Rouge.

CTH. (1955). "Investigation of salinity intrusion and related phenomena, interim report on results of flume control tests." USAE Comm. on Tidal Hydr., Vicksburg, MS.

CTH. (1960). "Soil as a factor in shoaling processes: a literature review." *Tech. Bul. 4,* USAE Comm. on Tidal Hydr., Vicksburg, MS.

CTH. (1971). "Estuarine navigation projects." *Tech. Bul. 17,* USAE Comm. on Tidal Hydr., Vicksburg, MS.

Daily, J. W., and Harleman, D. R. F. (1973). *Fluid Dynamics.* Addison-Wesley, Reading, MA.

Daisley, R. E., Fuchs, M., and Fuchs, N. A. (1989). *The Mechanics of Aerosols.* Dover, New York.

Delichatsios, M. A., and Probstein, R. F. (1975). "Coagulation in turbulent flow: theory and experiment." *J. Colloid Interface Sci.,* 51(1), 71-81.

Dixit, J. G., Mehta, A. J., and Partheniades, E. (1982). "Redepositional properties of cohesive sediments deposited in a long flume." *UFL/COEL-82/002,* Coastal and Oceanogr. Engrg. Dept., University of Florida, Gainesville.

Donnell, B. P., Letter, J. V., and Teeter, A. M. (1991). "The Atchafalaya River delta, report 11: two-dimensional modeling." *T.R. HL-82-15, No. 11,* USAE Waterways Exp. Sta., Vicksburg, MS.

Dyer, K. R. (1989). "Sediment processes in estuaries: future research requirements." *J. Geophys. Rsch.* 94(C10), 14,327-14,339.

Dyer, K. R., Cornelisse, J., Dearnaley, M. P., Fennessy, M. J., Jones, S. E., Kappenberg, J., McCave, I. N., Pejrup, M., Puls, W., van Leussen, W., and Wolfstein, K. (1996). "A comparison of *in situ* techniques for estuarine floc settling velocity measurements." *J. Sea Rsch.,* 36(112), 15-29.

Ebersole, B. A. (1985). "The Atchafalaya River delta, report 9: numerical modeling of hurricane-induced storm surge." *T.R. HL-82-15, No. 9*, USAE Waterways Exp. Sta., Vicksburg, MS.

Edzwald, J. K., and O'Melia, C. R. (1975). "Clay distributions in recent estuarine sediments." *Clays and Clay Minerals*, 23, 39-44.

Edzwald, J. K., Upchurch, , J.B., and O'Melia, C. R. (1974). "Coagulation in estuaries." *Envir. Sci. Tech.*, 8(1), 58-63.

Einstein, A. (1905). "On the movement of small particles suspended in a stationary liquid demanded by the molecular-kinetic theory of heat." *Ann. Physik*, 17, 549-554

Einstein, H. A., and Krone, R. B. (1962). "Sediment transport in salt water." *J. Geophys Rsch.*, 67(3), 1451-1461.

Eisma, D., Schuhmacher, T., Boekel, H., van Heerwarden, J., Franken, H., Laan, M., Vaars, A., Eijgenram, F., and Kalf, J. (1990). "A camera and image analysis system of *in situ* observation of flocs in natural waters." *Netherlands J. Sea Rsch.*, 27(1), 43-56.

Fennessy, M. J., and Dyer, K. R. (1996). "Floc population characteristics measured with INSSEV during the Elbe estuary intercalibration experiment." *J. Sea Rsch.*, 36(½), 55-62.

Fennessy, M. J., Dyer, K. R., Huntley, D. A., and Bale, A. J. (1997). "Estimation of settling flux spectra in estuaries using INSSEV." *Cohesive Sediments*, N. Burt, W. R. Parker, and J. Watts, eds., Wiley, Chichester, UK, 88-105.

Fort, R. (1997). "Problem solving in organic chemistry." *Course notes for CHY558*, http://oldblue.umche.maine.edu/newbasic.html/, University of Maine, Orono.

Gibbs, R. J. (1977). "Clay mineral segregation in the marine environment." *J. Sed. Petr.*, 47(1), 237-243.

Gibbs, R. J. (1983). "Coagulation rates of clay minerals and natural sediments." *J. Sed. Petr.*, 53(4), 1193-1203.

Gibbs, R. J. (1985). "Estuarine flocs: their size, settling velocity and density." *J. Geophys. Rsch.*, 90(C2), 3249-3251.

Gibbs, R. J., Tshudy, D. M., Konwar, L., and Martin, J. M. (1989). "Coagulation and transport of sediments in the Gironde estuary." *Sedimentol.*, 36, 987-999.

Graf, W. H. (1984). *Hydraulics of sediment transport*. Water Resources Pub., Littleton, CO.

Grim, R. E. (1968). *Clay Mineralogy*. McGraw-Hill, New York.

Gust, G. (1976). "Observations on turbulent-drag reduction in a dilute suspension of clay in sea-water." *J. Fl. Mech.*, 75(1), 29-47.

Gust, G., and Southard, J. B. (1983). "Effects of weak bed load on the universal law of the wall." *J. Geophys. Rsch.*, 88(C10), 5939-5952.

Hahn, H. H., and Stumm, W. (1970). "The role of coagulation in natural waters." *Am. J. Sci.*, 268, 354-368.

Han, M. (1989). "Mathematical modeling of heterogeneous flocculent sedimentation." Ph.D. thesis, University of Texas, Austin.

Hawley, N. (1982). "A numerical model of cohesive suspended sediment dynamics." Great Lakes Envir. Rsch. Lab., Ann Arbor, MI.

Heffler, D. E., Syvitski, J. P. M., and Asprey, K. W. (1991). "The floc camera assembly." *Principles, methods, and application of particle size analysis*. J. P. M. Syvitski, ed., Cambridge University Press, UK, 209-221.

Hess, K. W. (1988). "Lagrangian drift model of suspended sediment transport in Chesapeake Bay." *Understanding the Estuary: Advances in Chesapeake Bay Rsch., Proc. of a Conf. 29-31 Mar., 1988. Chesapeake Rsch. Const. Pub. 129*, Chesapeake Bay Prog., Annapolis, MD, 352-368.

Hogg, R., Klimpel, R. C., and Ray, D. T. (1985). "Structural aspects of floc formation and growth." *Flocculation, sedimentation and consolidation*, B. M. Moudgil and P. Somasundaran, eds., Engr. Foundation, New York, 217-231.

Hunt, J. R. (1982). "Self-similar particle-size distributions during coagulation: theory and experimental verification, *J. Fl. Mech.*, 122, 169-185.

Hunter, K. A., and Liss, P. S. (1982). "Organic matter and the surface charge of suspended particles in estuarine waters." *Lim. Oceanog.*, 27(2), 322-335.

Hwang, K. N. (1989). "Erodibility of fine sediment in wave dominated environments." *Rpt. UFL/COEL/89-017*, Coastal and Oceanogr. Engrg. Dept., University of Florida, Gainesville.

Jensen, R. E. (1985). "The Atchafalaya River delta, report 10: wave hindcasts, main text and appendices A and B." *T.R. HL-82-15, No. 10*, USAE Waterways Exp. Sta., Vicksburg, MS.

Jiang, J. (1999). "Lutocline dynamics in estuaries." Ph.D. thesis, University of Florida, Gainesville.

Jimenez, J., Wray, A. A., Saffman, P. G., and Rogallo, R. S. (1993). "The structure of intense vorticity in isotropic turbulence." *J. Fl. Mech.*, 255, 65-90.

Jobson, H. E., and Sayre, W. W. (1970). "Vertical transfer in open channel flow." *J. Hydr. Div.* ASCE, 96(HY3), 703-724.

Johnson, B. H., Teeter, A. M., Wang, H. V., Cerco, C. F., and Moritz, H. R. (1999). "Modeling the fate and water quality impacts of dredged material placement at Site 104." *Tech. Rpt.* USAE Waterways Exp. Sta., Vicksburg, MS, in press.

Johnson, C. P., Li, X., and Logan, B. E. (1996). "Settling velocities of fractal aggregates." *Envir. Sci. and Tech.*, 30, 1911-1918.

Kranck, K. (1973). "Flocculation of suspended sediment in the sea." *Nature*, 26(Dec. 7), 348-350.

Kranck, K. (1980a). "Experiments on the significance of flocculation in the settling of fine-grained sediment in still water." *Can. J. Earth Sci.*, 17(11), 1517-1526.

Kranck, K. (1980b). "Sedimentation processes in the sea." *Handbook of Environmental Chemistry*, 2(A), Springer-Verlag, Berlin, 61-75.

Kranck, K. (1980c). "Variability of particulate matter in a small coastal inlet." *Can. J. Fisheries and Aquat. Sci.*, 1209-1215.

Kranck, K. (1986). "Particulate matter grain-size characteristics and flocculation in a partially mixed estuary." *Sedimentol.*, 18, 107-114.

Kranck, K., and Milligan, T. G. (1992). "Characteristics of suspended particles at an 11-hour anchor station in San Francisco Bay, California." *J. Geophys. Rsch.*, 97(C7), 11,373-11,382.

Kranck, K., Petticrew, E., Milligan, T. G., and Droppo, I. G. (1993). "*In situ* particle size distributions resulting from flocculation of suspended sediment." *Nearshore and Estuarine Cohesive Sediment Transport*, Vol. 42 Coastal and Estuarine Studies, A. J. Mehta, ed., Am. Geophys. Union, Washington, DC, 60-74.

Kranenburg, C. (1994). "The fractal structure of cohesive sediment aggregates." *Estuarine Coastal Shelf Sci.,* 39, 451-460.

Krone, R. B. (1962). "Flume studies of the transport of sediment in estuarial shoaling process, final report." Hydr. Engrg. Lab. and San. Engrg. Rsch. Lab., University of California, Berkeley, CA.

Krone, R. B. (1963). "A study of rheologic properties of estuarial sediments." *Tech. Bul. 7,* USAE Comm. on Tidal Hydr., Vicksburg, MS.

Krone, R. B. (1978). "Aggregation of suspended particles in estuaries." *Estuarine Transport Processes,* Belle Baruch Lib. Mar. Sci. No. 7, University of South Carolina Press, Columbia, 177-190.

Krone, R. B. (1986). "The significance of aggregate properties to transport processes." *Estuarine Cohesive Sediment Dynamics,* A. J. Mehta, ed., Vol. 14 Lecture Notes on Coastal and Estuarine Studies, Springer-Verlag, New York, 66-84.

Krone, R. B. (1993). "Sedimentation revisited." *Nearshore and Estuarine Cohesive Sediment Transport,* Vol. 42 Coastal and Estuarine Studies, Am. Geophys. Union, Washington, DC, 108-125.

Kruyt, H. R. (1952). *Colloid Chemistry,* Elsevier, London.

Lapin, L. L. (1990). *Probability and Statistics for Modern Engineering.* PWS-Kent, Boston, MA.

Lau, Y. L. (1994). "Temperature effect on settling velocity and deposition of cohesive sediments." *J. Hydr. Rsch.,* 32(1), 41-51.

Lee, S. C., and Mehta, A. J. (1994). "Cohesive sediment erosion." *C. R. DRP-94-6,* USAE Waterways Exp. Sta., Vicksburg, MS.

Letter, J. V. (1982). "The Atchafalaya River delta, report 3: extrapolation of delta growth." *T.R. HL-82-15, No. 3,* USAE Waterways Exp. Sta., Vicksburg, MS.

Letter, J. V., and McAnally, W. H. (1981). "Physical hydraulic models: assessment of predictive capabilities, Brunswick Harbor shoaling studies." *R. R. H-75-3,* USAE Waterways Exp. Sta., Vicksburg, MS.

Li, Y. (1996). "Sediment associated constituent release at the mud-water interface due to monochromatic waves." *UFL/COEL-TR/111,* Coastal and Oceanogr. Engrg. Dept., University of Florida, Gainesville.

Li, Y., and Parchure, T. M. (1998). "Mudbanks of the southwest coast of India. VI: suspended sediment profiles." *J. Coastal Rsch.,* 14(4), 1363-1372.

Lick, W., and Huang, H. (1993). "Flocculation and the physical properties of flocs." *Nearshore and Estuarine Cohesive Sediment Transport,* Vol. 42 Coastal and Estuarine Studies, A. J. Mehta, ed., Am. Geophys. Union, Washington, DC, 21-39.

Lick, W., Huang, H., and Jepsen, R. (1993). "Flocculation of fine grained sediments due to differential settling." *J. Geophys. Rsch.,* 98(C6), 10,279-10,288.

Lick, W., and Lick, J. (1988). "Aggregation and disaggregation of fine-grained lake sediments." *J. Great Lakes Rsch.,* 14(4), 514-523.

Lick, W., Lick, J., and Ziegler, C. K. (1992). "Flocculation and its effect on the vertical transport of fine-grained sediments." *Sed./Water Interactions, Hydrobiologia,* B. T. Hart and P. G. Sly, eds., 235/236(July 17), 1-16.

Lick, W., Xu, Y. J., and McNeil, J. (1995). "Resuspension properties of sediments from the Fox, Saginaw, and Buffalo Rivers." *J. Great Lakes Rsch.,* 21(2), 257-274.

Luettich, R. A., Jr., Wells, J. T., and Kim, S. Y. (1993). "*In situ* variability of large aggregates: preliminary results on the effects of shear." *Nearshore and Estuarine Cohesive Sediment Transport,* Vol. 42 Coastal and Estuarine Studies, A. J. Mehta, ed., Am. Geophys. Union, Washington, DC, 447-466.

MacFarlane, J. J. (1997). "IONMIX: a code for computing the equation of state and radiative properties of LTE and non-LTE plasmas, program summary." http://www.cps.cs.qub.ac.uk/cpc/summaries/ABJT/, *Comptnl. Phys. Commun.,* Elsevier, London.

Malcherek, A., and Zielke, W. (1995). "The role of macroflocs in estuarine sediment dynamics and its numerical modeling." *Proc. 4th Int. Conf. Estuarine and Coastal Modlng.,* ASCE, 695-706.

Matsuo, T., and Unno, H. (1981). "Forces acting on floc and strength of floc." *J. Envir. Engrg. Div.,* ASCE, 107(EE3), 527-545.

McAnally, W. H. (1989). "Lessons from 10 years experience in 2D sediment modeling." *Sediment Transport Modlng.,* ASCE, 231-236.

McAnally, W. H., Thomas, W. A., Letter, J. V., and Stewart, J. P. (1985). "The Atchafalaya River delta, report 6: interim summary report of delta growth." *T.R. HL-82-15, No. 6*, USAE Waterways Exp. Sta., Vicksburg, MS.

McCave, I. N. (1984). "Size spectra and aggregation of suspended particles in the deep ocean." *Deep Sea Rsch.*, 31(4), 329-352.

Meakin, P. (1988). "Fractal aggregates." *Adv. Colloid Interface Sci.* 28, 249-331.

Mehta, A. J. (1973). "Depositional behavior of cohesive sediments." Ph.D. thesis, University of Florida, Gainesville.

Mehta, A. J. (1991). "Review notes on cohesive sediment erosion." *Coastal Sediments '91*, N. C. Kraus, K. J. Gingerich, and D. L. Kriebel, eds., ASCE, 40-53.

Mehta, A. J. (1996). "Interaction between fluid mud and water waves." *Environmental Hydraulics*, V. P. Singh and W. H. Hager, eds., Kluwer, Dordrect, Netherlands.

Mehta, A. J., and Li, Y. (1997). "A PC-based short course on fine-grained sediment transport engineering." Coastal and Oceanogr. Engrg. Dept., University of Florida, Gainesville.

Mehta, A. J., and Lott, J. W. (1987). "Sorting of fine sediment during deposition." *Coastal Sediments '87*, N. C. Kraus, ed., ASCE, 348-362.

Mehta, A. J., Nayak, B. U., and Hayter, A. J. (1983). "A preliminary investigation of fine sediment dynamics in Cumbarjua Canal, Goa." *Mahasagar-Bull. Natl. Inst. Oceanog.* India, 16(2), 95-108.

Mehta, A. J., and Parchure, T. M. (1999). "Surface erosion of fine-grained sediment revisited." *Proc. Int. Conf. Muddy Coasts*, in press.

Mehta, A. J., and Partheniades, E. (1975). "An investigation of the deposition properties of flocculated fine sediments." *J. Hydr. Rsch.*, IAHR, 12(4), 361-381.

Mehta, A. J., and Srinivas, R. (1993). "Observations on the entrainment of fluid mud by shear flow." *Nearshore and Estuarine Cohesive Sediment Transport*, Vol 42 Coastal and Estuarine Studies, A. J. Mehta, ed., Am. Geophys. Union, Washington, DC, 224-246.

Mendoza, C., and Zhou, D. (1995). "A dynamic approach to sediment-laden flows." *Wat. Resrcs. Rsch.*, 31(12), 3075-3087.

Munk, W. H., and Anderson, E. R. (1948). "Notes on a theory of the thermocline." *J. Mar. Rsch.*, 1, 276-295.

Narimousa, S., and Fernando, H. J. S. (1987). "On the sheared interface of an entraining stratified fluid." *J. Fl. Mech.*, 174, 1-22.

Newman, K. A. (1990). "Cycling of fine particles between water and sediments." Ph.D. thesis, Massachusetts Institute of Technology, Cambridge, MA.

Nichols, M. M., and Thompson, G. S. (1978). "A field study of fluid mud dredged material: its physical nature and dispersal." *T.R. D-78-40*, USAE Waterways Exp. Sta., Vicksburg, MS.

Ochi, M. K. (1990). *Applied Probability and Stochastic Processes*, Wiley, New York.

O'Melia, C. R. (1985). "The influence of coagulation and sedimentation on the fate of particles, associated pollutants, and nutrients in lakes." *Chemical Processes in Lakes*, W. Strom, ed., Wiley, New York, 207-224.

Overbeek, J. T. G. (1952). "Kinetics of flocculation." Chap. VIII in *Colloidal Science, Vol. 1*, R. Kruyt, ed., L. C. Jackson, trans., Elsevier, Amsterdam, 278-300.

Parchure, T. M. (1984). "Erosional behavior of deposited cohesive sediments." Ph.D. thesis, University of Florida, Gainesville.

Parker, D. S., Kaufman, W. J., and Jenkins, D. (1972). "Floc breakup in turbulent flocculation processes." *J. San. Engrg. Div.*, ASCE, 98(SA1), 79-99.

Parker, W. R., and Kirby, R. (1982). "Time dependent properties of cohesive sediment relevant to sedimentation management—European experience." *Estuarine Comparisons*, V. S. Kennedy, ed., Academic Press, New York.

Parker, W. R., Smith, T. J., and Kirby, R. (1980). "Observation of density stratification due to suspended fine sediments." *Secnd. Int. Symp. on Strat. Flows*, T. Carstens and T. McClimans, eds., Trondheim, Norway, 77-86.

Partheniades, E. (1962). "A study of erosion and deposition of cohesive soils in salt water." Ph.D. thesis, University of California, Berkeley.

Partheniades, E. (1971). "Erosion and deposition of cohesive materials." *River Mechanics*, H. W. Shen, ed., Shen, Ft. Collins, CO, 25-1 - 25-91.
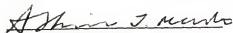
Partheniades, E. (1977). "Unified view of wash load and bed material load." *J. Hydr. Div.,* ASCE, 103(HY9), 1037-1057.

Partheniades, E. (1993). "Turbulence, flocculation, and cohesive sediment dynamics." *Nearshore and Estuarine Cohesive Sediment Transport,* Vol. 42 Coastal and Estuarine Studies, A. J. Mehta, ed., Am. Geophys. Union, Washington, DC, 40-59.

Pritchard, D. W. (1952). "Estuarine Hydrography." *Adv. Geophys.,* 1, 243-280.

Rabinowitch, E. (1937). "The recombination-velocity of free atoms." *Trans. Faraday Soc.,* 33, 283-293.

Raveendran, P., and Amirtharajah, A. (1995). "Role of short-range forces in particle detachment during filter backwashing." *J. Envir. Engrg.,* 121(13), 860-868.

Ross, M. A. (1988). "Vertical structure of estuarine fine sediment suspensions." *Rpt. FL/COEL-TR/079,* Coastal and Oceanogr. Engrg. Dept., University of Florida, Gainesville.

Saffman, P. G., and Turner, J. S. (1956). "On the collision of drops in turbulent clouds." *J. Fl. Mech.,* 1, 16-30.

Sakamoto, W. (1972). "Study on the process of river suspension from flocculation to accumulation in estuary." *Bul. Ocean Rsch. Inst. of Tokyo,* 5, 46-52.

Salim, I. A., Miller, C. J., and Howard, J. L. (1996). "Sorption isotherm-sequential analysis of heavy metal retention in landfill liners." *Soil Sci. Soc. of Am. J.,* 60(1), 107-114.

Smoluchowski, M. Z. von. (1917). "Versuch einer mathematische theorie der koagulations-kinetic kolloider losungen." *Ziet. fur Phys. Chem.,* 92, 129-168.

Stolzenbach, K. D., and Elimelich, M. (1994). "The effect of density on collisions between sinking particles: implications for particle aggregation in the ocean." *J. Deep Sea Rsch.,* 41(3), 469-483.

Stronach, J. A., Webb, A. J., Murty, T. S., and Cretney, W. J. (1993). "A three-dimensional numerical model of suspended sediment transport in Howe Sound, British Columbia." *Atmos.-Ocean,* 31(1), 73-97.

Streeter, V. L. (1966). *Fluid Mechanics.* McGraw-Hill, New York.

Sumer, B. M., and Diegaard, R. (1981). "Particle motions near the bottom in turbulent flows in an open channel." *J. Fl. Mech.,* 109, 311-337.

Swift, D. L., and Friedlander, S. K. (1964). "The coagulation of hydrosols by Brownian motion and laminar shear flow." *J. Colloid Sci.*, 19, 621-647.

Tambo, N., and Watanabe, Y. (1979). "Physical characteristics of flocs I. The floc density function and aluminum floc." *Water Resrcs.*, 13, 409-419.

Teeter, A. M. (1993). "Suspended transport and sediment-size transport effects in a well mixed, mesotidal estuary." *Nearshore and Estuarine Cohesive Sediment Transport*, Vol. 42 Coastal and Estuarine Studies, A. J. Mehta, ed., Am. Geophys. Union, Washington, DC, 411-429.

Teeter, A. M. (1999a). "Fine-grained modeling using multiple grain classes: Part I. Cohesive sediment settling and deposition." *Coastal and Estuarine Fine Sediment Transport: Processes and Applications*, W. H. McAnally and A. J. Mehta, eds., Elsevier, Amsterdam, in press.

Teeter, A. M. (1999b). "Fine-grained modeling using multiple grain classes: Part II. Application to shallow water resuspension and deposition." *Coastal and Estuarine Fine Sediment Transport: Processes and Applications*, W. H. McAnally and A. J. Mehta, eds., Elsevier, Amsterdam, in press.

Teeter, A. M., and Callegan. C. (1999). "Effects of Channel Modifications on Currents, Salinity, and Sedimentation near Daniel Island, Charleston Harbor, SC." *Tech. Rept.*, USAE Waterways Exp. Sta., Vicksburg, MS, in press.

Teeter, A. M., and Pankow, W. (1989). "The Atchafalaya River Delta, report 2: field data, section 2: settling characteristics of bay sediments." *T.R. HL-82-15, No. 3*, USAE Waterways Exp. Sta., Vicksburg, MS.

Teeter, A. M., Parchure, T. M., and McAnally, W. H. (1997). "Size-dependent erosion of two silt-clay mixtures." *Cohesive Sediments*, N. Burt, W. R. Parker, and J. Watts, eds., Wiley, Chichester, UK, 253-262.

Teisson, C. (1997). "A review of cohesive sediment transport models." *Cohesive Sediments*, N. Burt, W. R. Parker, and J. Watts, eds.,Wiley, Chichester, UK, 367-381.

ten Brinke, W. B. M. (1997). "Temporal variability in aggregate size and settling velocity in the Oosterschelde (The Netherlands)." *Cohesive Sediments*, N. Burt, W. R. Parker, and J. Watts, eds., Wiley, Chichester, UK, 63-74.

Tennekes, H., and Lumley, J. L. (1972). *A First Course in Turbulence*. MIT Press, Cambridge, MA.

Thomas, W. A., Heath, R. E., Stewart, J. P., and Clark, D. G. (1988). "The Atchafalaya River delta, report 5: quasi-two-dimensional model of delta growth and impacts on river stages." *T.R. HL-82-15, No. 5*, USAE Waterways Exp. Sta., Vicksburg, MS.

Thomas, W. A., and McAnally, W. H. (1985). "User's manual for the generalized computer program system, open channel flow and sedimentation, TABS-2." *I. R. HL-85-1*, USAE Waterways Exp. Sta., Vicksburg, MS.

Tominaga, A., Nezu, I., Ezaki, K., and Nakagawa, H. (1988). "Three-dimensional turbulent structure in straight open channel flows." *J. Hydr. Rsch.*, IAHR, 27(1), 149-173.

Triple E. (1999). "The great mothers." *Eclectic Explicit Encyclopedia*, http://clix.net/5thworld/5thwnew/noosphere/3e/devi/mothers.html.

Tsai, C. H., and Hu, J. Q. (1997). "Flocculation of particles by fluid shear in buffered suspensions." *Proc. of the 7th Int. Symp. on Interactions Between Seds. and Water*, Kluwer, Dordrect, Netherlands, 55-62.

Tsai, C. H., and Hwang, S. C. (1995). "Flocculation of sediment from Tanshui River estuary." *Mar. Freshwater Rsch.*, 46(1), 383-392.

Tsai, C. H., Iacobellis, S., and Lick, W. (1987). "Flocculation of fine-grained lake sediments due to a uniform shear stress." *J. Great Lakes Rsch.*, 13(2), 135-146.

Van Beek, J. L. (1977). "A jetty from Point Chevreuil: an evaluation of a proposal to reduce sedimentation in the Cote Blanche Bays and Vermillion Bay." Coastal Environments, Inc., Baton Rouge, LA.

van Dam, G. C., and Louwersheimer, R. A. (1995). "A three-dimensional transport model for dissolved and suspended matter in estuaries and coastal seas." *Dynamics and Exchanges in Estuaries and the Coastal Zone*, Vol. 40 Coastal and Estuarine Studies, D. Prandle, ed., Am. Geophys. Union, Washington, DC, 481-506.

Van Heerden, I. L., and Roberts, H. H. (1980). "The Atchafalaya Delta—Louisiana's prograding coast." *Trans. Gulf Coast Assoc. of Geological Soc.*, XXX, 497-506.

van Leussen, W. (1994). "Estuarine macroflocs and their role in fine-grained sediment transport." Ph.D. thesis, University of Ultrecht, Netherlands.

van Leussen, W. (1997). "The Kolmogorov microscale as a limiting value for floc sizes of suspended fine-grained sediments in estuaries." *Cohesive Sediments*, N. Burt, W. R. Parker, and J. Watts, eds., Wiley, Chichester, UK, 45-62.
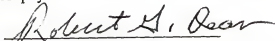
van Leussen, W., and Cornelisse, J. M. (1993). "The role of large aggregates in estuarine fine-grained sediment dynamics." *Nearshore and Estuarine Cohesive Sediment Transport,* Vol. 42 Coastal and Estuarine Studies, A. J. Mehta, ed., Am. Geophys. Union, Washington, DC, 75-91.

Wells, M. L., and Goldberg, E. D. (1993). "Colloid aggregation in seawater." *Marine Chem.,* 41, 353-358.

Whitehouse, U. G., Jeffrey, L. M., and Debbrecht, J. D. (1960). "Differential settling tendencies of clay minerals in saline waters." *7th Nat. Conf. on Clays and Clay Minerals,* Pergamon Press, New York. 1-79.

Wiesner, M. R. (1992). "Kinetics of aggregate formation in rapid mix." *Water Resrcs.,* 26(3), 379-387.

Winterwerp, J. C. (1998). "A simple model for turbulence induced flocculation of cohesive sediment." *J. Hydr. Rsch.,* IAHR, 36(3), 308-326.

Winterwerp, J. C. (1999). "On the dynamics of high concentration mud suspensions." Ph.D. thesis, Technical University of Delft, Netherlands.

Wolanski, E., and Gibbs, R. J. (1995). "Flocculation of suspended sediment in the Fly River estuary, Papua New Guinea." *J. Coastal Rsch.,* 11(3), 754-762.

Yalin, M. S., and Findlayson, G. D. (1972). "On the velocity distribution of flow carrying sediment in suspension." *Sedimentation,* H. W. Shen, ed., Shen, Ft. Collins, CO, 125-138.

Zeichner, G. R., and Schowalter, W. R. (1977). "Use of trajectory analysis to study stability of colloidal dispersions in flow fields." *Am. Inst. Chem. Engrs. J.,* 23(3), 243-254.

Zreik, D. A., Krishnappen, B. G., Germaine, J. T., Madsen, O. S., and Ladd, C. C. (1998). "Erosional and mechanical strengths of deposited cohesive sediments." *J. Hydr. Engrg.,* ASCE, 124(11), 1076-1085.

I certify that I have read this study and that in my opinion it conforms to acceptable standards of scholarly presentation and is fully adequate, in scope and quality, as a dissertation for the degree of Doctor of Philosophy.

Ashish J. Mehta, Chair
Professor of Coastal and Oceanographic
Engineering

I certify that I have read this study and that in my opinion it conforms to acceptable standards of scholarly presentation and is fully adequate, in scope and quality, as a dissertation for the degree of Doctor of Philosophy.
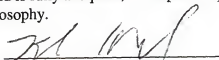
Robert G. Dean
Graduate Research Professor of Coastal
and Oceanographic Engineering

I certify that I have read this study and that in my opinion it conforms to acceptable standards of scholarly presentation and is fully adequate, in scope and quality, as a dissertation for the degree of Doctor of Philosophy.

Daniel M. Hanes
Associate Professor of Coastal and
Oceanographic Engineering

I certify that I have read this study and that in my opinion it conforms to acceptable standards of scholarly presentation and is fully adequate, in scope and quality, as a dissertation for the degree of Doctor of Philosophy.

Kirk Hatfield
Associate Professor of Civil Engineering

I certify that I have read this study and that in my opinion it conforms to acceptable standards of scholarly presentation and is fully adequate, in scope and quality, as a dissertation for the degree of Doctor of Philosophy.

Robert J. Thieke
Assistant Professor of Coastal and
Oceanographic Engineering

BIOGRAPHICAL SKETCH

William H. McAnally was born 28 January 1947 in Jacksonville, Florida, to Nell Collins McAnally and William H. McAnally, Sr. He grew up in Texas and Arizona. In Phoenix he met Carol Larner, and they married in 1967 after a brief, four-year engagement. He graduated from Arizona State University with a Bachelor of Science in Engineering (Civil) in 1969 and began employment at the U.S. Army Engineer Waterways Experiment Station (WES), Vicksburg, Mississippi. In 1973 he received a Master of Engineering degree in Coastal and Oceanographic Engineering from the University of Florida. In 1996 he resumed graduate study at the University of Florida. He currently serves as chief of the Estuaries and Hydrosciences Division of the WES Coastal and Hydraulics Laboratory.

He and Carol have four children—Michelle McAnally, Heather McAnally Ford, Sarah McAnally, and Adam McAnally; two sons-in-law—Michael Coody and Dow Ford; and one granddaughter—Hannah Ford.

This dissertation was submitted to the Graduate Faculty of the College of Engineering and to the Graduate School and was accepted as partial fulfillment of the requirements for the degree of Doctor of Philosophy.

May 1999

Winfred M. Phillips
Dean, College of Engineering

M. J. Ohanian
Dean, Graduate School